THE PREPARATION, CHARACTERISATION AND CATALYTIC ACTIVITY OF TUNGSTEN BRONZES

THESIS SUBMITTED FOR THE DEGREE OF

DOCTOR OF PHILOSOPHY

BY

SHEENA STEVENSON

OCTOBER 1987

Department of Chemistry,
Brunel University,
Uxbridge,
Middlesex.

ACKNOWLEDGEMENTS

I would like to thank my supervisor, Dr. P.A. Sermon for his constant encouragement and advice throughout the work described in this thesis.

I would also like to thank my colleagues in the Chemistry Department for their friendship and support.

I wish to thank the technical staff of the Chemistry Department for their invaluable assistance.

I would also like to thank Mrs. Speed for typing this thesis.

-----oOo-----

A B S T R A C T

The structure and catalytic aspects of tungsten bronzes have been considered. A series of potassium tungsten bronzes, K_xWO_3, $0.05 \leqslant x \leqslant 0.8$, and the corresponding series of sodium tungsten bronzes, Na_xWO_3, $0.05 \leqslant x \leqslant 0.8$ were prepared by a thermal method. The thermal stability of the prepared samples was studied in the presence of both an oxidising and a reducing gas. The number and strength of acid sites present on the bronzes was studied by temperature-programmed desorption of ammonia. Xps, xrd and electrical resistivity measurements gave information about the bulk and surface properties of the bronzes. The activity of the tungsten bronzes for isopropanol decomposition and propene metathesis was investigated. In addition, a silica-supported tungsten bronze and a copper-potassium tungsten bronze, $Cu_yK_xWO_3$, were prepared. Their structures and catalytic values were considered.

TO MY FAMILY

C O N T E N T S

CHAPTER 1

INTRODUCTION

1.1 Oxide Bronzes

The term 'oxide bronze' is commonly used to describe a class of ternary oxide phases A_xMO_n, formally derived by insertion of an electropositive element, A, into an oxide matrix MO_n of a transition metal M. Typical parent oxides MO_n include those of W, Mo, V and Ti, where M is in its highest oxidation state. The structures adopted bv the MO_n matrices in these compounds are closely related to (but not identical with) those of the normal oxides and involve open co-valent frameworks of linked metal-oxygen polyhedra enclosing sites available for occupation by the A species. The electropositive element A, for example an alkali metal, enters the matrix as a cation and the average oxidation state of M is lowered accordingly.

As early as 1823, Wöhler[1] prepared sodium tungsten bronzes and somewhat later Laurent[2], von Knorre[3], and Schäfer[4] reported the same type of compounds with potassium, lithium and rubidium respectively. These compounds were believed to be stoichiometric until 1935 when Hägg[5] in an x-ray diffraction study found that sodium tungsten bronzes of cubic symmetry belonged to a continuous series of solid solutions.

1.2 Structures of Oxide Bronzes

In A_xMO_n, the transition metal, M is usually in a high oxidation state and has a small crystal radius relative to O^{2-}. It exerts strong directional bonding effects on its nearest neighbours in the

crystal. Accordingly tunnel and layer structures occur, consisting of linked polyhedra. Such structural types can accommodate a large variation in A content, either in the interstices or between the layers.

The common structural unit of the transition metal oxides that form oxide bronzes is the MO_6 octahedron. The octahedra may be essentially regular, as found in W, Ti and Nb oxides, or severely deformed, as observed in the vanadium oxides where the coordination is closer to that of a trigonal bipyramid. The mode of linking the octahedra (i.e. vertex, edge or face sharing), also differs significantly among these transition metals. The possibilities are restricted by the stoichiometry of the framework, a small ratio of oxygen to metal atoms precluding extensive vertex sharing, but even when the stoichiometry is the same the transition metals exhibit individual behaviour. For example, WO_3 consists entirely of vertex-shared octahedra whereas MoO_3 is a layer structure of edge-shared octahedra.

The differences in the coordination of the transition metals in their oxides also persist in the bronzes which often possess structures closely related to the parent oxide. Thus, observed are the tunnel structures of the tungsten bronzes, the layer structures of the molybdenum bronzes and the complex vanadium bronzes containing irregular coordination. The geometry of the structure depends on the number of A ions to be inserted, their size, and their coordination requirements. The extent to which these requirements are met is determined by the flexibility of the host framework. This varies widely among the transition metals that form bronzes and is responsible for the very different types of structure observed.

Despite the complexity and variety of bronze structures, it is possible to describe their structures in terms of surprisingly few simple groups of octahedra. This is an approach that has been emphasised by Wadsley in transition metal oxide chemistry[6] and implies an extended covalent bonded system beyond the immediate environment of the metal atom. Attention here will be focused on the simple tunnel structures of W, which consist of three-dimensional frameworks constructed from infinite chains of octahedra, the octahedral clusters of the molybdenum bronzes and the vanadium bronzes which contain common ribbons and sheets of octahedra.

Tungsten Bronzes

All the known tungsten bronze structures contain a three-dimensional tunnel framework of the host lattice of stoichiometry WO_3, consisting of single ReO_3 chains (Figure 1.1) which share all equatorial vertices with four other chains.

Alkali metal tungsten bronzes adopt four different types of structures. These are (i) perovskite tungsten bronzes, PTB, (ii) tetragonal tungsten bronzes, TTB, (iii) hexagonal tungsten bronzes, HTB and (iv) intergrowth tungsten bronzes.

Perovskite tungsten bronzes are formed only by lithium and sodium at atmospheric pressure. The perovskite type structure exhibits the highest symmetry among the bronze structures. It is analogous to that of perovskite, ABO_3 but with the A positions only partially occupied. It can also be regarded as consisting of four-membered rings of WO_6 octahedra forming tunnels of square cross-section running along the cube axes as shown in Figure 1.2. The

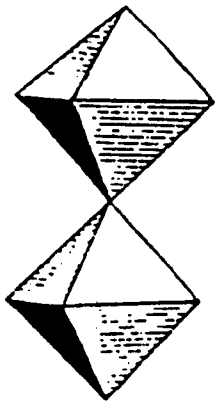

Figure 1.1 Single ReO_3 chain

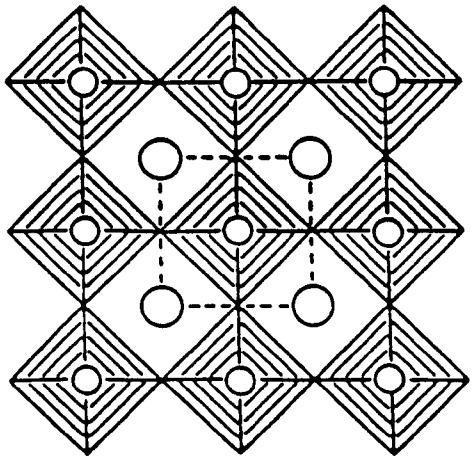

Figure 1.2 The structure of perovskite tungsten bronze, PTB. The large circles indicate interstitial metal atoms and the small circles tungsten atoms.

maximum radius of the sphere that can be accommodated in the 12 coordinated sites (square tunnels) formed by the regular WO_6 octahedra is 0.13nm (assuming rO^{2-} = 0.14nm and a = 0.38nm). This permits only light alkali atoms (lithium and sodium) to occupy these sites. Potassium, rubidium and cesium have effective ionic radii greater than 0.13nm and do not form PTB phases at atmospheric pressure. Magnéli[7] determined the structure of a sodium bronze of composition, $Na_{0\text{-}10}WO_3$. This phase is very closely related to that of a perovskite bronze. The tungsten atoms in this phase are displaced in alternating directions along the c-axis forming puckered layers. Due to this puckering the unit cell becomes tetragonal rather than cubic and the cell volume is doubled. This phase also forms with lithium.

Among the alkali metals only sodium and potassium form tetragonal tungsten bronzes. The structure can be regarded as built up of three - four - and five-membered rings of WO_6 octahedra as shown in Figure 1.3. The interstitial holes thus formed are of three types: trigonal, tetragonal and pentagonal. The tungsten atoms in potassium TTB lie in the same plane and are thus not puckered. However, in the corresponding sodium TTB phase, the tungsten atoms form puckered layers when x is 0.33 while they lie in the same plane when x is 0.48. The alkali metal atoms are located in the tetragonal and pentagonal tunnels. If all these available sites are completely filled x becomes 0.66.

The hexagonal tungsten bronzes are formed by a considerable number of elements. Like TTB it is built up of WO_6 octahedra sharing corners and arranged in layers normal to the hexagonal axis stacked on top of each other and connected by common corners perpendicular to this axis as shown in Figure 1.4. The WO_6 octahedra form a network

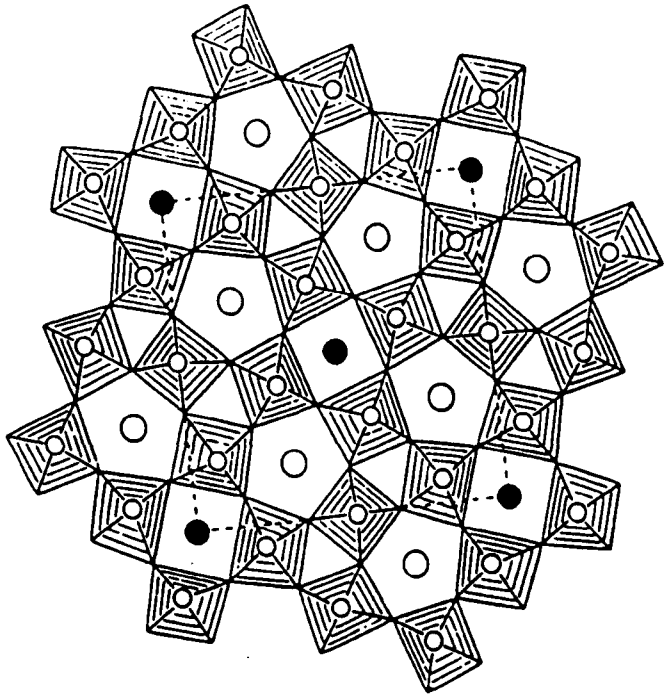

Figure 1.3 The crystal structure of tetragonal tungsten bronze, TTB, projected onto the xy plane. The WO_6 octahedra are shown shaded. The large open and filled circles indicate the alkali metal atoms, located in tetragonal and pentagonal tunnels respectively.

of three and six membered rings. The unit cell of the hexagonal phase contains two WO_6 layers along the hexagonal axis, which differ only by a small displacement of the atoms in opposite directions. The alkali metal atoms normally occupy the hexagonal tunnels only. The maximum theoretical x is 0.33 when the tunnels are completely occupied. At atmospheric pressure only the heavier alkali HTB's (i.e. involving K, Rb and Cs) are stable. (Thus those of Na and Li HTB's can only be prepared exclusively at high pressure[8]). Mixed HTB's in which one of the alkali metals is sodium or lithium are also known[9]. In the case of $(K,Li)_x WO_3$ Banks and Goldstein[10] have shown that the smaller Li ions are probably located in the tunnels of trigonal cross-section, because the maximum value of x is as high as 0.51.

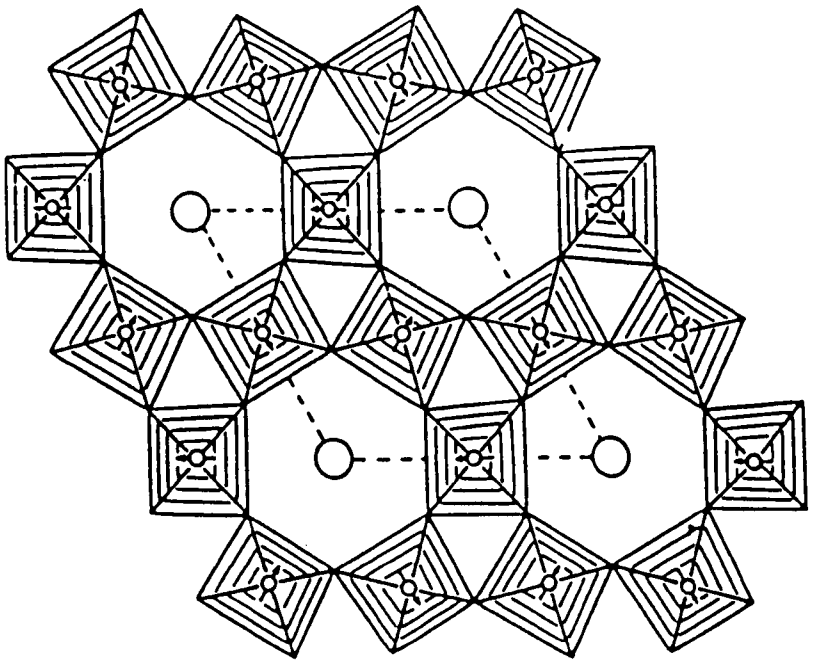

Figure 1.4 The crystal structure of hexagonal tungsten bronze, HTB. The small circles represent tungsten atoms. The displacements of the tungsten atoms in this layer with respect to the corresponding atoms in the layers above and below are shown by arrows. The large circles in the hexagonal tunnels are the alkali metal atoms (K, Rb and Cs). The unit cell extends over two layers.

A fourth type of bronze, called "Intergrowth tungsten bronze, ITB" was discovered recently[11]. This type forms with potassium, rubidium, cesium and also with thallium. The structure type shown in Figure 1.5 can be regarded as an intergrowth of HTB and WO_3 slabs. The WO_6 octahedra in the WO_3 slabs are tilted through 15^o (ideally) in an alternating sequence to make the two structure elements fit together. The alkali metals are located in the hexagonal tunnels. ITB's are formed at very low concentrations ($x < 0.10$) of the heavy alkali metals.

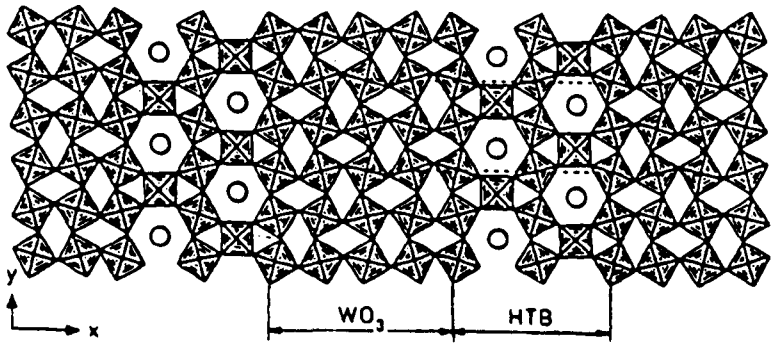

Figure 1.5 The structure of an intergrowth tungsten bronze. The HTB and WO_3 slabs are marked. The large circles in the hexagonal tunnels indicate the positions of the heavy alkali metal atoms.

Molybdenum Bronzes

MoO_3 itself has a layer structure. The layers consist of double ReO_3 chains sharing edges in the staggered manner shown in Figure 1.6. In the hydrogen molybdenum bronze, H_xMoO_3, the H atoms are inserted as hydroxyl groups between the layers, in the basic framework. The lithium molybdenum bronze, Li_xMoO_3 is also closely related structurally to the parent oxide. In contrast the well characterised molybdenum bronzes $K_{0.33}MoO_3$ and K_xMoO_3 ($0.28 \leqslant x \leqslant 0.30$) have structures derived from octahedral clusters. The red $K_{0.33}MoO_3$ phase contains a cluster of six octahedra as shown in Figure 1.7. The potassium ions completely occupy positions of irregular eightfold coordination and bond the layers together, with a theoretical composition limit of $x = 0.33$.

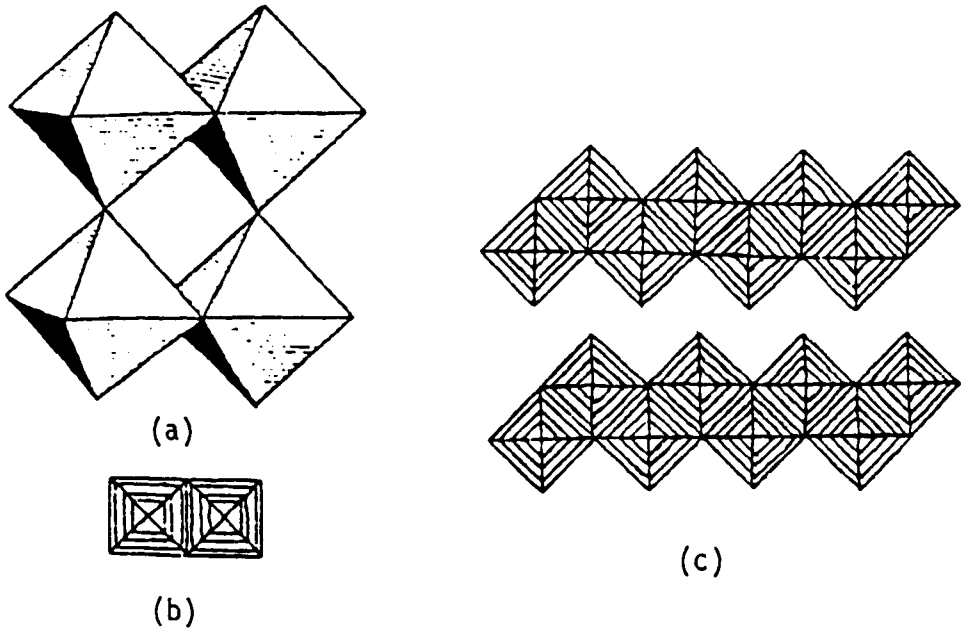

Figure 1.6 (a) The double ReO_3 chain,
(b) Projection along chain axis and,
(c) MoO_3 layer structure.

Blue K_xMoO_3 ($0.28 \leqslant x \leqslant 0.30$) contains a different cluster consisting of ten edge-shared octahedra as shown in Figure 1.8. The potassium ions again occupy sites between the layers which are fully occupied at $x = 0.30$. The molybdenum bronzes have been found to be much less stable than the tungsten bronzes, due mainly, to the tendency of molybdenum +5 to disproportionate.

Vanadium Bronzes

The idealized V_2O_5 structure Figure 1.9(a) can be generated by linking together single octahedral ribbons, Figure 1.9(b), formed by shearing two ReO_3 chains together along common octahedral edges. Each ribbon connects via its free vertices to four similar ribbons.

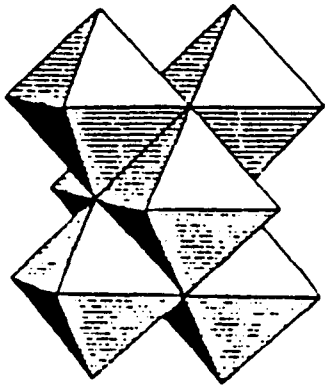

Figure 1.7 Six-unit cluster in red $K_{0.33}MoO_3$

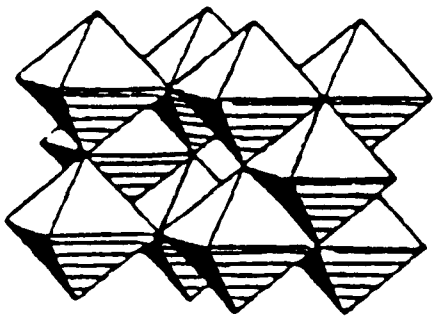

Figure 1.8 Ten unit cluster in blue $K_{0.30}MoO_3$

In the actual structure considerable distortion from this simple representation occurs; the coordination is closer to fivefold (trigonal pyramidal), and the compound has a layer structure rather than a tunnel structure (Figure 1.9(c)). One vanadium bronze structure, the α-phase, is based on this structure. It is found for small concentrations of A atoms, e.g. $Na_xV_2O_5$ ($0 \leqslant x \leqslant 0.02$) where the inter-layer sites of a more symmetrical V_2O_5 lattice are occupied. The α´- $Na_xV_2O_5$ phase ($0.70 \leqslant x \leqslant 1$) has a similar structure. The β - $Na_xV_2O_5$ structure ($0.22 \leqslant x \leqslant 0.40$) contains irregularly shaped tunnels enclosed by both double (essentially octahedral) and single (trigonal bipyramidal) ribbons, as shown in Figure 1.10. The sodium atoms in the β-phase occupy the tunnel sites M_1, but the proximity of neighbouring sites prohibit their simultaneous occupation. The upper composition level is $x = 0.33$, corresponding to a zig-zag arrangement by the A ions down the tunnel. The extra positions M_2 and M_3 may be occupied by smaller insertion elements, e.g. in

β´- $Li_xV_2O_5$ ($0.44 \leqslant x \leqslant 0.49$) and

β - $Cu_xV_2O_5$ ($0.26 \leqslant x \leqslant 0.64$)

1.3 Properties of Oxide Bronzes

The tungsten bronzes have been the subject of many investigations due to their interesting properties. Some of their physical properties are described below to illustrate those of oxide bronzes more generally.

1.3.1 Electronic Properties

The oxide bronzes are electronic conductors either metallic, as for example A_xWO_3[12], $A_{0.5+x}NbO_3$[13], $NaMo_6O_{17}$[14] or semiconducting as in the case of $A_xV_2O_5$[12], $K_{0.33}MoO_3$[15] and A_xMnO_2[16]. A consistent

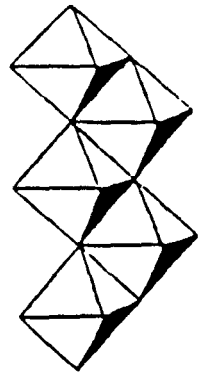

(a)

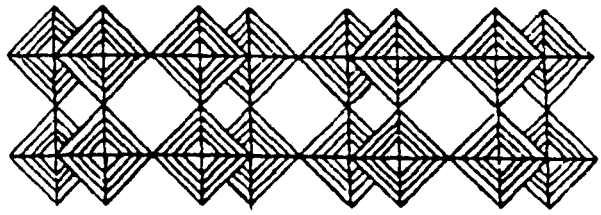

(b)

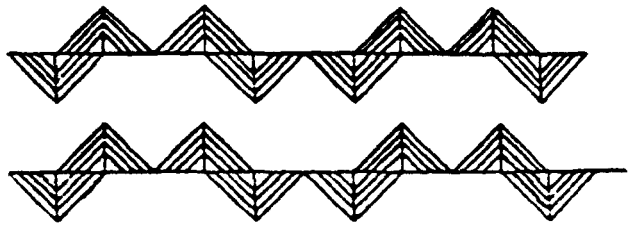

(c)

Figure 1.9 (a) V_2O_5 structure (idealised) represented as octahedra,
(b) The single octahedra ribbon, and
(c) V_2O_5 represented as bipyramids.

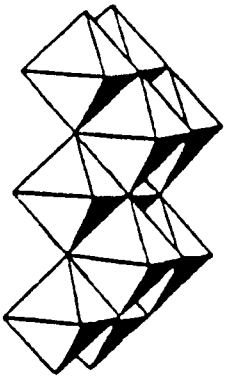

(a)

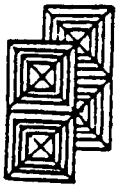

(b)

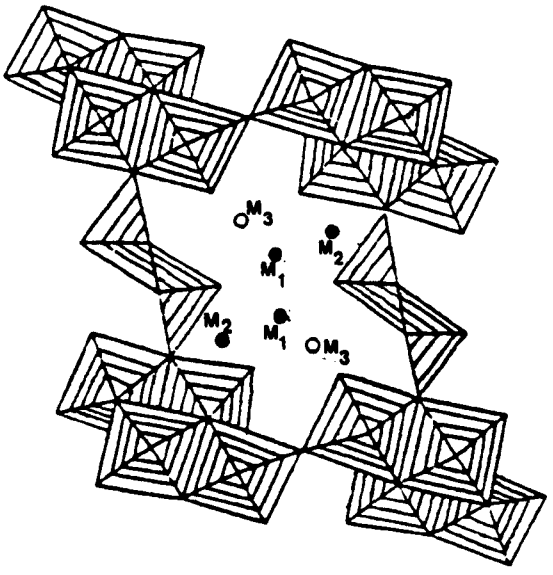

(c)

Figure 1.10 (a) The double octahedra ribbon,

(b) projection along chain length, and

(c) β - $Na_xV_2O_5$ structure

model for their electronic structures suggests that the inserted element A enters the oxide matrix MO_n as a cation and its valence electrons are donated to the transition metal oxide framework. The donated electrons either occupy a delocalised conduction band, in which case metallic behaviour results, or are trapped at individual metal sites, causing the material to behave as a semiconductor. The main lines of evidence for this general viewpoint can be summarised as follows; (a) the nature of A in A_xMO_n affects the electronic conductivity of the bronze only through the number, Zmx of valence electrons provided[17], (b) N.M.R. measurements on Na_xWO_3[18] and $Li_xV_2O_5$[19] reveal the absence of a Knight shift at the alkali metal nuclei, a result consistent with their presence as cations, (c) in the case of the metallic bronzes, collective electron behaviour as determined by measurements of magnetic susceptibility[20], electronic specific heat[21], optical reflectivity[22], and Seebeck and Hall coefficients[23,24] is consistent with participation of Zmx nearly free electrons in a broad conduction band, and (d) in the case of semiconducting vanadium bronzes, measurements of magnetic susceptibility[25] and e.p.r.[19], confirm the presence of isolated V^{4+} levels.

The band structure in various oxides has been discussed by Goodenough[26] and his description of the binding in cubic Na_xWO_3 is a useful prototype for the electronic structures of metallic oxide bronzes.

The extent of the interaction between the transition metal orbitals in A_xMO_n, either by direct overlap or through M-O-M, will depend on the spatial extent of the d orbitals involved. On this basis the elements of the second and third transition series are more

likely to form delocalised band structures than are the corresponding (later) members of the first transition series, V, Cr, Mn. The observed localised electron behaviour of these elements in $Na_xV_2O_5$, $Na_2Cr_3O_9$[27] and K_xMnO_2 is consistent with this.

Several, more subtle, relationships between structure and electronic behaviour have not yet been satisfactorily explained. Thus the origins of the metal-semiconductor transitions in Na_xWO_3[17] (at $x \sim 0.25$) and $K_{0.30}MoO_3$[15,25] (at $T \sim 173K$) are uncertain as is the observation that superconductivity is found for tetragonal and hexagonal tungsten bronzes but not for cubic phases[28,29-31]. A recent study by Sermon et al[32] has shown that tungsten bronzes prepared under vacuum have ionic conductivity properties.

1.3.2 Magnetic Properties

Greiner[33] measured the magnetic susceptibility of single crystals of sodium tungsten bronzes and found them to be temperature-independent paramagnetic. Dickens and Whittingham[34] reported that the measurements made on powder samples of the alkali metal tungsten bronzes reveal similar behaviour. Sienko measured the susceptibility of alkali metal tungsten bronzes (Li, Na, K and Rb)[35]. They found Rb[36] and some of the Li[37] and K[38] bronzes diamagnetic while Na[38] are weakly paramagnetic. The reasons for such deviations is not clear, however, in some cases it may be due to different measurement techniques. It is of interest to mention that Bouchard and Gillson[39] reported hexagonal indium bronze as diamagnetic. According to them this is due to the compensation of the very weak Pauli paramagnetism by the diamagnetism of the indium ions. Their studies also included measurements of the magnetic susceptibility of single crystals of In_xWO_3 along both the crystallographic axes, but no

difference was observed.

1.3.3 Optical Properties

One of the most interesting features of the tungsten bronzes is their optical properties. The colour of the cubic Na_xWO_3 changes with increasing sodium content. According to Hagg[40] this is connected with the proportion of penta- and hexavalent tungsten atoms in the lattice. Magnéli[41] reported that the colour of the tungsten oxides and bronzes are dependent on the average valency of the tungsten atoms. Recently electro-chromic effects were observed in the Na_xWO_3, K_xWO_3 and Rb_xWO_3 systems which may have great practical applicability[42].

1.3.4 Chemical Properties

The tungsten bronzes are characterised by a very great chemical inertia, which makes chemical analysis difficult[43]. They react only with chemical agents capable of attacking the WO_3 lattice, the location of the insertion ions within the channels effectively protecting them from their usual reagents. Hence acids, even in relatively strong concentrations, have no reaction with the phases M_xWO_3. These properties are of obvious applied interest for applications purposes and their use as catalysts in an acid solution has been considered. However, tungsten bronzes are unstable in an alkaline medium.

The vanadium bronzes are also very inert to chemical reaction, except in an oxidising environment. However, they are less resistant to acid attack than are the tungsten bronzes. One interesting feature of the vanadium bronzes is that they can fix oxygen which they lose again at higher temperatures. The amount of fixed oxygen depends on the composition of the bronze and on the nature and

duration of the heat treatment.

1.4 Preparation of Oxide Bronzes

Generally oxide bronzes may be prepared by thermal and electrochemical methods. Wöhler[1] first prepared tungsten bronzes by reducing a mixture of sodium tungstate and tungsten trioxide in gaseous hydrogen. Later[44] reducing agents such as Sn, Zn, and Fe were used.

Electrolytic reduction is generally used to obtain single bronze crystals and was applied at an early stage[45] using a molten mixture of metal tungstate and tungstic acid.

The molybdenum bronzes are much less stable than the tungsten bronzes and this lack of stability explains why until recently it has been possible to prepare them by only two methods : electrolytic reduction and high-pressure synthesis. These two methods give, with only one exception, phases having entirely different structures. Whereas the first produces new structural types, the second leads to the various structures already described for the tungsten bronzes. Recently Réau et al[14] have studied the MoO_3- MoO_2M_2O (M = Li, Na, K) systems in sealed gold tubes and in a limited temperature range (833K - 863K). They found not only the phases obtained by electrolytic reduction, but also a number of new ones. The role of the sealed tube is to prevent decomposition.

Hydrogen bronzes may be prepared by spillover from phases active in hydrogen dissociation[46]. Thus the formation of $H_{0.5}WO_3$, $H_{1.7}MoO_3$ and $H_{3.3}V_3O_8$ has been reported[47,48] and also $H_{1.4}ReO_3$[49].

1.5 Catalysis - General Theories

A catalyst is a substance which increases the rate of attainment of equilibrium of a reacting system without causing any great alteration in the free energy changes involved and without itself undergoing a chemical change. In heterogeneous catalysis, the catalyst is in a different phase from the reactant and is usually a solid. In such a system the reaction takes place at the interface between the catalyst and the less-dense phase. A necessary precursor to reaction is the adsorption of the reactant at the catalyst surface. The adsorption of molecules at solid surfaces is a long known and much studied phenomenon[50]. A catalysed reaction must therefore involve more than one rate process : adsorption, the formation and breakup of an activated complex, and desorption of the products. Each of these has its own activation energy. The rate of each is also determined by the total surface area of the catalyst present, or, more precisely, the number of active sites, and by the concentration on the catalyst surface of various adsorbed species.

Heterogeneous catalysts may be divided into two distinct groups : (i) metals, and (ii) non-metals. The former group is comprised largely of the metals of Group VIII and IB, and the latter of metal oxides and sulphides, and acids. The non-metal catalysts may be further subdivided according to their electrical conductivity into (a) semiconductors, and (b) insulators. Metals, in general, are good catalysts for reactions involving hydrogen atom addition or abstraction. Semiconductor catalysts are good for oxidation-reduction processes. Insulators, of which alumina and silica are the most important, are good dehydration catalysts.

1.6 Catalysis and Solid State Chemistry

1.6.1 Oxide Bronzes as Catalysts

Solid state chemistry and physics are increasingly brought to bear on the formation of catalytic materials. The interdisciplinary field of solid state science, touching on the relation between the properties of materials and atomic structure provides a natural matrix for the elucidation of structure-property relationships of defect solids used as catalysts. The earliest application of oxide bronzes for the catalysis of a desired chemical reaction was in the field of electrocatalysis as electrodes in fuel cells[51]. Recently, there have been scattered reports of activity in other processes as well. Bronzes could play an important role for the correlation of solid state chemistry and physics with catalytic properties. Metallic Tungsten bronzes, M_xWO_3, $x \gtrsim 0.25$, have been used for various electrode processes but are particularly interesting as oxygen electrodes (cathodes) in fuel cells. Sodium tungsten bronzes have shown considerable activity in the electrode reactions of peroxo species in acid media. The hydrogen electrode reactions over tungsten bronzes in acid media have been studied for the cathodic hydrogen evolution reaction and the anodic hydrogen oxidation reaction

1.6.2 Alcohol Decomposition

The two basic modes of alcohol decomposition are: (a) dehydrogenation to form an aldehyde (in the case of primary alcohols) or a ketone and hydrogen (in the case of secondary alcohols), and (b) dehydration to form an alkene and water. According to current theories, catalyst activity and selectivity in this reaction may be related to lattice parameters, type of conductivity and width of the forbidden

zone as well as to the acidic properties of the surface[52-55]. Many workers[56-58] have used the activity for the decomposition of 2-Propanol (Isopropyl alcohol) as a measure of the acidity of various catalyst systems and found good correlations with acidity measured by adsorption of ammonia or pyridine. The two main paths of the decomposition of 2-Propanol (IPA) are given in Figure 1.11. The catalytic activity for dehydration of IPA to propene has been found to

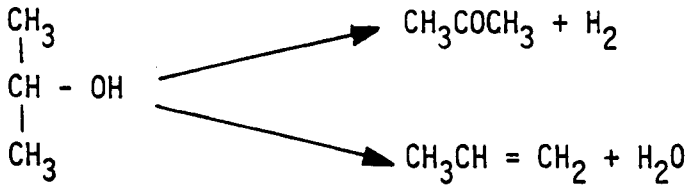

Figure 1.11

be proportional to the acidity of a catalyst[59], whereas the activity for dehydrogenation of IPA to acetone is assumed to be proportional to the basicity of a catalyst[60-62]. The tungsten bronzes, M_xWO_3 where M = Na or K and $0 \leqslant x \leqslant 0.8$, may be thought to contain both acidic and basic sites, which vary according to alkali ion content. Thus the decomposition of isopropanol was chosen as a probe reaction for characterising the acid-base properties of the sodium and potassium bronzes prepared here.

1.6.3 Alkene Metathesis

Since first discovered by Banks and Bailey[63], the alkene metathesis (disproportionation) reaction has been the subject of many investigations[64]. The reaction may be regarded as a net breaking and re-formation of two olefinic carbon-carbon bonds, as depicted by Figure 1.12 for the metathesis of propene, producing a mixture of ethene and cis- and trans-2-butene. Olefin metathesis is catalysed by a

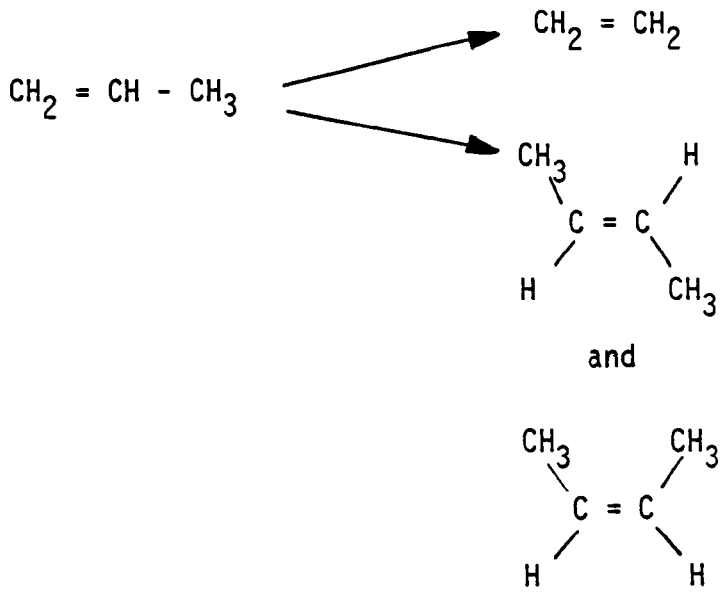

Figure 1.12

variety of both heterogeneous and homogeneous systems[65], in heterogeneous catalysts it is known to occur mainly over rhenium, tungsten and molybdenum compounds[66]. For the metathesis of propene in particular, the catalyst Re_2O_7/Al_2O_3 can catalyse the reaction at low temperatures, with good activity and a high selectivity[67,64]. It has recently been shown for the same metathesis reaction, dimerisation (producing mainly hexenes) was dominant over insulating WO_3, while the major products over metallic ReO_3 were those of metathesis of propene (i.e. ethene and but-2-enes). Metallic ReO_3 may be thought of as an isoelectronic analog of both $NaWO_3$ and KWO_3. WO_3 and MWO_3 (M = Na or K) are end members of M_xWO_3 and have insulating properties when $x < 0.25$ and metallic conductivity when $x > 0.25$[68]. Thus an interesting reaction to probe the bulk properties of the potassium and sodium bronzes prepared here will be that of the catalytic reaction of propene, which could change from dimerisation to metathesis over M_xWO_3 (M = Na or K) when x is increased from zero to 0.8 due to changes in electrical properties.

1.6.4 Ammonia Synthesis on Supported Potassium Tungsten Bronzes

Since the early nineteenth century, many attempts have been made to catalyse the synthesis of ammonia from nitrogen and hydrogen:

$$N_2 + 3H_2 \longrightarrow 2NH_3 \qquad \Delta H = -109 kJmol^{-1}$$

The quantity of nitrogen and hydrogen combining into ammonia depends on the operating pressure, temperature and H_2/N_2 ratio. Table 1.1 shows the equilibrium yields in percentage of ammonia at different pressures and temperatures.

	2.5MPa	5MPa	10MPa	20MPa	40MPa
373K	91.7	94.5	96.5	98.4	99.4
573K	63.6	73.5	82.0	89.0	94.6
673K	27.4	39.6	53.1	66.7	79.7
773K	8.7	15.4	25.4	38.8	55.4
873K	2.9	5.6	10.5	18.3	39.1

Table 1.1 Equilibrium yields of ammonia at different temperatures and pressures

Two fundamental facts are shown in Table 1.1; (a) under the same pressure conditions, the ammonia equilibrium yields decrease with increasing temperature, and (b) under equal temperature conditions, the equilibrium ammonia yield increases with increasing pressure. From these facts it is clear that the exothermic synthesis of ammonia is thermodynamically favoured at low temperature and high pressure.

The rate-determining step in the reaction was first associated

with the adsorption of nitrogen in the early 1930s[69]. This view was then substantiated by the pioneering kinetic studies of Emmett and Brunauer[70] who found that the overall rate of N_2 adsorption is of the same order of magnitude as the rate of ammonia synthesis on the catalyst surfaces studied. In addition, Kozhenova and Kagan later showed that the hydrogenation proceeds much faster than nitrogen adsorption[71]. Although there was a general consensus about the rate-determining step, the nature of the catalytically active nitrogen species was in contention. Formally, the overall reaction can be divided into the following sequence of individual molecular steps assuming that (a) dissociatively adsorbed nitrogen, N_{ad}, or (b) molecular nitrogen, N_{2ad}, is hydrogenated stepwise to NH_3.

(a) Dissociative mechanism

$$N_{2g} + 3H_{2g} \rightleftharpoons 2N_{ad} + 6H_{ad}$$

$$2N_{ad} + 6H_{ad} \rightleftharpoons 2NH_{ad} + 4H_{ad}$$

$$2NH_{ad} + 4H_{ad} \rightleftharpoons 2NH_{2ad} + 2H_{ad}$$

$$2NH_{2ad} + 2H_{ad} \rightleftharpoons 2NH_{3ad}$$

$$2NH_{3ad} \rightleftharpoons 2NH_{3g}$$

(b) Molecular mechanism

$$N_2 + 3H_2 \rightleftharpoons N_{2ad} + 6H_{ad}$$

$$N_{2ad} + 6H_{ad} \rightleftharpoons N_2H_{2ad} + 4H_{ad}$$

$$N_2H_{2ad} + 4H_{ad} \rightleftharpoons N_2H_{4ad} + 2H_{ad}$$

$$N_2H_{4ad} + 2H_{ad} \rightleftharpoons 2NH_{3ad}$$

$$2NH_{3ad} \rightleftharpoons 2NH_{3g}$$

The dissociative adsorption of hydrogen on iron and other metal catalysts was always well-established and therefore a reaction mechanism via molecular hydrogen species need not be considered. In the reaction sequence (a), it is assumed that atomic nitrogen and hydrogen react via intermediate imine and amine surface species while in sequence (b), the reaction of molecularly adsorbed N_2 proceeds through the formation of diimine and hydrazine to finally give ammonia. The final step in both models is the desorption of ammonia from the catalyst surface.

A variety of catalysts have been used for ammonia synthesis, including Pt foil, Os, dispersed iron and electrolytically deposited Mn. A promoted iron catalyst that, with the addition or substitution of other promoters, was eventually developed, and is still the catalyst universally used today. Recent studies[72] have shown that potassium tungsten bronzes supported on Al_2O_3 have shown some catalytic activity for the synthesis of ammonia from its elements. The bronzes were prepared by impregnation of an alumina support with an aqueous solution of potassium tungstate followed by reduction in hydrogen at high temperature. The rate of ammonia synthesis on these bronzes was observed to increase with temperature, the initial rate however was seen to decrease rapidly with time. This rapid fall in rate was explained in terms of an intermediate species being strongly adsorbed on the surface.

1.6.5 Methanol Synthesis and the Water-Gas-Shift Reaction on Copper Based Catalysts

Methanol synthesis consists of the hydrogenation of carbon monoxide or carbon dioxide according to:

$$CO + H_2 \rightleftharpoons CH_3OH \qquad \Delta H_{600K} = -100.46 kJmol^{-1}$$

and

$$CO_2 + 3H_2 \rightleftharpoons CH_3OH + H_2O \qquad \Delta H_{600K} = -61.59 kJmol^{-1}$$

The catalysts used for this synthesis are based on copper and combinations of various oxides (ZnO, Al_2O_3, Cr_2O_3 and TiO_2). Copper based catalysts have also shown considerable activity for the water-gas-shift reaction:-

$$CO + H_2 \rightleftharpoons CO_2 + H_2 \qquad \Delta H = -40.6 kJmol^{-1}$$

which is a reaction most frequently used in conjunction with the production of hydrogen via the steam reforming of hydrocarbons. For methanol synthesis and the shift reaction, copper is more active when supported on ZnO than on titania[73]. There is current uncertainty regarding the precise oxidation state of ZnO supported Cu under conditions of use[74], however very recent work[75] has shown that Cu (II) in $CuFe_xCr_{z-x}O_4$ spinels is as active as Cu/ZnO under conditions when it would not have been significantly reduced.

1.7 Present Study

The present study was undertaken to understand the surface and bulk properties of some unsupported tungsten bronzes M_xWO_3, where M = Na or K and $0 \leqslant x \leqslant 0.8$, and establish their catalytic activity towards the decomposition of isopropanol and the metathesis of propene. The programme of work was as follows:

(1) Preparation of the potassium and sodium tungsten bronzes by the following reaction;

$$3xM_2WO_4 + (6-4x)WO_3 + xW \xrightarrow{\sim 1173K} 6M_xWO_3$$

where M = Na or K

(2) Surface characterisation and morphology of the potassium and sodium tungsten bronzes.

(3) Study of the thermal stability of the bronzes in hydrogen and in air.

(4) Characterisation of the bronze samples by x-ray photoelectron spectroscopy and x-ray diffraction.

(5) Study of the electrical properties of the bronze samples.

(6) Study of the catalytic activity of the bronzes for the decomposition of isopropanol and for the metathesis of propene.

(7) Preparation of $Cu_yK_xWO_3$ by an ion-exchange method since preparation of such a sample by a thermal method is difficult due to thermodynamic limitations required at the high temperature to overcome the slow rate of formation.

(8) Previous studies[72] have shown that potassium bronzes supported on alumina have a slight catalytic activity for ammonia synthesis. A silica-supported bronze was prepared for comparison with the alumina supported bronzes.

The results of the work carried out on the alumina-supported potassium tungsten bronzes is described in Appendix I.

CHAPTER 1

REFERENCES

1. F. Wöhler, Ann. Chim. Phys., (2), 43, 29, (1823).
2. A. Laurent, Ann. Chim. Phys., (2), 67, 215, (1838).
3. G. von Knorre, J. Prakt. Chem., (2), 27, 49, (1883).
4. E. Schäfer, Z. Anorg. Allg. Chem., 38, 142, (1903).
5. G. Hägg, Z. Phys. Chem., B29, 192, (1935).
6. A.D. Wadsley, Helv. Chim. Acta. Fascic. Extraord., Alfred Werner, 207, (1967).
7. A. Magnéli, Nova. Acta. Regiae Soc. Sci., Upsaliensis, 14, 4, (1950).
8. T.A. Bither, J.L. Gillson and H.S. Young, Inorg. Chem., 5, 1559, (1966).
9. E.O. Brimm, J.C. Brantky, J.H. Lorenz and M.H. Jellinek, J. Am. Chem. Soc., 73, 5427, (1951).
10. E. Banks and A. Goldstein, Inorg. Chem., 7, 966, (1968).
11. A. Hussain, L. Kihlborg, Acta. Crystallogr., A32, 551, (1976).
12. P. Hagenmuller, 'The Chemistry of Extended Defects in Non-Metallic Solids', (1970), L. Eyring, M.O'Keefe, Editors. (Amsterdam : North Holland Publishing Co.)
13. D. Ridgley and R. Ward, J. Am. Chem. Soc., 77, 6132, (1955).
14. J.M. Reau, C. Fouassier and P. Hagenmuller J. Solid State Chem., 1, 326, (1970).
15. G.H. Bouchard, J. Perlstein and M.J. Sienko, Inorg. Chem., 6, 1682, (1967).
16. J.P. Parant, R. Olazcuaga, M. Devalette, C. Fouassier and P. Hagenmuller, J. Solid State Chem., 3, 1, (1971).
17. H.R. Shanks, P.R. Sidles and G.C. Danielson, 'Non-Stoichiometric Compounds', Chemistry Series No. 39, 237, (1963).

18. W.H. Jones, E.A. Gabarty and R.G. Barnes, J. Chem. Phys., 36, 494, (1962).

19. G. Gendell, R. Cotts and M.J. Sienko, J. Chem. Phys., 37, 220, (1962).

20. J.D. Greiner, H.R. Shanks and D.C. Wallace, J. Chem. Phys., 34, 772, (1962).

21. R.W. Vert, M. Griffel and J.F. Smith, J. Chem. Phys., 28, 293, (1958).

22. P.G. Dickens, R.M.P. Quilliam, M.S. Whittingham, Mater. Res. Bull, 3, 941, (1968).

23. L.D. Muhlestein and G.C. Danielson, Phys. Rev., 158, 825, (1967).

24. L.D. Muhlestein and G.C. Danielson, Phys. Rev., 160, 562, (1967).

25. A. Wold, W. Kunnmann, R.J. Arnott and A. Ferretti, Inorg. Chem., 3, 545, (1964).

26. J.B. Goodenough, Prog. in Solid State Chem., 5, 145, (1971).

27. T.A. Bither, J.L. Gillson and H.S. Young, Inorg. Chem., 5, 1559, (1966).

28. T.E. Gier, D.C. Pease, A.W. Sleight and T.A. Bither, Inorg. Chem., 7, 1646, (1968).

29. A. Narath and D.C. Wallace, Phys. Rev. 127, 724, (1962).

30. A.R. Sweedler, C.J. Raub and B.T. Matthias, Phys. Lett, 15, 108, (1965).

31. J.R. Remeika, T.H. Geballe, B.T. Matthias, A.S. Cooper, G.W. Hall and E.M. Kelly, Phys. Lett, 24A, 565, (1967).

32. S.A. Lawrence, S. Stevenson, K. Mavadia and P.A. Sermon, Proc. R. Soc., A411, 95, 1987.

33. J.O. Greiner, H.R. Shanks and D.C. Wallace, J. Chem. Phys., 36, 772, (1962).

34. P.G. Dickens and M.S. Whittingham, Quart. Rev., 22, 30, (1968).

35. M.J. Sienko, 'Non-Stoichiometric Compounds', Adv. in Chemistry Series No. 39, 224, (1963).

36. D.R. Wanlass and J.J. Sienko, J. Solid State Chem., 12, 362, (1975).

37. M.J. Sienko and S.M. Morehouse, Inorg. Chem., 2, 485, (1963).

38. M.J. Sienko and T.B.N. Troung, J. Am. Chem. Soc., 83, 3939, (1961).

39. R.J. Bouchard and J.L. Gillson, Inorg. Chem., 7, 969, (1968).

40. G. Hägg, Z. Phys. Chem., B29, 192, (1935).

41. A. Magnéli, Nova.Acta.Regine.Soc. Sci. Upsaliensis, 14, 4, (1950).

42. I. Lefkowitz and G.W. Taylor, Optics Commun., 15, 340, (1975).

43. A. Magnéli, Arkiv. Kemi., 1, 273, (1949).

44. E. Banks and A. Wold, Prepn. Inorg. Reactions, 4, (1968) Interscience.

45. E. Zettnow, Pogg. Ann., 130, 240, (1967).

46. P.A. Sermon and G.C. Bond, Catal. Rev., 8, 211, (1973).

47. P.A. Sermon and G.C. Bond, J. Chem. Soc., Faraday Trans. I, 72, 730, (1976); G.C. Bond, P.A. Sermon and C.J. Wright, Mater. Res. Bull., 19, 701, (1984).

48. P.A. Sermon and A.R. Berzins, Metal Hydrogen Systems. Ed. T.N. Verziroglu, 451, (1982).

49. P.G. Dickens and M.T. Weller, J. Solid State Chem., 48, 407, (1983).

50. G.C. Bond, Heterogeneous Catalysis, Principles and Applications, Oxford University Press, (Ed. P.W. Atkins, J.S.E. Holker, and A.K. Holliday), (1974).

51. J. McHardy, J.O'M. Bockris, 'From Electrocatalysis to Fuel Cells', G. Sandstede, Ed., University of Washington Press, Seattle and London, (1972).

52. S.Z. Roginski, Zh. Fiz. Khim., 6, 334, (1935).

53. S.Z. Roginski, Dokl. Akad. Nauk., USSR, 67, 97, (1949).

54. K. Hauffe, Reactions on Solids and their Surfaces, Russ. L. (1962).

55. G.M. Schwar, Adv. Catal., 2, 229, (1952).

56. M. Ali and S. Suzuki, Bull. Chem.Soc., Jap. 47,(12), 3074, (1974).

57. M. Ali, S. Suzuki, Bull. Chem. Soc., Jap. 46, 321, (1973).

58. K.T. Seo, S.C. Kang, H.J. Kim and S.K. Moon, Korean J. Chem. Eng., 2, (2), 163, (1985).

59. H. Pines, Adv. Catal., 16, 49, (1966).

60. M. Ali, Bull. Jap. Petrol. Inst., 18, 50, (1976).

61. M. Ali, Bull. Chem. Soc. Jap., 50, 355, (1977).

62. M. Ali, Bull Chem. Soc. Jap., 50, 2579, (1977).

63. R.L. Banks and C.G. Bailey, Ind. Eng. Chem. Prod. Res. Develop., 3, 170, (1964).

64. G.C. Bailey, Catal. Rev., 3, 37, (1969).

65. R.L. Banks, Top. Curr. Chem., 52, 39, (1972).

66. J.C. Mol and A.J. Movlijn in 'Advances in Catalysis', 24, 131, Academic Press N.Y. (1975).

67. L. Turner, E.J. Howman and K.V. Williams, British Patent No. 1,106,015

68. P.A. Lightsey, D.A. Lilienfeld and D.F. Holcomb, Phys. Rev. B. Condens. Matter., 14, 4730, (1976).

69. E. Winter, Z. Phys. Chem. B, 13,401, (1931).

70. P.H. Emmett and S. Brunauer, J. Am. Chem. Soc.,56, 35, (1934).

71. K.T. Kozhenova and M.Y. Kagan, J. Phys. Chem., USSR, 14, 1250, (1940).

72. S. Stevenson, M.Phil. Thesis, Brunel University, (1985).

73. E.M. Calverley and R.B. Anderson, J. Catal., 104, 434, (1987).

74. G.C.Chinchen and K.C. Waugh, J. Catal., 97, 280, (1980).

75. M.S.W. Vong, P.A. Sermon, M.A. Yates, A. Perryman and P. Reyes, Unpublished Work.

CHAPTER 2

PREPARATION OF POTASSIUM AND SODIUM TUNGSTEN BRONZES

2.1 Introduction

The tungsten bronzes are non-stoichiometric ternary metal oxides of general formula M_xWO_3 where M is a metal and $0< x < 1$. These compounds have been known from the beginning of the 19th century[1]. In recent years, many research groups have been studying these types of materials because of their interesting physical and chemical properties. The metal, M, to form bronzes of tungsten include potassium and sodium.

2.2 Synthesis of Tungsten Bronzes

A number of methods have been used to prepare tungsten bronzes. In 1823 Wöhler[1] first prepared the tungsten bronzes by reducing a mixture of sodium tungstate - tungsten trioxide with hydrogen gas. In 1838 Laurent[2] obtained a similar product using potassium tungstate. Later other reducing agents such as tin, zinc, and iron were also used[3].

Brunner[4] prepared the potassium bronzes by heating a mixture of K_2WO_4, WO_3 and WO_2 in vacuum. Later Straumanis[5] and also Brimm[6] used tungsten as a reducing agent to prepare sodium and potassium bronzes according to the following reaction;

$$3x\ M_2WO_4 + (6-4x)\ WO_3 + xW \xrightarrow[1173K]{} 6M_xWO_3$$

Metal chloride can be used instead of tungstate as a starting material[7]. Conroy and Yokokawa[8] prepared tetragonal barium tungsten bronzes using barium chloride as a starting material according to the

following reaction;

$$xBaCl_2 + WO_3 + xWO_2 \xrightarrow{1173K} Ba_xWO_3 + xWO_2Cl_{2(g)}$$

This method has also been used to prepare other alkaline earth metal tungsten bronzes with the possible substitution of bromine or iodine for chlorine[9]. Hexagonal tungsten bronzes have been prepared by the reaction of hexagonal WO_3 with metal vapours, within the temperature range of 473K - 673K[10]. The solid state reaction has been found quite versatile and is the most frequently used method for the preparation of bronzes.

Electrolytic reduction is generally used to obtain large single crystals of bronzes and was first applied by Zettnow[11] in 1867; a molten mixture of metal tungstate and tungstic acid was electrolytically reduced. Hägg[12], in his study of sodium bronzes, used this technique which was then further developed by Ellerbeck[13] and by Kunnman and Ferretti[14].

Sienko[15] prepared single crystals of Tl_xWO_3 by vapour-phase reaction of WO_3 and metallic Tl according to the following reaction;

$$xTl_{(g)} + WO_{3(g)} \xrightarrow{1173K} Tl_xWO_3$$

The crystals were deposited on a cold finger in the reaction vessel. This method is suitable if the metal is appreciably volatile at high temperatures. Aluminium bronzes have also been prepared by this method.

The hexagonal phases of lithium[16], ammonium[16], and the cubic potassium tungsten bronzes[17] which are not possible to prepare at atmospheric pressure may be synthesised at high pressure. This method permits in some cases the extension of compositional range to

higher x values, particularly of atoms having a valency state higher than one[18].

Tungsten bronzes prepared by the electrolytic methods are often obtained impure and thus require purification. They are remarkably stable against chemical reagents such as acids and use of this has been made in the purification process. Impurities can be removed by successive treatment of the sample with (i) boiling water[19]; (ii) boiling conc. HCl or aqua regia[20]; (iii) boiling in 40% hydrofluoric acid[20,21].

Recently[22] supported hexagonal potassium tungsten bronzes have been prepared by impregnation of a support with a solution of K_2WO_4, followed by reduction at 1023K in hydrogen gas.

2.3 Present Method of Preparation

2.3.1 Potassium and Sodium Bronzes

In the present study a series of potassium tungsten bronzes and a series of sodium tungsten bronzes was prepared by the solid state reaction using tungsten as the reducing agent according to the following equation;

$$3xM_2WO_4 + (6-4x)WO_3 + xW \xrightarrow{1173K} 6M_xWO_3$$

where M = K or Na

Both potassium and sodium tungstate were commercially available (KOCH Light Laboratories, 99.9%) together with WO_3 (Koch-Light, 99.5%), and W powder (BDH, 98%).

The appropriate weight of these starting materials was used to give an alkali metal ion content of 0.05, 0.2, 0.3, 0.6 and 0.8 mole fraction

(0.84% - 13.5%) in both the potassium and sodium tungsten bronzes. K_2WO_4, WO_3 and W powder were ground together placed in a silica reactor and heated at 1173K in flowing argon for approximately 48h - 72h to produce homogeneous polycrystalline bronze samples. The resultant bronzes were intensely coloured, those with lower alkali ion content being generally darker in colour. The samples were labelled and stored 0.05KW, 0.2KW, 0.3KW, 0.6KW and 0.8KW where K refers to potassium, W to tungsten and the preceding number to the intended potassium ion content on a mole basis. A similar labelling system was used for the sodium bronzes with Na representing the sodium ion.

2.3.2 Supported Potassium Bronze

A supported potassium tungsten bronze was prepared by impregnating a silica support (Aerosil 200, surface area $200m^2g^{-1}$) to incipient wetness with a solution of potassium polytungstate to give a tungsten loading of 30% by weight. After removing any excess water on a steam bath and drying in an air oven at 373K for 12h, the sample was reduced in flowing hydrogen ($40cm^3\ min^{-1}$, 101kPa) at 770K for about 2h. The polytungstate solution was obtained by adjusting the pH of a solution of potassium tungstate to 4 (using nitric acid). Previous studies[22] by Raman spectroscopy have shown that at such a pH the paratungstate species ($W_{12}O_{42}^{12-}$) is formed. Such species are more easily reducible to the bronzes than the monotungstate[22]. A high metal loading was selected because it was observed that in the previous studies[22] the bronzes are more readily formed at loadings much higher than that required to form a monolayer.

2.3.3 $Cu_yK_xWO_3$

An ion-exchange method was used in trying to obtain highly

dispersed Cu ions in the potassium bronze structure. Attempts to prepare such a sample by thermal methods have not been very successful since only a minimum of copper ions enter the lattice framework due to thermodynamic limitations at the high temperatures required to overcome kinetics. An initial study was first made in order to establish the optimum conditions of exchange of potassium ions for cupric ions. A $CuCl_2$ (J.M.C. Speciality Products AR:) solution was used as the Cu precursor and the method was used for the potassium tungsten bronze with x = 0.2. The initial study involved varying the temperature of the Cu solution (294K - 353K), the concentration of Cu ions in solution (between 10 - 300 times the concentration of K ions present) and the time for exchange (24h - 120h). Usually about 1g of bronze and $60cm^3$ of cupric chloride solution were used for each study. In each series of experiments a blank was prepared by allowing 1g of 0.02KW to equilibrate in $60cm^3$ of distilled water.

In the first series of experiments the concentration of the Cu solution was varied between 0.139M to 4.17M (the amount of copper present in $60cm^3$ of solution is between 10 to 300 times those of the K ions in the bronze). The solutions were allowed to equilibrate with 1g of the bronze at room temperature for 24h. A second series of experiments in which the concentration of the copper solution, maintained at room temperature, was kept at a concentration of 2.78M but the time period was varied between 24h to 120h in an attempt to follow the kinetics of ion-exchange. In the final series of experiments the temperature of the copper solution was varied between 288K and 353K but the concentration of the solution (Cu^{2+} = 2.78M) and the time of equilibrium (96h) were kept constant. In each case the solution was stirred continuously using a magnetic stirrer. After each experiment the mixture was centrifuged and the aliquot was analysed for potassium

content using atomic absorption (Perkin Elmer 2380). It was difficult to analyse for the high Cu concentration in the solution and hence the accuracy in determining the amount exchanged. In each case the blank samples prepared showed no potassium ions present in the aliquot as observed by atomic absorption.

Figure 2.1 gives the amount of potassium removed from the bronze as a function of the concentration of copper present in $60cm^3$ of solution. The isotherm shows that the maximum amount of potassium removed is achieved at a copper concentration of 2.8M after which increases in the Cu^{2+} concentration in solution have no effect. Figure 2.2 shows that maximum amount of potassium exchanged at room temperature with a solution of 2.78M Cu is achieved after about 48h; this means exchange kinetics are rather slow. Figure 2.3 shows that the minimum temperature required to achieve maximum exchange of K ions with a solution of 2.78M Cu and a time period of 96h is about 294K. The study has therefore shown that the optimum conditions required for the maximum exchange of K ions for Cu ions, (XPS has shown directly the presence of Cu ions in the bronze $Cu_yK_xWO_3$ see Chapter 6). These were, for 1g of bronze: a solution of 2.78M Cu, a temperature of 294K and a time period of 48h.

The conditions used for preparation of $Cu_yK_xWO_3$ were:- a temperature of 313K; 96h equilibrium time and a Cu solution of concentration 2.78M.

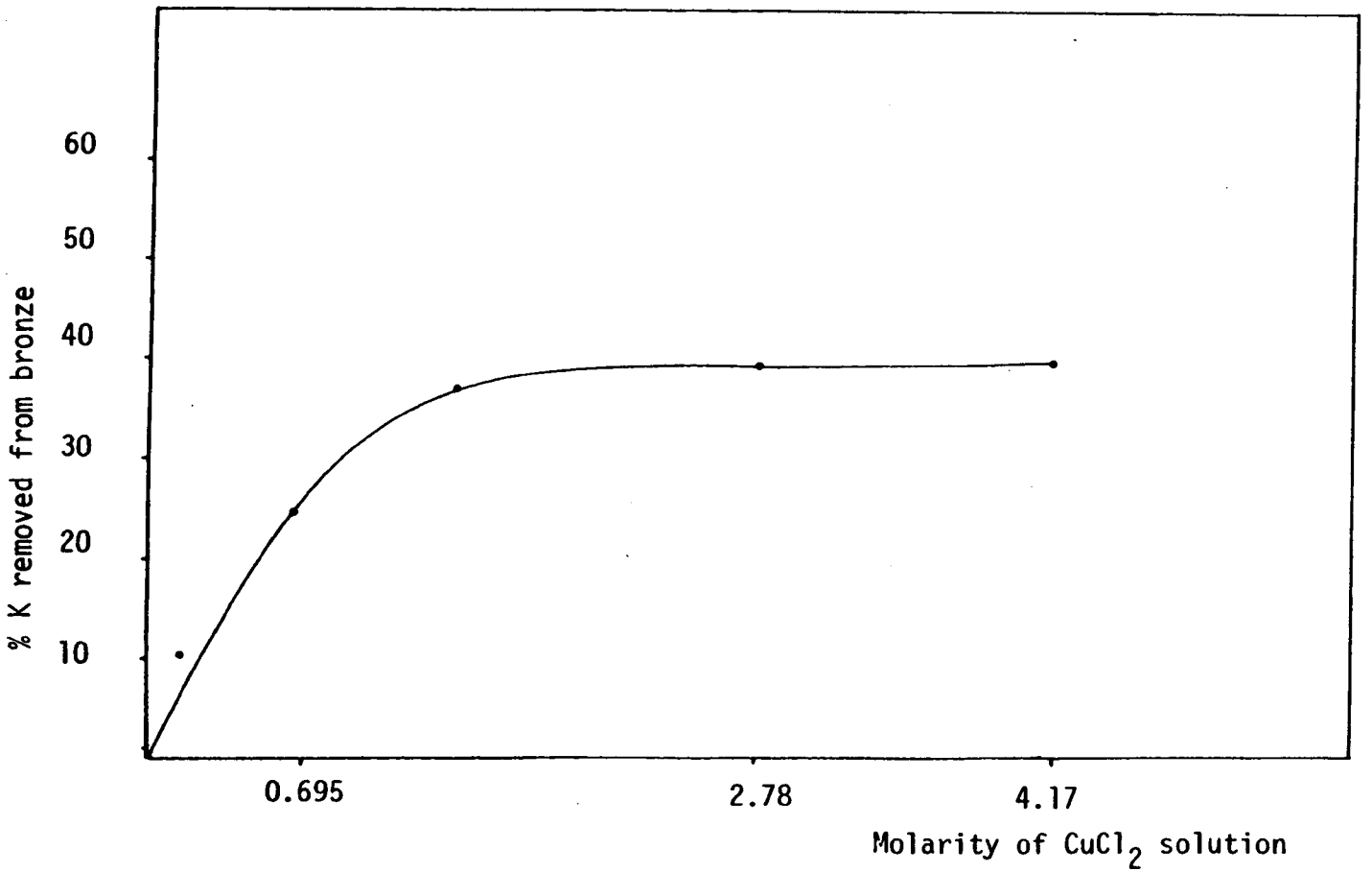

Figure 2.1 % K removed from bronze versus molarity of $CuCl_2$ solution (room temperature)

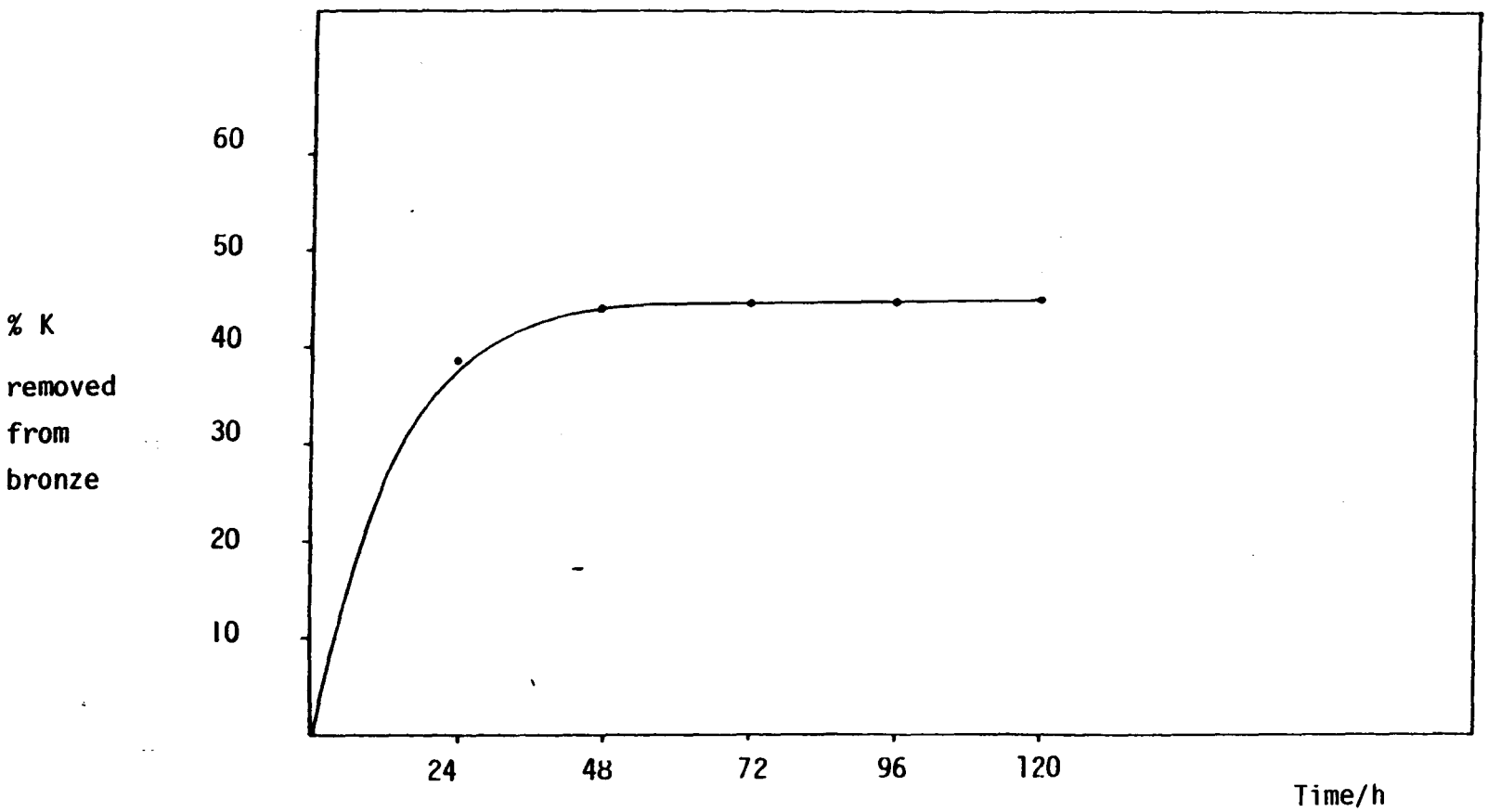

Figure 2.2 % K removed from bronze versus time
(2.78M Cu^{2+}, room temperature)

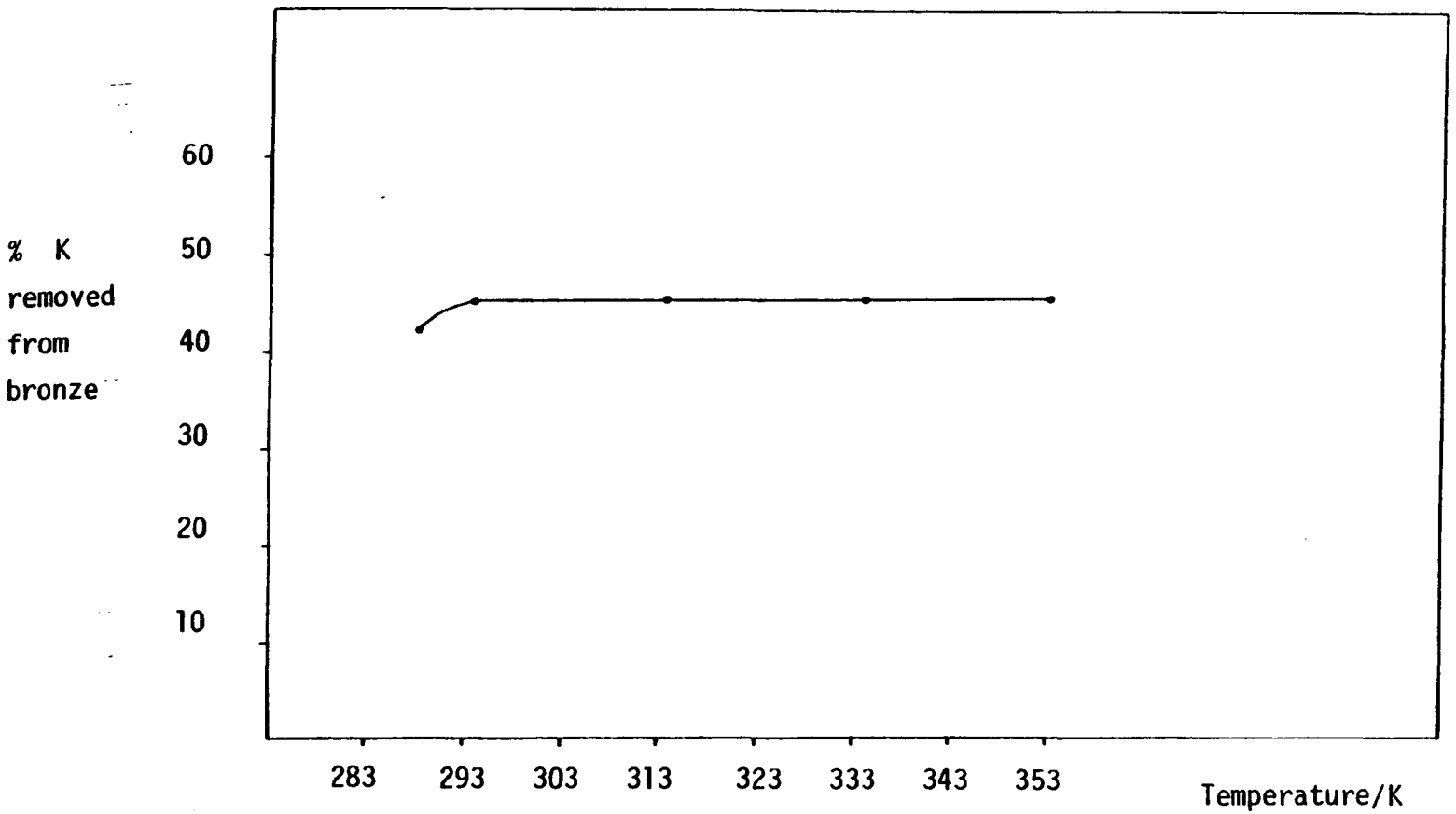

Figure 2.3 % K removed from bronze versus temperature (2.78M Cu^{2+}, after 96h)

CHAPTER 2

REFERENCES

1. F. Wöhler, Ann. Chim. Phys., (2), 43, 29, (1823).
2. A. Laurent, Ann. Chim. Phys., (2), 67, 215, (1838).
3. E. Banks and A. Wold, Preparative Inorganic Reactions, 4, (1968), Interscience Publishers (Ed. L.J. William).
4. O. Brunner, Diss. Zurich, (1903).
5. M.E. Straumanis, J. Am. Chem. Soc., 71, 679, (1949).
6. E.O. Brimm, J.C. Brantley, J.H. Lorenz and M.H. Jellink, J. Am. Chem. Soc., 73, 5427, (1951).
7. A. Hussain, Chem. Commun. Univ. Stockholm, No. 2, (1978).
8. L.E. Conroy and T. Yokokawa, Inorg. Chem., 4, 994, (1965).
9. L.E. Conroy and G. Podolsky, Inorg. Chem., 7, 614, (1968).
10. M. Figlarz and B. Gerand, Mater. Sci. Monogr., 10, (Reacts.Solids, 2), 887, (1982).
11. E. Zettnow, Pogg. Ann., 130, 240, (1967).
12. G. Hägg, Z. Phys. Chem., B29, 192, (1935).
13. L.D. Ellerbeck, H.R. Shanks, P.H. Sidles and G.C. Danielson, J. Chem. Phys., 35, 298, (1961).
14. A. Ferretti and W. Kunnmann, Rev. Sci. Inst., 35, 465, (1944).
15. M.J. Sienko, J. Am. Chem. Soc., 81, 5556, (1959).
16. T.E. Gier, D.C. Pease, A.W. Sleight and T.A. Bither, Inorg. Chem., 7, 1646, (1968).
17. T.A. Bither, J.L. Gillson and M.S. Young, Inorg. Chem., 7, 1646, (1968).
18. P. Hagenmuller, Comp. Inorg. Chem., 4, 1973, Pergamon Press, (Ed. J.C. Bailer, H.J. Emeléus, R. Nyholm and A.F. Tortman-Dickson).
19. M.E. Straumanis and S.S. Hsu, J. Am. Chem. Soc., 72, 4027, (1950).

20. A. Magnéli and B. Blomberg, Acta. Chem. Scand., 5, 372, (1951).

21. E. Banks and A. Goldstein, Inorg. Chem., 7, 966, (1968).

22. S. Stevenson, M. Phil. Thesis, Brunel University, (1985).

CHAPTER 3

PHYSICAL CHARACTERISATION AND SURFACE MORPHOLOGY

3.1 Introduction

Many reactions of both theoretical and practical interest occur on the surface of solid catalysts. An important parameter which determines the catalytic activity is the available surface area or the number of active sites per unit total surface area. The course of reaction, however, is, in a considerable number of cases, determined by the acidic number and strength of acid sites at the surface, (or the acidic nature of the surface).

The potassium tungsten bronzes, the sodium tungsten bronzes and WO_3 were analysed for their BET surface area using krypton adsorption. The use of the physical adsorption of gases by solids for the determination of their surface area, porosity and texture is now well-established in many fields of scientific investigation. The theory of gas adsorption by solids with special emphasis on the characterisation of porous solids by gas adsorption has been extensively developed and discussed in recent years. Transmission Electron Microscopy, (TEM) was also used to obtain a more detailed morphological study of these materials. Temperature programmed desorption of ammonia was used to measure the amount and distribution of acid sites on WO_3, K_xWO_3 and Na_xWO_3 ($0.05 \leqslant x \leqslant 0.8$). Acidity is often an important characteristic which makes a solid catalytically effective. Silica-aluminas and, more recently, zeolites with acidic surfaces play a very important catalytic role in industrial processes, in particular in the petroleum industry.

3.2 The BET Method of Surface Area Determination

The BET method[1] has been adopted as a standard procedure for surface area determination of solids. The BET model[1] extends the dynamic condensation - evaporation mechanism previously suggested by Langmuir[2] to describe localised monolayer adsorption to a multi-layer adsorption of gases on solid surfaces. The BET equation has been represented in different forms[3], a convenient and widely used one being

$$\frac{p}{V(p_o-p)} = \frac{1}{V_m C} + \frac{C-1}{V_m C}\,\frac{p}{p_o}$$

where; V is the amount of gas adsorbed at the equilibrium pressure p.

V_m is the amount of gas required to give monolayer coverage.

p_o is the saturated vapour pressure of the adsorbate.

C is a constant which may be regarded as a free energy term.

The theory assumes (i) that the heat of adsorption in all layers above the first is equal to the latent heat of condensation, (ii) that all rates of evaporation and condensation in all layers above the first are identical, (iii) and that when p becomes equal to the saturation vapour pressure of the adsorbate, the latter condenses as an ordinary liquid into the adsorbed film. The BET model also assumes that the surface of the solid is energetically uniform and ignores the fact that most solid surfaces are energetically heterogeneous. The theory also neglects any interactions between adsorbed species horizontal to the solid surface, taking into account only those perpendicular to the surface. The BET theory also fails to account for the fact that at saturation vapour pressure often only a finite number of molecular layers are adsorbed.

Despite its minor failures, the BET theory is remarkably success-

ful when used in the calculation of specific surface area of solids.

The BET equation predicts that a plot of $\frac{p}{V(p_o-p)}$ against $\frac{p}{p_o}$ should be linear, yielding $\frac{C-1}{V_mC}$ as the slope j, and $\frac{1}{V_mC}$ as the intercept i and solving these two simultaneous equations give

$$V_m = \frac{1}{(i+j)}$$

$$C = \frac{i+j}{i}$$

The range of linearity of the BET plot is normally, but not always, between $0.005 < \frac{p}{p_o} < 0.35$. The specific surface area, S, in m^2g^{-1} is given by the relationship

$$S = \frac{V_m}{22414} \cdot N \cdot A_m \cdot 10^{-18}$$

where V_m is expressed in cm^3 (S.T.P.) of adsorbate per gram of solid, N is Avogadros constant, 6.023×10^{23} and A_m is the cross-sectional area of the adsorbed molecules in nm^2. A_m cannot be measured independently and its value is usually estimated[4] by assuming (i) close hexagonal packing of the species in the monolayer,and (ii) a packing density in the monolayer equal to the bulk density of the adsorbate. In general, the value of A_m varies from adsorbate to adsorbate; thus, for krypton gas as an adsorbate at 77K, the recommended value of A_m is $0.195nm^2$ whilst for water vapour A_m is usually taken to be $0.106nm^2$ at 293K. Nitrogen adsorption is the most commonly used technique for determination of surface areas as low as approximately $1m^2$ can be measured. The principle obstacle to measuring areas lower than this with nitrogen in a volumetric system lies in accurately measuring the void or "dead space" volume. On small areas, the quantity of adsorbate remaining in the void volume is large compared to the amount adsorbed, and indeed

the void volume error can be larger than the volume adsorbed. The number of molecules trapped in the void volume can be reduced by using adsorbates with low vapour pressures such as krypton. The vapour pressures of krypton at liquid nitrogen temperature is 350.64 Pa. Therefore, the amount of krypton remaining in the void volume, when monolayer coverage occurs, will be much less than nitrogen, whereas the amount of adsorption will be only slightly less by approximately the ratio of cross-sectional areas of nitrogen and krypton, or about 0.162/0.195. In the present study krypton adsorption at liquid nitrogen temperature was used to determine the surface areas of the bronzes and WO_3. At liquid nitrogen temperature, krypton may condense as a liquid but since the vapour pressure used is very low, such a possibility is non-existent.

3.3 Surface Acidity

The concept of surface acidity of highly divided solids was derived originally to explain the action of acid surfaces in catalytic reactions. A description of acidity in general, and surface acidity more specifically, requires the determination of the nature, the strength, and the number of acid sites. A solid acid is capable of transforming an adsorbed basic molecule into its conjugated acid form. In its most general definition an acid is an electron-pair acceptor. So the Brönsted acid site is able to transfer a proton from the solid to the adsorbed molecule. In this way an ion is generated and an ion-dipole interaction with the solid exists. The Lewis acid site is able to accept an electron pair from the adsorbed molecule and a coordinative bond with the surface is formed.

3.3.1 Nature of Surface Acidity

Brönsted acid sites in solids can be generated when a trivalent

cation is present in tetrahedral coordination with oxygen. The most common example is aluminium. When all tetrahedral oxygen anions are shared between two cations, net negative charges are created for cations with charges lower than 4. A schematic diagram is given for aluminosilicate, the most common case encountered, in Figure 3.1. When the excess negative charges are

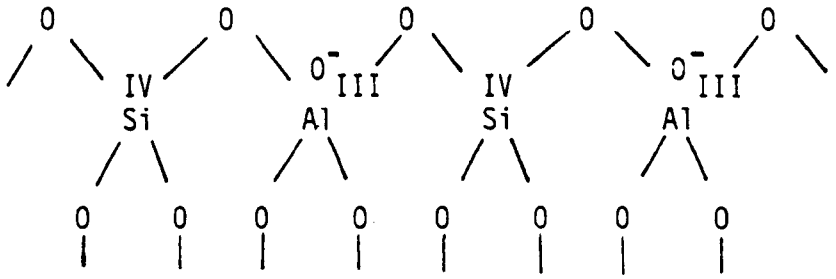

Figure 3.1

compensated for by protons, silanol groups are formed, which are represented in Figure 3.2

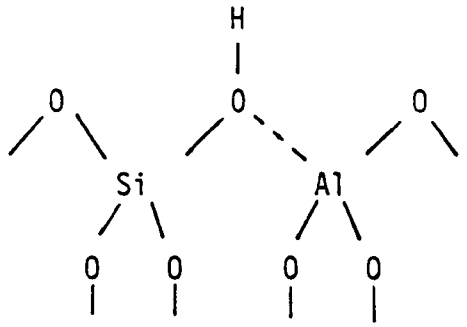

Figure 3.2

It has to be understood that in such a structure a trigonal oxygen does not exist; it indicates only that Si as well as Al retain their tetrahedral coordination. Upon interaction with a basic molecule (e.g. an alkene), the following equilibrium is established:

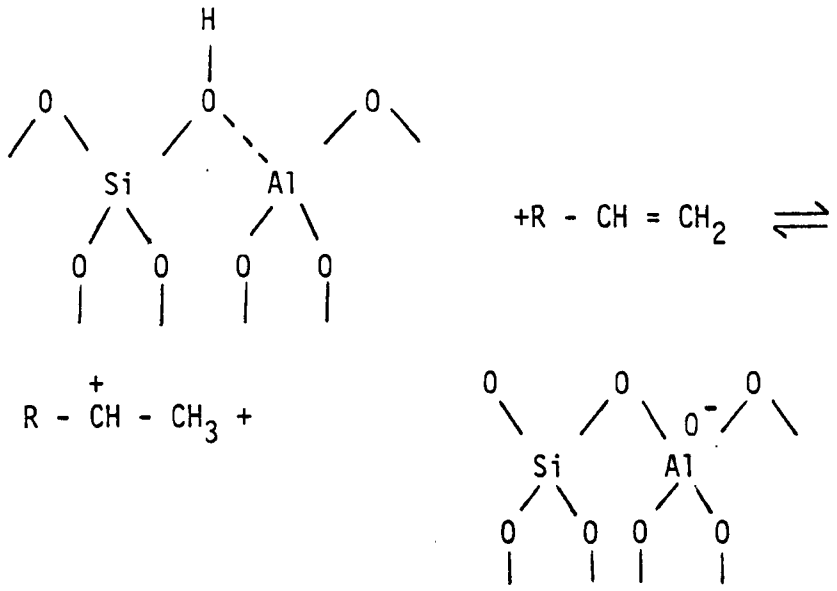

Depending on the strength of the Brönsted site this equilibrium will be shifted. It seems, therefore, the surface acidity is dynamic in character and is dependent on the chemical nature of both the adsorbed base and the solid. When coordinative unsaturated sites by some mechanism are generated, acid sites of the Lewis type are created which are able to accept electrons. The silica-aluminium example is schematized in Figure 3.3.

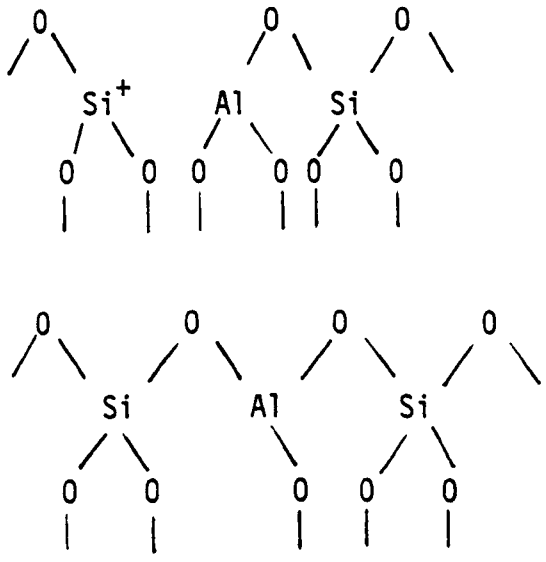

Figure 3.3

A given acidic solid usually does not have a single class of acidic sites, but shows a large distribution of strengths of acid sites. This may be the result of inhomogeneity in the composition of the solid, or the existence of short-range interactions or of surface structures.

3.3.2 Measurement of Acidity of Surfaces

There are many publications dealing with the measurement of surface acidity[5,6] some of which are described below.

3.3.2.1 Non-aqueous titrations

Historically the first method to be used for the determination of surface acid sites concentration (SASC) was by Johnson[7]. He suspended some powdered sample in dry benzene and titrated it by slowly adding a dilute solution of n-butylamine in benzene until the indicator adsorbed on the surface was converted permanently to its basic form. Since an indicator is converted to its conjugate acid only by acid sites which have acid strengths equal or more than the pK_b of the indicator (i.e. equal or lower than the Brönsted acidity), use of indicators of varying pK_b yields a distribution of acid sites concentration with strength. By using a series of indicators with increasing pK_b, Johnson, determined the lowest value of pK_b for which the indicator is converted to its conjugate acid. Thus, the limiting strength for the stronger acid sites can be determined. The disadvantages of this method are that the equilibrium between the solid and the base is often reached very slowly and hence the method can be time-consuming and inaccurate, indicators can alter colour through physisorption rather than adsorption at acid sites and the base used is sometimes adsorbed on sites other than acidic ones.

3.3.2.2 Aqueous Titrations

This can be used to determine Brönsted acidity. It is basically an ion exchange method where surface protons are replaced by other hydrated cations[8]. The method consists of equilibrating the solid with a known amount of base and backtitrating the excess with acid. The disadvantages of this method are that it will not distinguish between acid sites of different strength, while the addition of water to the system may create new Brönsted sites.

3.3.2.3 Infra-red Spectroscopy

This method enables the measurement of the extent of protonation of a chemisorbed base, and therefore Brönsted acidity can be distinguished from Lewis acidity. Mapes and Eischens[9] studied the chemisorption of ammonia on catalysts. Infrared spectra of such samples contained H - N - H bending bands due both the NH_4^+ and to coordinated ammonia. This was the first direct evidence of the existence of both Brönsted and Lewis acid sites on aluminosilicate surfaces. Pyridine is also commonly used, and being a weaker base than ammonia, is more selective for the stronger acid sites. Pyridine adsorbs on Brönsted acid sites giving a peak at 1545 cm^{-1} due to the pyridinium ion, and adsorbs on Lewis acid sites giving a band in the region 1440 - 1465 cm^{-1} due to coordinated pyridine.

3.3.2.4 Temperature-programmed desorption (tpd) of chemisorbed bases

A gaseous base adsorbed on a strong acid site is more stable than one adsorbed on a weak acid site, and is more difficult to desorb. As elevated temperatures stimulate desorption of the adsorbed bases from acid sites, those at weaker sites will be desorbed,

preferentially. Thus, the proportion of adsorbed base desorbed at various temperatures can give a measure of the amount and distribution of acid sites. The bases used normally are quinoline, pyridine or ammonia. Tpd of ammonia, has been widely used to measure the acidity of various zeolites[10]. Ammonia is an excellent probe molecule because it can be stabilised on acid sites and can penetrate into pores due to its strong basicity and small size. However, the transport of this base molecule into the zeolite material may not be completely rapid. In some cases, the thermal behaviour could be influenced by these diffusion problems. Such a condition may be plausible at lower temperatures, Kanazirev[11] used tpd of NH_3 to study the problem of diffusion in a zeolite matrix and found broad peaks around or lower than 373K influenced by the diffusibility of ammonia. Hidalgo[10] et al overcame this problem by using a relatively high temperature for attaining equilibrium with the zeolite surface and using a slow rate of temperature increase.

In the present study tpd of ammonia was used to show the distribution and strength of acid sites on the alkali metal tungsten bronzes. Ammonia was used as the probing molecule in preference to other bases because of the low surface area of the bronzes requiring a molecule with a small cross-sectional area.

3.4 Transmission Electron Microscopy

Electron microscopy is an extremely versatile technique capable of providing structural information over a wide range of magnification. At one extreme, scanning electron microscopy (SEM) complements optical microscopy for studying the texture, topography and surface features of powders; features up to tens of micrometers in size can be seen and, because of the depth of focus of SEM instruments, the resulting

pictures have a definite three-dimensional quality. At the other extreme, high resolution electron microscopy (HREM) is capable, under favourable circumstances of giving information on an atomic scale, by direct lattice imaging. Resolution of approximately 0.2nm has been achieved, meaning it has become possible to 'see' individual atoms.

Electron microscopes are of either transmission or reflection design. For examination in transmission (TEM), samples are usually thinner than 200nm. This is because electrons interact strongly with matter and are completely absorbed by thick particles. In order to use electrons, instead of light, in a microscope it is necessary to be able to focus them, this is achieved by an electric or magnetic field. In order to minimise electron scattering a high vacuum is used. Electron microscopes contain several electromagnetic lenses. The condenser lenses are used to control the size and angular spread of the electron beam that is incident on the sample. Transmitted electrons then pass through a sequence of lenses, objective, intermediate and projector, and form a magnified image of the sample on a fluorescent viewing screen from which photographs are then taken. A schematic representation of the transmission electron microscope is shown in Figure 3.4

3.5 Experimental Procedures

3.5.1 Krypton Adsorption Measurement

The BET surface areas of WO_3, K_xWO_3 and Na_xWO_3 were determined using krypton adsorption at liquid nitrogen temperature. The measurements were undertaken on a Micromeritics Surface Area Pore Volume Analyser 2100D. This is a volumetric adsorption apparatus which essentially consists of:-

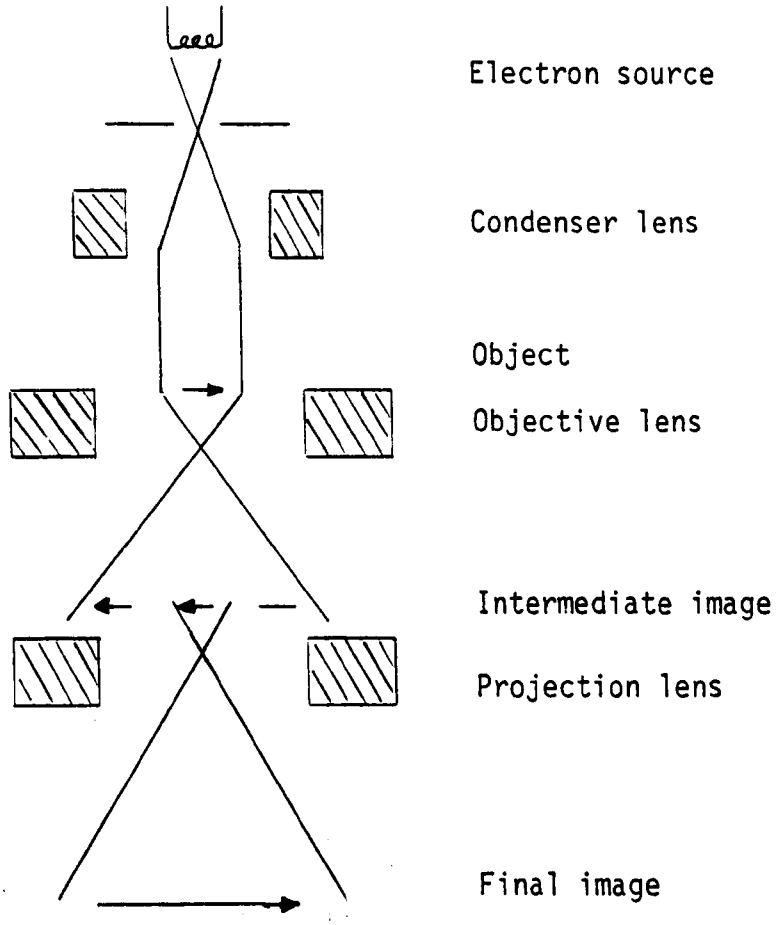

Figure 3.4 Representation of the transmission electron microscope

(1) A device for the introduction and removal of the adsorbate.

(2) A system for measuring and recording the equilibrium pressure.

(3) Temperature monitors for measuring both the sample outgassing and liquid nitrogen temperatures.

The sample was contained in a burette which after connection to the system manifold was evacuated at room temperature using rotary and mercury diffusion pumps to less than 10mPa. The "dead space", i.e. the volume within the sample burette exclusive of the sample itself was then determined by expanding helium, a non-adsorbing gas, from a fixed volume at a known pressure into the sample burette maintained at liquid nitrogen temperature and recording the equilibrium pressure. The sample was again evacuated and krypton adsorption measurements were

performed by repeating the above procedure but using krypton and increasing the dosing pressure in successive doses. The equilibrium pressure observed after each dose was corrected for thermal transpiration effects. Once the gas volume introduced and the volume not adsorbed at a given pressure were known (±2%) it was possible to calculate the volume adsorbed at various equilibrium pressures. The surface area was calculated by plotting $\frac{p}{V(p_o-p)}$ against $\frac{p}{p_o}$ where p_o was the saturation vapour pressure of krypton (0.33kPa).

The analyser allows the measurement of surface areas as low as 0.1 m^2g^{-1} (±2-5%) when krypton gas is used as the adsorbate molecule.

3.5.2 Temperature Programmed Desorption (tpd) of Ammonia

Tpd of ammonia was carried out on WO_3 and both the potassium and sodium bronzes. A schematic diagram of the tpd apparatus used is shown in Figure 3.4. In the apparatus the desorbed ammonia molecules were measured by a digital conductivity meter, Fissons PT1-18.

Nitrogen gas was purified by passing through a 5A molecular sieve at 298K. 6% NH_3/94% N_2 was purified by passing through a trap containing silica gel at 298K. Gas flow rates were kept constant (to within ±0.5cm^3min^{-1}) and were for N_2, 20cm^3min^{-1} and 6% NH_3 in N_2, 10cm^3min^{-1}.

The sample (1-2g) was placed in a Pyrex reactor fitted with a thermocouple (Chromel-Alumel) to measure the sample temperature of the solid sample, and surrounded by a tubular furnace whose temperature was controlled by a linear programmer to within ±5K. N_2 gas was admitted and the temperature raised to 773K and held for 1h. The sample was cooled to room temperature in N_2 gas. 6% NH_3 in N_2 was

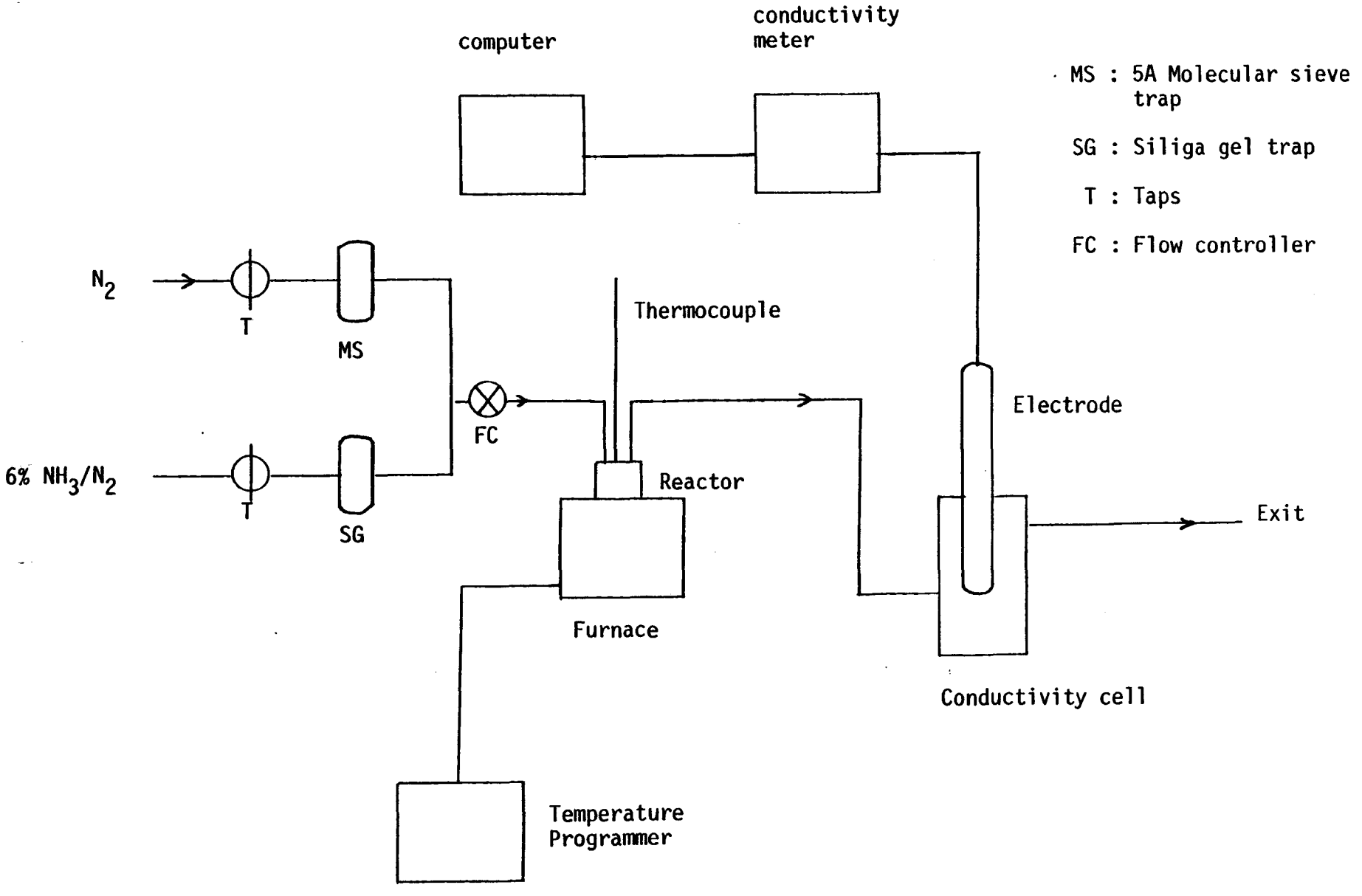

Figure 3.5 Tpd Apparatus

then admitted and the sample allowed to equilibrate for 10 min. The diluted ammonia flow was then replaced by pure N_2. The gas from the reactor was then bubbled through a cell containing $20cm^3$ of de-ionised water. The de-ionised water was obtained by passing doubly distilled water through an ion-exchange column packed with Duolite. The conductivity of the water in the cell was continuously monitored using a conductivity meter. When the conductivity of the de-ionised water was constant, indicating any excess ammonia or physisorbed ammonia had been removed, the sample temperature was raised to 773K at 5K min^{-1}, and the concentration of desorbed ammonia in the exit gas was continuously monitored as a change in conductivity of the de-ionised water in the cell. The output on the conductivity meter and the thermocouple was fed to a Commodore CBM 4032 computer (1 bit per μmole of ammonia) through an amplifier and an analogue to digital converter for data processing.

Calibration of the conductivity meter for ammonia was done by measuring the conductivity of $20cm^3$ of de-ionised water containing varying amounts of ammonia solution. A calibration curve between the conductivity and the number of moles of ammonia present was then derived. The amount of ammonia desorbed was then estimated using this relationship. A previous study[12] has shown that the results obtained by the conductivity method are reproducible and the error is within ±3nmol of ammonia.

3.5.3 Transmission Electron Microscopy

For TEM, the sample was crushed using a pestle and mortar, ultrasonically dispersed in acetone and a drop of the suspension was placed onto a 200 mesh carbon coated copper grid. The dried grid,

clamped on the sample holder was transferred to the TEM (Jeol Temscan 100CX). The sample was evacuated to less than 0.1 mPa before exposure to the electron beam at an accelerating voltage of 100kV. Micrographs of the magnified samples were taken by a Joel Plate Camera containing Agfa Gevaert Scientia films. The negatives were developed using an Agfa G170C developer, fixed by Ilford Hypam fixer and printed on Kodak Photographic paper.

3.6. Results

3.6.1 BET Surface Area

The surface area of WO_3 and the sodium and potassium bronzes was determined from the measurement of krypton adsorption at 77.15K. Figures 3.6 - 3.16 show the plots of $\frac{p}{V(p_o-p)}$ versus $\frac{p}{p_o}$ for the different samples. The gradient $\left(\frac{C-1}{V_mC}\right)$ and intercept $\frac{1}{V_mC}$ of these plots permit the monolayer capacity V_m to be derived and hence the surface area assuming a cross-sectional area of $0.195nm^2$ for the krypton atom assuming liquid krypton. Table 3.1 gives the surface area values for WO_3, K_xWO_3 and Na_xWO_3 where, $0.05 \leqslant x \leqslant 0.8$.

WO_3 has a higher surface area than any of the bronze samples; this could be expected since the bronzes were prepared at a very high temperature. In general, for any given series of bronze, the surface area tends to decrease with increasing alkali ion concentration. This could not be due to a structural effect since although the potassium bronzes with low alkali metal content are mostly hexagonal and those with $x \leqslant 0.3$ tetragonal, the sodium bronzes with $x \leqslant 0.3$ are tetragonal and at high sodium content hexagonal. The bronzes were prepared at high temperature and it is possible that the difference in surface area is caused by sintering. It appears that the extent to

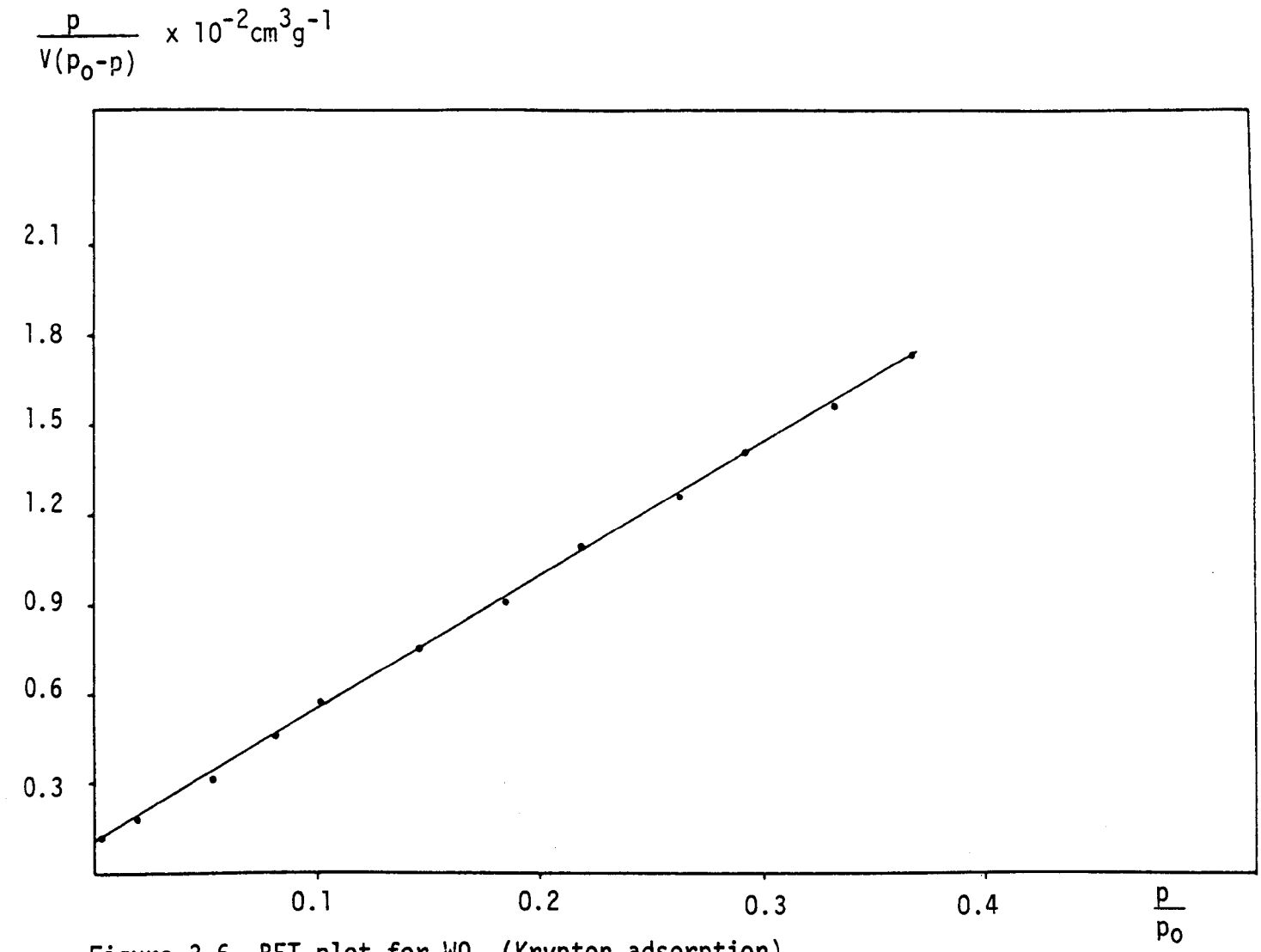

Figure 3.6 BET plot for WO_3 (Krypton adsorption)

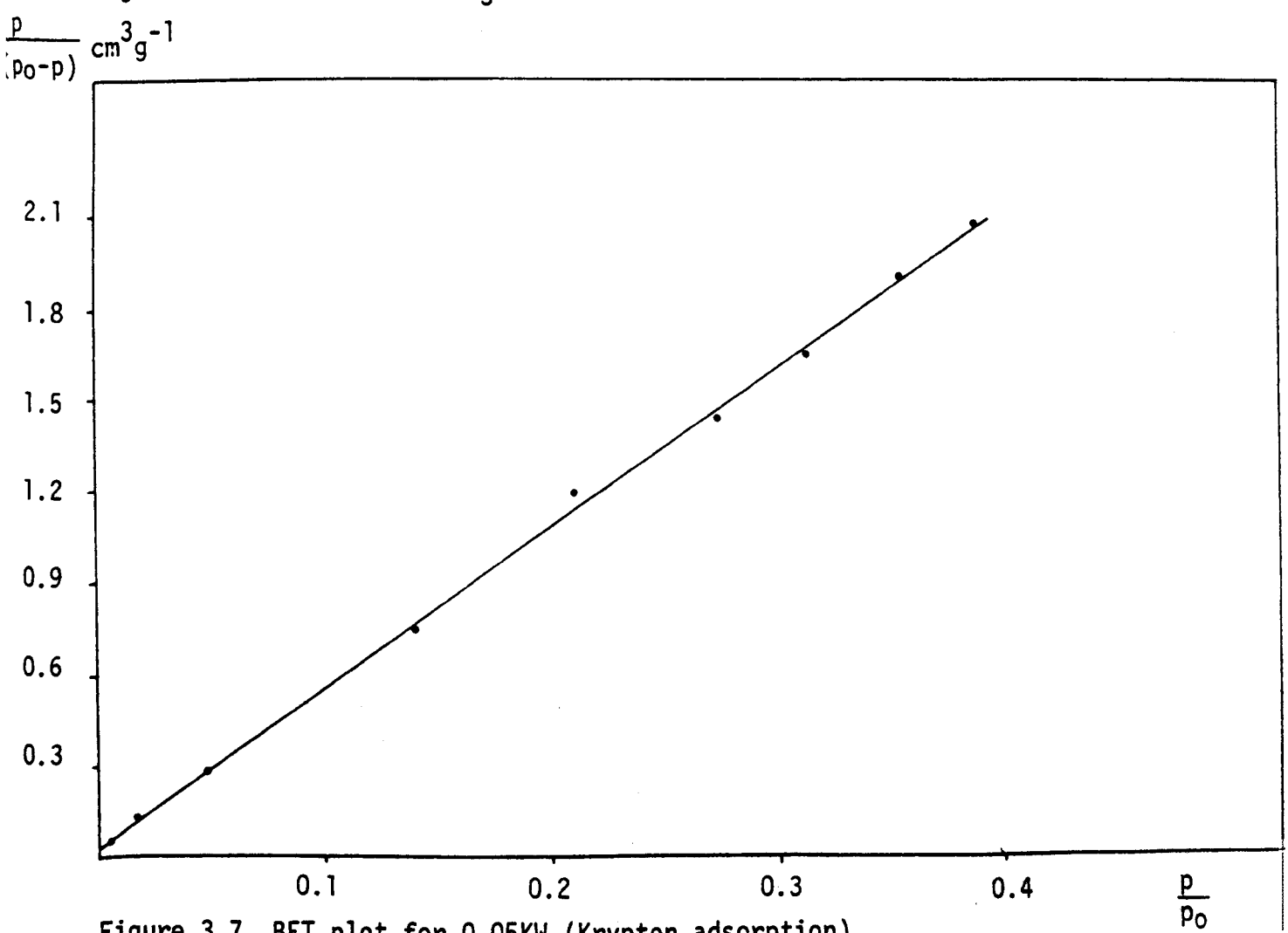

Figure 3.7 BET plot for 0.05KW (Krypton adsorption)

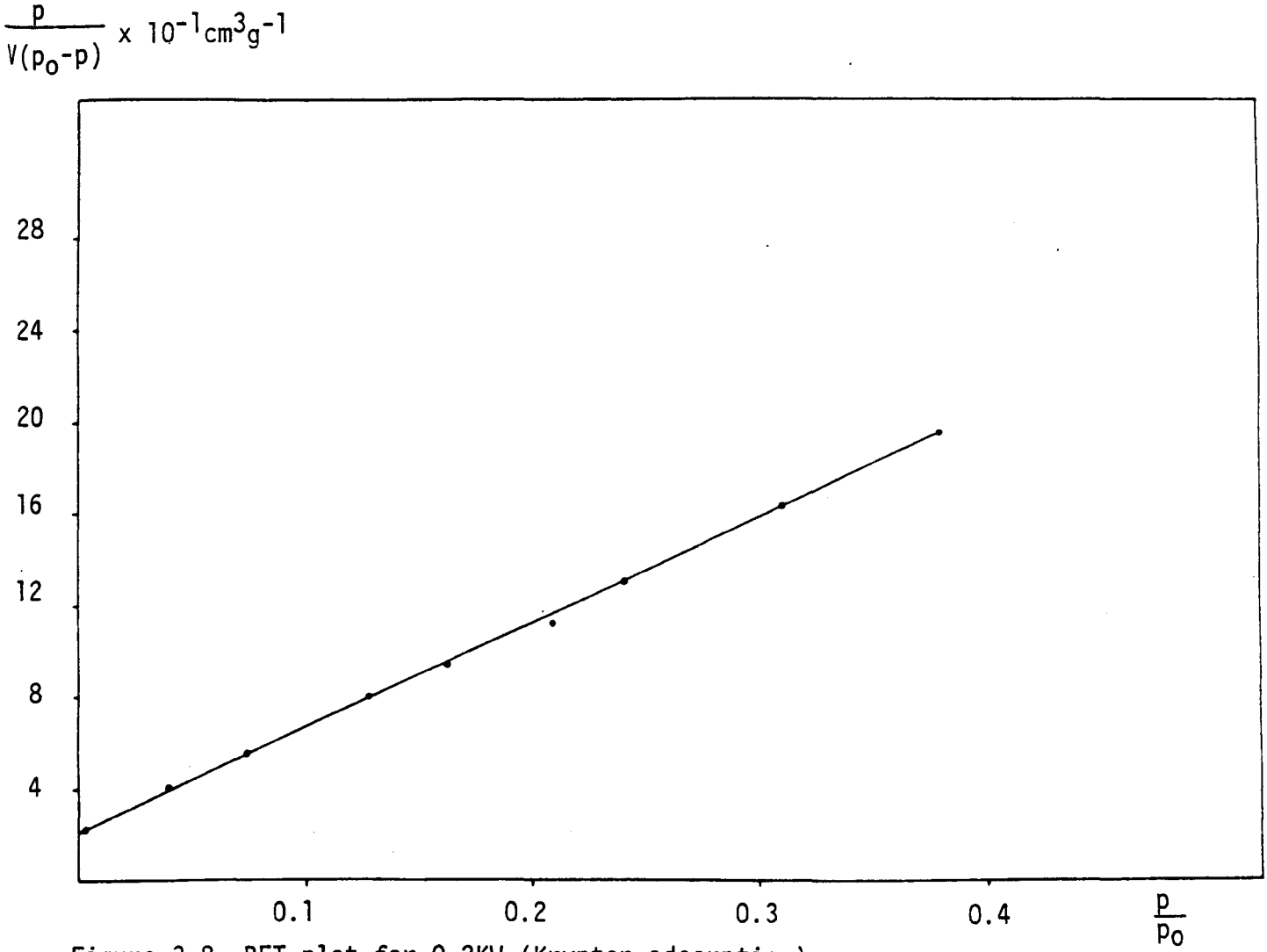

Figure 3.8 BET plot for 0.2KW (Krypton adsorption)

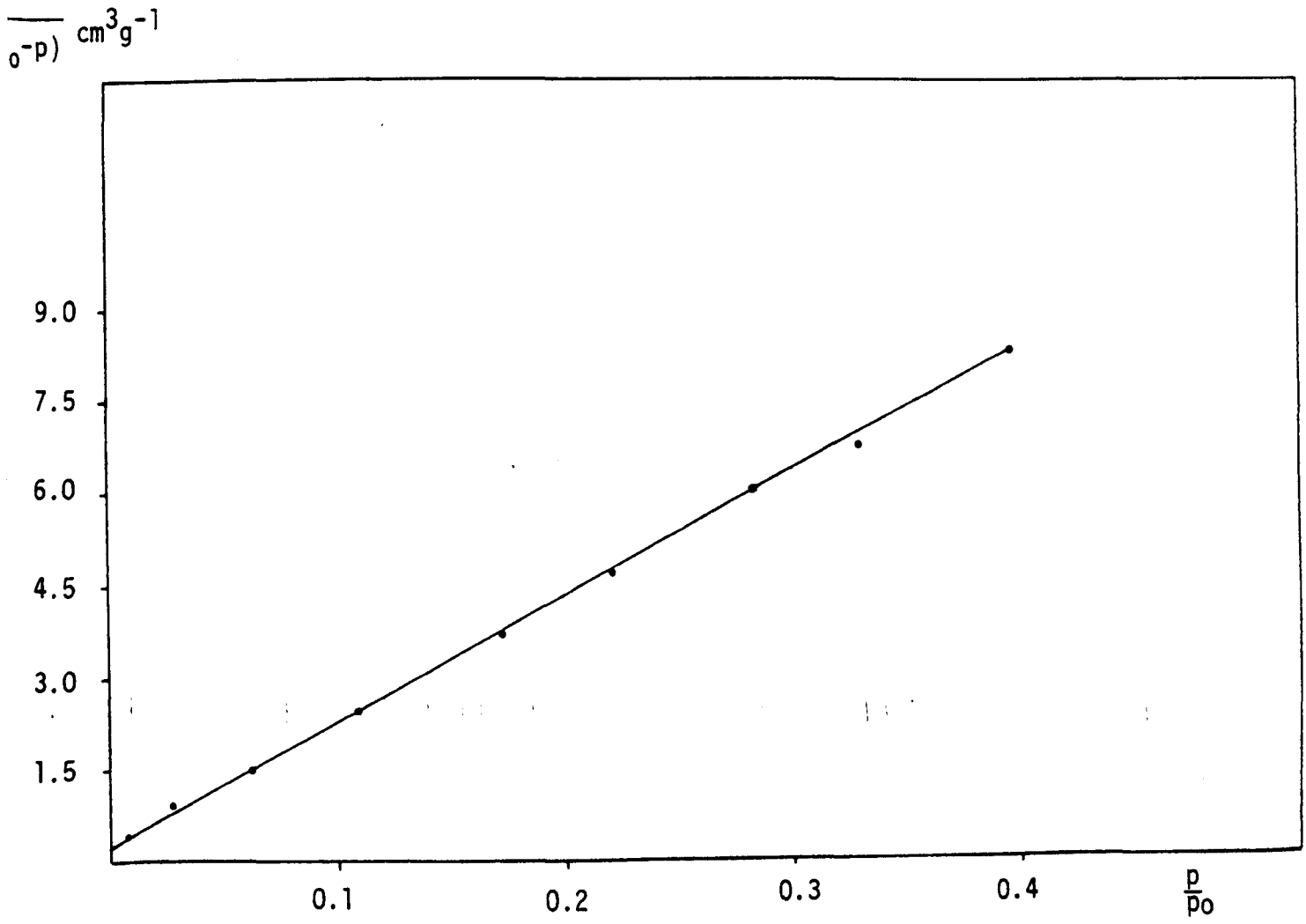

Figure 3.9 BET plot for 0.3kW (Krypton adsorption)

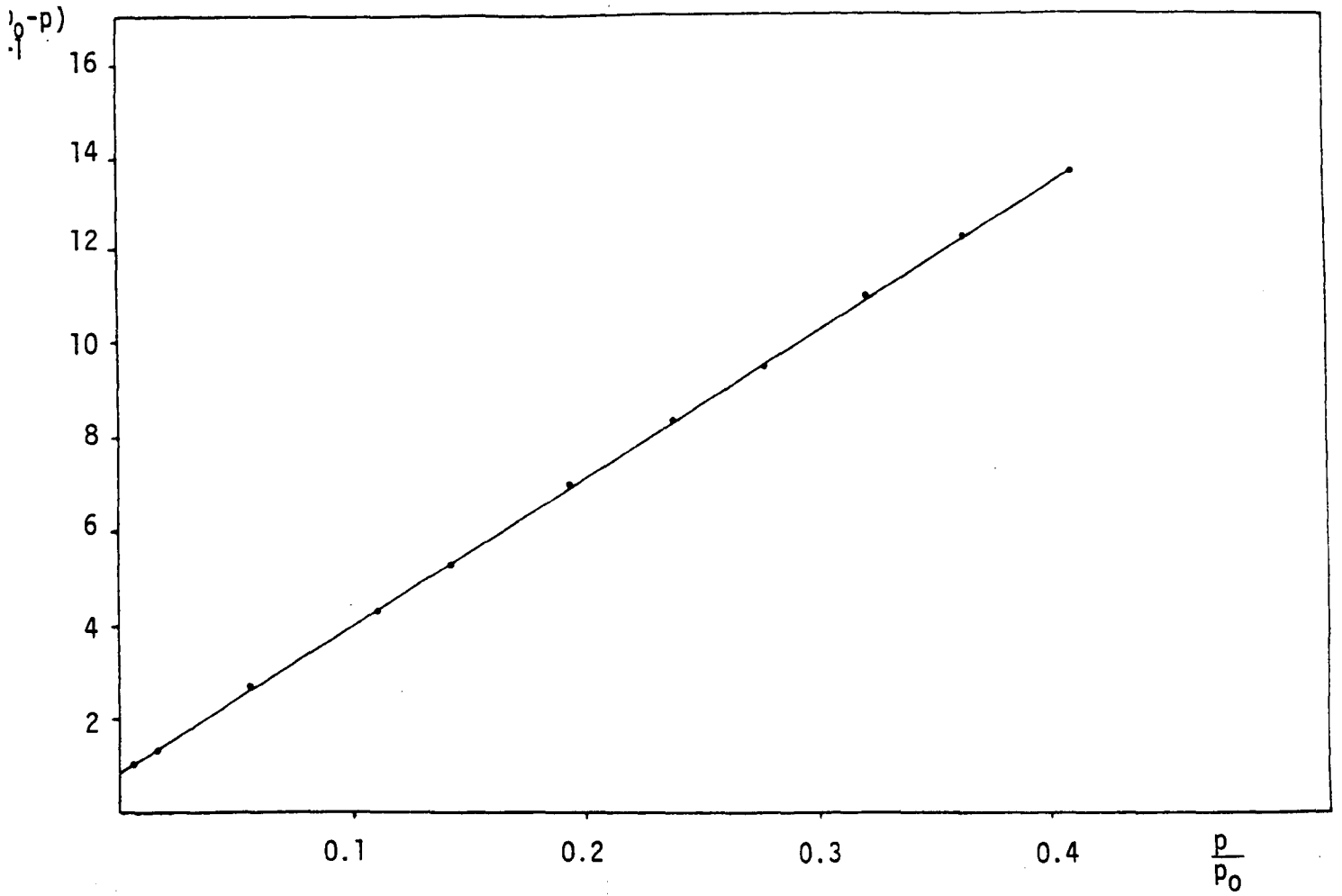

Figure 3.10 BET plot for 0.6KW (Krypton adsorption)

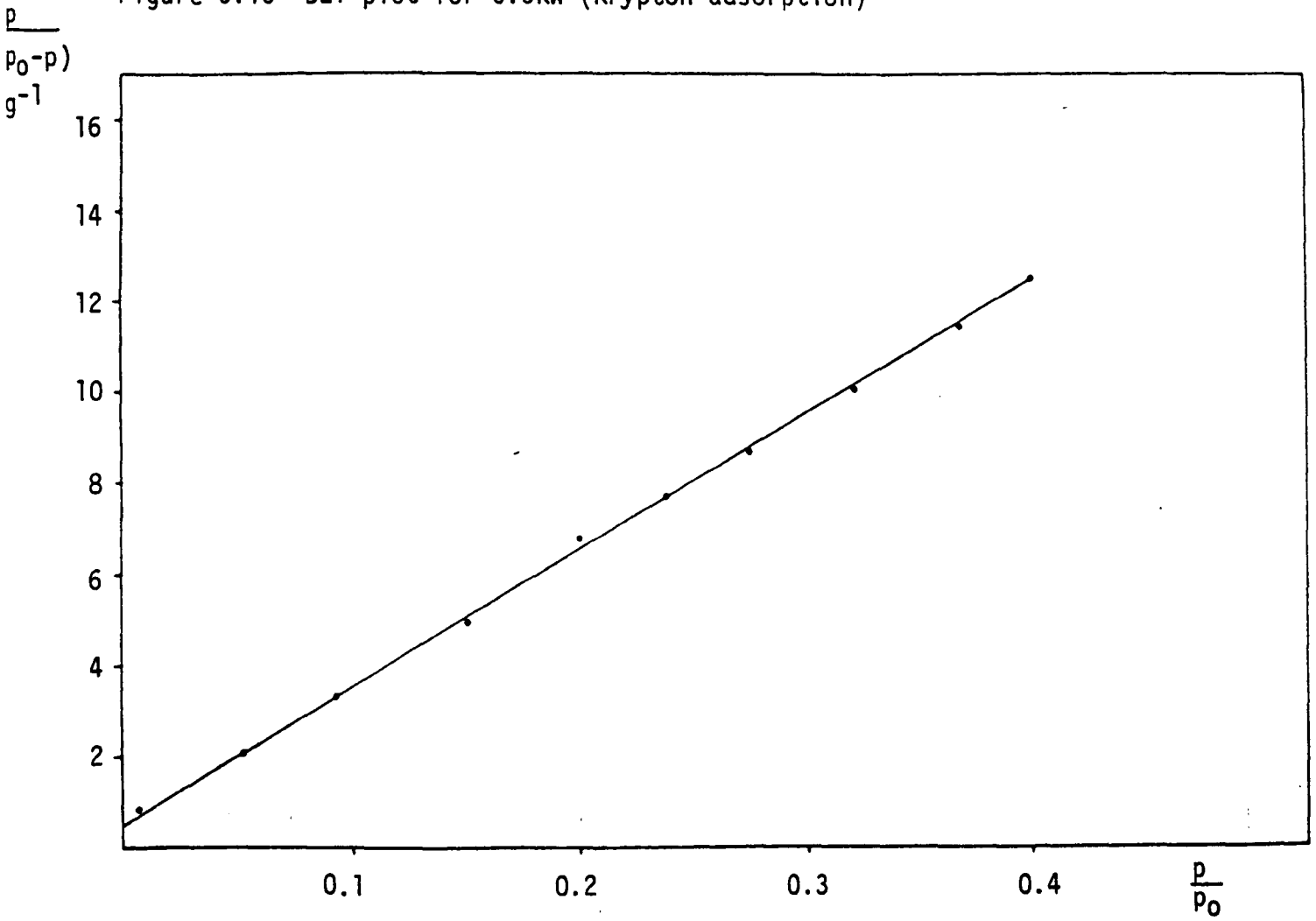

Figure 3.11 BET plot for 0.8KW (Krypton adsorption)

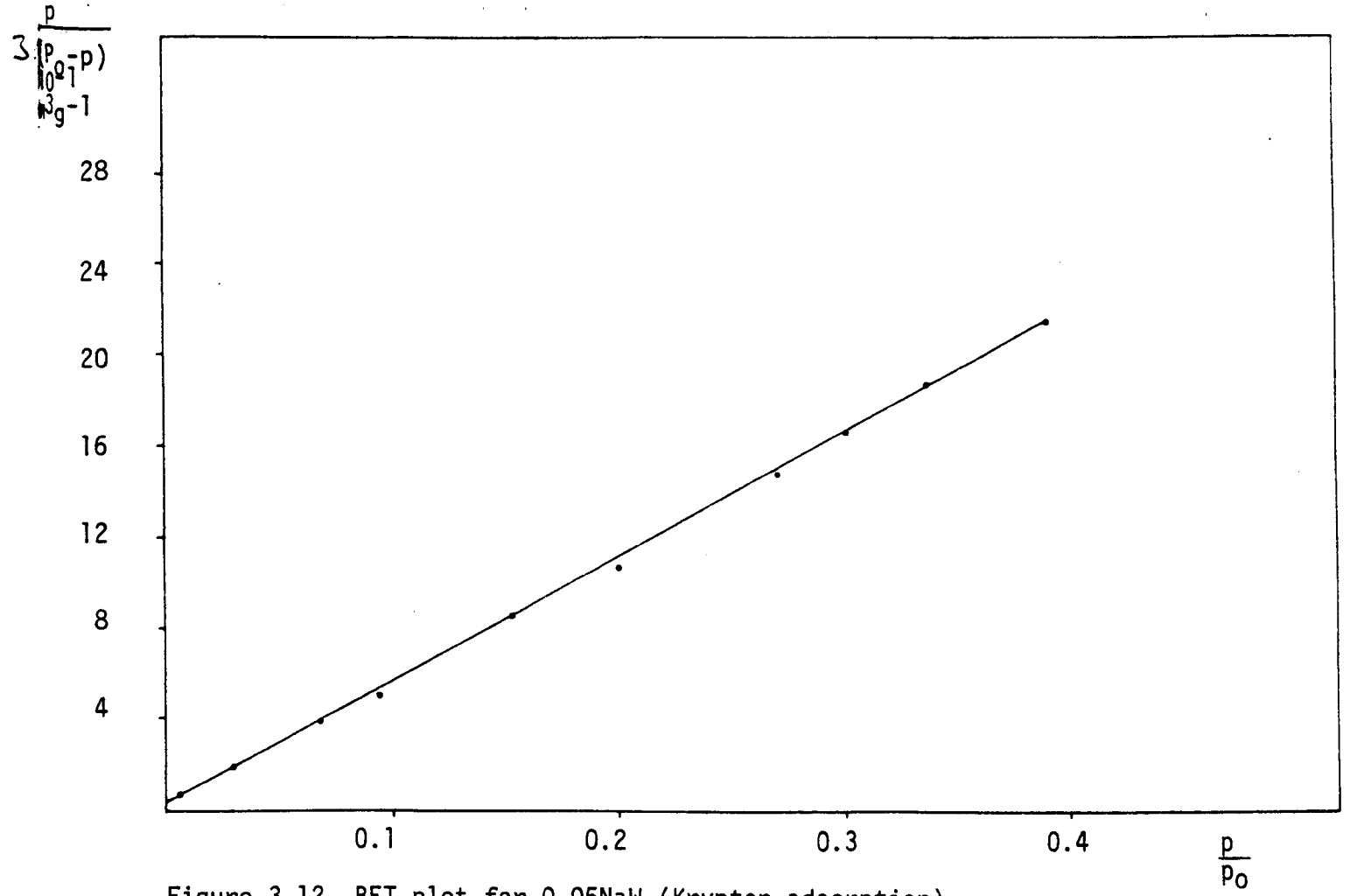

Figure 3.12 BET plot for 0.05NaW (Krypton adsorption)

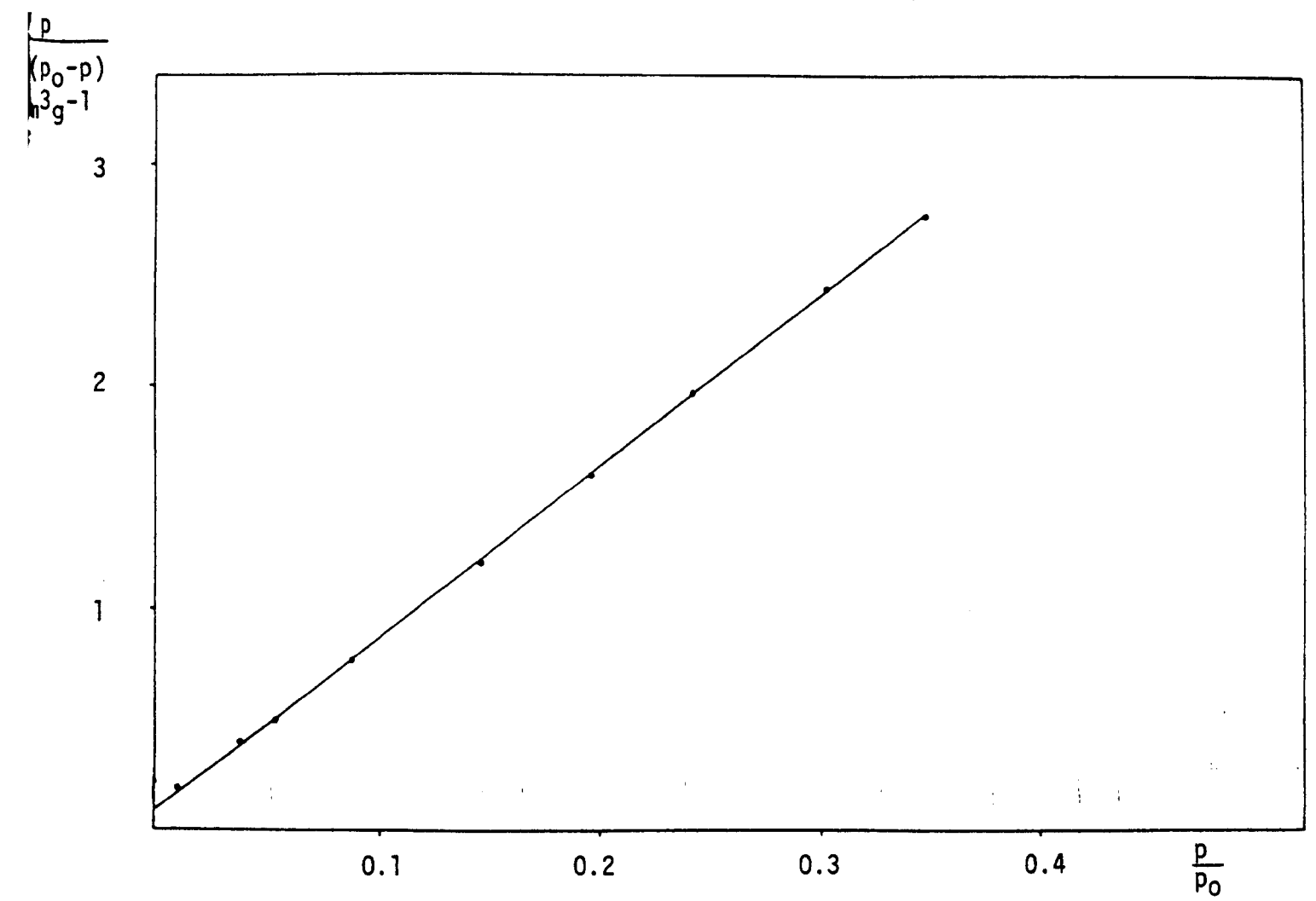

Figure 3.13 BET plot for 0.2NaW (Krypton adsorption)

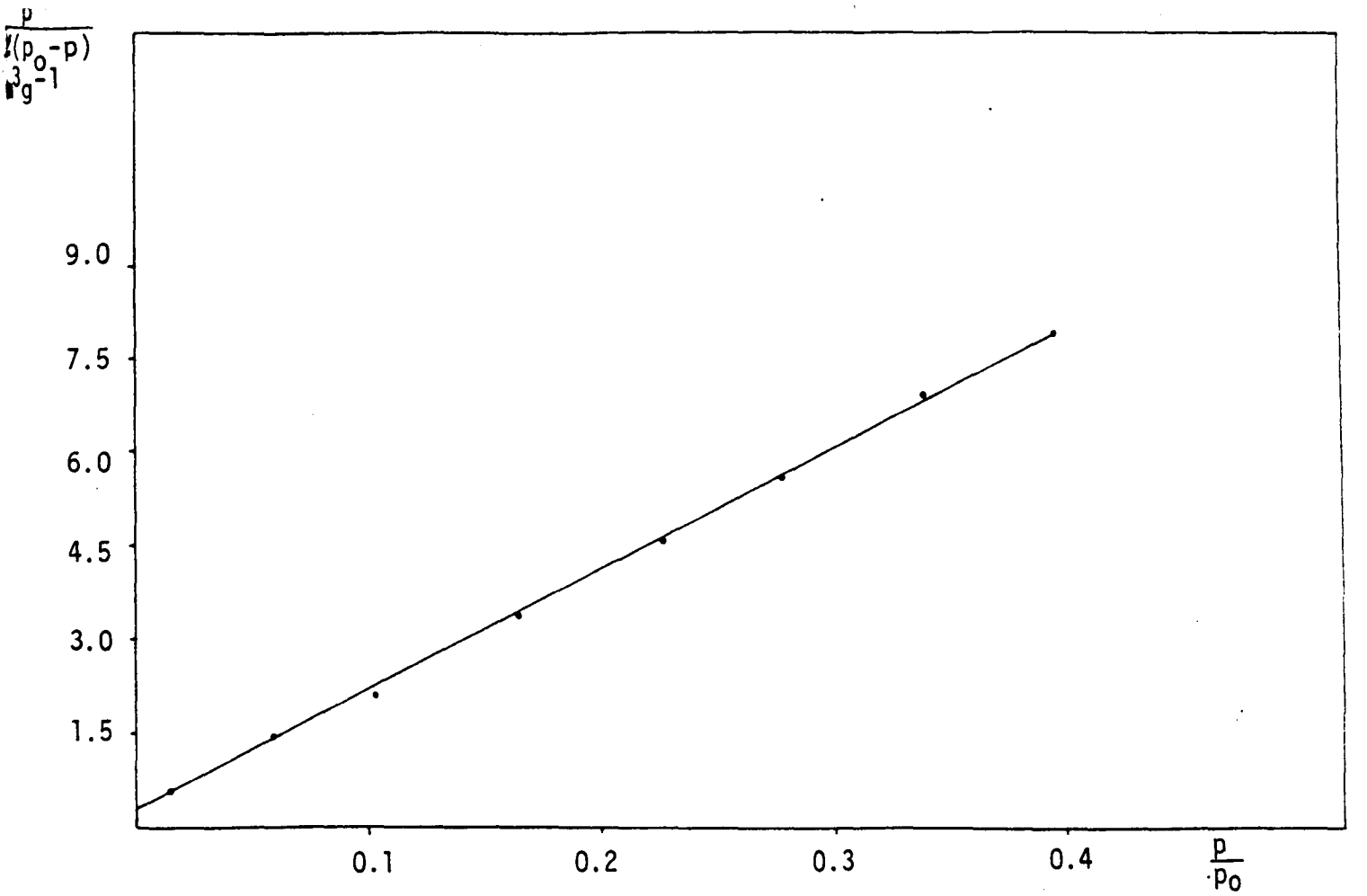

Figure 3.14 BET plot for 0.3NaW (Krypton adsorption)

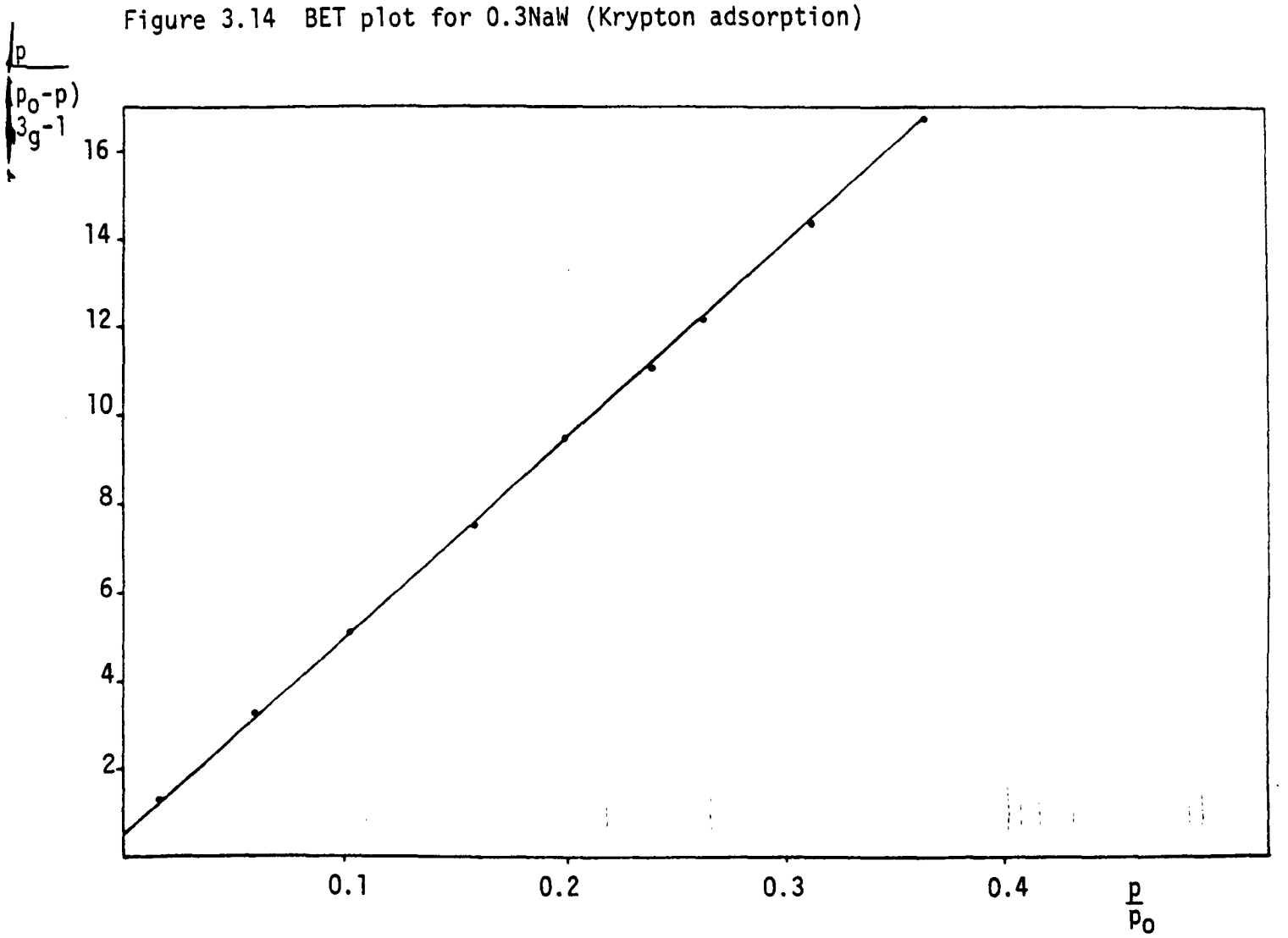

Figure 3.15 BET plot for 0.6NaW (Krypton adsorption)

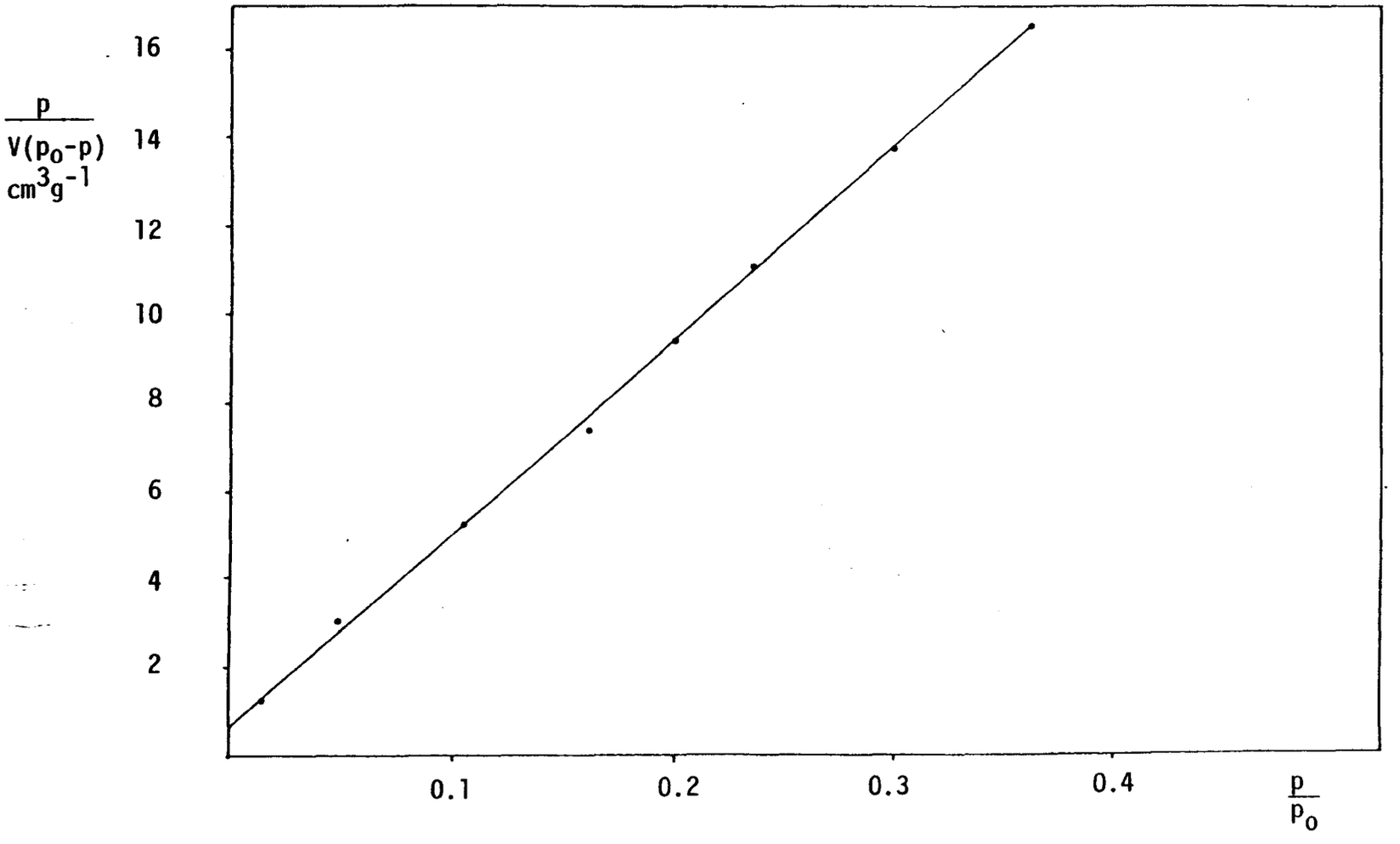

Figure 3.16 BET plot for 0.8NaW (Krypton adsorption)

which the bronzes are sintered depend on the alkali metal concentration, the higher this concentration, the greater is the loss of surface area due to sintering.

Table 3.1

Surface Area Values

Sample	Surface Area/m^2g^{-1} $\pm 0.05 m^2g^{-1}$
WO_3	1.15
0.05KW	1.05
0.2KW	0.77
0.3KW	0.26 (0.24)
0.6KW	0.16
0.8KW	0.16
0.05NaW	0.96
0.2NaW	0.64
0.3NaW	0.42 (0.39)
0.6NaW	0.13
0.8NaW	0.13

Good reproducibility is indicated by duplicate data in brackets.

3.6.2 Tpd of Ammonia

3.6.2.1 Tpd of Ammonia on WO_3 and K_xWO_3

Temperature programmed desorption of chemisorbed ammonia could show a picture of the distribution of the strength of the acid sites on the alkali metal tungsten bronzes. The rate of ammonia desorption as a function of temperature is considered for this purpose.

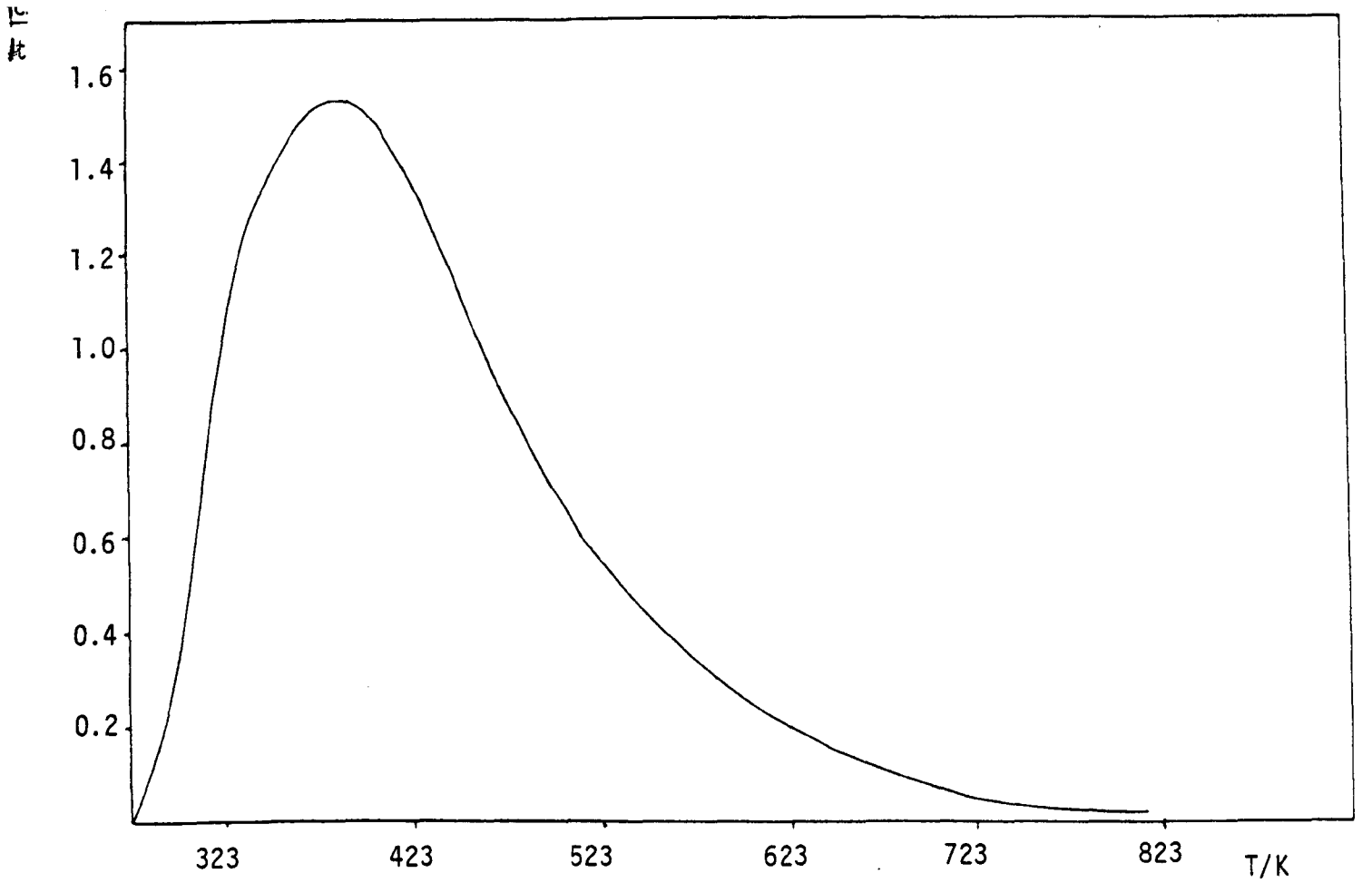

Figure 3.17 Tpd profile of NH_3 on WO_3

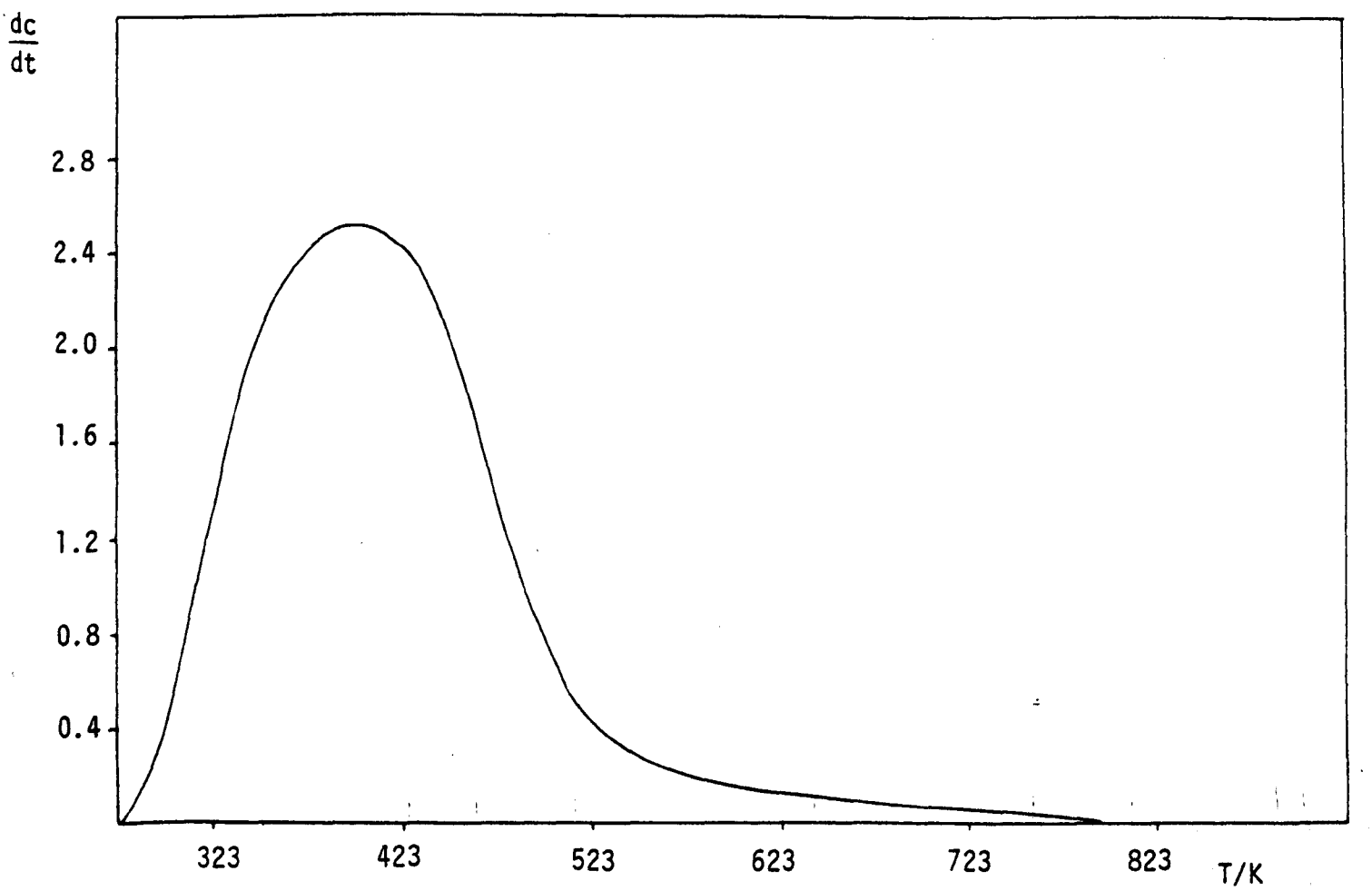

Figure 3.18 Tpd profile of NH_3 on 0.05KW

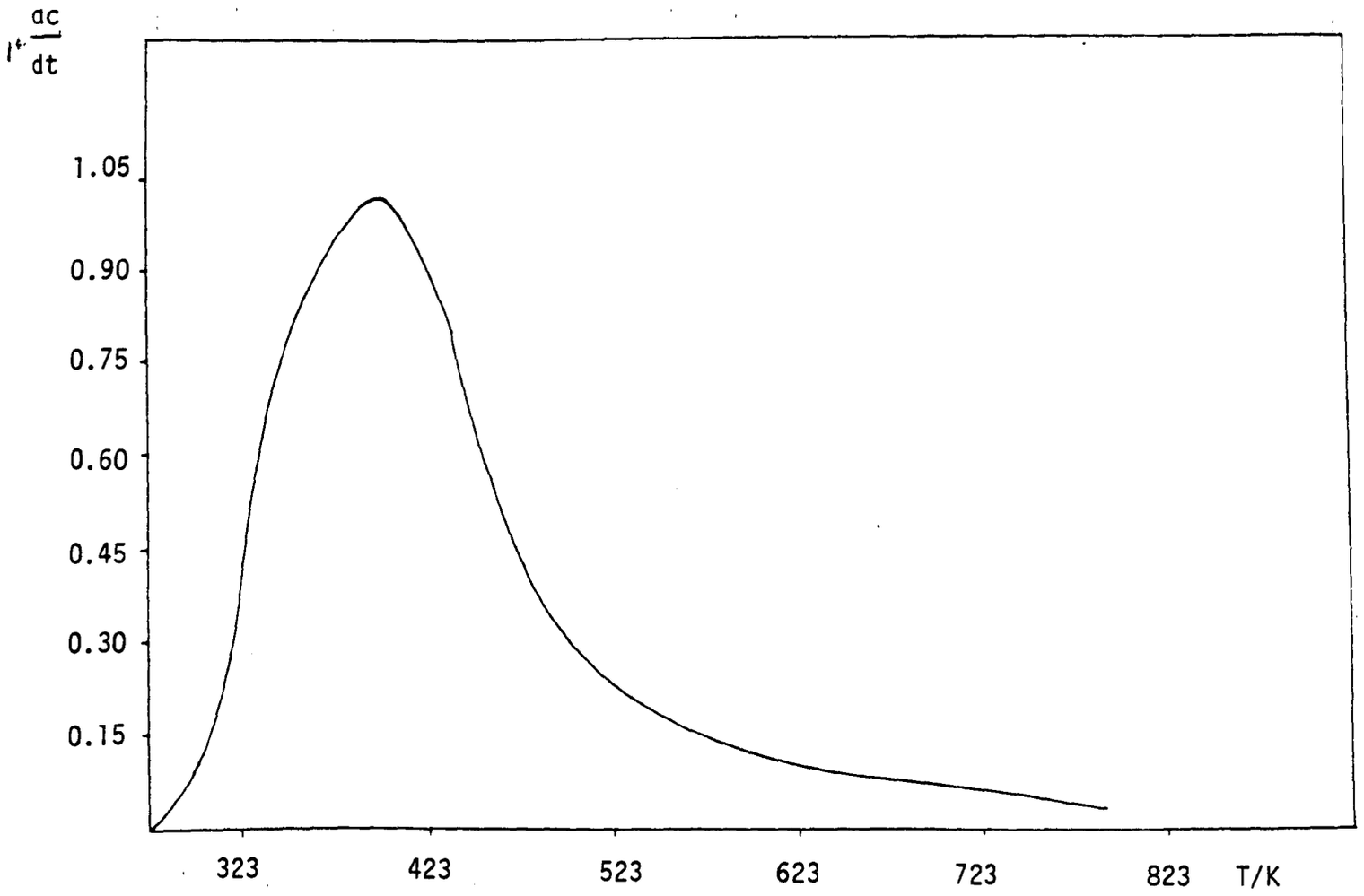

Figure 3.19 Tpd profile of NH_3 on 0.2KW

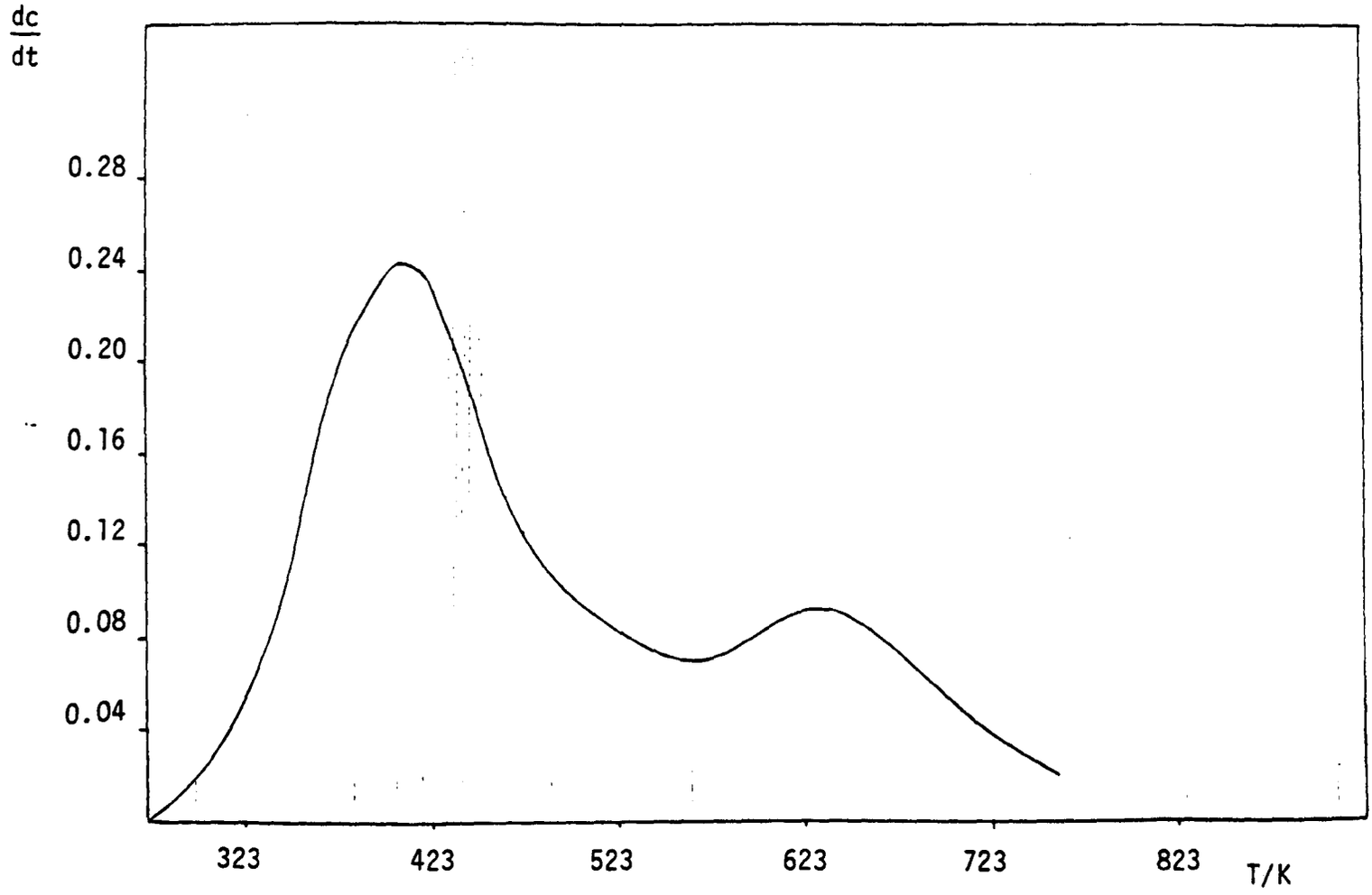

Figure 3.20 Tpd profile of NH_3 on 0.3KW

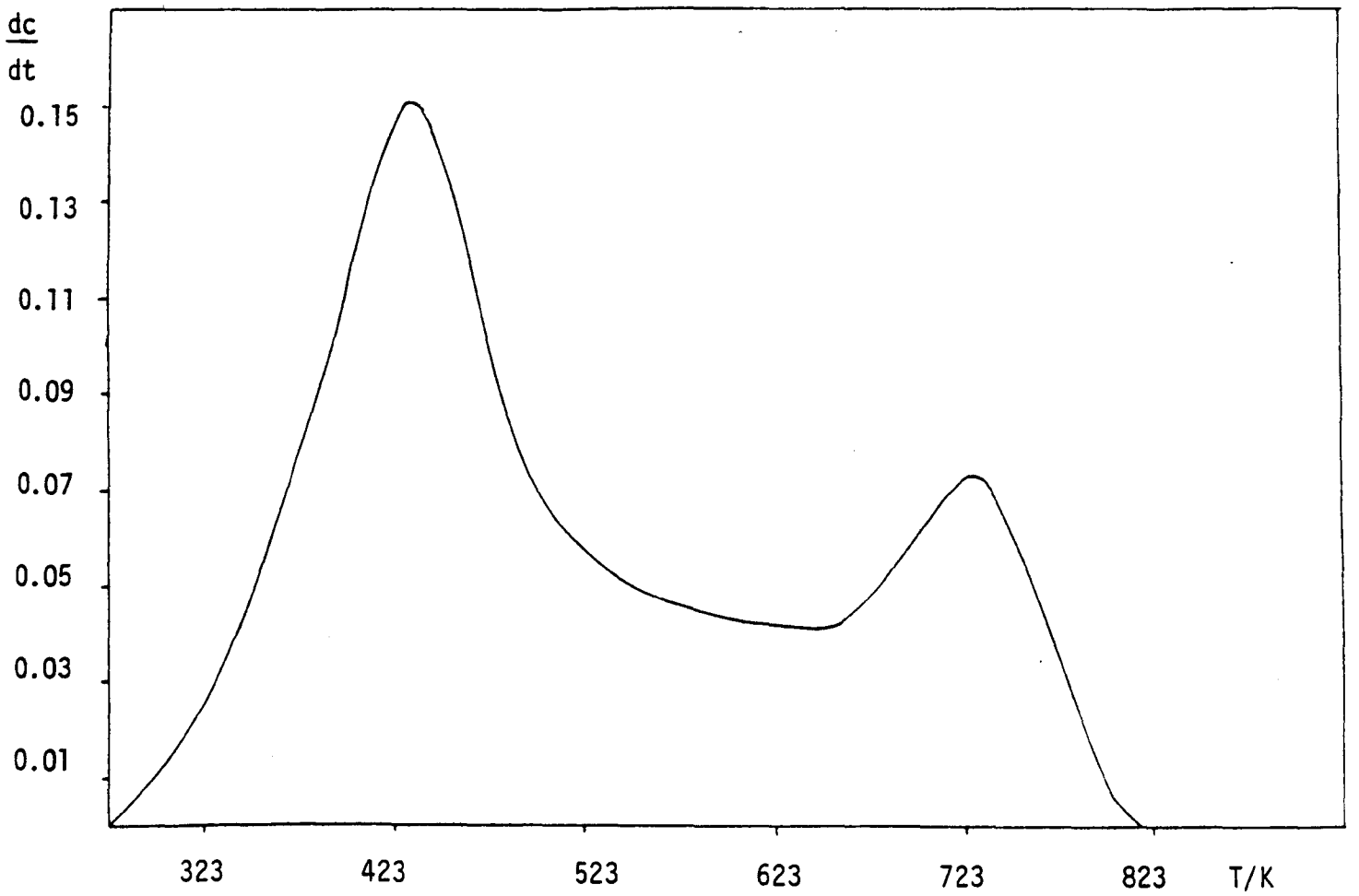

Figure 3.21 Tpd profile of NH_3 on 0.6KW

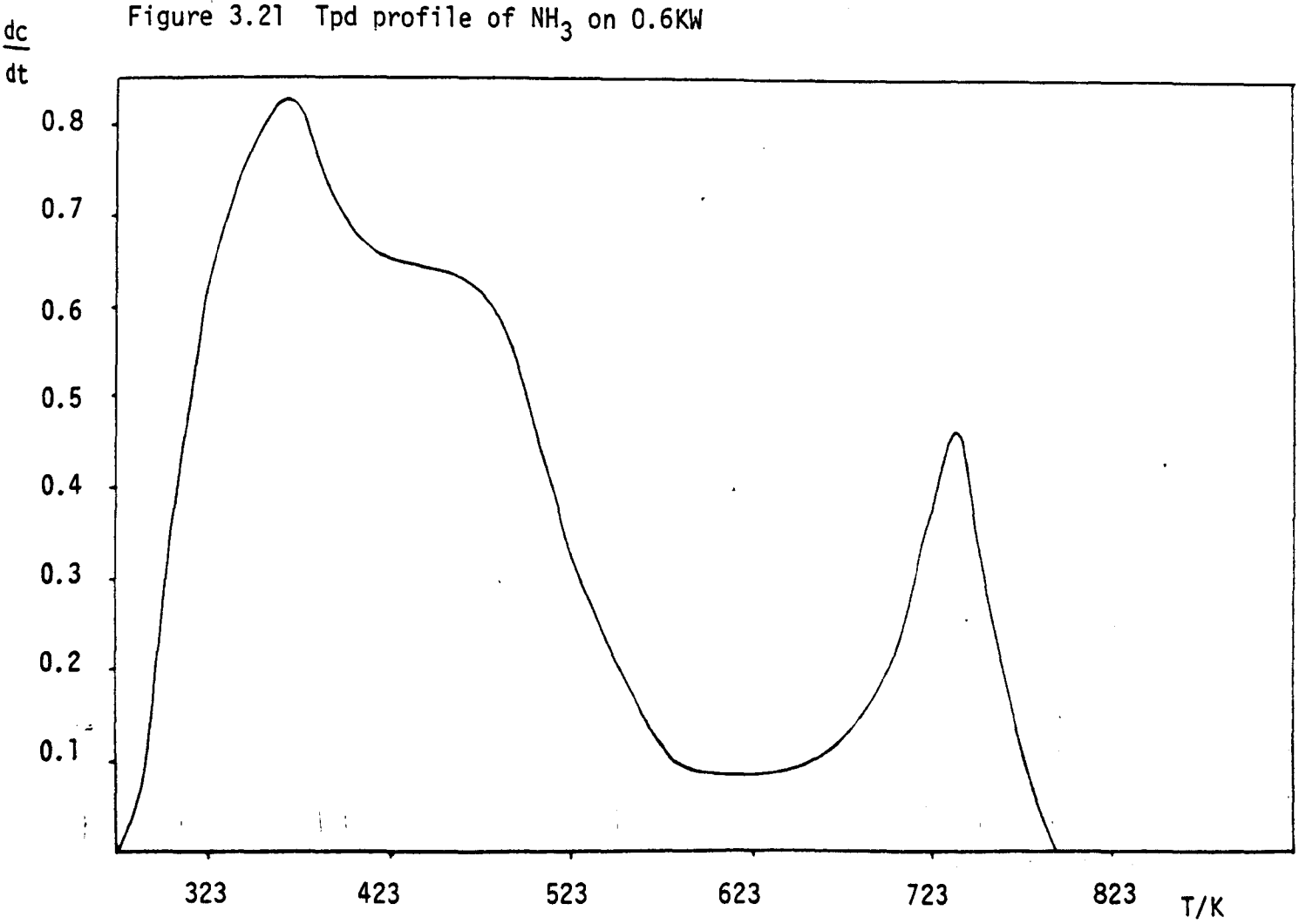

Figure 3.22 Tpd profile of NH_3 on 0.8KW

The tpd profiles of ammonia on samples of WO_3 and the potassium tungsten bronzes are shown in Figures 3.17 - 3.22 respectively. In general the profiles obtained for samples WO_3, 0.05KW and 0.2KW are quite similar : showing one broad desorption peak with a maximum at approximately 398K. The profile obtained for sample 0.3KW exhibits two overlapping peaks with maxima at 448K and 635K. The rate of ammonia desorption from sample 0.6KW also gives two peaks with maxima at 435K and 729K. The tpd profile for sample 0.8KW gives two peaks with maxima at 363K and 753K with a distinguished shoulder at 473K. The total amount of ammonia desorbed from these samples together with the temperature at which the maximum rate of desorption occurs are summarised in Table 3.2. In general it would appear that there are at least three different types of acid sites present on the potassium bronzes and these can then be correlated to the peak maxima. There is a low temperature peak at about 390K which is mostly present on bronzes with $x \lesssim 0.2$; however, the peak is also present on 0.8KW. There is a high temperature peak at $\sim$730K and another at $\sim$450K for bronzes with $x \lesssim 0.3$.

One obvious factor that can influence the nature of the acid site is the structure of the bronze, since it is possible that bronzes with the same structure will possess cages which are geometrically identical thus showing a similar distribution of acid sites. Although the assumption is true for bronzes with $x \lesssim 0.2$ (0.2KW is hexagonal and 0.05KW is an intergrowth tungsten bronze, which is a mixture of hexagonal and WO_3 phases), 0.3KW possessing the hexagonal structure has a quite similar distribution of acid sites to 0.6KW which has a tetragonal structure. It is possible that the alkali metal ion modifies the nature of the acid sites probably through an electronic effect;

thus its concentration could be important. It could explain why bronzes with high alkali metal content show more than one type of acid site. It will also be interesting to compare the acid site concentration on the bronzes as the alkali metal ion concentration is increased. Table 3.3 gives the BET surface area of the potassium bronzes and the acid site concentration (moles of NH_3 desorbed per m^2 of surface). The table also reports the surface area of acid sites calculated from the number of molecules of ammonia desorbed and assuming a cross-sectional area of $13.2 \times 10^{-20} m^2$ for the ammonia molecule. In general both the acid site surface areas and the acid site surface density tends to decrease with increasing potassium content; the only exception being 0.3KW which has a slightly higher surface concentration of acid sites than 0.2KW. Although the difference is within experimental error (normally ± 20%) for surface area and tpd measurements), it is possible that the stronger acid sites present on 0.3KW are each capable of adsorbing more than one molecule of ammonia.

Table 3.2

Sample	Molecules NH_3 desorbed/g	T_{max}/K
WO_3	6.98×10^{18}	385
0.05KW	4.40×10^{18}	398
0.2KW	1.34×10^{18}	398
0.3KW	5.28×10^{17}	448, 635
0.6KW	1.22×10^{17}	435, 729
0.8KW	3.07×10^{16}	363, 473(S) 735

(S) = shoulder

Table 3.3

Sample	No. of moles of NH_3 desorbed/m^2 of surface	Acid site surface area/ m^2g^{-1}	BET surface area/m^2g^{-1}
WO_3	10.07×10^{-6}	0.92	1.15
0.05KW	6.96×10^{-6}	0.58	1.05
0.2KW	2.89×10^{-6}	0.18	0.77
0.3KW	3.37×10^{-6}	0.07	0.26
0.6KW	1.27×10^{-6}	0.016	0.16
0.8KW	0.32×10^{-6}	0.004	0.16

3.6.2.2 Tpd of Ammonia on Na_xWO_3

The tpd profiles of the sodium tungsten bronzes are shown in Figures 3.23 - 3.27. The profiles for samples 0.05NaW, 0.2NaW and 0.3NaW comprise a single peak in each case, with the peak for 0.05NaW being sharper than for the other two bronzes. The peak maximum tends to move to lower temperatures increasing sodium content. The rate of ammonia desorption from sample 0.6NaW gives a very broad peak with a maximum at 493K and distinct shoulders at 411K and 623K. The tpd profile of 0.8NaW shows a broad peak with maxima at 543K and 698K and a shoulder at 411K. Table 3.4 records the amount of ammonia desorbed from these samples and the temperature at which the maximum rate of desorption occurs. As for the potassium bronzes, the sodium analogues with low alkali ion concentration, $x \leqslant 0.2$, have mostly one type of acid site present. However T_{max} tends to indicate that the sites present on the sodium bronzes with $x \leqslant 0.2$ could be of a stronger nature than those on the corresponding potassium bronzes. These sodium bronzes have a tetragonal structure and their distribution of acid sites should relate to those present on 0.6KW which is also

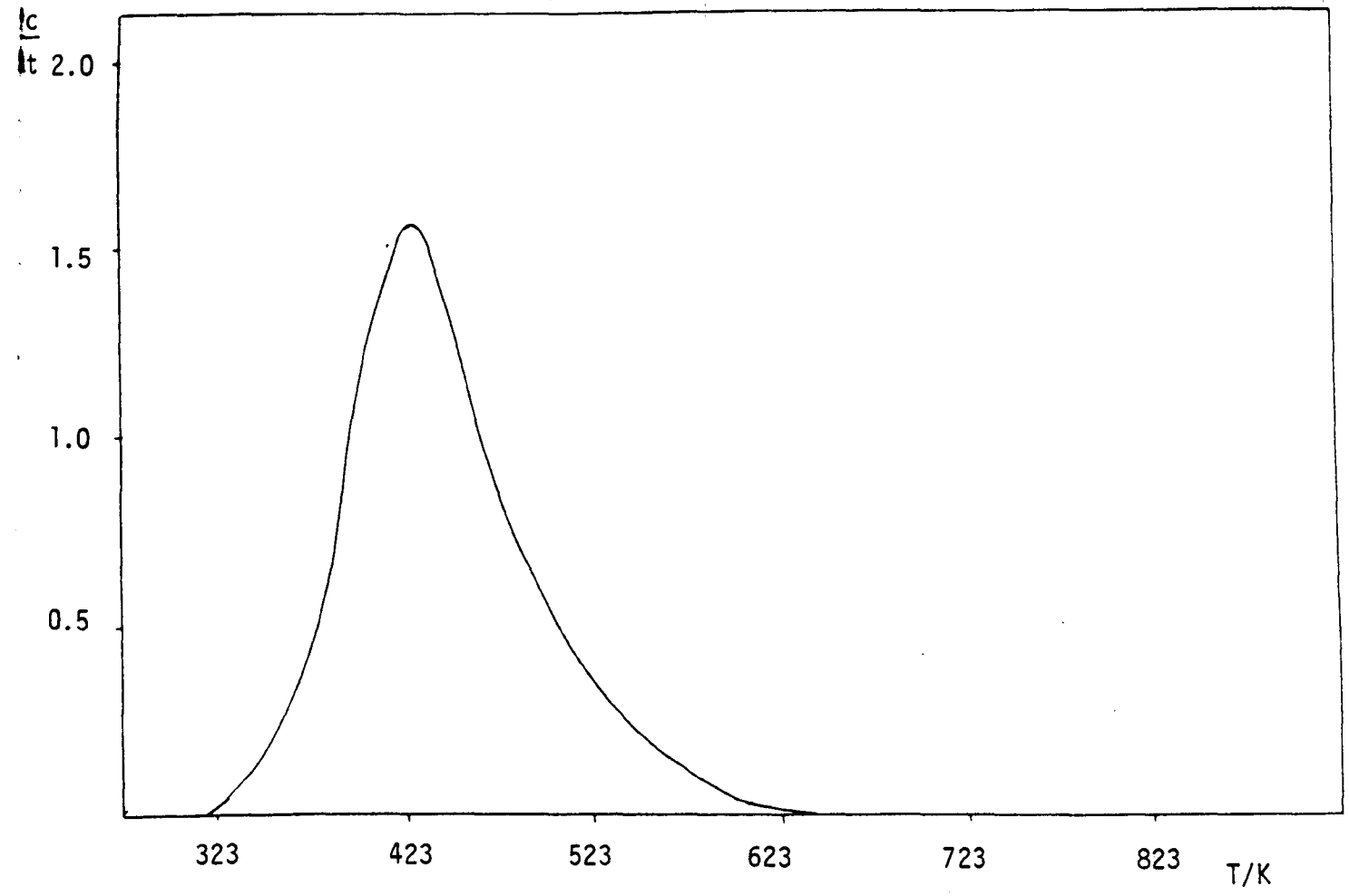

Figure 3.23 Tpd profile of NH_3 on 0.05NaW

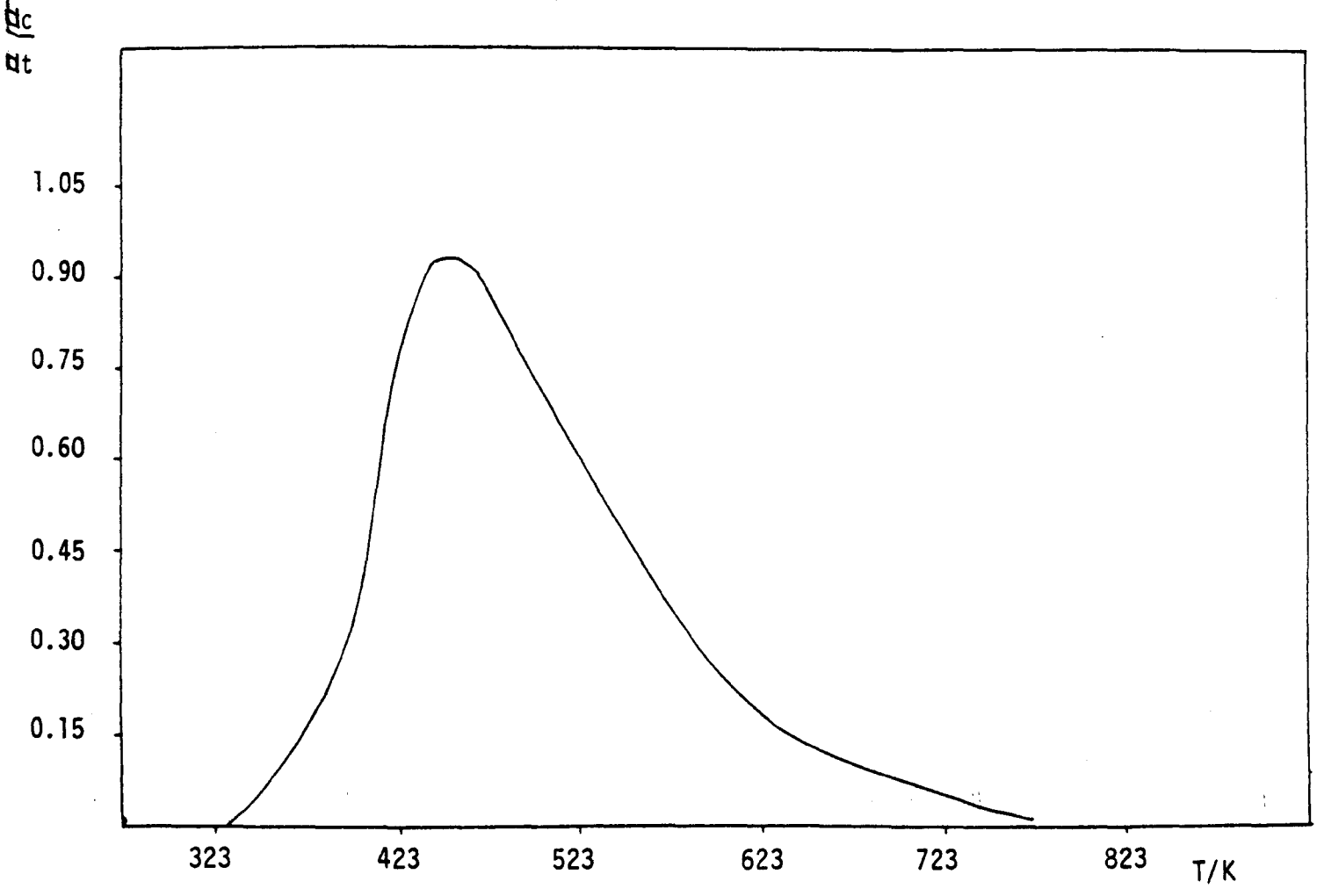

Figure 3.24 Tpd profile of NH_3 on 0.2NaW

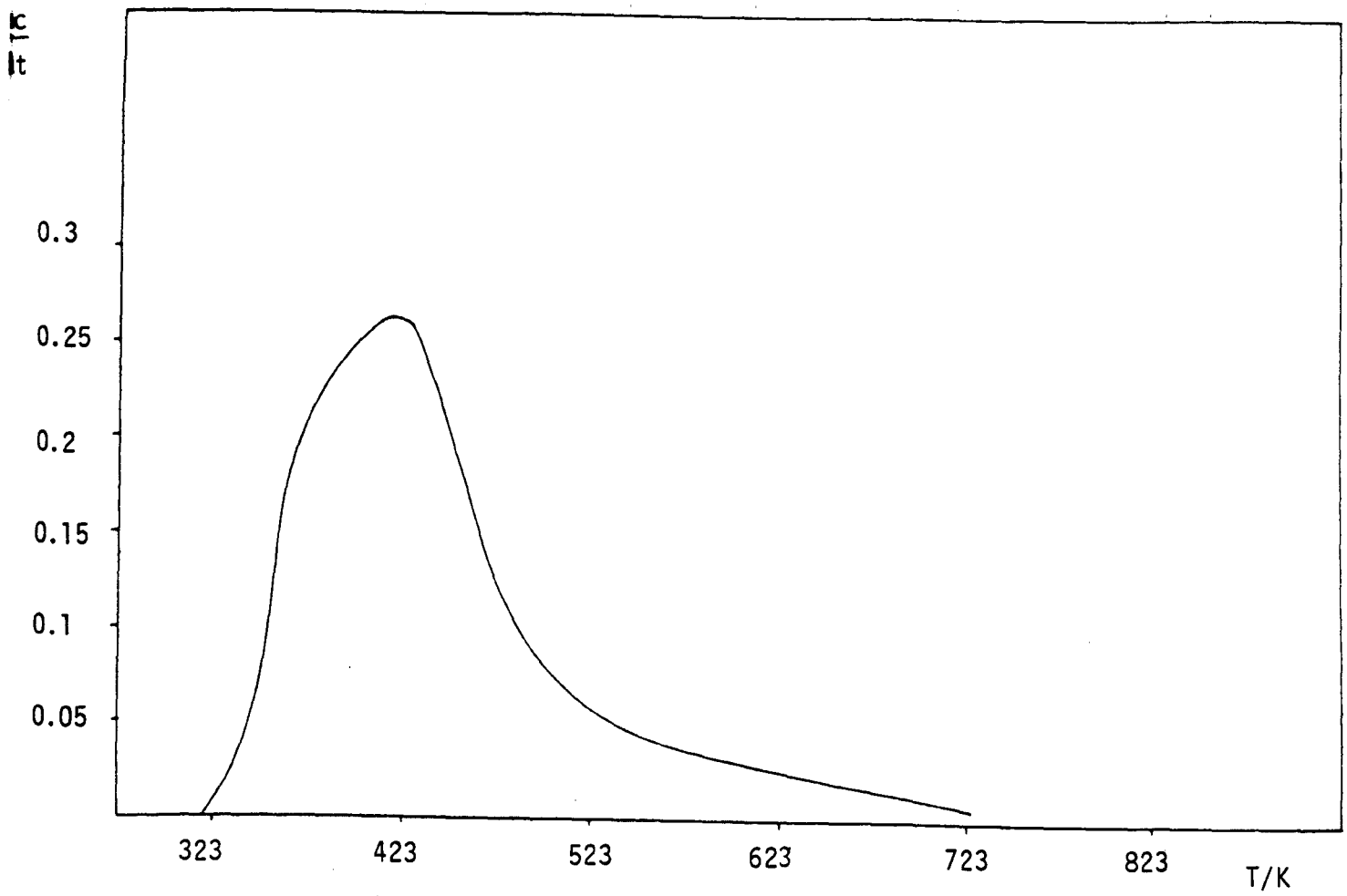

Figure 3.25 Tpd profile of NH_3 on 0.3NaW

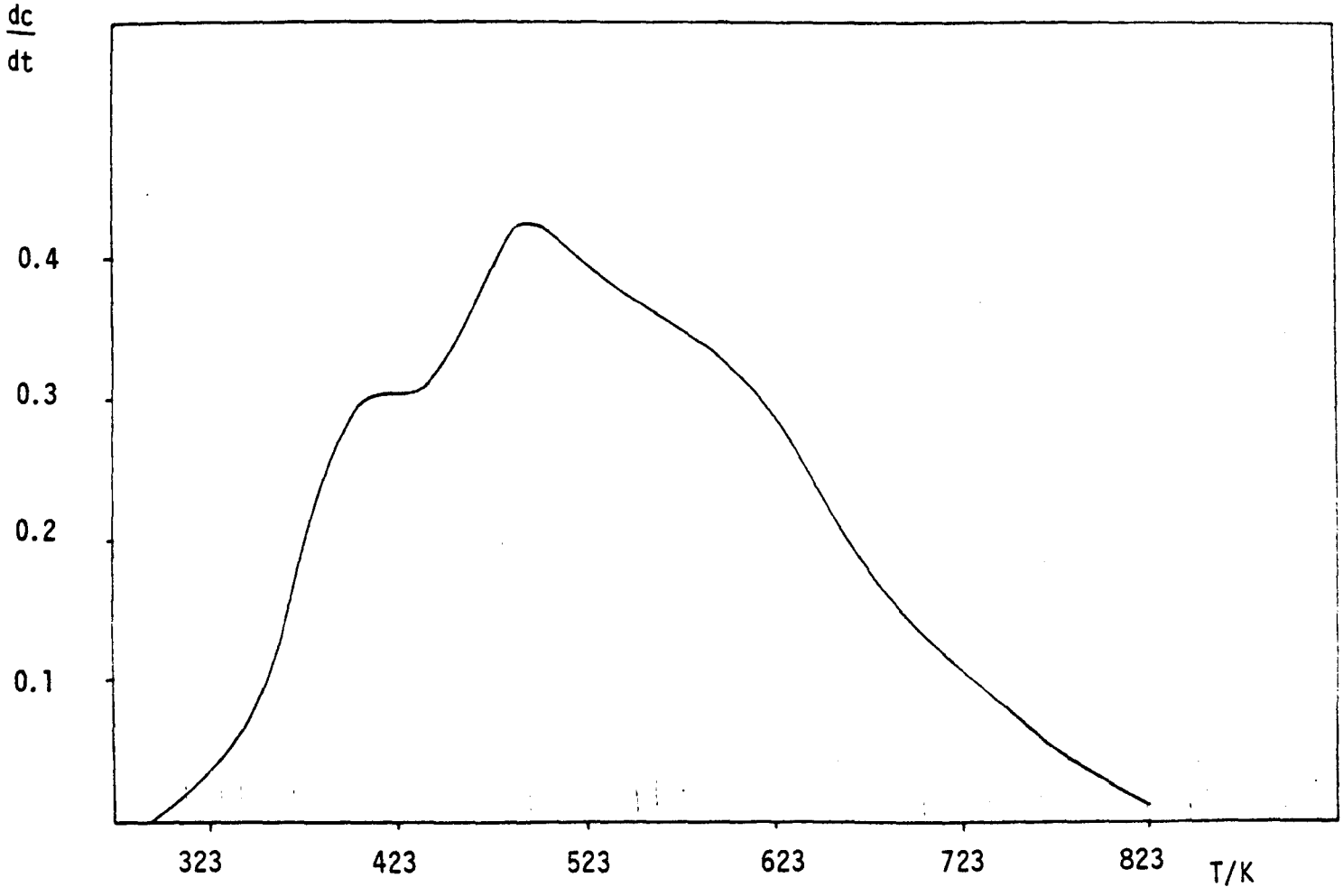

Figure 3.26 Tpd profile of NH_3 on 0.6NaW

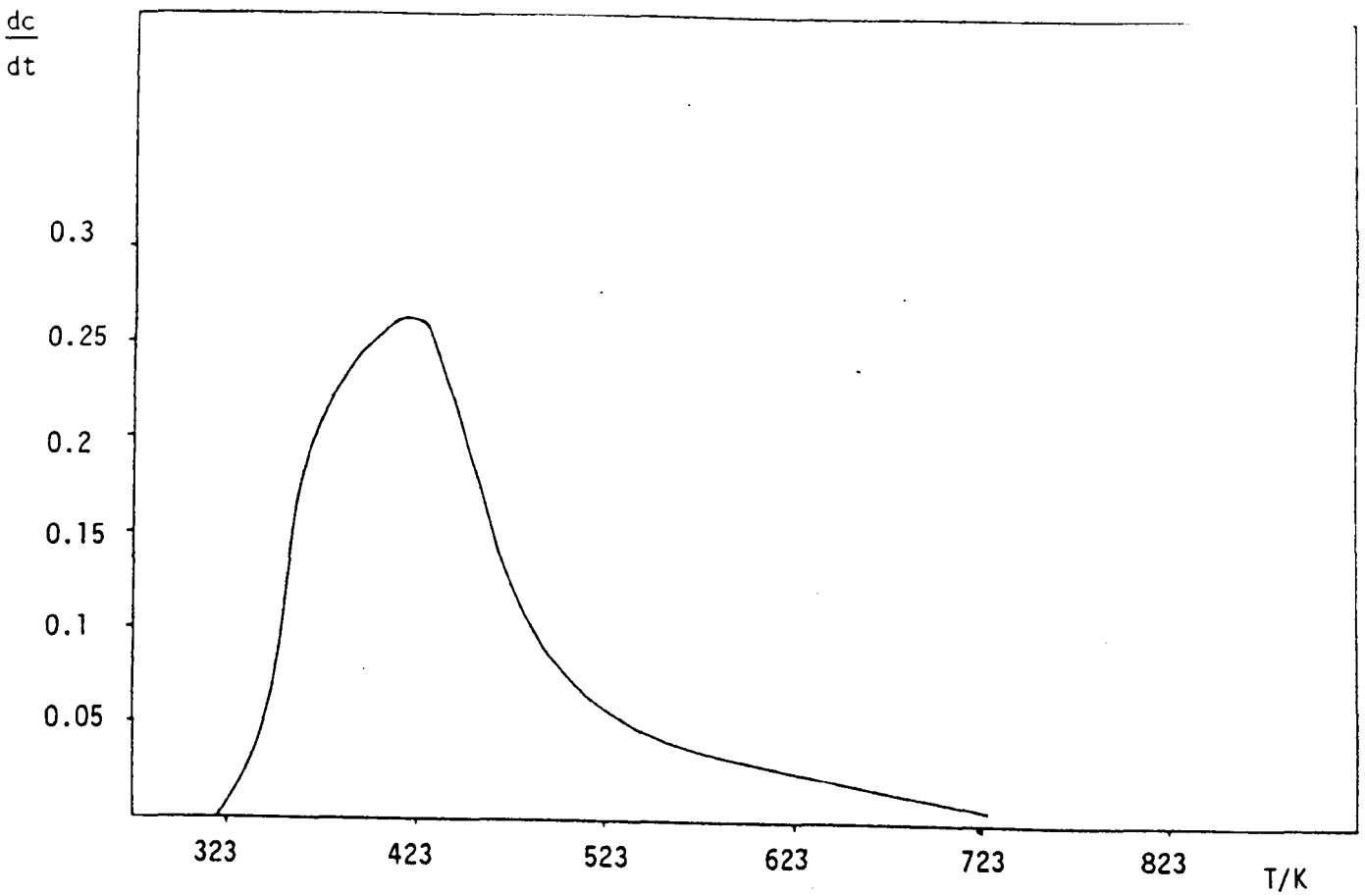

Figure 3.25 Tpd profile of NH_3 on 0.3NaW

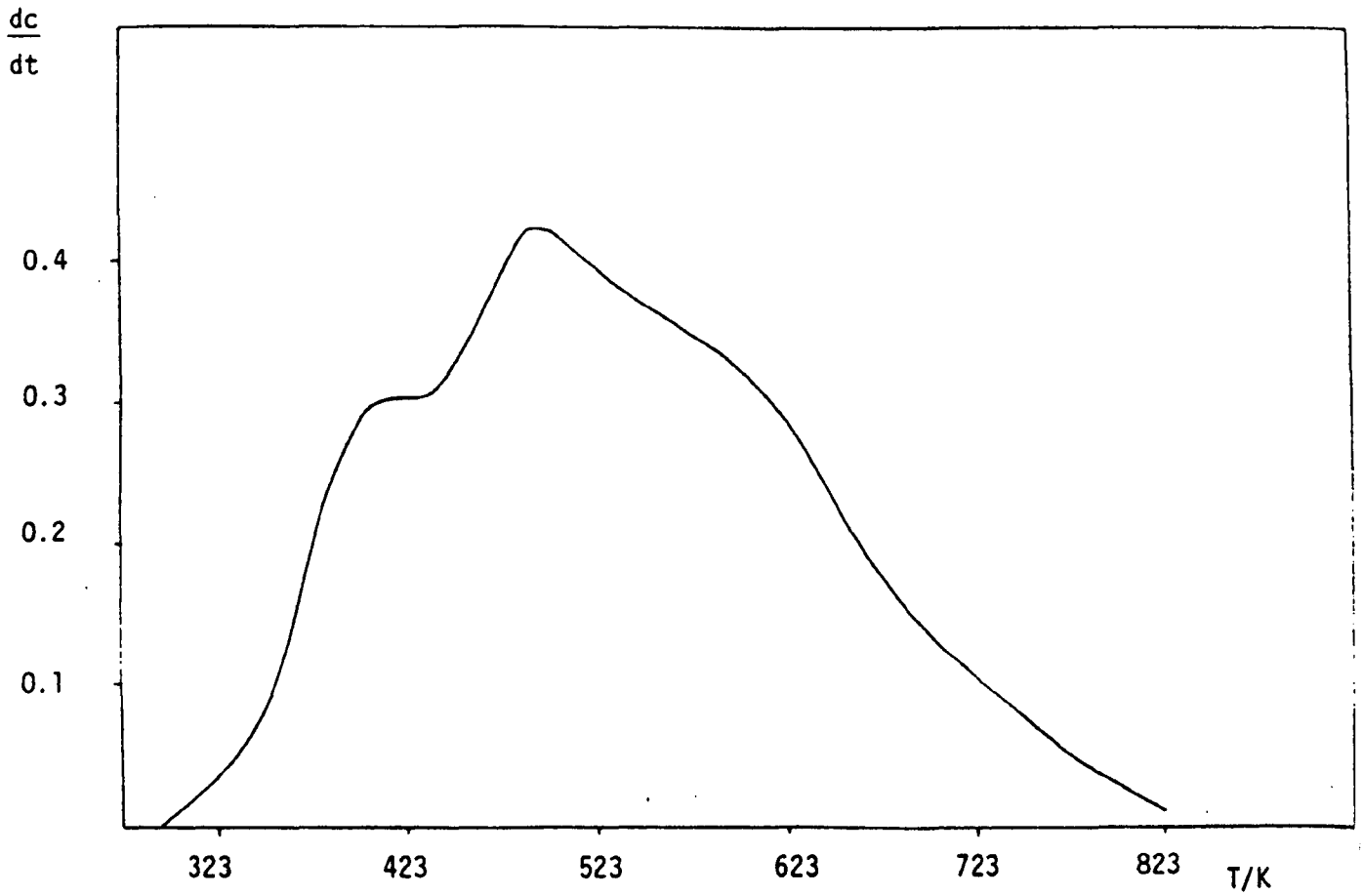

Figure 3.26 Tpd profile of NH_3 on 0.6NaW

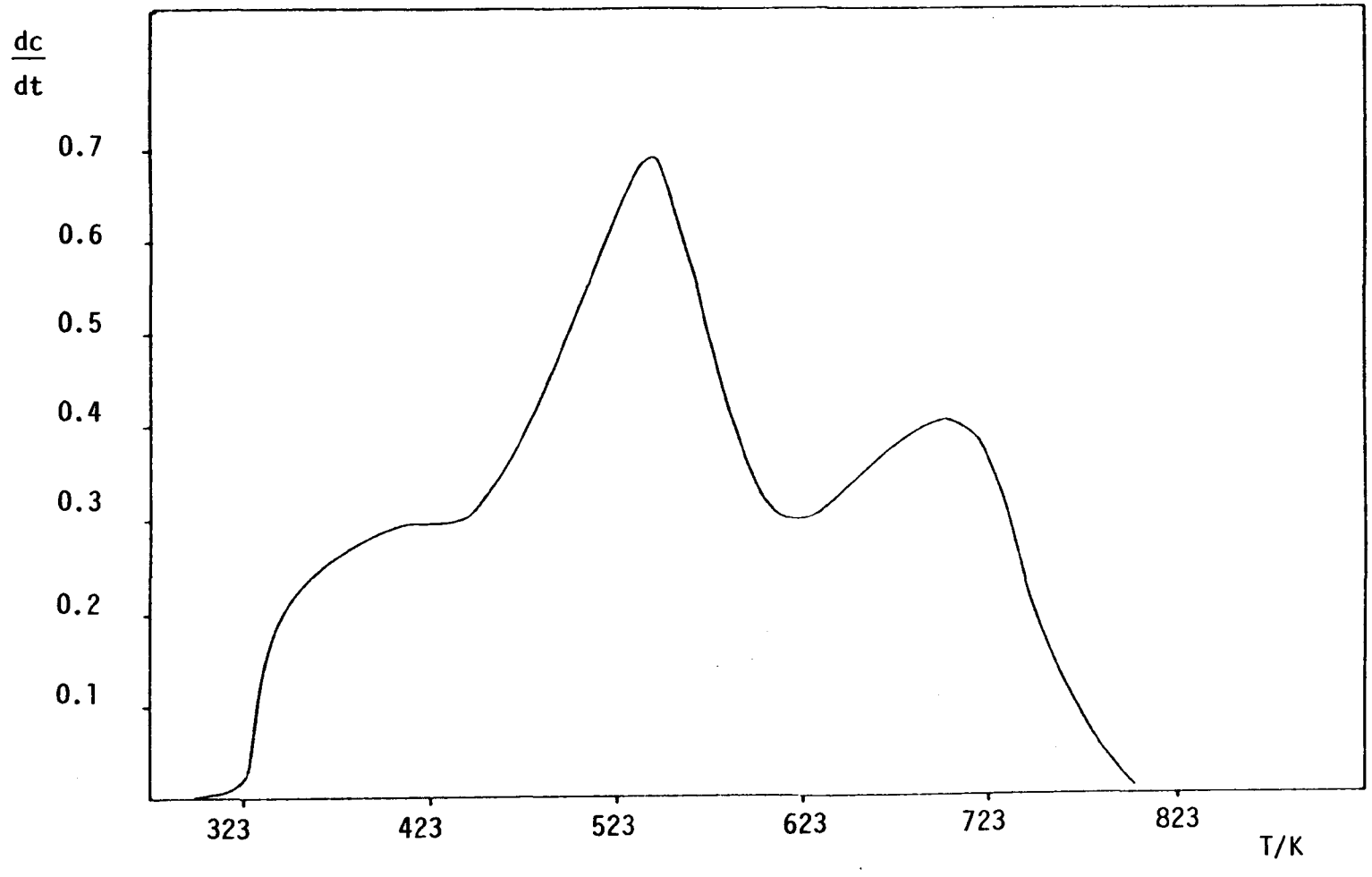

Figure 3.27 Tpd profile of NH_3 on 0.8NaW

tetragonal, but however, possess two types of acid sites with T_{max} at 435K and 729K. 0.3NaW contains only one type of acid site which is weaker than those present on the hexagonal 0.3KW. The sodium bronzes with higher sodium concentration contains more than one type of acid site. Table 3.5 gives the BET surface area of the sodium bronzes, the acid site concentration and the acid site surface area. The acid site surface concentration decreases with increasing sodium content similar to the potassium bronzes.

The type of acid site present on the alkali tungsten bronzes appears to be influenced by the structure of the bronzes, the concentration and nature of the alkali metal ion. In general there is a higher concentration of acid sites present on the potassium bronzes than the corresponding sodium bronzes. However at low alkali metal ion concentration the acid sites present on the sodium bronzes are of a stronger nature than those on the potassium bronzes. At high alkali ion concentration, different types of acid sites are present on both bronzes. Bronzes with the same structure also give acid sites of different strengths depending on the concentration and nature of alkali ion present.

The nature of the acid sites present on WO_3 and the bronze samples observed from ammonia desorption will be discussed later in conjunction with the isopropanol decomposition reaction.

3.6.3 Transmission Electron Microscopy

High Resolution Electron Microscopy (HREM) has previously been used to study the structure of tungsten bronzes[13]. In the present study, only in a few cases, especially for sample 0.05KW and 0.2KW,

Table 3.4

Sample	Molecules HN_3 desorbed/g	$T_{max}K$
0.05NaW	1.36×10^{18}	428
0.2NaW	5.05×10^{17}	453
0.3NaW	3.20×10^{17}	416
0.6NaW	3.87×10^{16}	411(s),493, 623(s)
0.8NaW	2.80×10^{16}	411(s),543, 698

(s) = shoulder

Table 3.5

Sample	No. of moles of NH_3 desorbed/m^2 of surface	Acid site surface area /m^2g^{-1}	BET surface area/m^2g^{-1}
0.05NaW	2.34×10^{-6}	0.18	0.96
0.2NaW	1.31×10^{-6}	0.067	0.64
0.3NaW	1.26×10^{-6}	0.042	0.42
0.6NaW	0.49×10^{-6}	0.005	0.13
0.8NaW	0.36×10^{-6}	0.004	0.13

were successful images obtained. Figures 3.29 - 3.32 show electron images of samples 0.05KW and 0.2KW. Sample 0.05KW is an intergrowth tungsten bronze and may be considered as a lamellar intergrowth of hexagonal tungsten bronze (HTB) and WO_3. The formation of this type of structure can be regarded as a way of adapting to alkali poor conditions by "diluting" the HTB with slabs of pure WO_3, whereby a

certain minimum degree of filling of the tunnels can be maintained. Kihlborg[13] employed HREM to obtain images of ITBs prepared with K, Rb, Cs and Tl. The images obtained enabled identification of vertical slabs of HTB and WO_3 in ITBs and of distorted ITBs containing single and double HTB tunnel rows and WO_3 slabs of varying widths. Figures 3.29 and 3.30 give the electron images of the ITB, 0.05KW, and shows signs of the vertical slabs of HTB and WO_3 present in this type of bronze. Figures 3.31 and 3.32 give the electron images of sample 0.2KW, and show signs of vertical slabs and layers. Bando et al[14] has studied HTBs using HREM and has proposed a model in which layers occur with the alkali sites either completely filled or completely empty. Stacking of these two types of layers occurs so that 4 or 5 filled layers are followed by a vacant one.

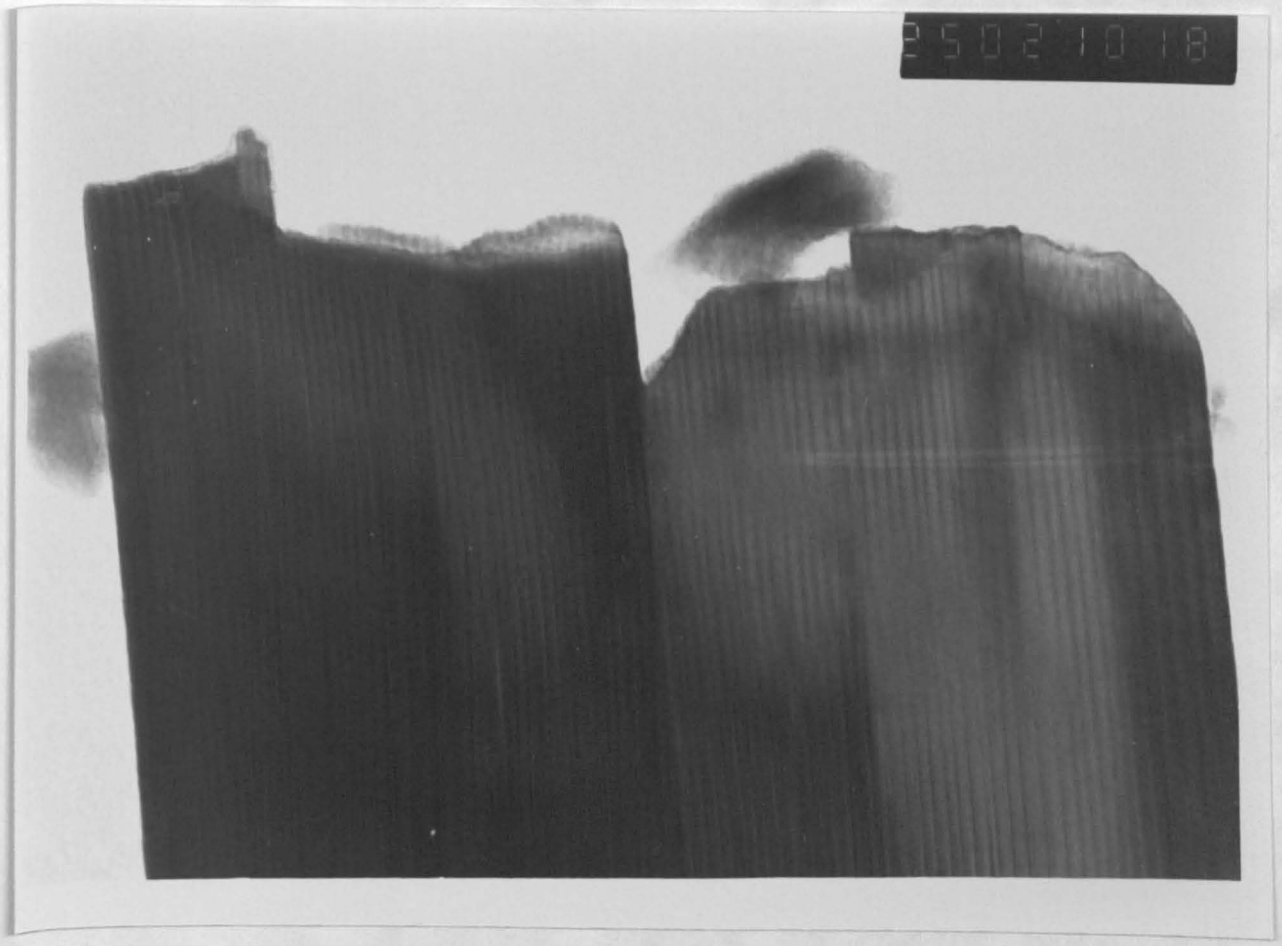

Figure 3.29 Electron image of 0.05KW

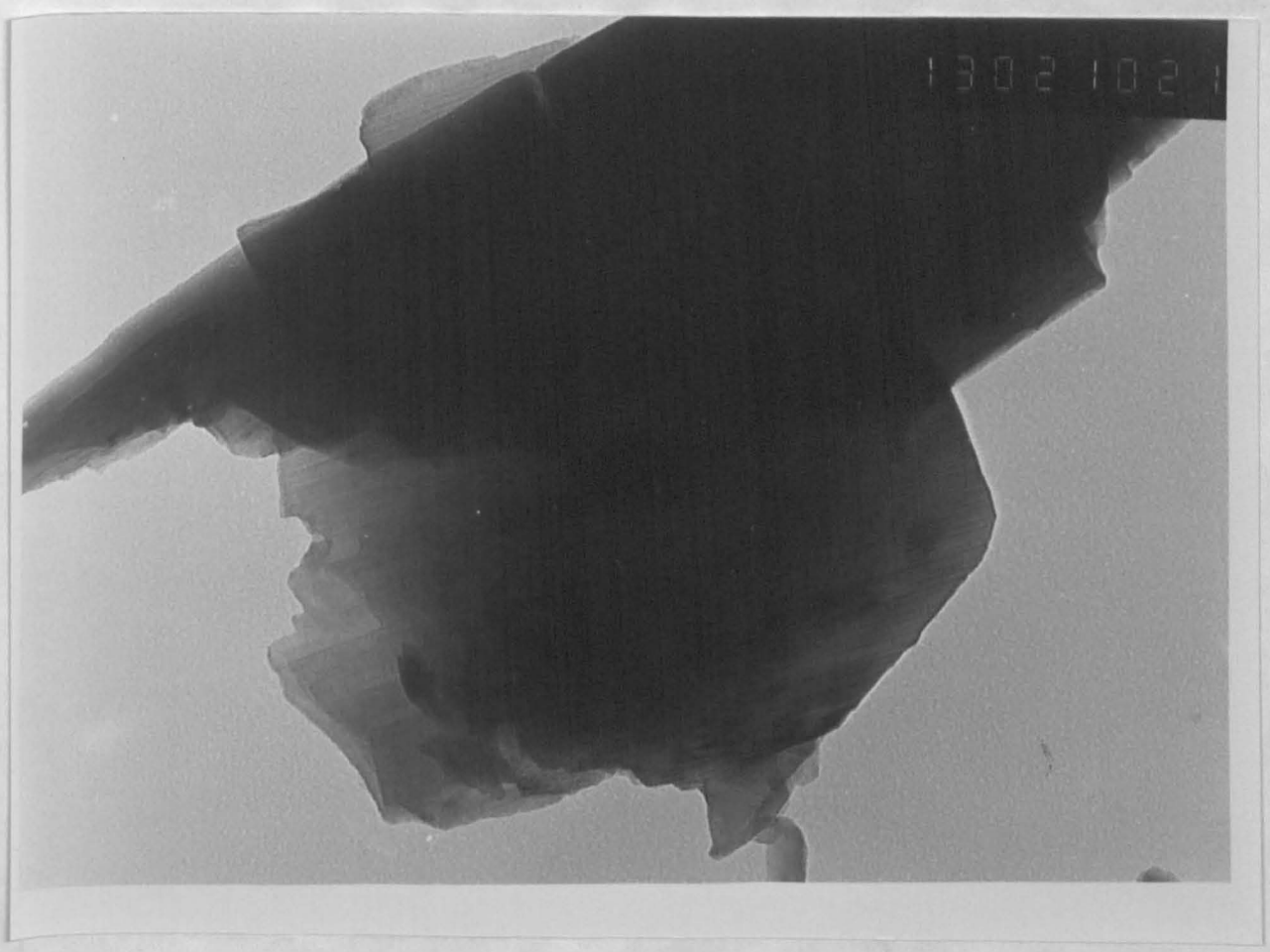

Figure 3.30 Electron image of 0.05KW

Figure 3.31 Electron image of 0.2KW

Figure 3.32 Electron image of 0.2KW

CHAPTER 3

REFERENCES

1. S. Brunauer, P.H. Emmett and E. Teller, J.Am. Chem. Soc., 60, 309, (1938).
2. I. Langmuir, J. Am. Chem. Soc., 40, 1368, (1918).
3. S.J. Gregg and K.S.W. Sing, Surface and Colloid Science, 9, Ed. Matijevic, John Wiley and Sons, (1976).
4. S.J. Gregg and K.S.W. Sing, Adsorption, Surface Area and Porosity, Academic Press, (1984).
5. B.S. Green, M. Lahav and G.M.J. Schmidt, Mol. Cryst. Liq. Cryst., 29, 187, (1975).
6. P.C. Chenchalah, H.L. Hollands and M.F. Richardson, J. Chem. Soc. Chem. Commun., 436, (1982).
7. O. Johnson, J. Phys. Chem., 59, 827, (1955).
8. S. Ramdas, W. Jones, J.M. Thomas and J.P. Desvergne, Chem. Phys. Lett., 57, 468 (1978).
9. J.E. Mopes and R.P. Eischens, J. Phys. Chem., 58, 1059, (1954).
10. C.V. Hidalgo, H. Itoh, T. Hattori, M. Niwa and Y. Murakami, J. Catal., 85, 362, (1984).
11. V. Kanazirev and N. Borisova, Zeolites, 2, 23, (1982).
12. S. Stevenson, M. Phil. Thesis, Brunel University (1985).
13. L. Kihlborg and R. Sharma, J. Microsc. Spectrosc. Electron, 7, 1892, 387, (1982).
    L. Kihlborg, Solid State Chemistry, 3, 143, (1982).
14. Y. Bando and S. IIJima, Acta. Cryst. A37, C-303, (1981).

CHAPTER 4

THERMAL ANALYSIS

4.1 Introduction

The alkali metal tungsten bronzes which are non-stoichiometric compounds attract attention because of the possibility of their use in modern technology as electrode materials for fuel cells, as electrically conductive transparent films and in semiconductor devices. Although they were discovered at the beginning of the last century, their thermodynamic properties or chemical stability in the presence of oxidising or reducing gases is still a subject of great interest.

The reduction of alkali metal tungsten bronzes has previously appeared in the literature. Dickens[1] has studied the reduction of the oxides and the bronzes of tungsten. Lower oxides of tungsten reduced directly to tungsten; the α form in the case of WO_2 and $W_{18}O_{49}$ and the β form for $W_{20}O_{58}$. WO_3 however, first formed $W_{20}O_{58}$ in a hydrogen atmosphere, which then reduced to β tungsten. The low alkali containing tungsten bronzes were shown to reduce initially to an oxygen deficient modification of WO_3 and subsequent reduction gave sodium tungstate and both forms of tungsten. For the sodium bronzes, as the sodium content increases it was found that the formation of a higher content bronze occurred, the excess tungsten initially being removed as tungsten dioxide and finally α- and β- tungsten. The sodium content of the bronze increases until it is converted to the cubic peroskite structure and finally to $NaWO_3$ which then reduced to Na_2WO_4. For all bronzes the final products of reduction were tungsten metal and tungstate. Bulk oxidation of the tungsten bronzes is thought to produce either X_2WO_4 and WO_3 or the x-polytungstate and WO_{3-x} and

involves an oxygen uptake which increases as the alkali metal ion content increases. Deschanures[2] and Hussain[3] et al suggest conversion of tungsten bronzes to polytungstates quickly at 873 - 973K and then oxidation of the lower tungsten oxide to the trioxide at about 1223K.

The sodium and potassium bronzes prepared here have been compared for their reactivities as exemplified by their reduction in hydrogen gas and their oxidation in a diluted oxygen gas stream.

4.1.2 Thermal Methods of Analysis

Thermal analysis involves heating a sample at a constant rate in a certain atmosphere or under vacuum and observing some changes in the sample or its surroundings. Thermogravimetric analysis (tga) is the simplest of the thermal analysis techniques and involves measurement of the mass of the sample as a function of temperature. Differential thermal analysis (dta) monitors the temperature difference between the sample and a reference material and thus gives an indication of whether an exothermic or endothermic reaction is occurring in the sample.

In temperature programmed reduction (tpr) the hydrogen consumed in a reduction step is being monitored as the sample is being heated in a diluted hydrogen atmosphere. Temperature programmed oxidation (tpo) involves measurement of the oxygen uptake as the sample is heated in a dilute oxygen atmosphere.

4.2 Experimental Thermal Analysis

4.2.1 Tga and Dta Techniques

Thermogravimetric and differential thermal analysis was performed

on a Stanton Redcroft STA 780 Simultaneous Thermal Analyser, which is designed to give simultaneous thermogravimetric records and differential thermal analysis curves. The sample (usually about 20mg ± 0.01mg) and the reference material, α-alumina were contained in rhodium-platinum crucibles. The crucibles were mounted on top of flat plates, Pt-Pt/Rh thermocouple system. To eliminate possible factors which may affect the thermogravimetric and dta curves the same sample size, heating rate 10K min^{-1} and gas flow rate of 40$cm^3 min^{-1}$ were used for the different samples. The nitrogen and hydrogen gases were purified by passing through a 5A molecular sieve trap at 295K. Before each reduction run, the sample and the system were flushed with nitrogen for about 15 minutes. The sample was then heated in nitrogen to 373K to remove any moisture. When the weight had stabilised the sample was cooled to room temperature and the nitrogen flow was replaced by hydrogen flow. When the weight was constant, heating was started and the weight change and the temperature difference between the sample and the reference material was recorded as a function of temperature to 1223K.

4.2.2 Tpr Technique

A schematic drawing of the tpr apparatus used in the present work is shown in Figure 4.1.

The sample was placed in a silica reactor fitted with a thermocouple to measure the sample temperature and surrounded by a tubular furnace whose temperature was controlled by a linear temperature programmer. The reducing gas 5% H_2/95% Ar was purified by passing through a trap containing Pd/Al_2O_3 at 295K to remove any oxygen and another trap of 5A molecular sieve at 295K to remove any moisture. It is important that the oxygen content of the gas stream be reduced

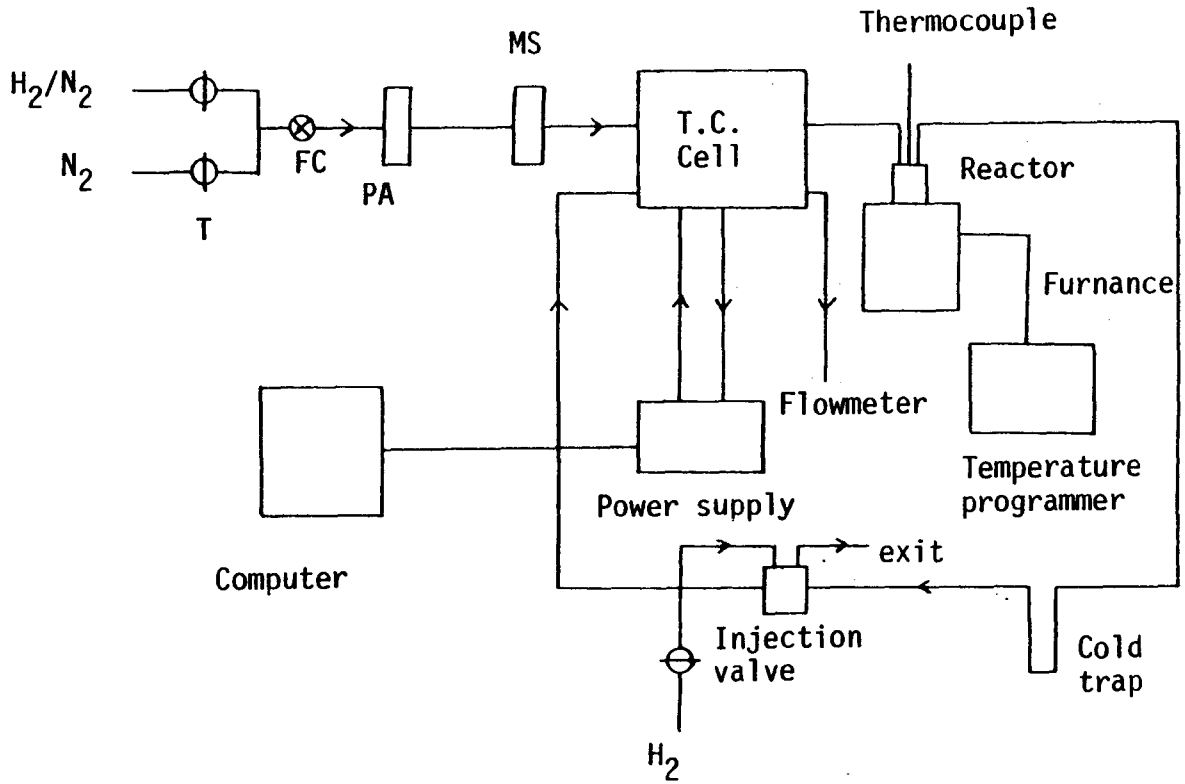

T = Tap
FC = Flow Controller
PA = Pd/Al_2O_3 Trap
MS = Molecular Sieve

Figure 4.1 Tpr Apparatus

to as low a level as possible. The reducing gas purified and dry was then directed through one arm of a conductivity cell (Gow Mac Katharometer No. 40-201). Leaving the katharometer the gas then passed through the reactor containing the sample and finally via a cold trap kept at 203K to remove the reduction products. After the trap the gas stream passed through the other arm of the conductivity cell. In this way a reduction process on the sample was detected by an imbalance in the thermal conductivity cell. The change in hydrogen concentration was displayed as a peak or several peaks on a chart recorder. The output on the conductivity bridge and thermocouple (Chromel-Alumel) was fed to a BBC microcomputer through an amplifier for data processing. Since the gas flow was kept constant, the change in hydrogen concentration was proportional to the rate of sample reduction. The experimental conditions used are listed in Table 4.1.

Table 4.1

Experimental Conditions

Gas mixture	5% H_2/95% Ar
Heating rate	5K min^{-1}
Flow rate	40 $cm^3 min^{-1}$
Mass of sample	∿50mg

The amount of hydrogen consumed was determined at the end of each run by injecting a known volume of pure hydrogen into the gas stream as a calibration standard. The peak areas were calculated using the computer data processing facility.

4.2.3 Tpo Technique

A schematic diagram of the tpo system used is shown in

Figure 4.2. A 6% O_2 in N_2 gas stream was used. The gas stream ($40cm^3\ min^{-1}$) was purified by passing through a 5A molecular sieve before being admitted to the sample reactor. The sample (1 - 1.5g) was placed in a silica reactor fitted with a thermocouple well to monitor its temperature. The reactor was placed in a tubular furnace whose temperature can be raised by linear programming. The sample was first flushed with argon before admitting the 6% O_2 mixture. The mixture was passed through the sample until the output from the oxygen detector was stable and the linear heating started. A heating rate of $10K\ min^{-1}$ was used. A calibrated oxygen detector (Draeger Oxywarn 100R) was used to monitor the oxygen level (with an accuracy of ± 0.05%) as a function of temperature. The oxygen uptake was displayed as a peak or peaks on a chart recorder connected to the oxygen detector. The consumption of O_2 was calculated by integration of the peak areas. Values were expressed as mol O_2 per mol sample.

4.3 Results

4.3.1 Tga and Dta Results

4.3.1.1 Reduction of WO_3 and the Potassium Tungsten Bronzes

Tga reveals that there was only a slight weight loss (∿0.3%) on heating the potassium tungsten bronze samples in nitrogen to 373K. The results obtained by tga and dta on heating samples WO_3, 0.05KW, 0.2KW, 0.3KW, 0.6KW and 0.8KW in hydrogen to 1223K are shown in Figures 4.3 - 4.8 respectively. Reduction of pure WO_3 is endothermic starting at 773K with two overlapping processes having minima at 861K and 985K. The reduction is complete at 998K with a total weight loss of 22.09% which agrees well with a theoretical weight loss of 20.70% assuming that WO_3 is completely reduced to W metal. The thermogram seems to indicate that a suboxide of tungsten is first formed which is

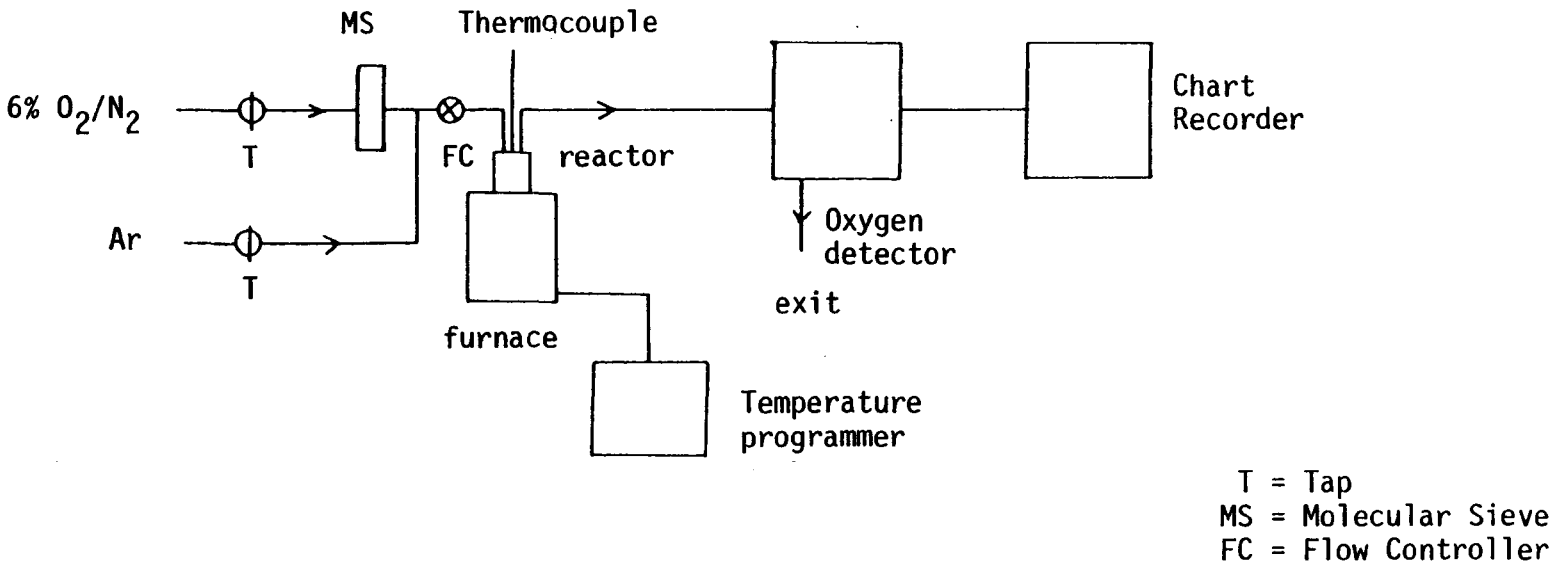

Figure 4.2 Tpo Apparatus

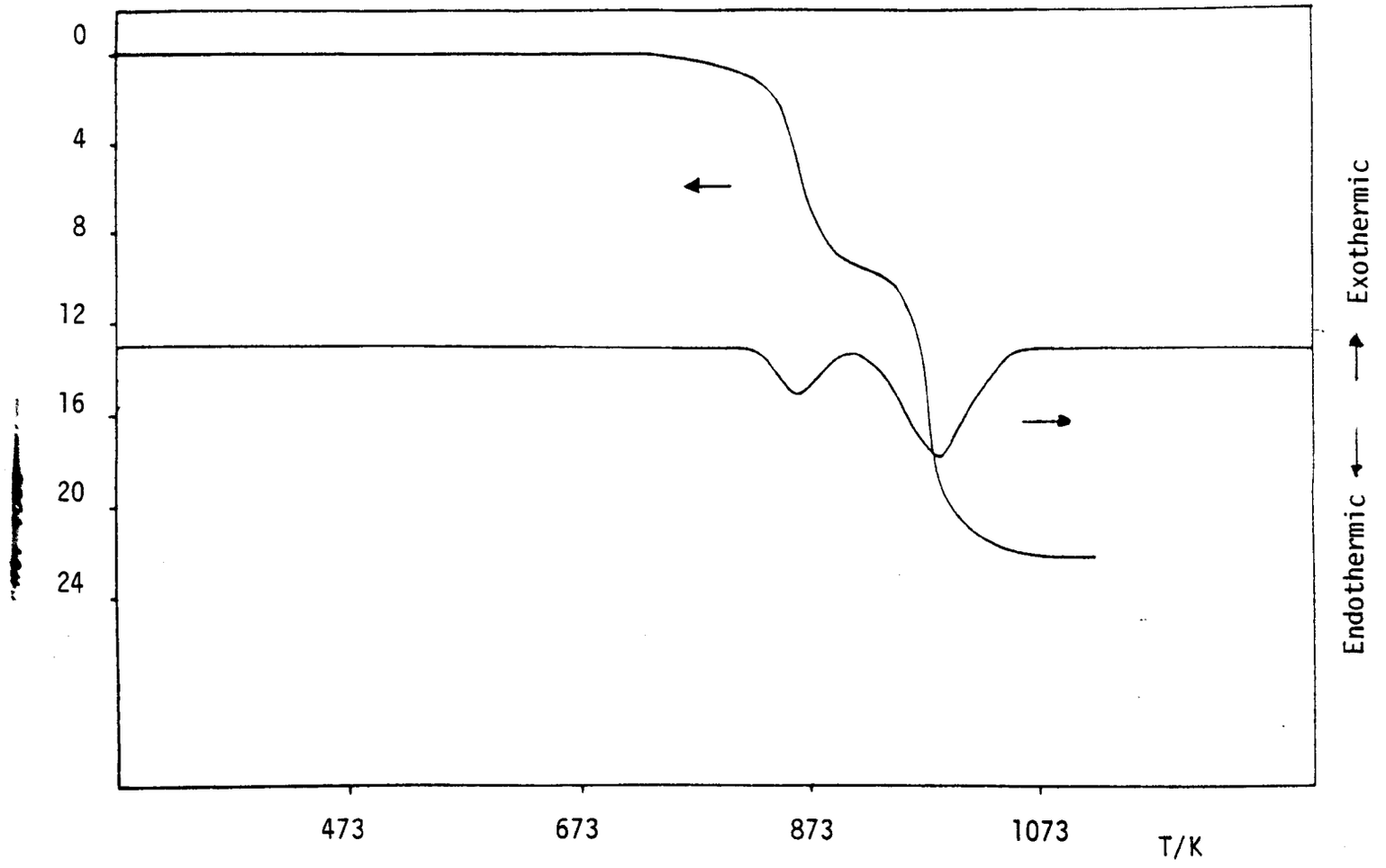

Figure 4.3 Dta and tga curve of WO_3

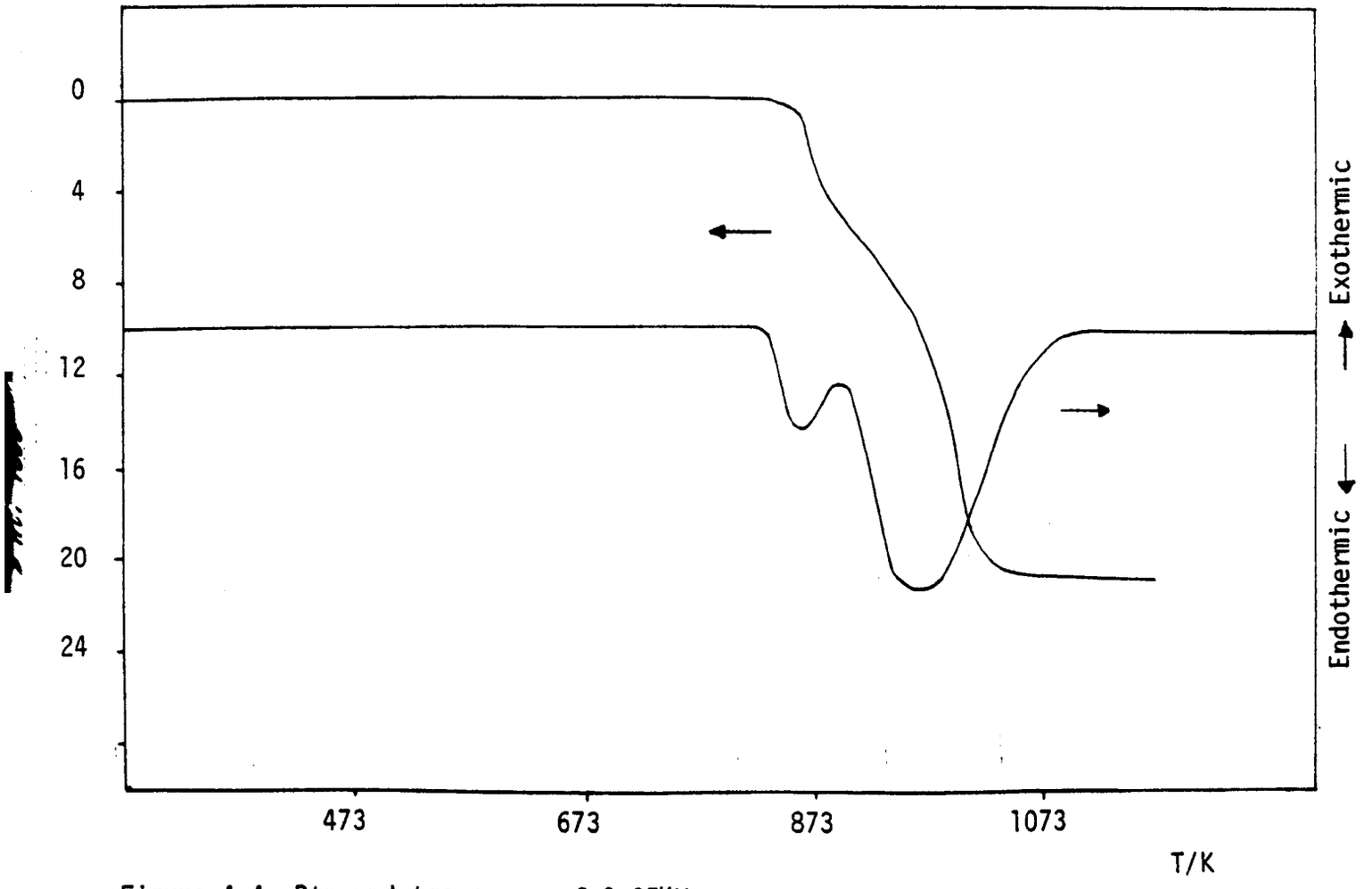

Figure 4.4 Dta and tga curve of 0.05KW

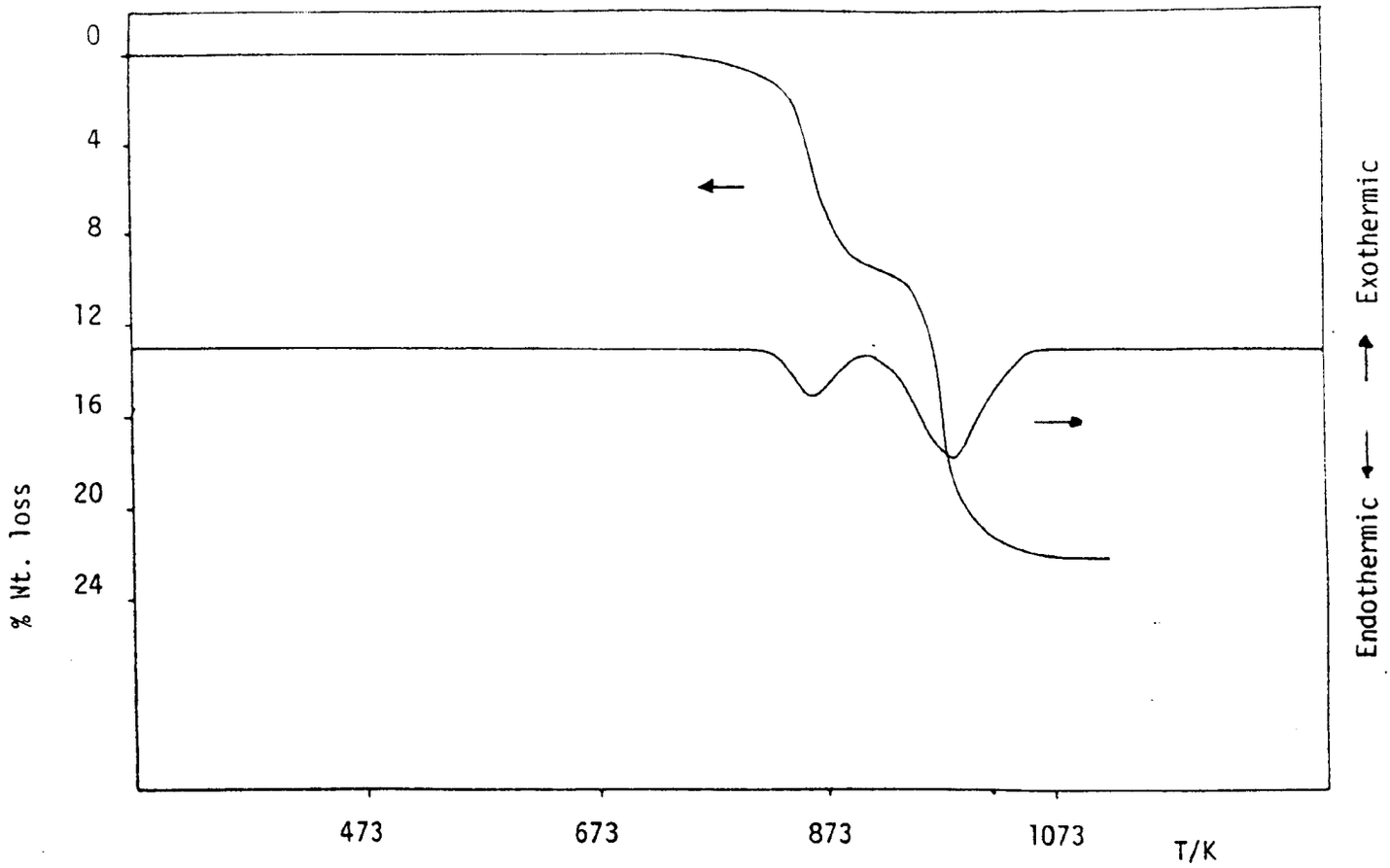

Figure 4.3 Dta and tga curve of WO_3

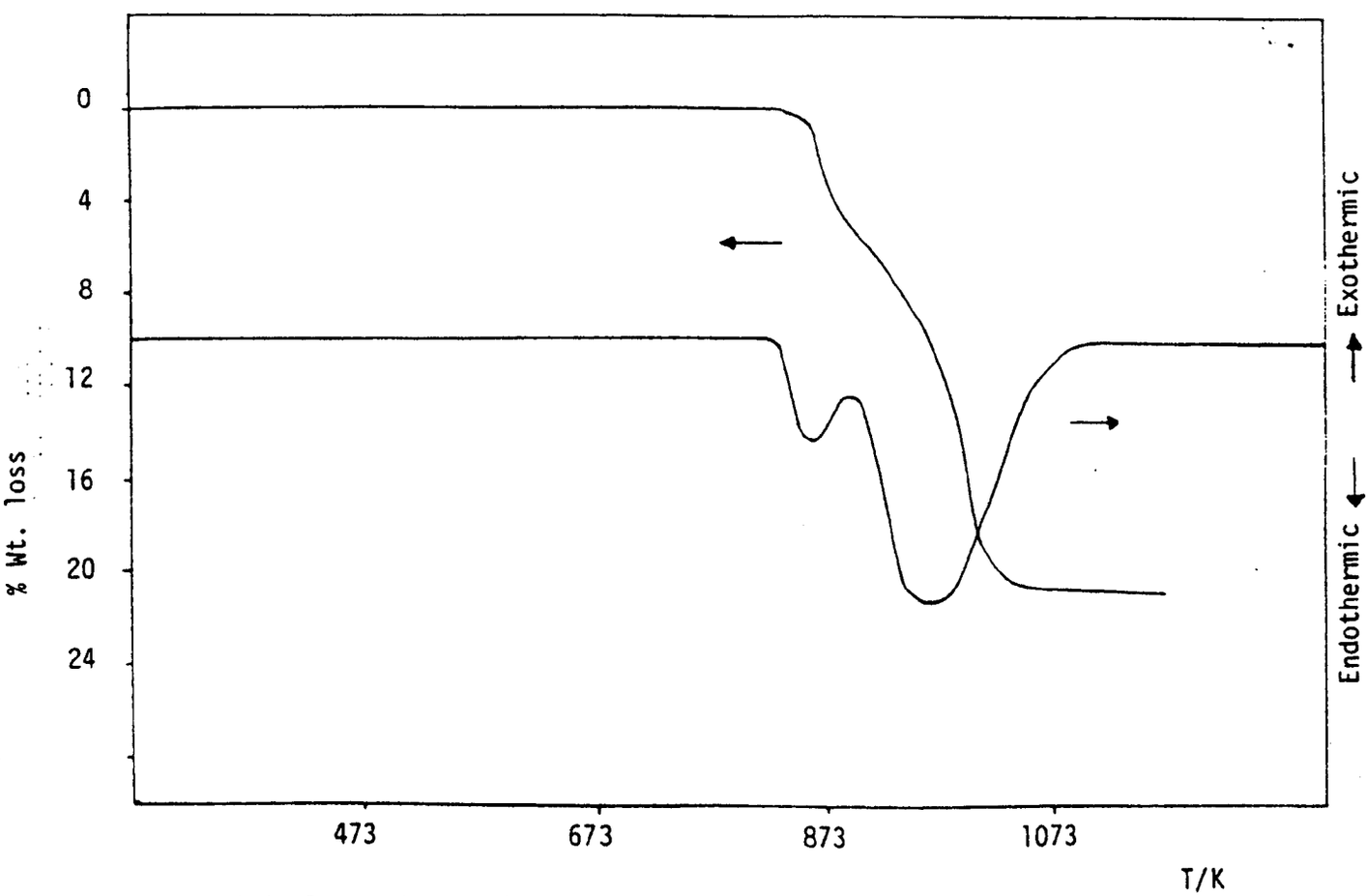

Figure 4.4 Dta and tga curve of 0.05KW

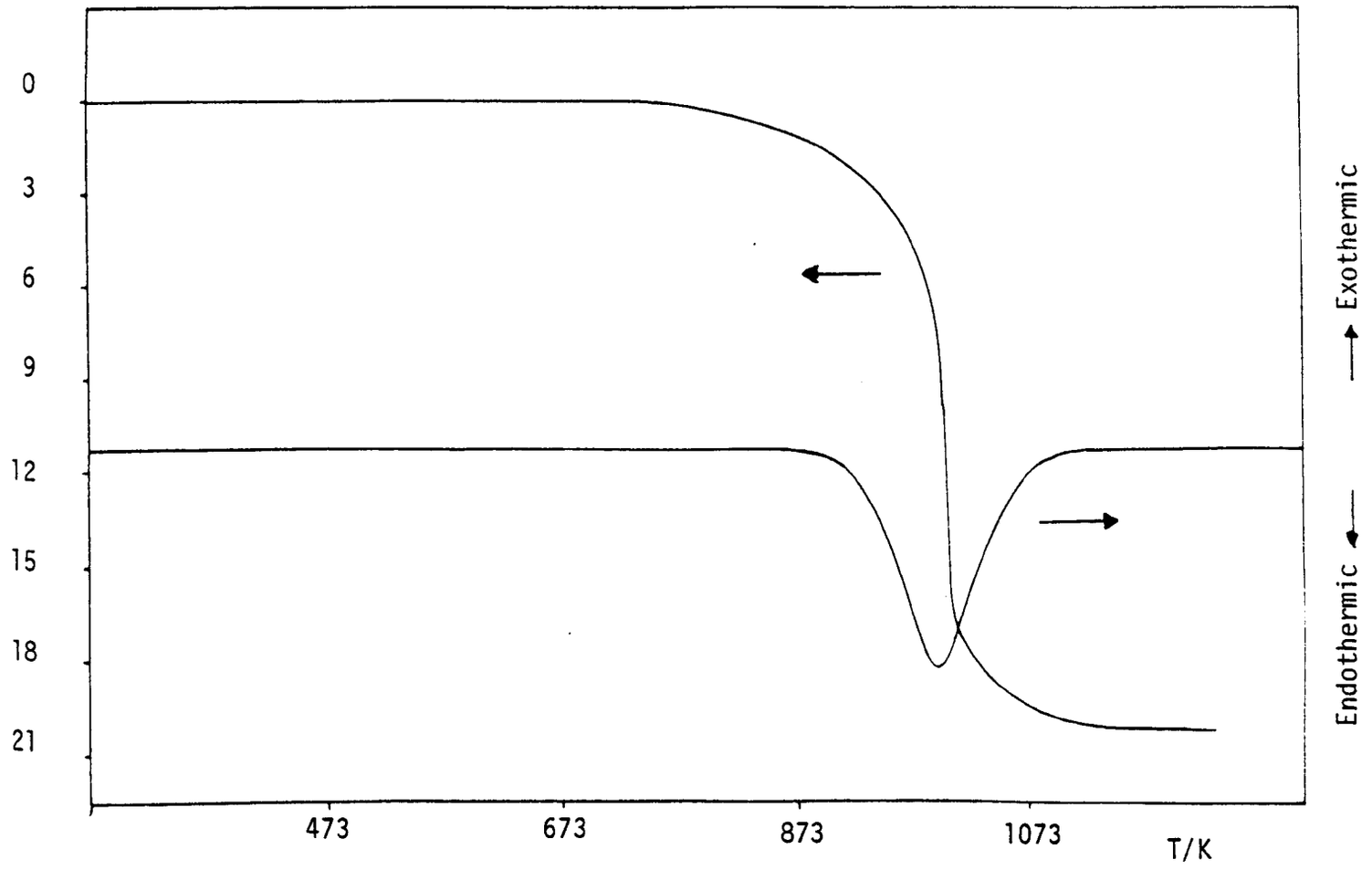

Figure 4.5 Dta and tga curve of 0.2KW

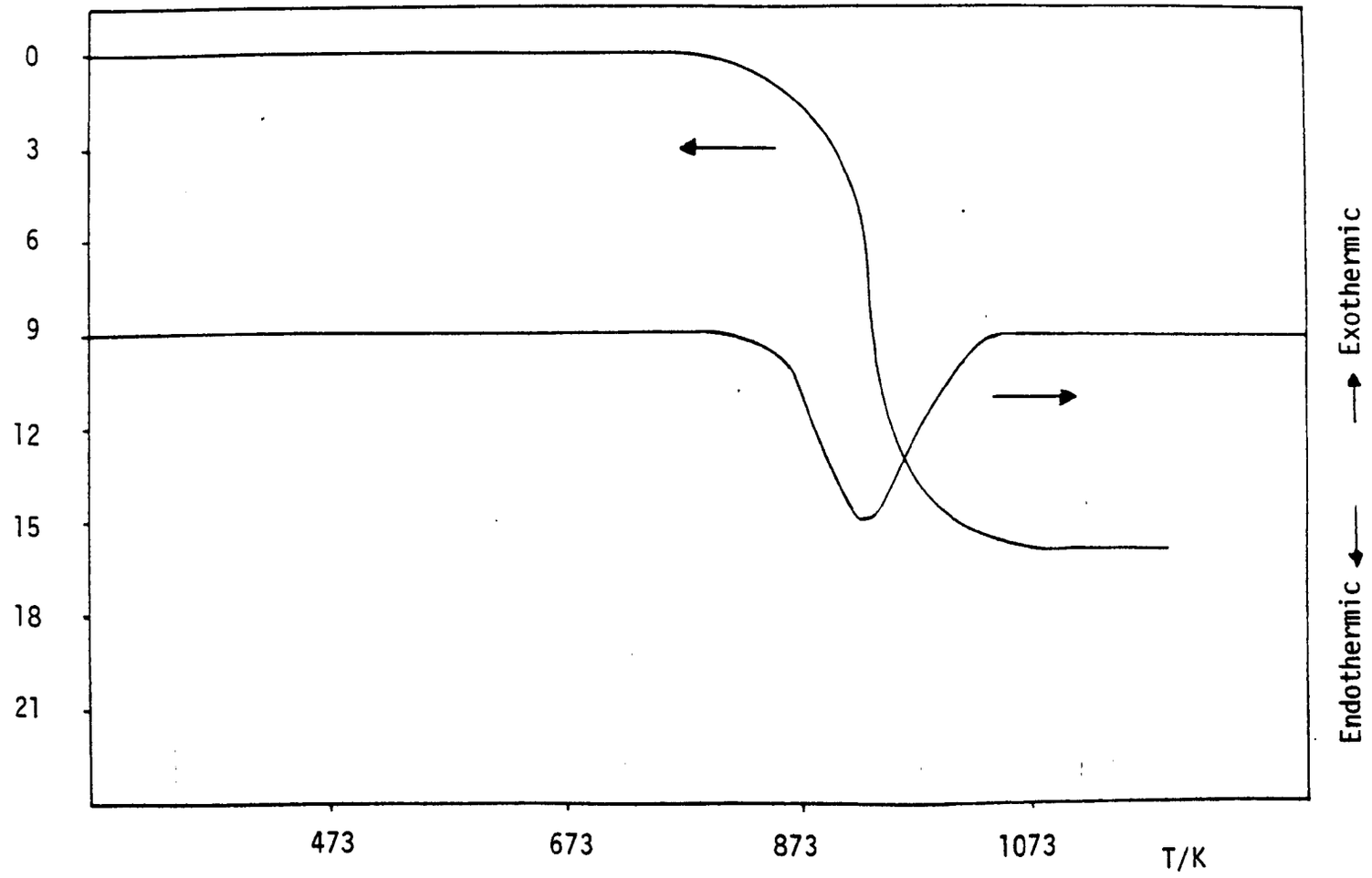

Figure 4.6 Dta and tga curve of 0.3KW

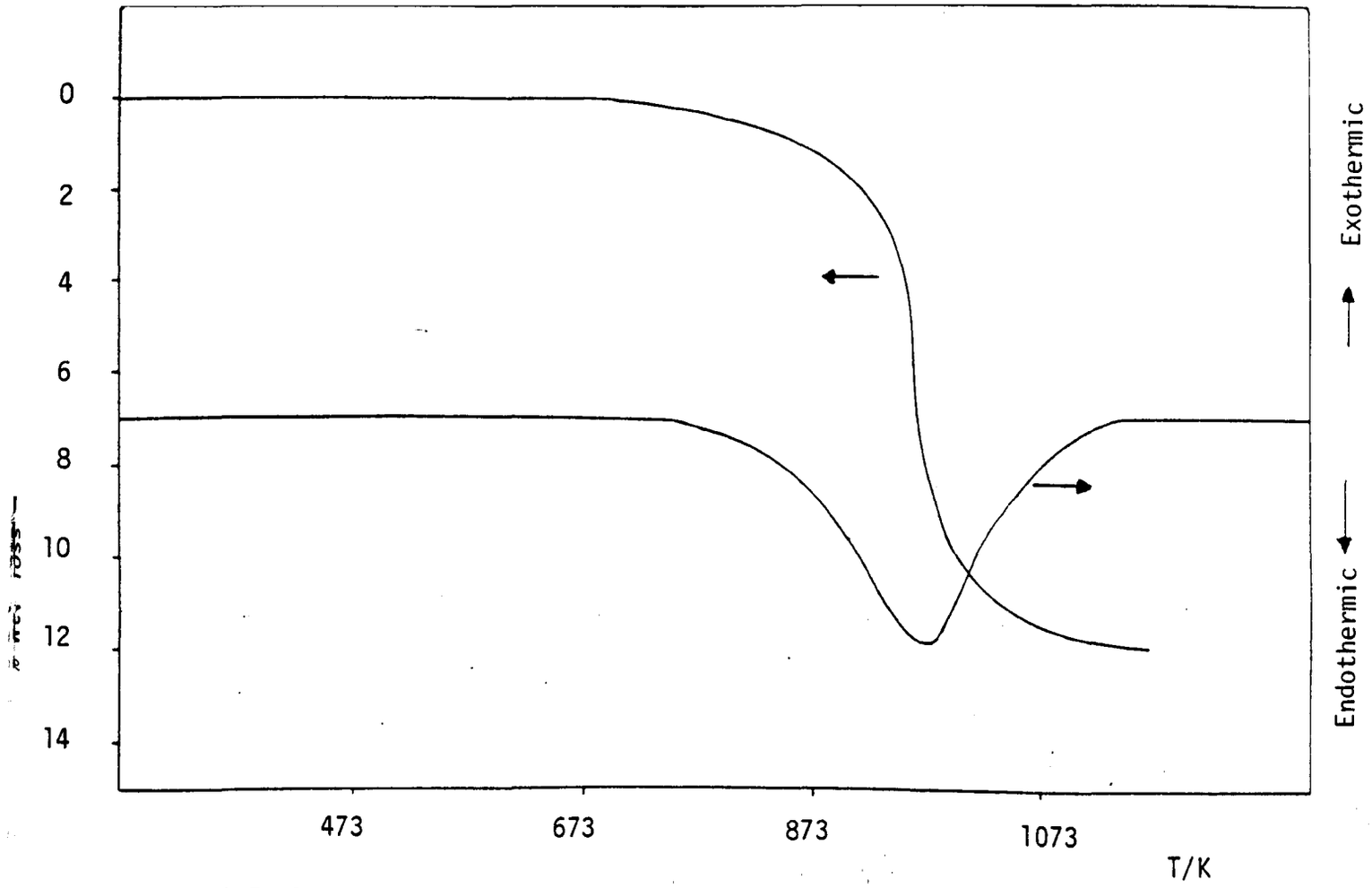

Figure 4.7 Dta and tga curves of 0.6KW

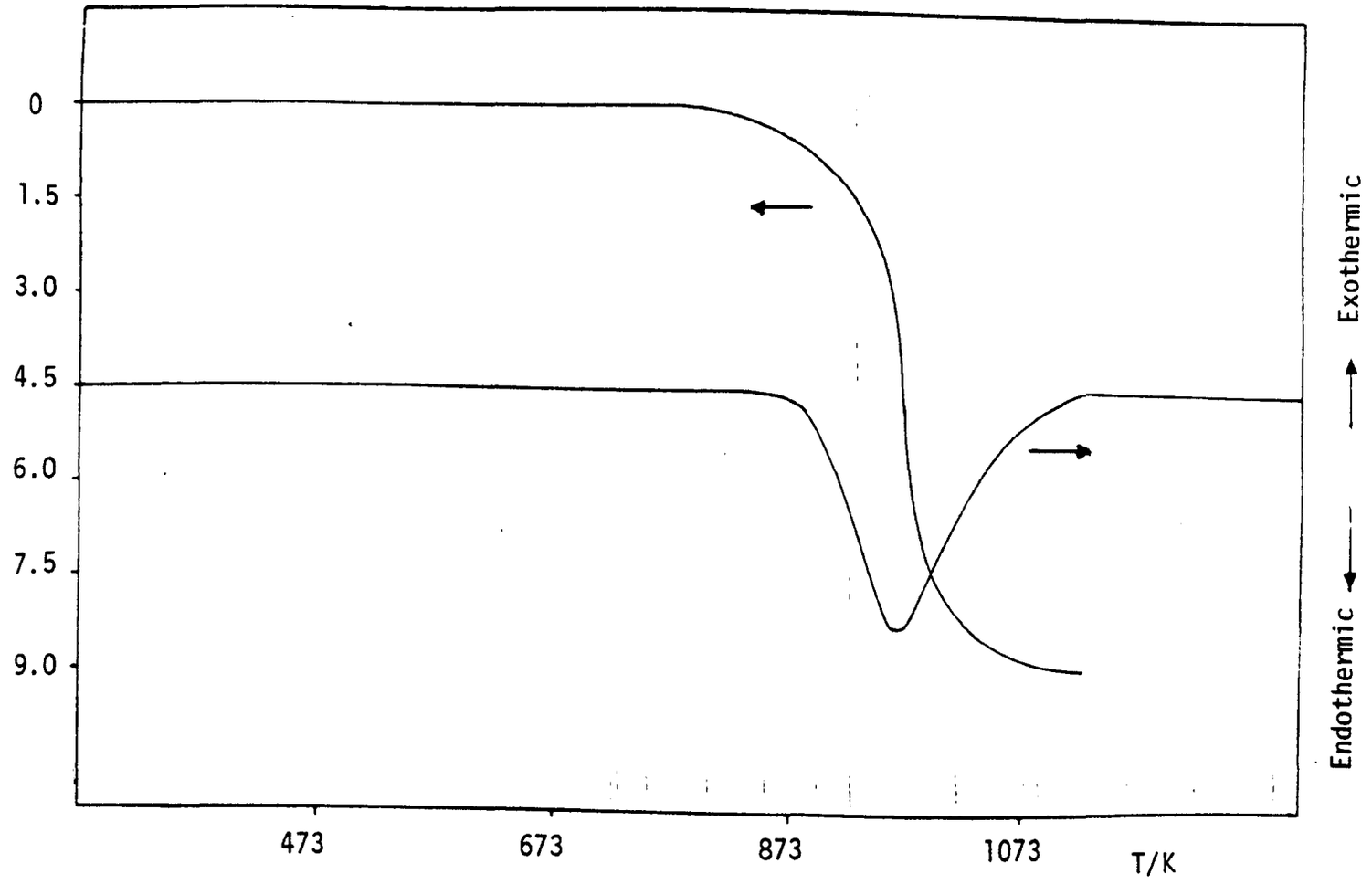

Figure 4.8 Dta and tga curves of 0.8KW

then reduced to tungsten. The tga and dta curves obtained on heating 0.05KW in H_2 show much similarity to that of pure WO_3. A total weight loss of 20.78% occurred in two overlapping endothermic processes with minima at 861K and 965K. The lowest content potassium bronze appears to reduce initially to an oxygen deficient modification of WO_3; subsequent reduction gives sodium tungstate and tungsten. The theoretical weight loss for such a process agrees well with the observed weight loss. For the reduction of 0.05KW the following stoichiometric equation may be written;

$$40K_{0.05}\ WO_3 + 116H_2 \longrightarrow K_2WO_4 + 39W + 116H_2O$$

The dta and tga results for samples 0.2KW - 0.8KW show that reduction is a single endothermic process usually in the temperature range 773 - 1123K. The total weight loss in each case agrees well with a reduction process that leads to the formation of K_2WO_4 and W. Table 2 gives the experimental and theoretical weight loss and the temperature of the minima for the reduction process for each of these samples.

Table 4.2

Sample	Theoretical % weight loss	Experimental % weight loss	$T_{min.}$/K for endotherm
0.2KW	17.35	19.87	993
0.3KW	15.76	15.96	933
0.6KW	11.28	11.93	965
0.8KW	8.51	8.90	923

4.3.1.2 Reduction of the Sodium Tungsten Bronzes

Tga results show that the sodium bronzes, similar to the potassium bronzes lose only minimal weight on heating in nitrogen to 373K. The dta and tga results obtained for samples 0.05NaW; 0.2NaW; 0.3NaW; 0.6NaW and 0.8NaW on heating in hydrogen to 1223K are shown in Figures 4.9 - 4.13 respectively. The profiles show a similarity to those obtained for the reduction of the potassium bronzes. However, unlike sample 0.05KW, reduction of 0.05NaW occurred in only one step, with the endotherm having a minimum at 953K, perhaps suggesting no WO_3 is present in the sodium bronze sample. For samples with $x \geq 0.2$ there was an endothermic process usually occuring between 823K and 1123K. In all cases the total weight loss was assumed to be associated with the formation of Na_2WO_4 and W. For the sodium bronzes, the experimental and theoretical weight losses and the temperature of the minima for the reduction process is given in Table 4.3

Table 4.3

Sample	Theoretical % weight loss	Experimental % weight loss	$T_{min.}$/K for endotherm
0.05NaW	19.91	20.60	953
0.2NaW	17.94	19.25	1003
0.3NaW	16.08	16.45	945
0.6NaW	11.72	12.50	1021
0.8NaW	8.95	10.53	953

In all cases the weight loss obtained on both the potassium and sodium bronzes agrees well with the theoretical weight loss for the reduction of each bronze to the corresponding tungstate and W metal.

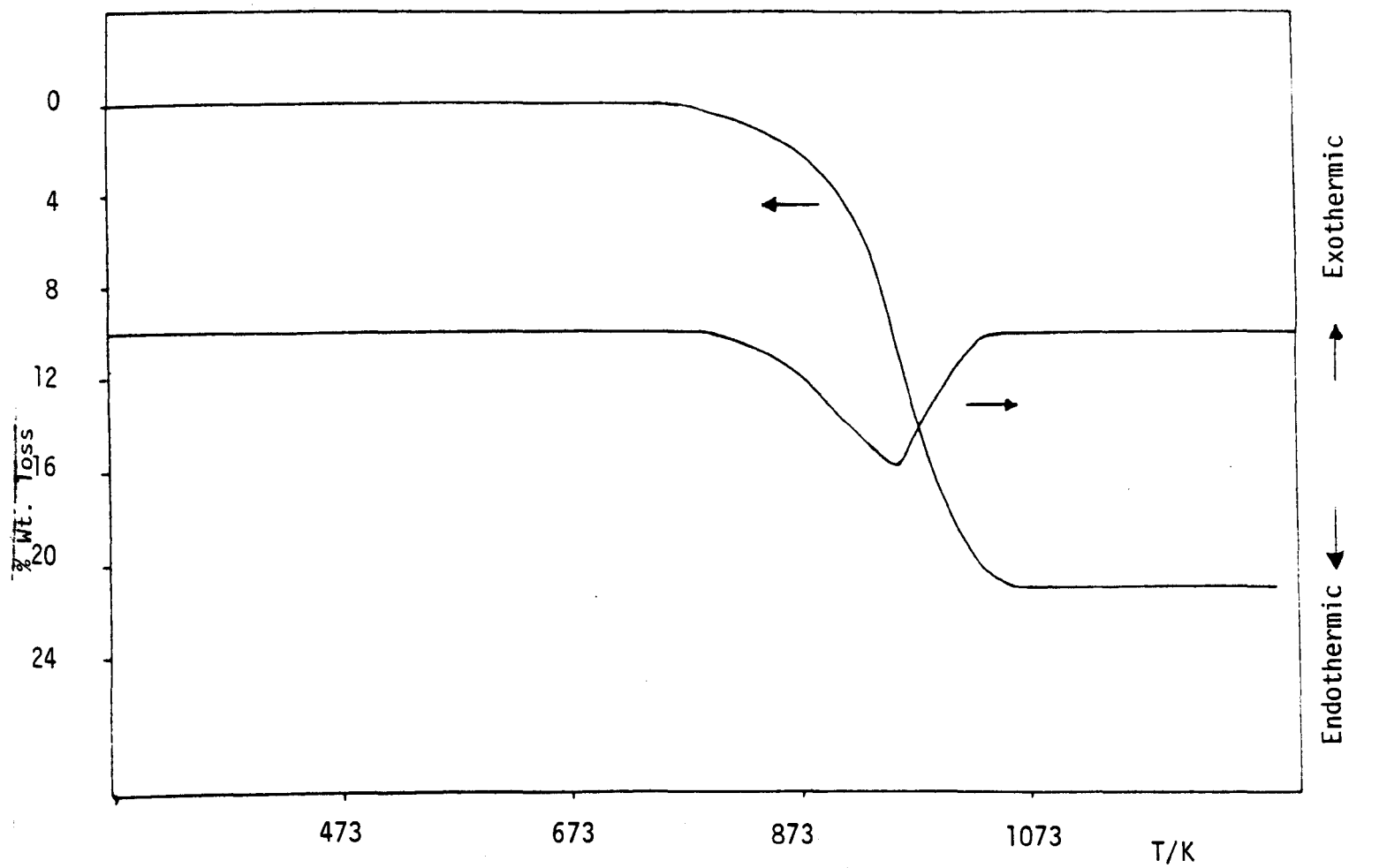

Figure 4.9 Dta and tga curves of 0.05NaW

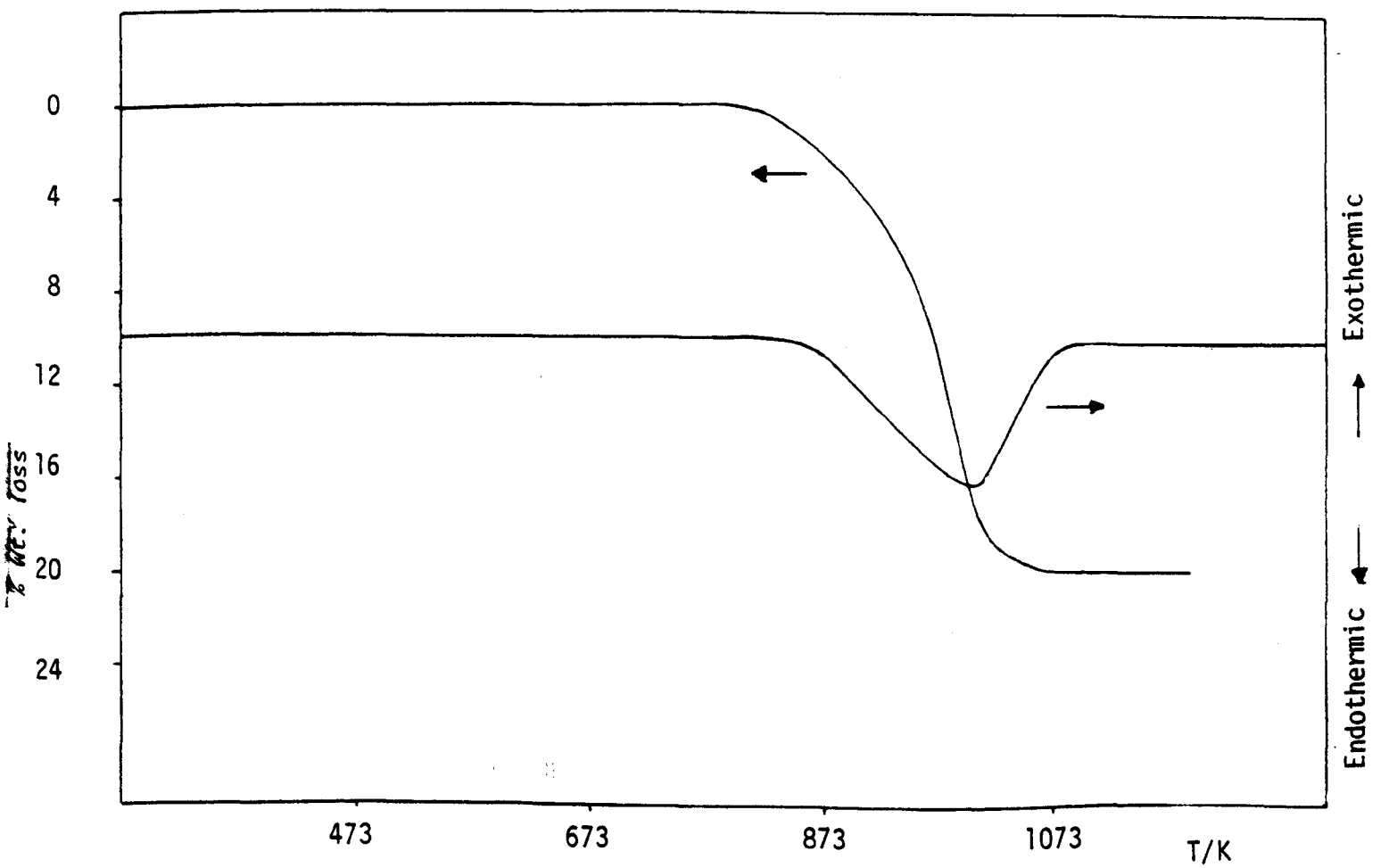

Figure 4.10 Dta and tga curves of 0.2NaW

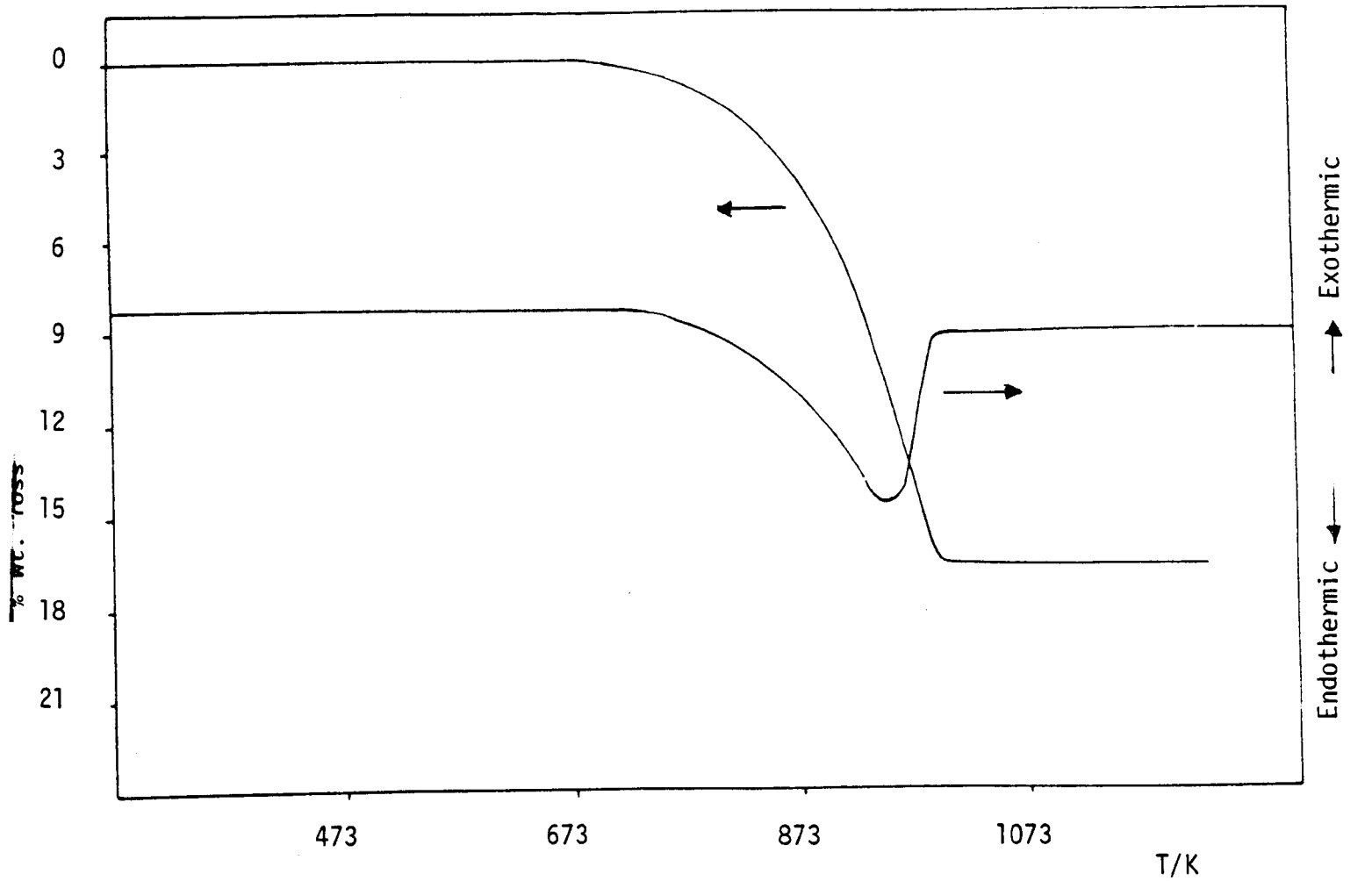

Figure 4.11 Dta and tga curves of 0.3NaW

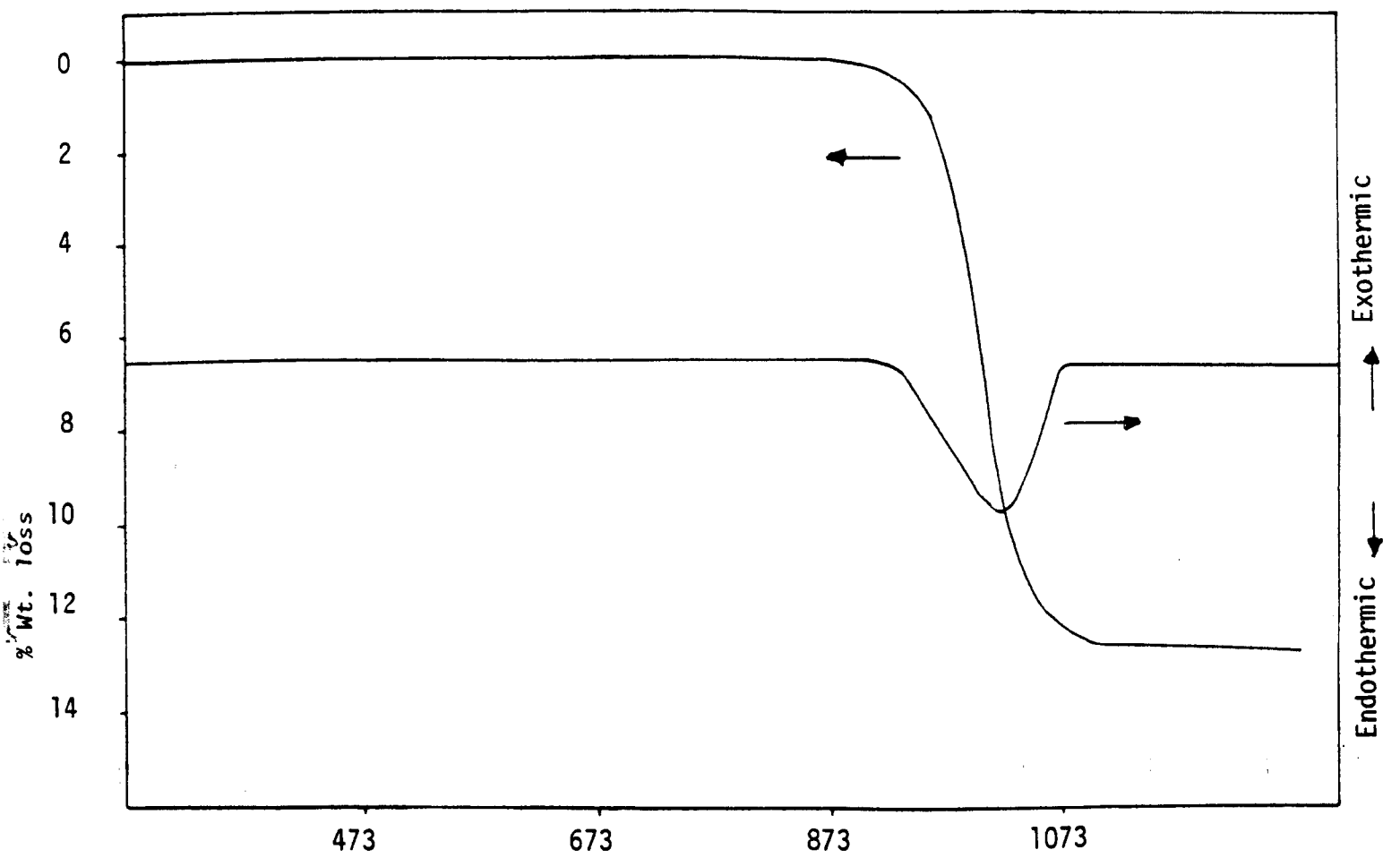

Figure 4.12 Dta and tga curve of 0.6NaW

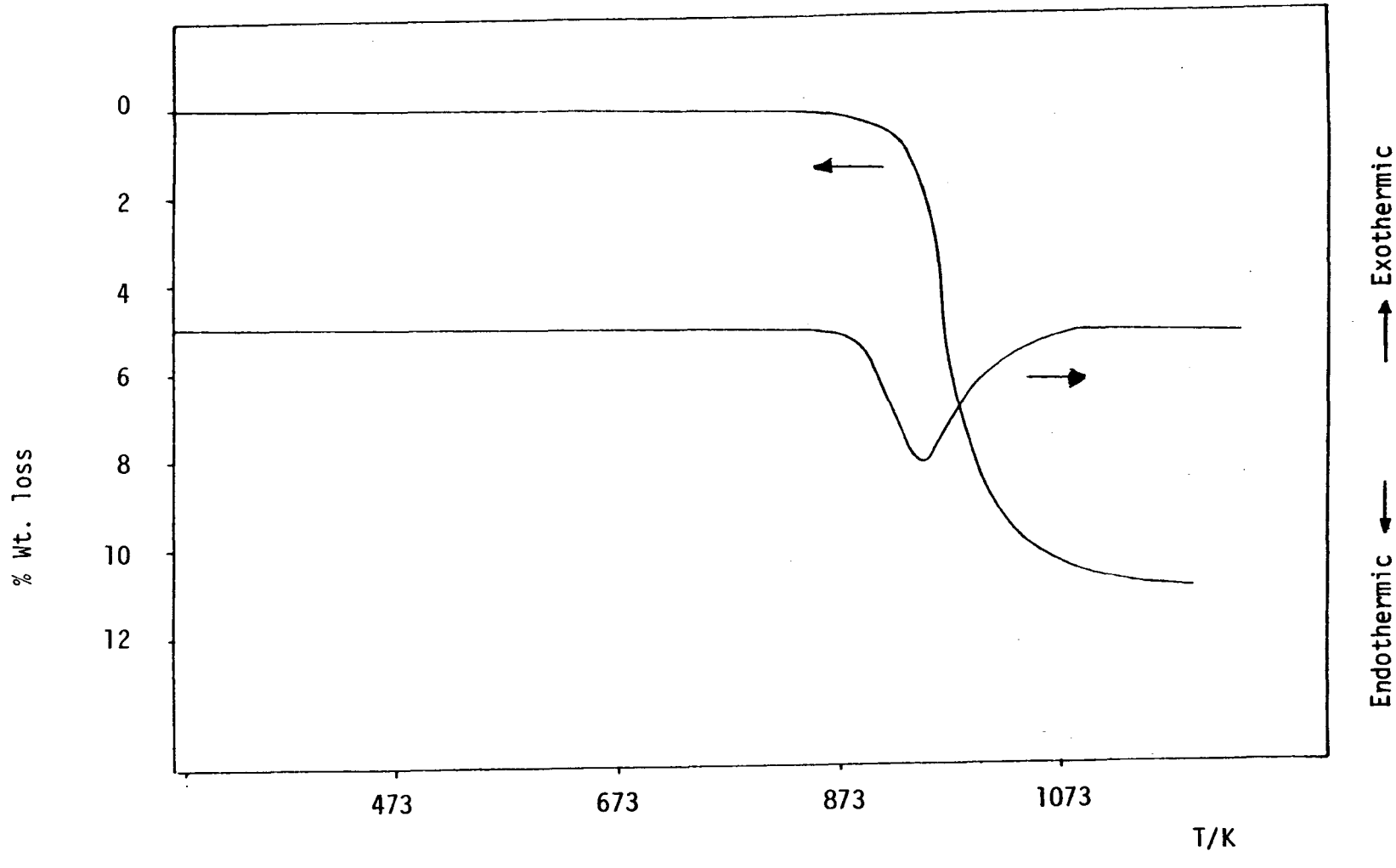

Figure 4.13 Dta and tga curve of 0.8 NaW

Variation in the temperature at the maximum rate of reduction occurs, i.e. the minima among the different samples, could be due to experimental artefact.

4.3.2 Tpr Results

4.3.2.1 Reduction of WO_3

The tpr profile of WO_3 on heating to 1473K is shown in Figure 4.14. The profile shows that reduction started at 758K with two overlapping processes having maxima at 1020K and 1180K. As found by the tga thermogram, the tpr profile also indicates the formation of a suboxide of tungsten which is then reduced to tungsten. The total hydrogen consumed was found to be 13.3 mmoles g^{-1} sample. The theoretical amount of hydrogen required for the reduction of WO_3 to W is 12.9 m moles g^{-1} sample. This value is lower than the observed and may partly be due to the accuracy of the method.

4.3.2.2 Reduction of Potassium Tungsten Bronzes

The tpr profiles of samples 0.05KW, 0.2KW, 0.3KW, 0.6KW and 0.8KW are shown in Figures 4.15 - 4.19 respectively. In general the profiles are similar showing reduction to occur in one step in the temperature range 850K - 1323K. However, the profile of sample 0.05KW appears to show a rather broad peak with a slight shoulder at 1123K perhaps suggesting the presence of two unresolved processes as indicated more clearly by tga results. The temperature at which each maxima occurred together with the total hydrogen consumed in the reduction process is given in Table 4.4. Similar to the tga results the total hydrogen consumed agrees well with a reduction process that leads to the formation of K_2WO_4 and W, which is illustrated below for

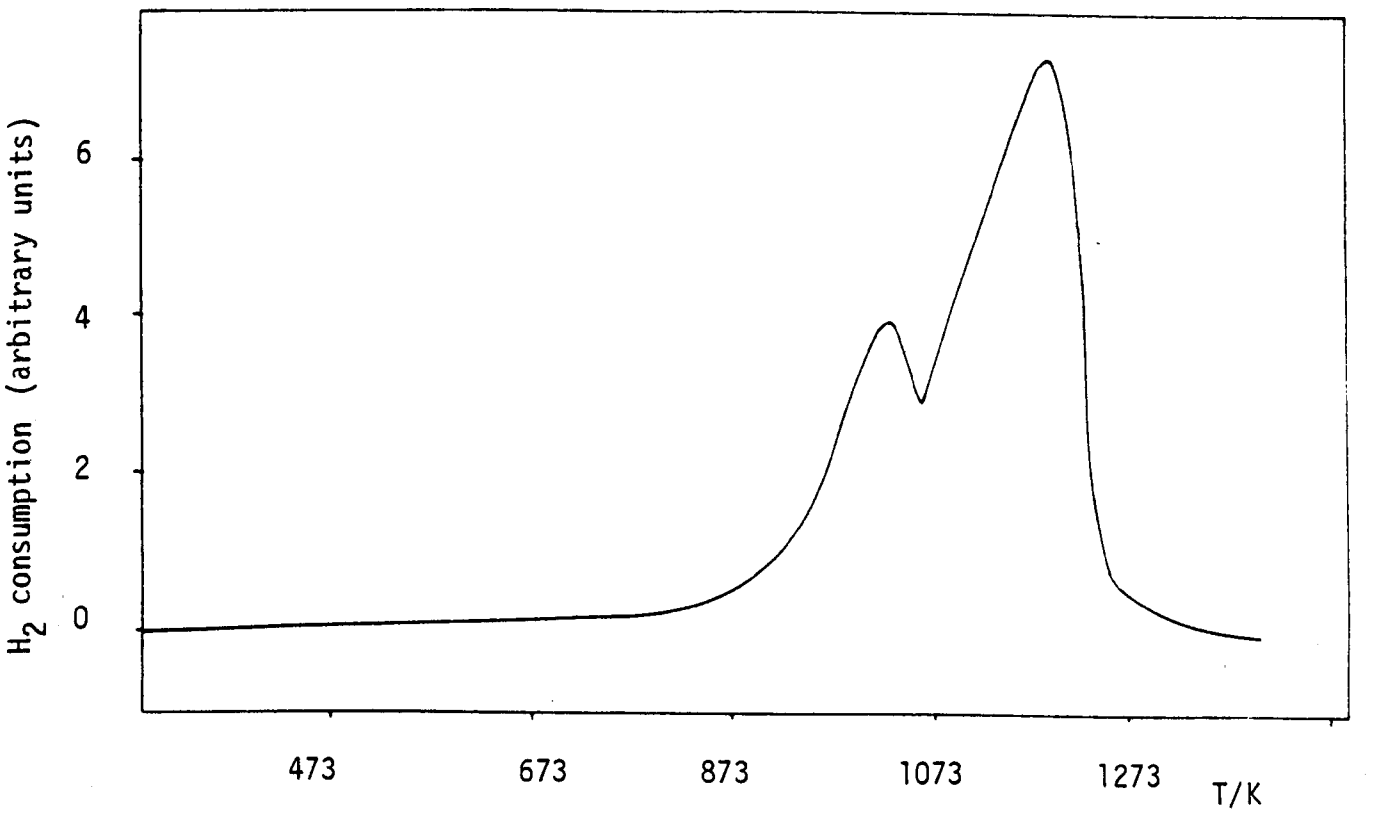

Figure 4.14 Tpr profile of WO_3

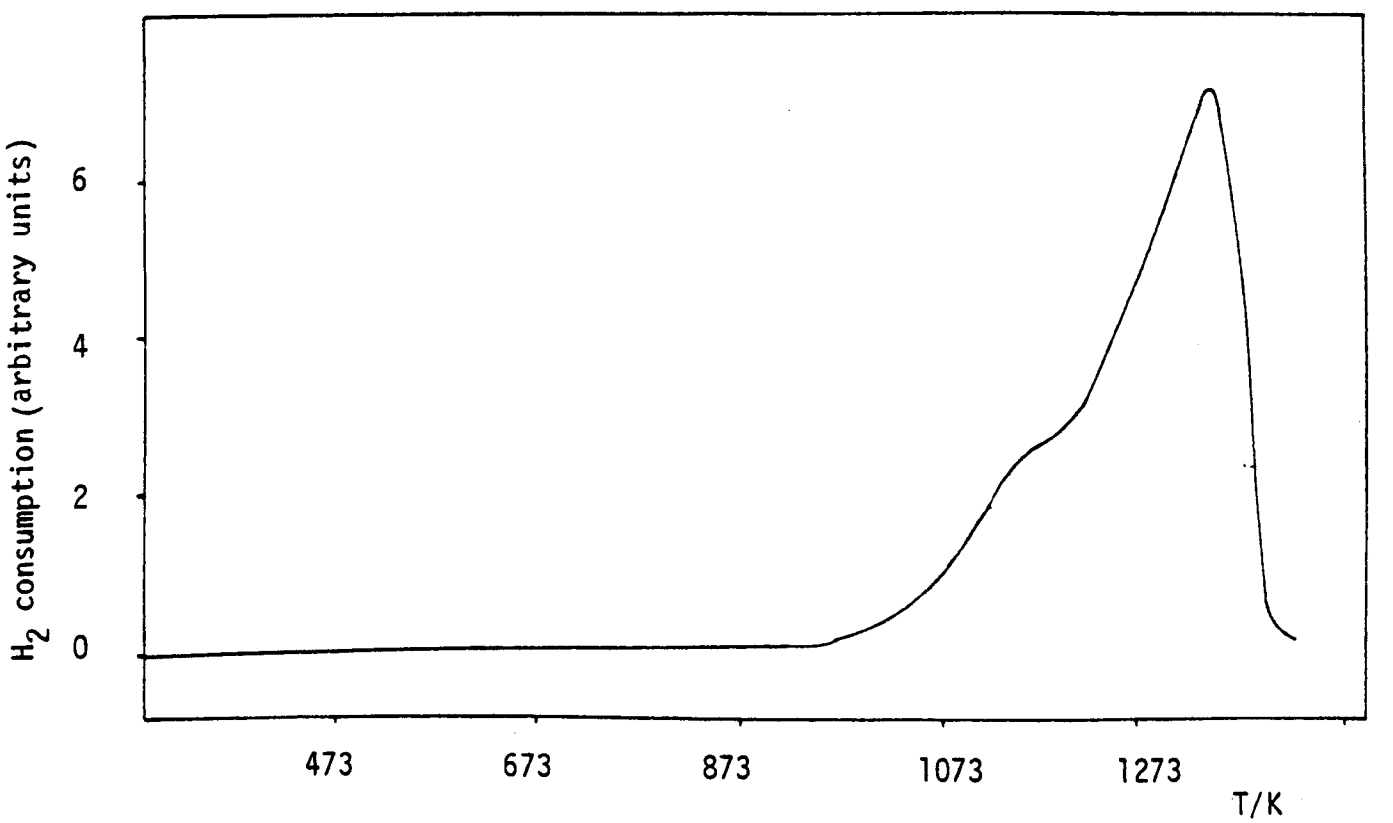

Figure 4.15 Tpr profile of 0.05KW

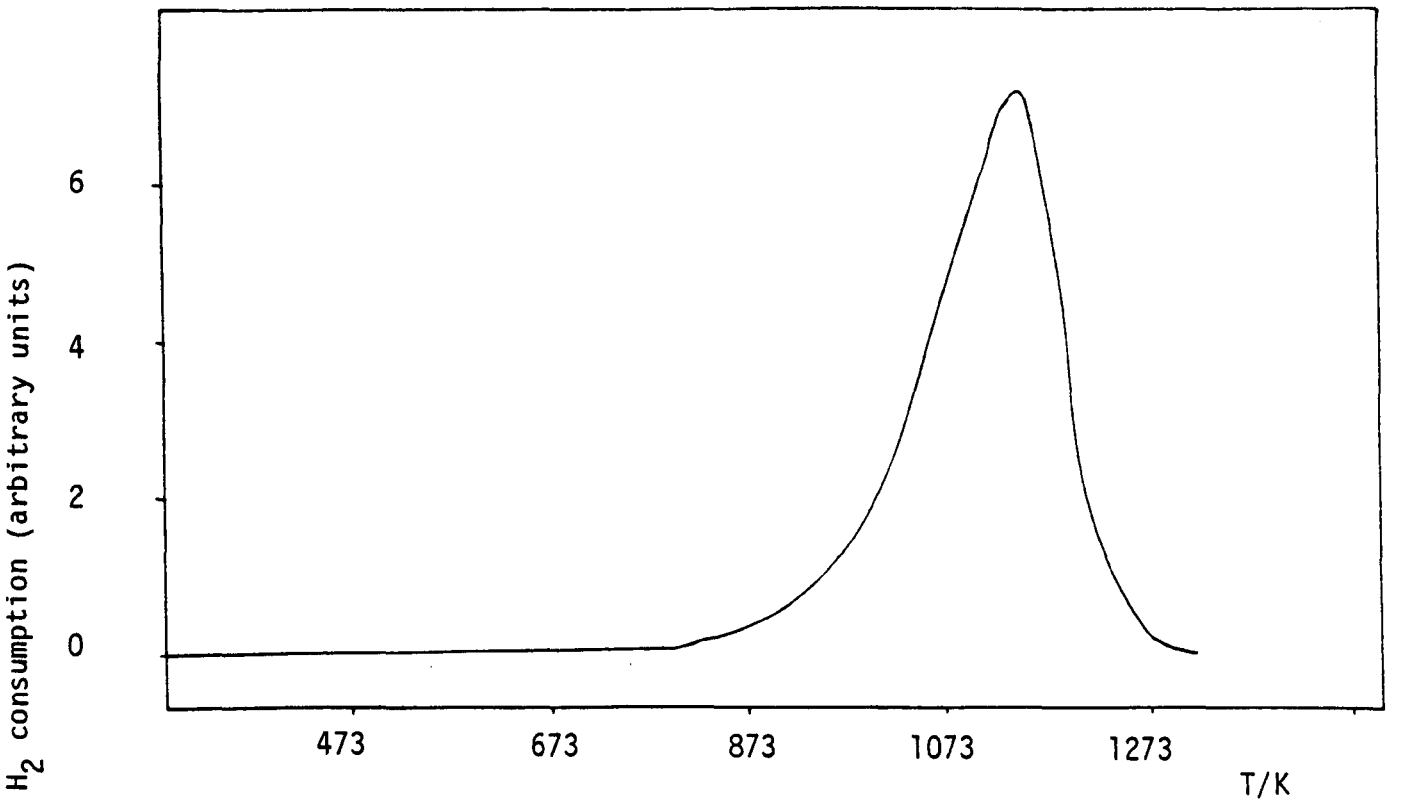

Figure 4.16 Tpr profile of 0.2KW

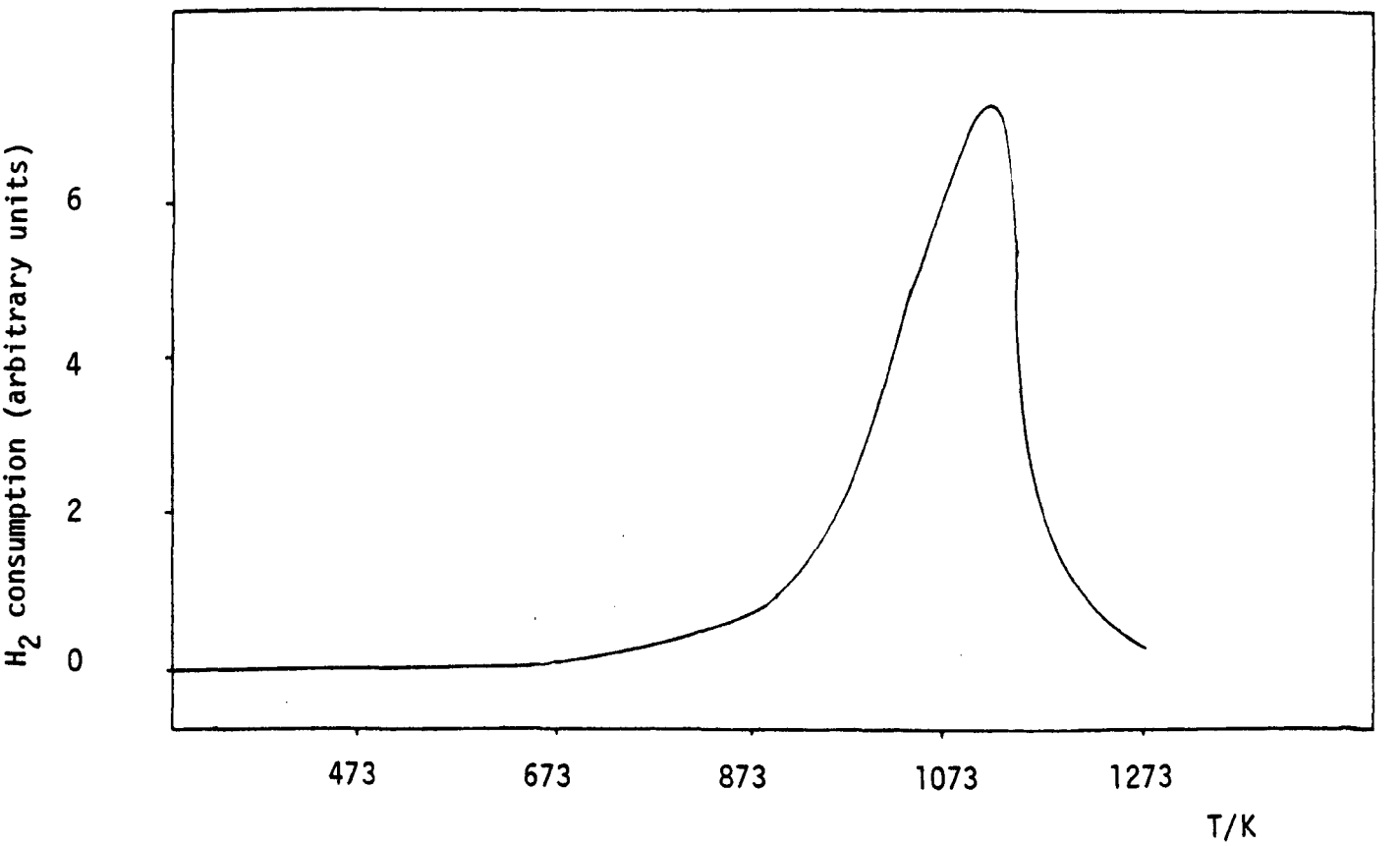

Figure 4.17 Tpr profile of 0.3KW

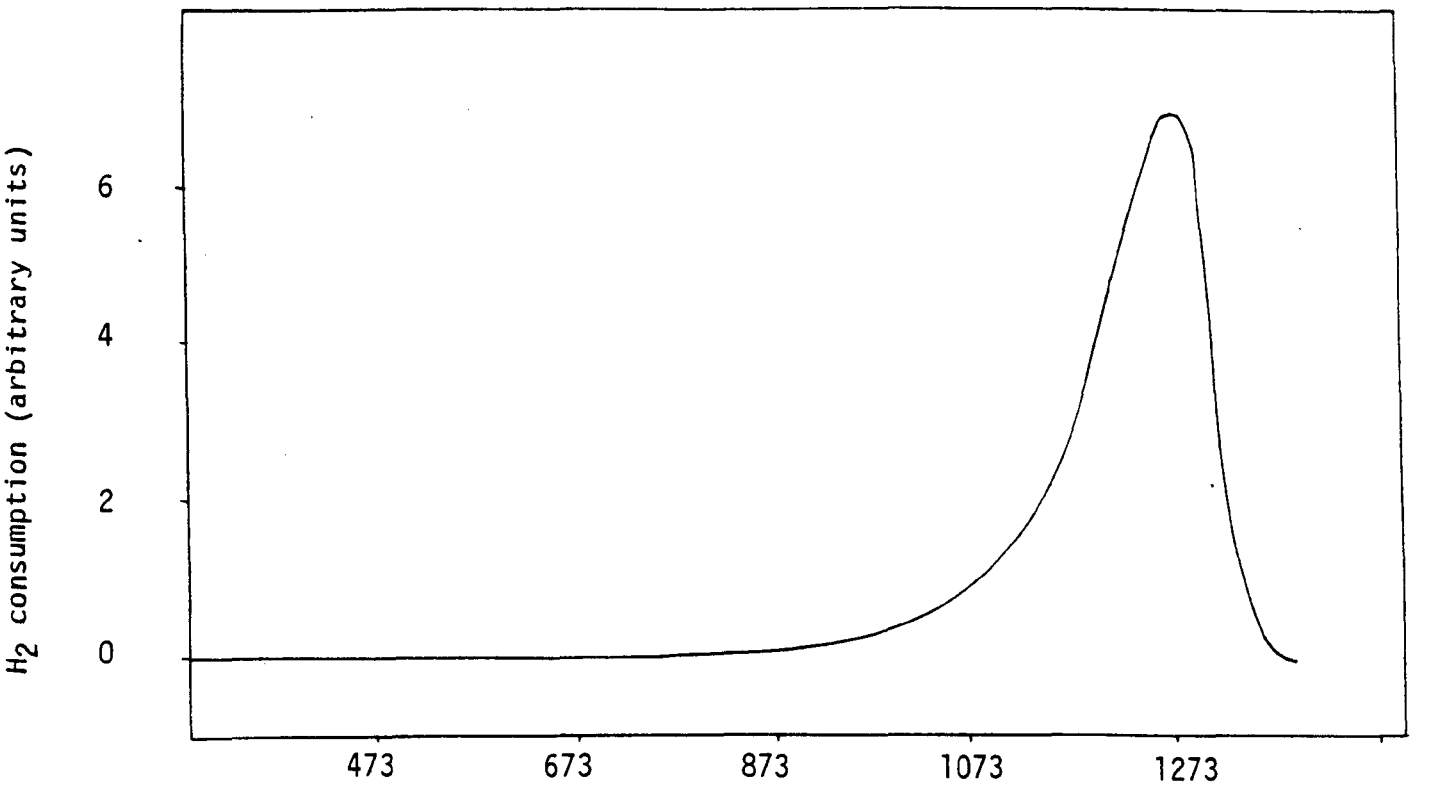

Figure 4.18 Tpr profile of 0.6KW

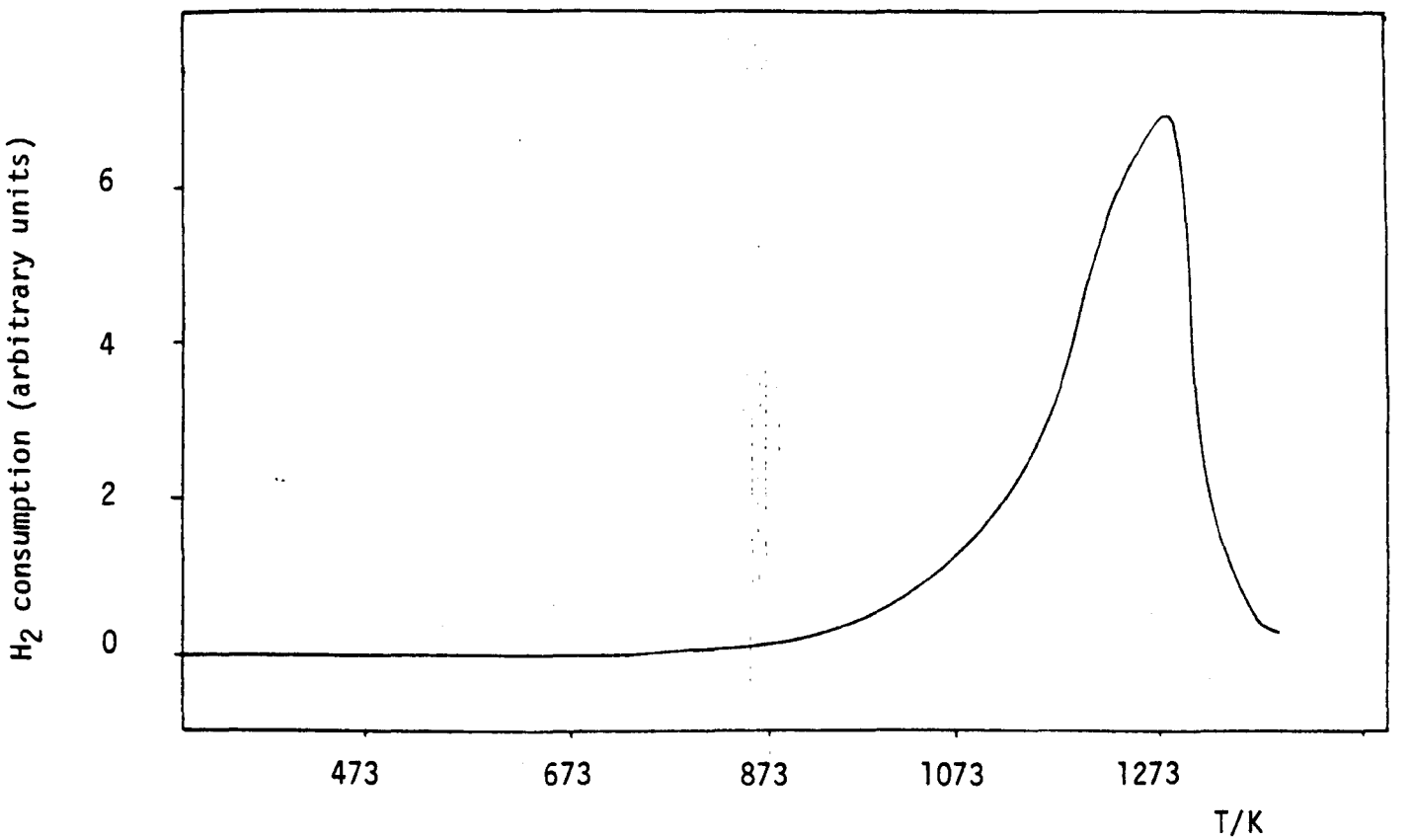

Figure 4.19 Tpr profile of 0.8KW

the reduction of sample 0.2KW

$$10K_{0.2}WO_3 + 26H_2 \longrightarrow K_2WO_4 + 9W + 26H_2O$$

The temperature at which the maximum rate of reduction occurs as observed by tpr is in all cases higher than those found by dta. This could partly be explained by the fact that in the dta experiment a pure hydrogen gas stream was used, whereas in the tpr experiments a dilute H_2 gas stream was used.

Table 4.4

Sample	Peak Maxima/ K	H_2 consumption/ $x^{-1}10^{-3}molg^{-1}$
0.05KW	1373	11.40
0.2KW	1143	11.79
0.3KW	1143	9.28
0.6KW	1273	7.00
0.8KW	1273	5.18

4.3.2.3 Reduction of Sodium Tungsten Bronzes

The tpr profiles of the sodium bronzes, 0.05NaW, 0.2NaW, 0.3NaW, 0.6NaW and 0.8NaW on heating to 1323K are shown in Figures 4.20 - 4.24 respectively. The profiles show that in all cases reduction occurs in one step in the temperature range 850K - 1250K, similar to the potassium bronzes, if the products of reduction are assumed to be Na_2WO_4 and W, then the observed value of hydrogen consumption agrees well with the theoretical value. Table 4.5 shows the temperature at which each maximum occurred together with the total hydrogen consumed in the reduction process. The tpr profiles for 0.05NaW and 0.2NaW show a

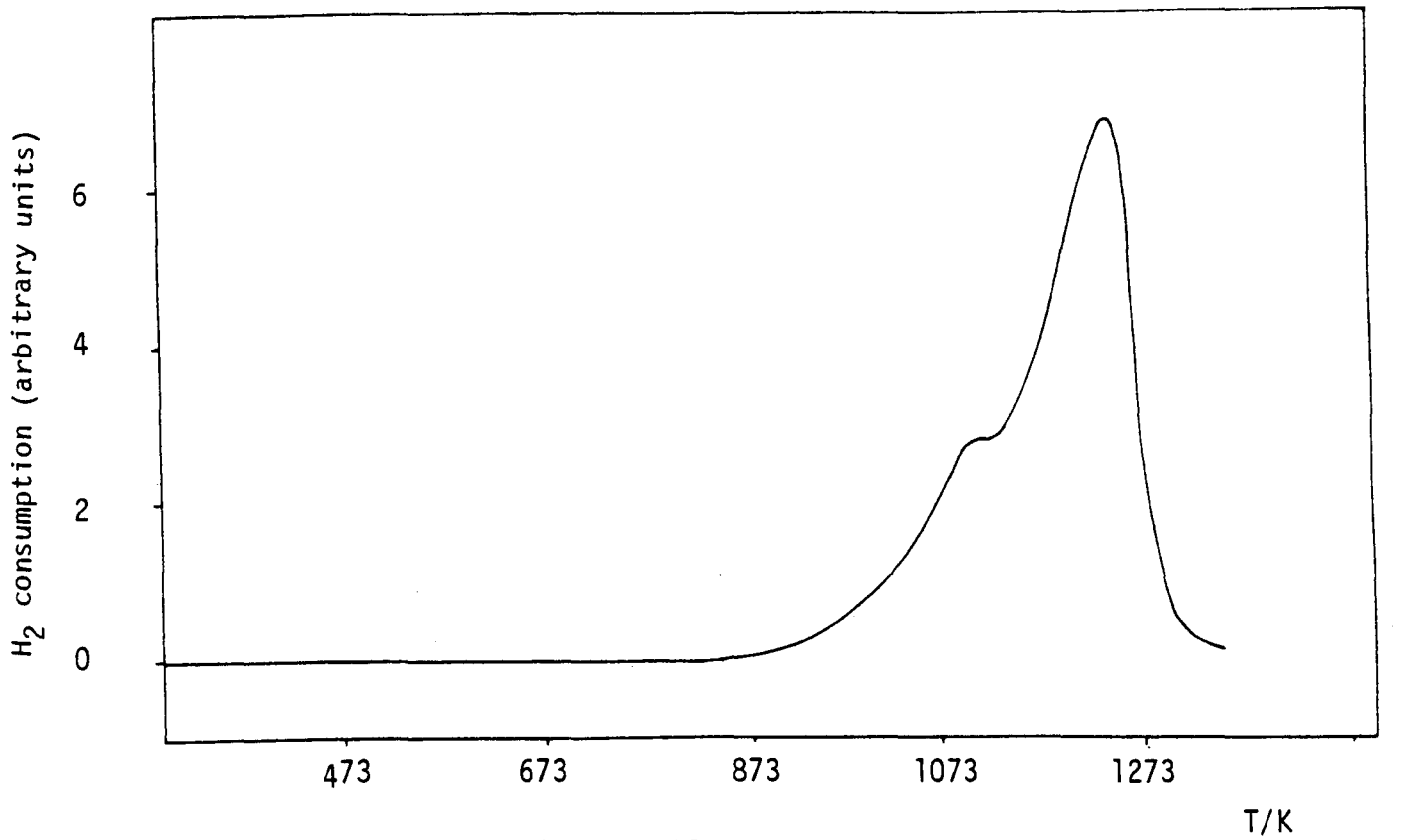

Figure 4.20 Tpr profile of 0.05NaW

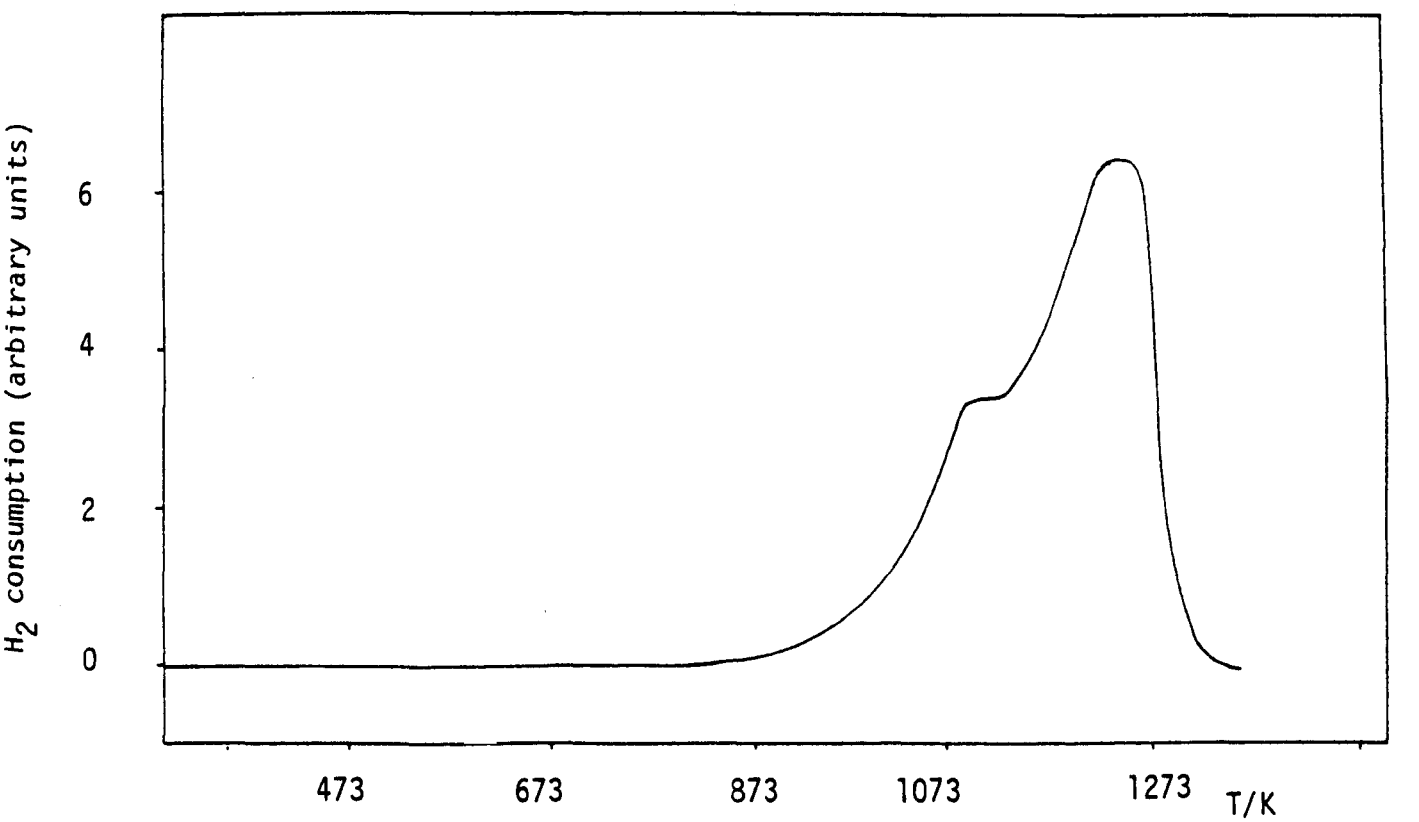

Figure 4.21 Tpr profile of 0.2NaW

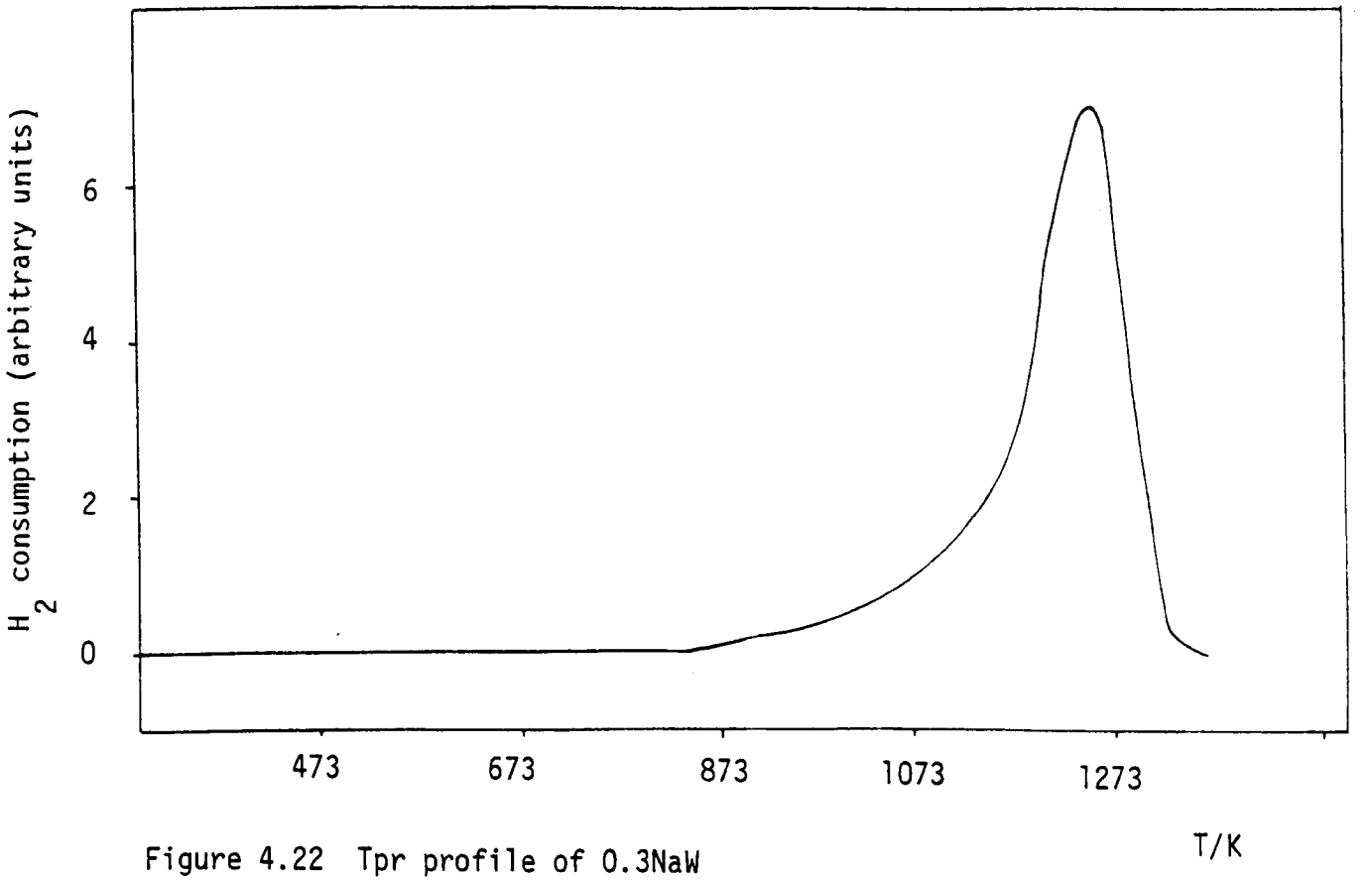

Figure 4.22 Tpr profile of 0.3NaW

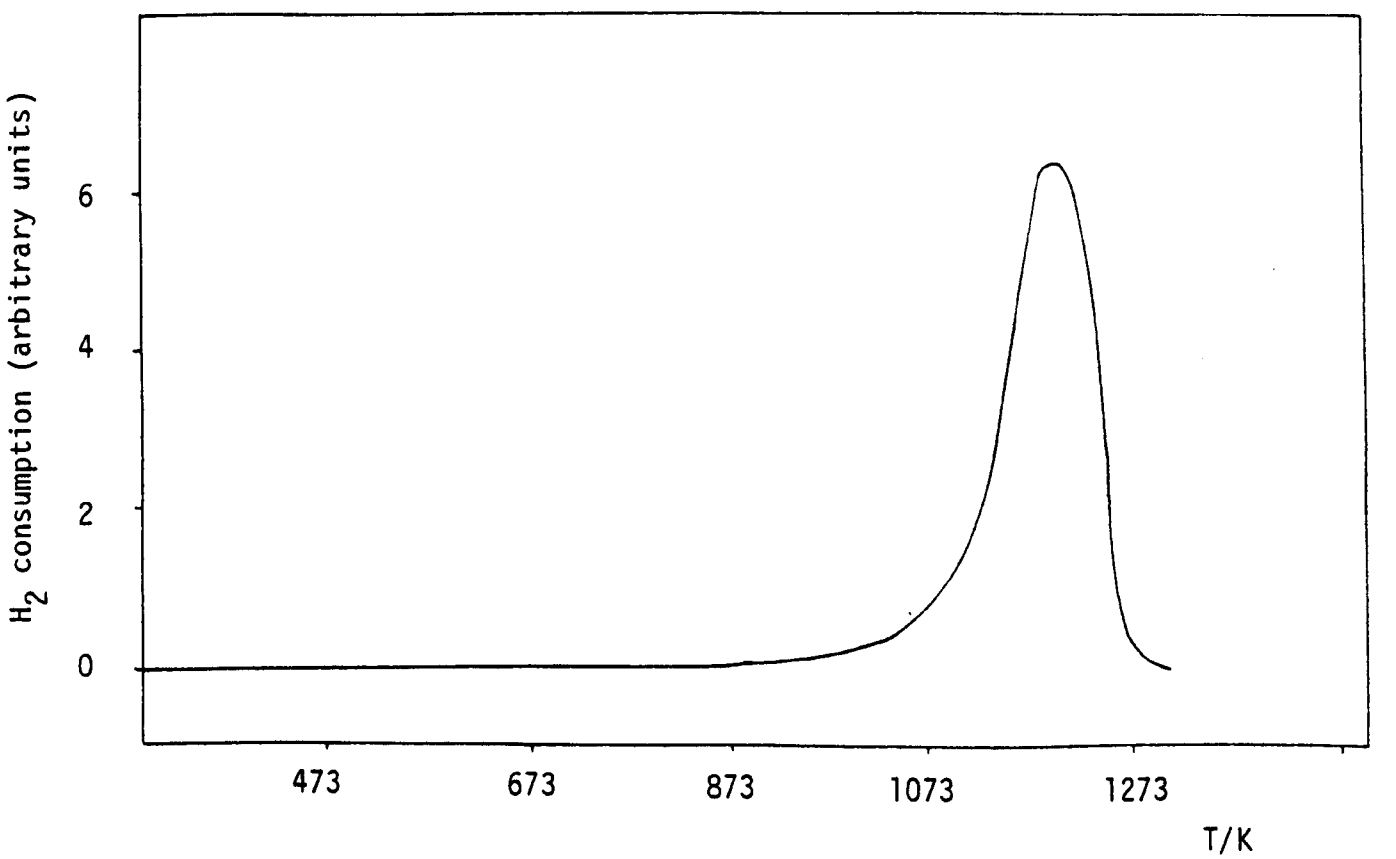

Figure 4.23 Tpr profile of 0.6NaW

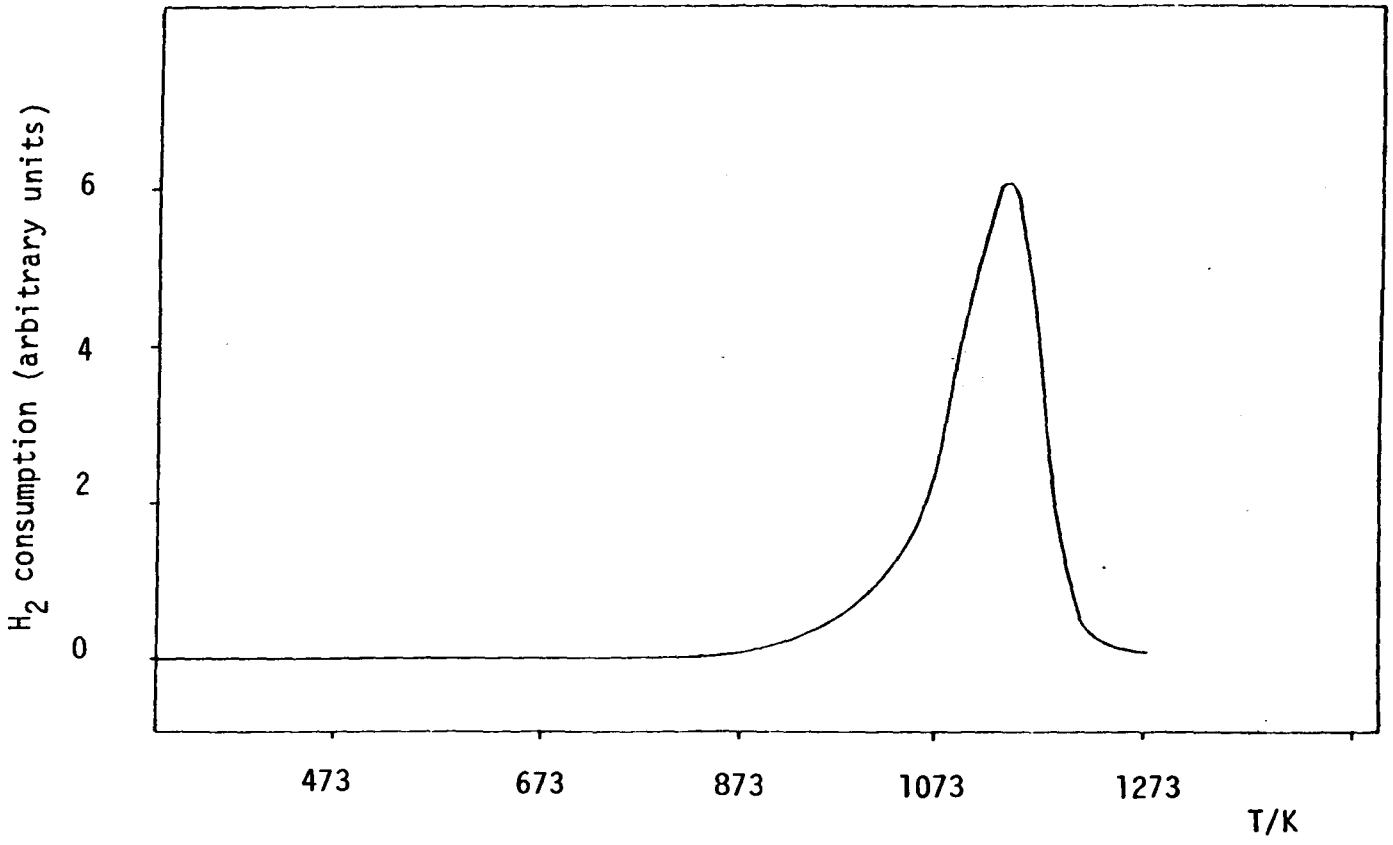

Figure 4.24 Tpr profile of 0.8NaW

slight shoulder at approximately 1098K possibly indicating that reduction may be occurring through an intermediate step which cannot be resolved by the techniques used under the present conditions.

Table 4.5

Sample	Peak Maxima/ K	H_2 Consumption/ $x10^{-3}$ $molg^{-1}$
0.05NaW	1245	12.40
0.2NaW	1250	10.90
0.3NaW	1250	9.14
0.6NaW	1202	8.69
0.8NaW	1140	5.49

4.3.3 T.p.o. Results

4.3.3.1 Oxidation of W Powder and Potassium Tungsten Bronzes

The sensitivity of the tpo method was demonstrated by a brief study of the oxidation of pure tungsten powder on heating in a diluted O_2 atmosphere. The profile given in Figure 4.25 shows that oxidation of tungsten powder starts at 655K and occurs in three overlapping processes with maxima at 755K, 790K and 935K. It is most likely that the different peaks can be associated with the gradual oxidation of tungsten from W^0 to W^{6+}. The total oxygen consumed (1.531 moles of O_2 per mole of W) is slightly higher than that theoretically required for the process (1.50 moles of O_2 per mole of W).

The tpo profiles obtained on oxidation of the potassium tungsten bronzes are given in Figure 4.26. Table 4.6 records the measured oxygen consumption and the percentage which this is, of that expected

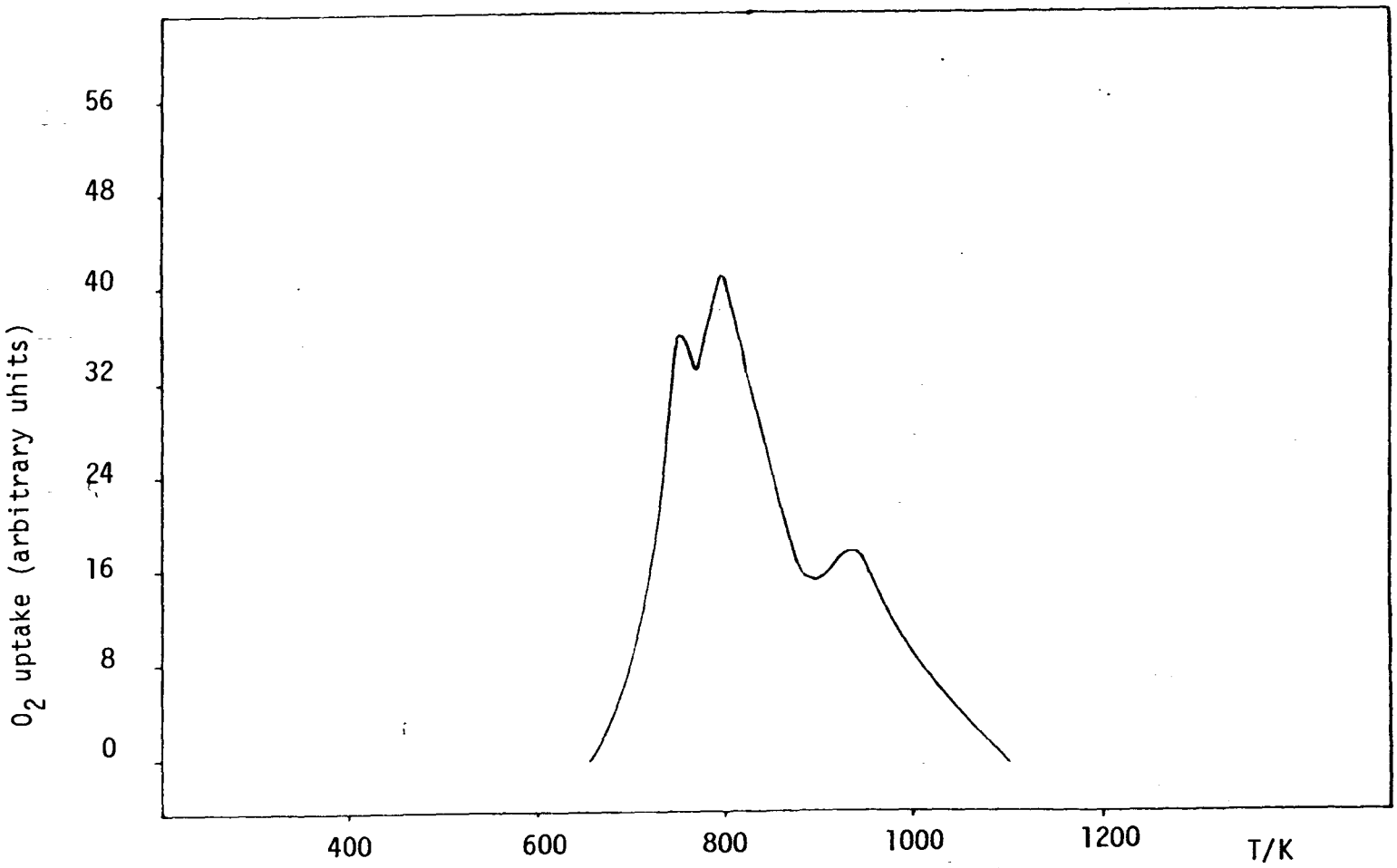

Figure 4.25 Tpo results of WO_3

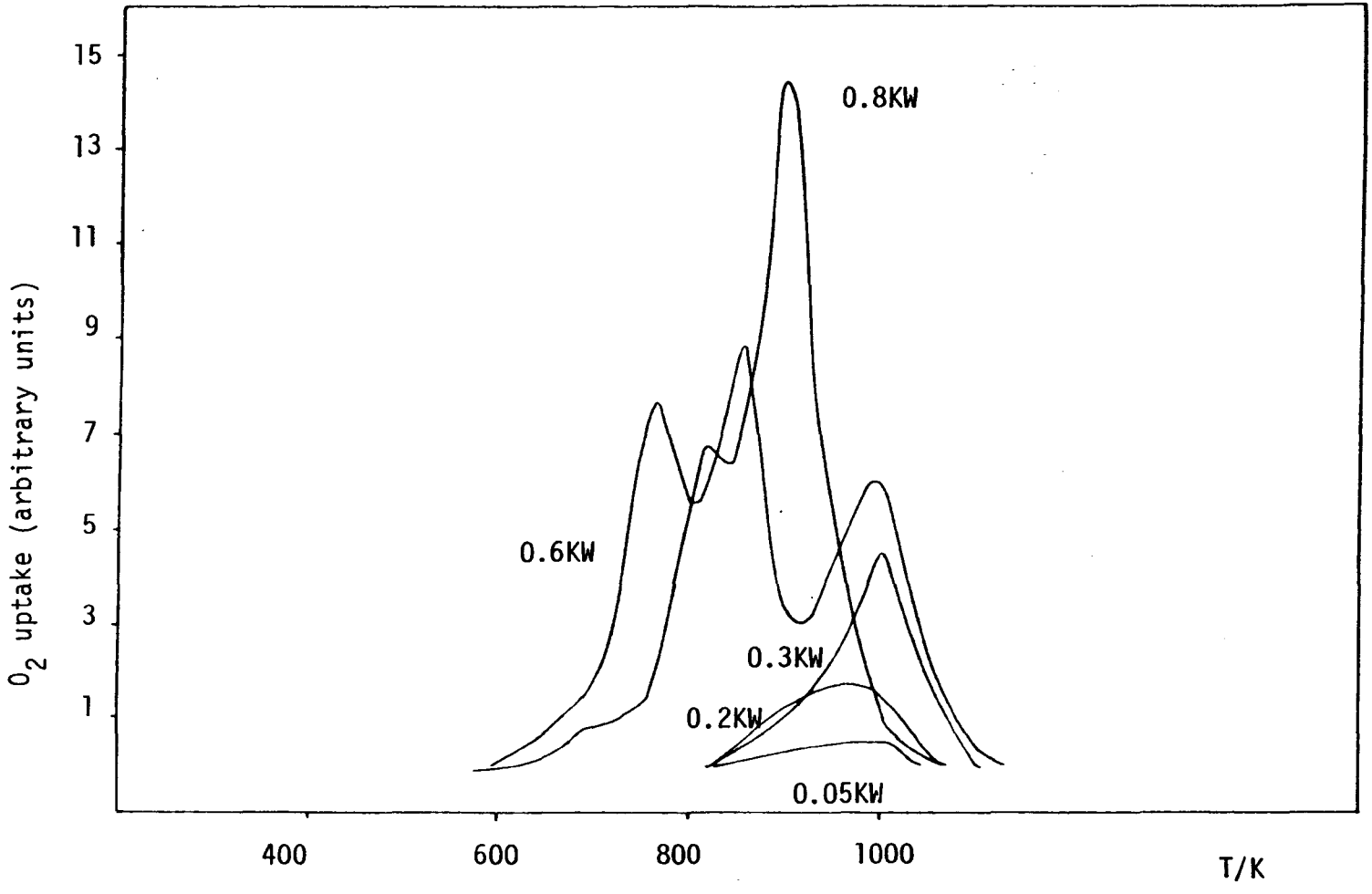

Figure 4.26 Tpo profiles of potassium tungsten bronzes

on the basis of total oxidation to potassium tungstate and tungsten trioxide as illustrated below:

$$K_xWO_3\ (0.05 \leqslant x \leqslant 0.8) + \frac{x}{4}\ O_2 \longrightarrow \frac{x}{2}\ K_2WO_4 + \left(\frac{1-x}{2}\right) WO_3$$

It is possible that a polytungstate first forms which then disproportionates to the tungstate and WO_3. XRD results of the oxidised products showed only the presence of K_2WO_4 and WO_3. The values are generally close to 100%. The table also contains the peak maximum temperatures observed in the oxidation of the various potassium tungsten bronzes. The tpo profiles of 0.05KW, 0.2KW and 0.3KW consist of broad peaks usually in the temperature range of 820K to 1075K with peak maxima at approximately 1000K. The tpo profile of 0.6KW shows that oxidation starts at 575K and exhibits peaks at 760K, 855K and 955K. The oxidation is complete at 1140K. The oxidation of 0.8KW occurs in the temperature range of 575K - 1090K and the profile shows distinct peaks at 820K and 900K, with a shoulder at 690K. Although the complete oxidation of all the potassium tungsten bronzes leads to the formation of K_2WO_4 and WO_3, the processes involved in the oxidation of the bronzes with higher potassium content appear more complex than those with lower alkali ion concentration. One possible explanation for this may be that the bronzes with low potassium content usually contain only the hexagonal phase which could oxidise in a single step at high temperature, whereas 0.6KW and 0.8KW contain mixed phases, normally tetragonal and others. The tetragonal phase could oxidise at lower temperature. It could be possible that the tetratungstate is more easily formed than the hexatungstate which then disproportionates.

Table 4.6

Sample	Expt. O_2 uptake/mmoles/ mole sample	Temperature maxima/K	% of theoretical
0.05KW	11.5	1000	92
0.2KW	55	1000	110
0.3KW	78	968	104
0.6KW	133	760,855,995	88.7
0.8KW	230	690(s),820,900	115

(s) = shoulder

4.3.3.2 Oxidation of Sodium Tungsten Bronzes

The tpo profiles for the sodium tungsten bronzes are shown in Figure 4.27. Table 4.7 gives the oxygen consumption and the percentage which this is, of the theoretical assuming that the final products of oxidation are sodium tungstate and tungsten trioxide. XRD of the oxidised products showed only the presence of Na_2WO_4 and WO_3. The peak maximum temperatures observed in the oxidation of the sodium tungsten bronzes are also recorded. The tpo profiles show a different pattern to those observed for the corresponding potassium tungsten bronzes with the peak maximum occurring at lower temperature. especially for bronzes with low sodium ion concentration. Sample 0.05NaW consumes oxygen in the temperature range of 560K - 800K in a single step with a maximum at 680K. The oxidation of sample 0.2NaW starts at 760K and shows two overlapping processes with maxima at 778K and 937K. The tpo profile of sample 0.3NaW shows oxidation to begin at 610K with one distinct maximum at 834K followed by a small shoulder at 943K. The profiles of samples 0.6NaW and 0.8NaW show oxidation to be a multistep process which in the case of sample 0.8NaW occurs in the

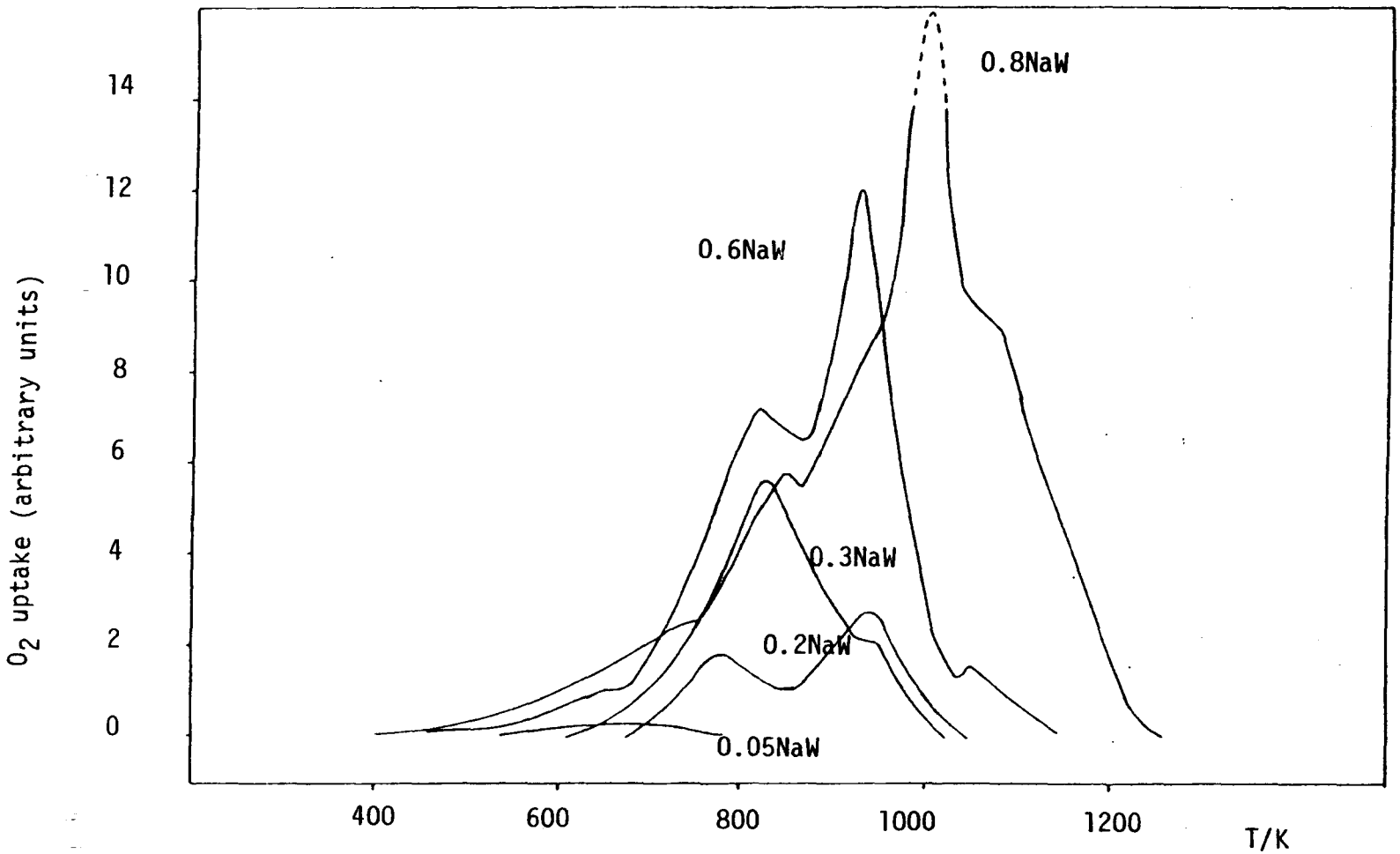

Figure 4.27 Tpo profiles of sodium tungsten bronzes

temperature range of 610K - 1260K. The O_2 consumed in the oxidation of the sodium tungsten bronzes agree well with the theoretical, although as mentioned previously, a polytungstate may be first formed which then disproportionates. The sodium tungsten bronzes with low alkali ion content are easier to oxidise than the corresponding potassium bronzes. The sodium bronzes with low alkali ion content have been shown to contain tetragonal phases; and like the potassium bronzes with similar phases (those with high alkali ion content) oxidise more readily to the tetratungstate which then disproportionates. The sodium bronzes with high alkali ion content contain mainly the cubic phase and this, similar to the hexagonal phase of the potassium bronzes is more difficult to oxidise.

Table 4.7

Sample	Expt. O_2 uptake/mmoles/ mole sample	Temperature maximum/K	% of theoretical
0.05NaW	12.4	680	99.2
0.2NaW	57	778,937	114
0.3NaW	64.5	834,943(s)	86
0.6NaW	128	650,828, 930,1050	85.3
0.8NaW	230	725(s),841 1002,1075(s)	115

(s) = shoulder

4.4 Conclusions

The reduction of the potassium and sodium tungsten bronzes appears to occur in one or more steps depending upon the concentration of the alkali metal ion content. But in all cases the final products

of reduction upon heating the samples to 1323K in hydrogen seems to be the alkali metal tungstate and tungsten metal. The reduction occurs according to the following stoichiometric equation:

$$M_xWO_3 + (3-2x)H_2 \longrightarrow \frac{x}{2} M_2WO_4 + (1 - \frac{x}{2}) W + (3-2x)H_2O$$

where M = K or Na.

A theoretical consideration of this equation would require both the hydrogen consumption and the weight loss to decrease with increasing alkali metal ion content in the bronze. This agrees with the observations made in the present study indicating formation of a separate tungstate phase. Reduction of WO_3 occurs in two steps. Various mentions have been made in literature[1] of the reduction of WO_3, first to an intermediate oxide and then finally to tungsten metal. It appears that a similar mechanism of reduction occurs on the present sample although it was not possible to distinguish the sub-oxide formed. Reduction of the bronzes could be occurring through more than one step as mentioned in literature[1], but the limitations of the present techniques or possibly the high heating rate used did not allow the resolution of the different processes, although in some cases more than one step was observed.

The products of oxidation of the alkali metal tungsten bronzes are the alkali metal tungstate and WO_3. There is indication that the bronzes first oxidise to a polytungstate and a sub-oxide of tungsten before complete oxidation. Bronzes with a tetragonal structure oxidise more easily than those with either an hexagonal or cubic structure, most probably because the tetratungstate is formed more readily. From the oxygen consumption there was no indication that the bronzes prepared by the present method were oxygen deficient, although a recent study[4] on tungsten bronzes prepared under vacuum have shown such characteristics.

CHAPTER 4

REFERENCES

1. P.G. Dickens and M.S. Whittingham, Proc. 7th Intern. Sym. on the React. of Solids, 640, (1972).

2. A. Deschanures, G. Desgardin, B. Raveau and J.C. Thomazeau, Bull. Soc. Chim. Fr., 4537, (1976).

3. A. Hussain, L. Kihlborg and A. Klug, J. Solid State Chem., 25, 189 (1978).

4. S.A. Lawrence, S. Stevenson, K. Mavadia and P.A. Sermon, Proc. R. Soc., A411, 95, (1987).

CHAPTER 5

X-RAY DIFFRACTION STUDIES

5.1 Introduction

X-ray diffraction allows study of the structure of matter and as such it provides complementary information to optical and electron microscopy. All the information is extracted by the use of monochromatic radiation and a relatively complex mathematical analysis. If single crystals are examined by this technique it is possible, by direct interpretation of the diffractogram, to obtain information on crystal planes and lattice spacing.

X-rays are a form of electromagnetic radiation differing from light waves (λ = 400 to 800nm) in that they have a shorter wavelength (λ = 0.1nm). These rays are produced when a metal target is bombarded with fast electrons in a vacuum tube. The radiation emitted can be separated into two components, a continuous spectrum which is spread over a wide range of wavelengths and a superimposed line spectrum characteristic of the metal being bombarded. (Figure 5.1(a)). The energy of the white radiation, as the continuous spectrum is called, increases as the atomic number of the target and as the square of the applied voltage, while the characteristic radiation is excited only when a critical voltage is exceeded. The white radiation results from the deceleration of the incoming high energy electrons by the strong electric field provided by the electrons surrounding the nucleus of an atom. The decrease in energy ΔE of these incoming electrons is given by $h\nu$. Concurrent deceleration appears as continuous radiation over a wide range of wavelength. Characteristic spectra are produced when incident electrons have sufficient energy to dislodge an electron

from one of the inner electron shells. If an electron from a higher energy shell then decays to the lower shell, the energy released is in the form of an X-ray. The difference in energy between two given shells determines the emitted wavelength and although an increase in electron acceleration voltage increases the intensity of characteristic radiation, it does not alter its wavelength.

If an electron is ejected from the K shell and the vacancy is filled by an L shell electron, the transition is termed K_α and if the vacancy is filled by an M shell electron, the transition is termed K_β. The characteristic X-ray produced by elements with low atomic numbers are very easily absorbed by matter and are therefore of little use in crystallography, whilst X-rays from target elements of high atomic number are the most useful for X-ray diffraction. The most often used target metals include copper, molybdenum and cobalt.

The characteristic radiation for copper shown in Figure 5.1(a) consists of X-rays arising from the K_β, $K_{\alpha 1}$ and $K_{\alpha 2}$ transitions. The respective wavelengths of these transitions are 0.139nm, 0.15405nm and 0.15445nm. Due to the similarity in wavelength of the $K_{\alpha 1}$ and $K_{\alpha 2}$ transitions, the wavelength usually quoted for CuK_α(weighted for relative intensities) is 0.15418nm. The presence of the K_β radiation makes interpretation confusing, therefore, a metal foil filter is employed. Superimposed on Figure 5.1(a) is the absorption spectrum of nickel. It will be noted that the absorption spectrum, unlike emission spectra for X-rays, consists not of a series of lines but of one or more absorption edges. Thus for nickel the absorption edge lies between CuK_β and K_α emissions. By calculating the thickness of nickel foil required to absorb most of the K_β emission without significantly affecting the K_α emission, a spectrum of the type shown in

Figure 5.1(b) will be obtained. In this way, it is possible to produce almost monochromatic X-rays which are suitable for X-ray diffraction purposes.

5.2 Theory

The basic theory of X-ray diffraction was originally deduced by W.L. Bragg. Consider Figure 5.2, which shows a series of parallel planes of atoms separated by a uniform distance d. A beam of X-rays incident at an angle θ to the atomic planes will be partially reflected by the outermost atoms at point A to point P such that the angle of incidence will equal the angle of reflection, (i.e. a total of 2θ). The remainder of the X-rays will penetrate the lattice, most being absorbed by lower planes of atoms. The angle of reflection for the lower planes of atoms will also be θ. Therefore, all X-rays reflected by a particular plane of atoms will be in phase, but only under strict angular conditions will X-rays reflected from a series of planes be in phase with each other and cause constructive interference. The condition for in phase reflection is that the path length difference must be an integral number of wavelengths ($n\lambda$) between waves reflected from successive planes.

Bragg deduced that,

$$n\lambda = 2d\sin\theta \qquad \ldots\ldots\ldots\ldots\ldots\ldots \quad 5.1$$

where the critical angular values of θ for which the law is satisfied are known as Bragg angles. The directions of the reflected beams are determined entirely by the geometry of the lattice which in turn is governed by the orientation and spacing of the crystal planes.

XRD THEORY

Fig 5.1(a)

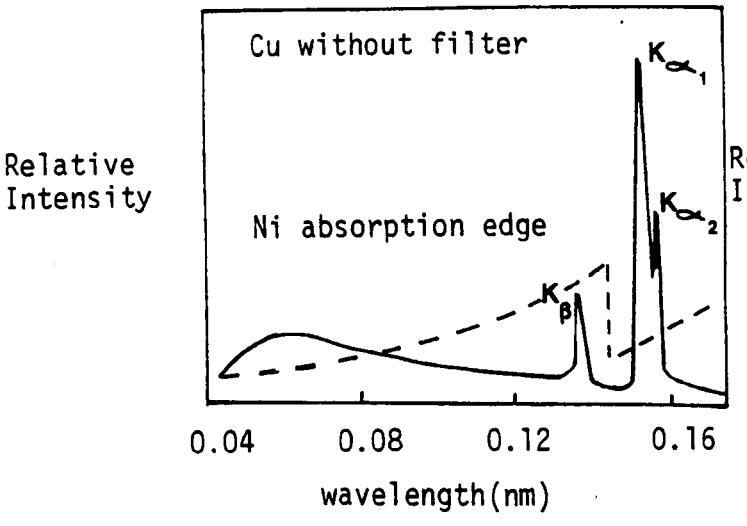

Fig. 5.1(b)

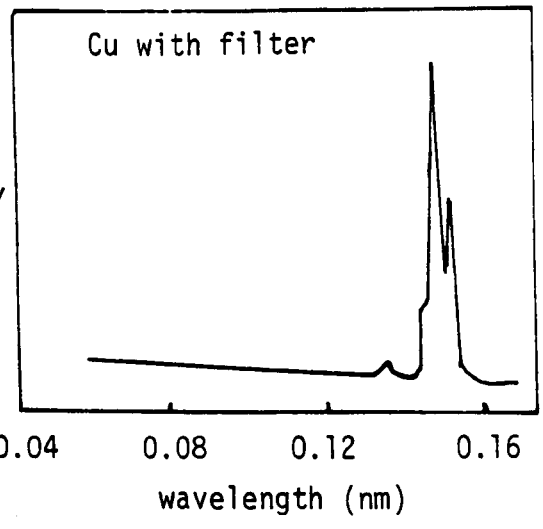

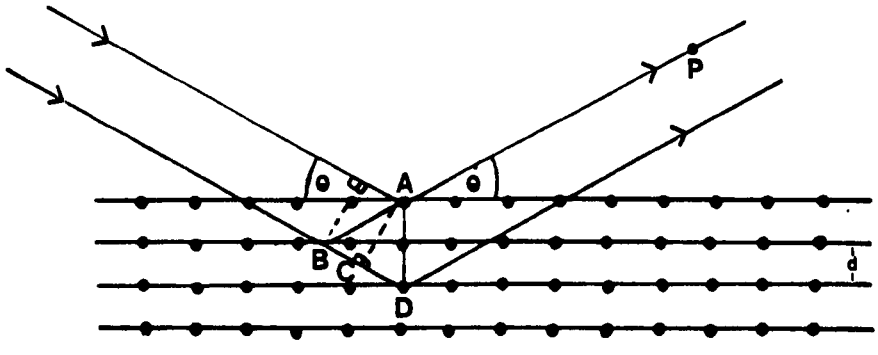

Figure 5.2

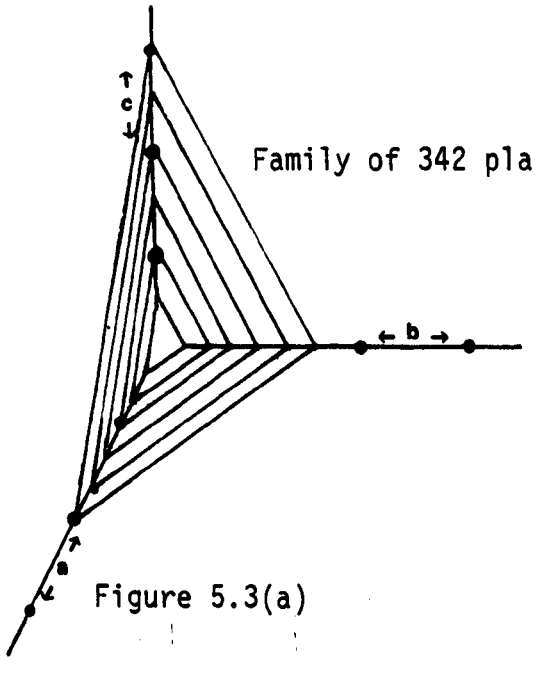

Figure 5.3(a)

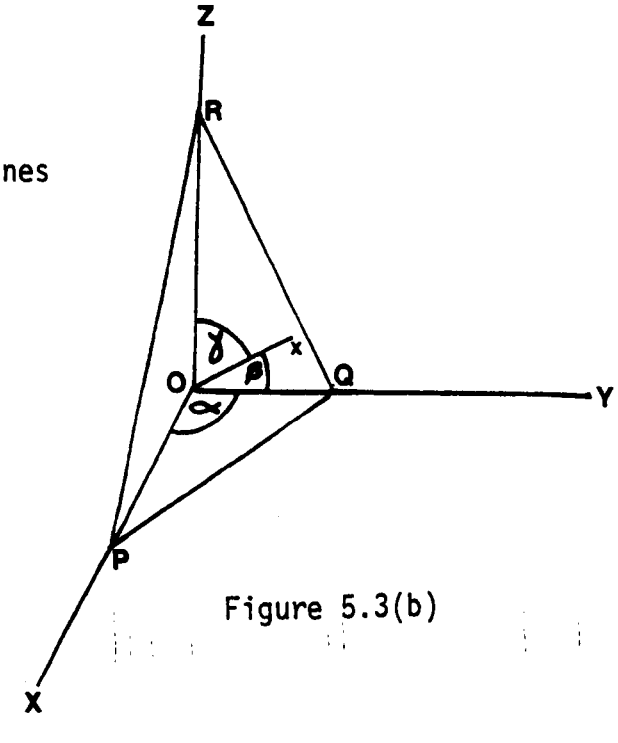

Figure 5.3(b)

5.3 Crystal Planes and Lattice Spacing

The crystalline state is a special form of solid where regular repeating units (known as the unit cell) are present. By repeated translations of the unit cell in three dimensions the overall crystal lattice is found. The shape and size of a unit cell is normally defined by lengths a, b and c, and the angles between these vectors given by α, β and γ (the angles between b and c, c and a, and a and b respectively). A regular three-dimensional array of atoms, which defines the crystalline structure can be considered as a series of parallel equivalent planes which are more or less densely populated with these atoms. In 1839, W.H. Miller proposed a system of indices to define numerically any series of planes. Consider Figure 5.3(a), the set of planes illustrated intercepting the x, y and z axis may be defined by the integral number of intercepts, given by h, k and l on the unit cell edges, a, b and c. If the intercept is length a (or b or c), then the value of h (or k or l) will be 1. If the intercept is one half of the unit cell edge, then the corresponding index will be 2. Thus the values of h, k and l can be used to define any family of planes. Figure 5.3(a) shows a family of 342 planes. For any lattice it is possible to find a set of axes on which the number of intercepts (h, k and l) are small whole numbers, although in some planes the intercepts are negative and are quoted by a bar over the particular index, (e.g. $\bar{h}$,k,l). Planes parallel to an axis are denoted by a zero (e.g. h,k,0).

Consider Figure 5.3(b) which shows the first 342 plane such that the length d is given by the normal from the origin O to point X on the plane which passes through points P, Q and R. The line so constructed can be seen to be perpendicular to the PQR plane and since

the origin lies in the adjacent (hkl) plane, the distance is equal to the separation between the individual members of the whole family of planes. The lines OP, OQ and OR have lengths given respectively by $^{a}/_{h}$, $^{b}/_{k}$, and $^{c}/_{l}$, and describe the angles α, β and γ respectively, with the line OX corresponding to distance d.

Therefore, $\cos\alpha = \frac{dh}{a}$; $\cos\beta = \frac{dk}{b}$; $\cos\gamma = \frac{dl}{c}$;

But for directional cosines

$$\cos^2\alpha + \cos^2\beta + \cos^2\gamma = 1$$

Therefore,

$$\frac{d^2h^2}{a^2} + \frac{d^2k^2}{b^2} + \frac{d^2l^2}{c^2} = 1$$

or,

$$\frac{1}{d^2} = \frac{h^2}{a^2} + \frac{k^2}{b^2} + \frac{l^2}{c^2} \quad \ldots\ldots\ldots\ldots\ldots\ldots 5.2$$

Combination of equation 5.2 with the Bragg equation 5.1 gives:

$$\sin^2\theta = \frac{\lambda^2h^2}{4a^2} + \frac{\lambda^2k^2}{4b^2} + \frac{\lambda^2l^2}{4c^2} \quad \ldots\ldots\ldots\ldots\ldots 5.3$$

Equation 5.3 can be considered to relate to an orthorhombic structure in which the three unit lengths are different but distributed along three mutually perpendicular axes. For a cubic cell in which the unit cell dimensions are all equal and taken as the value a, the equation simplifies to:

$$\sin^2\theta = \frac{\lambda^2}{4a^2}(h^2 + k^2 + l^2) \quad \ldots\ldots\ldots\ldots\ldots\ldots 5.4$$

5.4 Apparatus and Procedure

In the present study X-ray diffractometric analysis was performed on W powder; WO_3, K_2WO_4, Na_2WO_4, the potassium tungsten bronzes and the sodium tungsten bronzes.

A Philips PW 1729 X-ray generator with a copper target was used. It was operated at 50 kV and 24 mA and the X-ray beam passed through a nickel filter to give the $CuK\alpha_1$ radiation. In the diffractometer, a divergent beam of X-rays converges after reflection from the specimen, passes through a narrow slit and enters the detector which is a countertube with electrical circuitry. The detector is driven at twice the speed of the specimen so that the specimen surface is always at θ when the detector is at 2θ. Parallel slits are used normal to the focusing planes to obtain sharp lines. The intensity diffracted at the various angles is automatically recorded on a chart as a function of the reflection angles 2θ. The detector was scanned at 0.5^{o} of 2θ per minute and the recorder chart speed was 5mm min^{-1} so that 1cm on the chart was equivalent to 1^{o} of 2θ.

5.5 Results

5.5.1 X-Ray Diffractometer Studies

The parameter measured from the diffractogram was the Bragg angle 2θ. The measurement of the Bragg diffraction angles enable the interplanar spacings, d, to be calculated since

$$n\lambda = 2d_{hkl} \text{ Sin } \theta \qquad \ldots\ldots\ldots\ldots\ldots\ldots \quad 5.1$$

where λ is the incident X-ray wavelength, d the interplanar spacing for any family of crystal planes (hkl), and θ the Bragg diffraction angle.

5.5.2 W. Powder, WO_3, K_2WO_4 and Na_2WO_4

The d values calculated from the diffractograms of W powder, WO_3, K_2WO_4 and Na_2WO_4 are given in Appendix 2. Only the more intense lines are shown and compared with the d values given in ASTM powder diffraction file[1]. The d spacings of W powder show good agreement with those given in the literature for W metal having a cubic structure with cell parameter a_o - 0.3165nm. The d spacing calculated for WO_3 is identical for WO_3 with a monoclinic structure with cell parameters a_o = 0.7297nm, b_o = 0.7539nm and c_o = 0.7688nm, as quoted in the literature. K_2WO_4 normally adopts a monoclinic structure with cell parameters a_o = 1.238nm, b_o = 0.612nm and c_o = 0.755nm, and the d spacings calculated agree well with those for such a structure. The d spacings obtained for Na_2WO_4 agree with those for Na_2WO_4 with a cubic structure with cell parameter a_o = 0.9129nm.

5.5.3 Potassium Tungsten Bronzes

The d values calculated from the diffractogram of 0.05KW are given in Table 5.1. Previous structural studies[2] of potassium tungsten bronzes with low alkali ion content have suggested an intergrowth tungsten bronze, (ITB), structure to be present. The ITB can be regarded as an intergrowth of hexagonal tungsten bronze (HTB) and WO_3 providing a gradual transition from the HTB structure to that of WO_3. The symmetry of an ITB is normally that of an orthorhombic system. After elimination of those lines observed due to the presence of WO_3, the remaining d values calculated for 0.05KW correspond to an orthorhombic system with cell parameters a_o = 0.735nm, b_o = 3.850nm and c_o = 0.388nm.

Table 5.1

X-ray Diffraction of 0.05KW

θ	Sinθ	d/nm
6.765	0.117	0.654
11.390	0.197	0.390
11.665	0.202	0.381
12.019	0.208	0.370
13.009	0.225	0.342
13.815	0.238	0.322
14.217	0.245	0.314
16.487	0.284	0.271
16.624	0.286	0.269
16.929	0.291	0.264
17.429	0.299	0.257
17.677	0.303	0.254
18.329	0.314	0.245
20.664	0.353	0.218
24.774	0.419	0.184
27.592	0.463	0.166

The values of θ obtained from the diffractograms of samples 0.2KW and 0.3KW were used to determine the unit cells, calculate the lattice parameters and to index the lines. Structural studies of potassium tungsten bronzeswhere $0.19 \leqslant x \leqslant 0.33$[2,3] have suggested the unit cell to be hexagonal. On this basis the lines obtained for 0.2KW and 0.3KW were indexed employing the method for an hexagonal system detailed below for sample 0.3KW.

For an hexagonal system, equation 5.3 may be written as;

$$\sin^2\theta = A(h^2 + hk + k^2) + Cl^2 \quad \ldots\ldots\ldots\ldots\ldots 5.5$$

where $$A = \frac{\lambda^2}{3a^2} \quad \ldots\ldots\ldots\ldots\ldots 5.6$$

and $$C = \frac{\lambda^2}{4c^2} \quad \ldots\ldots\ldots\ldots\ldots 5.7$$

For the hk0 spectra;

$$\sin^2\theta_{100} = A \qquad \sin^2\theta_{210} = 7A$$

$$\sin^2\theta_{110} = 3A \qquad \sin^2\theta_{300} = 9A$$

$$\sin^2\theta_{200} = 4A \qquad \sin^2\theta_{220} = 12A$$

The ratio 3 occurs frequently, and is representative of the hexagonal system, occurring in other systems only by chance. If the ratio of the $\sin^2\theta$ values of two of the first three or four lines is 3, then the first one is probably the 100 line and the other the 110 line. Once the value of A has been found, the other lines can be indexed and the value of C can be determined. The lattice parameters can then be calculated from the values of A and C using equations 5.6 and 5.7. Table 5.2 shows the line spacings and the $\sin^2\theta$ values for the most intense lines of sample 0.3KW. Initially it is necessary to look for the significant ratio of 3 between two $\sin^2\theta$ values. The ratio of the third $\sin^2\theta$ value to the first in Table 5.2 is 3.007, hence it may be assumed that the first line corresponds to the 100 reflection and the third line, the 110 reflection. The term A which is equal to $\sin^2\theta$ when h,k and l correspond to the 100 plane has a value of 0.0144. If the l index of an hkl line is not zero, then the $\sin^2\theta$ value of that line must contain a term Cl^2 in accordance with equation 5.5. To facilitate the search for the factor C, the characteristic multiples of A are subtracted from the $\sin^2\theta$ values as shown in Table 5.2. It

can be seen that the term 0.0105 is common to the second line in the $\sin^2\theta$ column, to the fourth in the $\sin^2\theta$-A column and to the sixth in the $\sin^2\theta$-3A column and therefore corresponds to the value of C when l is equal to one.

These values of A(0.0144) and C(0.0105) were then used to index the lines by assuming different values of h, k and l using equation 5.5. These values are shown in Table 5.2. The lattice parameters a_o and c_o for the hexagonal structure were calculated from the values of A and C using equations 5.6 and 5.7 respectively. The values of a_o = 0.741nm and c_o = 0.751 for sample 0.3KW obtained from these relationships agree well with those quoted in literature[3].

The values of θ obtained for sample 0.2KW were used to index the lines and calculate the lattice parameters a_o and c_o using the same

Table 5.2

X-ray Diffraction of 0.3KW

θ	$\sin^2\theta$	$\sin^2\theta$-A	$\sin^2\theta$-3A	d/nm	hkl
6.895	0.0144	-	-	0.641	100
11.760	0.0415	0.0271	-	0.378	002
12.004	0.0433	0.0289	0.0001	0.370	110
13.405	0.0537	0.0393	0.0105	0.332	111
13.725	0.0563	0.0419	0.0131	0.325	102
13.925	0.0579	0.0435	0.0147	0.320	200
16.964	0.0851	0.0707	0.0419	0.264	112
18.412	0.0998	0.0854	0.0566	0.244	202
19.537	0.1118	0.0974	0.0686	0.230	211
25.724	0.1884	0.1740	0.1452	0.177	310
26.477	0.1988	0.1844	0.1556	0.173	311
27.677	0.2157	0.2013	0.1725	0.166	220

method described previously for an hexagonal system. These values together with the d values are given in Table 5.3. Sample 0.2KW corresponds to an hexagonal bronze with cell parameters a_o = 0.738nm and c_o = 0.751nm, which agree well with those in the literture[2].

Table 5.3

X-ray Diffraction of 0.2KW

θ	Sinθ	d/nm	hkl
6.907	0.120	0.640	100
11.832	0.205	0.376	002
12.042	0.208	0.369	110
13.429	0.232	0.332	111
13.757	0.237	0.324	102
13.917	0.240	0.320	200
17.010	0.292	0.263	112
18.442	0.316	0.243	202
19.557	0.335	0.230	211
24.247	0.411	0.188	004
24.640	0.417	0.185	202
28.412	0.476	0.162	222
28.772	0.481	0.160	400

The θ values obtained from the diffractogram of sample 0.6KW are given in Table 5.4. Structural studies[4] on potassium bronzes with higher alkali ion content have suggested the unit cell to be tetragonal, on this basis the relationships detailed below for a tetragonal system were used to index the lines and calculate the lattice parameters for sample 0.6KW.

For a tetragonal system, equation 5.3 may be written as:

$$\sin^2\theta_{hkl} = A(h^2 + h^2) + Cl^2 \qquad \ldots\ldots\ldots\ldots\ldots 5.8$$

where

$$A = \frac{\lambda^2}{4a^2} \qquad \ldots\ldots\ldots\ldots\ldots 5.9$$

and

$$C = \frac{\lambda^2}{4c^2} \qquad \ldots\ldots\ldots\ldots\ldots 5.10$$

For the hk0 spectra,

$$\sin^2\theta_{100} = A \qquad \sin^2\theta_{200} = 4A$$

$$\sin^2\theta_{110} = 2A \qquad \sin^2\theta_{220} = 8A$$

The ratio 2 occurs frequently and except by chance, the only other system in which this ratio is found is the cubic one. If the ratio of the $\sin^2\theta$ values of two low-angle lines are in the ratio of 2, it is probable that the substance is tetragonal and that the two lines are the 100 and 110 or 110 and 200 planes. Once the quantity A has been found, the other lines can be indexed and the value of C can be determined. The lattice parameters can then be calculated from the values of A and C using equations 5.9 and 5.10. Table 5.4 shows the line spacings and the $\sin^2\theta$ values for the most intense lines of sample 0.6KW. It can be seen that the ratio of the second $\sin^2\theta$ value to the first in Table 5.4 is 2.00, hence the first and second lines correspond to the 100 and 110 planes respectively. The term A which is equal to $\sin^2\theta$ when h, k and l correspond to the 100 plane has a value of 0.005. If the l index of an hkl line is not zero, then the $\sin^2\theta$ value of that line must contain a term Cl^2 in accordance with equation 5.8. To find the constant C, characteristic multiples of A must be subtracted from the $\sin^2\theta$ values as shown in

Table 5.4. It can be seen that the term 0.0403 ± 0.0003 is common to the fifth line in the $\sin^2\theta$ column, the fifth line in the $\sin^2\theta$-A column, and the fifth line in the $\sin^2\theta$-2A column, and corresponds to the value of C when l is equal to one. The values of A(0.0050)and C(0.0403) were then used to index the lines by using different values of h, k and l using equation 5.8. These values are given in Table 5.4. The lattice parameters a_0 and c_0 were calculated from the values of A and C using

Table 5.4

X-ray Diffraction of 0.6KW

θ	$\sin^2\theta$	$\sin^2\theta$-A	$\sin^2\theta$-2A	d/nm	hkl
4.055	0.0050	-	-	1.089	100
5.750	0.0100	0.0050	-	0.770	110
8.150	0.0201	0.0151	0.0051	0.542	200
11.399	0.0391	0.0340	0.0241	0.389	220
11.542	0.0400	0.0350	0.0250	0.385	001
12.330	0.0456	0.0406	0.0356	0.360	101
12.947	0.0502	0.0452	0.0402	0.344	111
14.492	0.0626	0.0576	0.0476	0.308	320
14.954	0.0665	0.0615	0.0515	0.298	211
16.347	0.0792	0.0742	0.0642	0.274	221
18.454	0.1002	0.0952	0.0902	0.244	420
20.321	0.1206	0.1156	0.1106	0.222	401
23.662	0.1611	0.1561	0.1461	0.192	002
25.585	0.1865	0.1815	0.1765	0.178	202
26.522	0.1994	0.1944	0.1894	0.173	441
26.657	0.2013	0.1963	0.1863	0.172	222

equations 5.9 and 5.10 respectively. For the tetragonal bronze 0.6KW. a_o = 1.089nm and c_o = 0.384nm which agree well with those quoted in literature for potassium tungsten bronzes having a tetragonal structure[4].

The diffractogram obtained for sample 0.8KW was much more complex than those obtained for the other potassium bronze samples and proved too complicated to interpret fully. The d values for the most intense lines obtained on sample 0.8KW are given in Table 5.5.

Table 5.5

X-ray Diffractogram of 0.8KW

θ	Sinθ	d/nm
2.949	0.051	1.496
4.304	0.075	1.026
6.394	0.111	0.691
6.529	0.1 3	0.677
7.989	0.139	0.554
9.002	0.156	0.492
9.134	0.159	0.485
9.534	0.165	0.465
9.937	0.172	0.446
10.229	0.177	0.434
11.352	0.197	0.391
12.552	0.217	0.355
14.059	0.243	0.317
18.637	0.319	0.204
21.302	0.363	0.212
21.602	0.368	0.209
23.472	0.398	0.193
24.052	0.407	0.189

5.5.4 Sodium Tungsten Bronzes

The θ values obtained for samples 0.05NaW, 0.2NaW, and 0.3NaW are given in Tables 5.6, 5.7 and 5.8 respectively. These sodium bronzes appear to be tetragonal bronzes. The method of calculating the lattice parameters and indexing the most intense lines obtained for these samples was that employed for the potassium bronze sample 0.6KW, and is given in detail in sub-section 3.5.3. Sample 0.05NaW has lattice parameters a_o = 0.524nm and c_o = 0.388nm, which agree well with those found in the literature[5] the d values for this sample together with the line indices are given in Table 5.6. The values of θ obtained from the diffractograms of samples 0.2NaW and 0.3NaW were used to calculate the lattice parameters and index the most intense lines, these values are given in Tables 5.7 and 5.8. Sample 0.2NaW is a tetragonal bronze with lattice parameters a_o = 1.215nm and c_o = 0.377nm. Sample 0.3NaW also corresponds to a tetragonal bronze with lattice parameters a_o = 1.209nm and c_o = 0.375nm. In both cases the calculated cell parameters agree well with those found in literature[6].

The sodium bronzes with higher alkali ion content, $x \geq 0.6$, gave relatively uncomplicated diffractograms. Upon inspection of the spectra obtained for samples 0.6NaW and 0.8NaW, a regular pattern was observed, suggesting the presence of cubic phases for these bronzes. The d values obtained for sample 0.6NaW are detailed in Table 5.9. For the cubic system;

$$\sin^2\theta_{hkl} = \frac{\lambda^2}{4a^2}(h^2 + k^2 + l^2) \quad \text{..... 5.4}$$

where $$A = \frac{\lambda^2}{4a^2} \quad \text{..... 5.11}$$

The characteristic of this system is that the values of $\sin^2\theta$ have a common factor. The values of $\sin^2\theta$ for sample 0.6NaW are given

Table 5.6

X-ray Diffractogram of 0.05NaW

θ	Sinθ	d/nm	hkl
11.563	0.200	0.384	0.01
11.833	0.205	0.376	110
14.365	0.248	0.310	101
16.675	0.287	0.268	111
17.105	0.294	0.262	200
18.348	0.315	0.245	210
20.808	0.355	0.217	201
23.593	0.400	0.192	002
25.221	0.426	0.181	102
26.719	0.449	0.171	112
27.939	0.468	0.164	310
30.537	0.508	0.152	311
38.283	0.619	0.124	401

Table 5.7

X-ray Diffractogram of 0.2NaW

θ	Sinθ	d/nm	hkl
8.181	0.142	0.541	210
11.328	0.196	0.392	300
11.602	0.201	0.383	310
11.882	0.206	0.374	001
14.157	0.244	0.315	211
16.558	0.285	0.270	311
20.470	0.349	0.220	421
20.607	0.352	0.219	440
23.802	0.403	0.191	002
24.382	0.413	0.186	102
24.855	0.420	0.183	112
26.817	0.451	0.171	302
27.232	0.457	0.168	312
27.592	0.463	0.166	322

Table 5.8

X-ray Diffractogram of 0.3NaW

θ	Sinθ	d/nm	hkl
8.143	0.142	0.544	210
11.642	0.202	0.382	310
12.562	0.217	0.354	101
13.272	0.229	0.335	112
15.244	0.263	0.293	410
16.597	0.286	0.269	311
20.507	0.350	0.220	421
23.852	0.404	0.190	002
25.317	0.427	0.180	202
26.892	0.452	0.170	312
29.654	0.495	0.156	332

in Table 5.9 and it can be seen that the first two lines have a common factor of about 0.0404 and dividing the first seven lines obtained by 0.0404, values of around 1, 2, 3, 4, 5, 6 and 8 are obtained, being characteristic values for a primitive cubic lattice. Sample 0.6NaW corresponds to a cubic bronze with lattice parameter a_o = 0.383nm, calculated from equation 5.11 with A = 0.0404, and is in good agreement with literature values of cubic sodium bronzes[7].

The θ and d values together with the line indices obtained for sample 0.8NaW are given in Table 5.10. Similar to sample 0.6NaW, it was found that sample 0.8NaW is a primitive cubic bronze with cell parameter a_o = 0.385nm, which agrees well with those mentioned in literature for sodium bronzes with high alkali ion content.

Table 5.9

X-ray Diffractogram of 0.6NaW

θ	Sinθ	$Sin^2θ$	d/nm	hkl
11.595	0.201	0.0404	0.386	100
16.504	0.284	0.0807	0.272	110
20.300	0.347	0.1203	0.222	111
23.639	0.401	0.1607	0.192	200
26.639	0.448	0.2010	0.172	210
29.432	0.491	0.2414	0.157	211
34.584	0.568	0.3221	0.135	220
37.013	0.602	0.3624	0.128	221
39.406	0.635	0.4030	0.121	310
41.745	0.666	0.4433	0.116	311
44.059	0.695	0.4836	0.111	222
46.377	0.724	0.5240	0.106	320
48.712	0.751	0.5646	0.103	321

It can be concluded that both the potassium and sodium bronzes may be regarded as mainly homogeneous bronzes with the exception of sample 0.05KW which showed the presence of WO_3 phases.

Table 5.10

X-ray Diffractogram of 0.8NaW

θ	Sinθ	d/nm	hkl
11.539	0.200	0.385	100
16.423	0.283	0.272	110
20.272	0.346	0.222	111
23.580	0.400	0.193	200
26.555	0.447	0.172	210
29.405	0.491	0.157	211
34.525	0.567	0.136	220
36.969	0.601	0.128	221
39.349	0.634	0.121	310
41.549	0.663	0.116	311

CHAPTER 5

REFERENCES

1. ASTM, Standard American Society for Testing Materials.
2. P.G. Dickens, Solid State Chemistry, 7, 211.
3. P.E. Werner, P. Kierkegaard and A. Magneli, Acta. Chem. Scand., 15, 427, (1961).
4. A. Magneli, Arkiv. Kemi., 1, 213, 269, (1949).
5. J.M. Reau, C. Fouassier, G. Le Flem, J.Y. Barraud, J.P. Doumerc and P. Hagenmuller, Rev. Chim. Miner., 7, 975, (1970).
6. F. Takusagawa and R.A. Jacobson, J. Solid State Chem., 18, 163, (1976).
7. B.W. Brown and E. Banks, J. Am. Chem. Soc., 76, 963, (1954).

CHAPTER 6

X-RAY PHOTOELECTRON SPECTROSCOPY

6.1 Introduction

X-ray photoelectron spectroscopy (XPS), also known as Electron Spectroscopy for Chemical Analysis (ESCA), has the ability to monitor the chemistry occurring on the outermost layers of a solid or catalyst, and irrespective of the elements from which the catalyst is prepared (with the exception of hydrogen and helium), to detect changes of relative concentration of surface atoms.

Since the 1970s, X-ray photoelectron spectroscopy has been widely used in chemical research. The method is based on the photo-electric effect. Bearing in mind that the physical principles of XPS and the problems concerned with the interpretation of the spectra have been reviewed[1-7], consideration will be confined to the basic concepts.

The principles are simple. A sample is bombarded with mono-energetic X-ray photons, normally Al Kα (1486.6eV) or Mg Kα (1253.6eV), which eject electrons from core and valence shells in which the ionisation potential, or binding energy, is less than the primary photon energy. The kinetic energy of the ejected electron is measured and is related to the binding energy by the relation:

$$E_{KE} = h\nu - E_{BE} - \phi_s \qquad \ldots\ldots\ldots\ldots\ldots\ldots 6.1$$

where $h\nu$ is the energy of the photon, E_{BE} is the binding energy of the electrons with respect to the Fermi level, and ϕ_s is the spectrometer work function. Samples of material which are poor conductors of electricity acquire a positive charge during their examination, and

this leads to the ejected electron having lower kinetic energy than it should, leading to too high a binding energy. This phenomenon is called "charging effect"[1,8-10]. The incorporation of ϕ_s, the work function, in equation 6.1 allows for the "charging effect" to be assessed since it is a measure of the voltage between the spectrometer and the sample. Its value should be a constant, thus any variation could mean a change in the "electronic" state of the sample. In the case of non-conductive samples, any change in the work function will probably mean that the sample is being charged.

Although the X-ray photons can penetrate deeply into the sample, the electrons which escape without energy loss come from the outermost surface layers, (i.e. from within 2nm of the surface), since low energy electrons have short, mean free paths. Further, it is only those electrons ejected which do not lose energy by inelastic scattering on their passage to the surface which will appear in the kinetic energy spectrum at their original characteristic positions. The rest contribute to the discrete and continuum background at lower kinetic energy.

The energies of the core electrons of a particular atom are sufficiently invariant to provide a finger-print of the atom. When a photon extracts an electron from a core sub-shell, a "hole" is produced, and this stage normally decays by one or two mechanisms; X-ray fluorescence or an Auger process. These processes are presented schematically below[7]

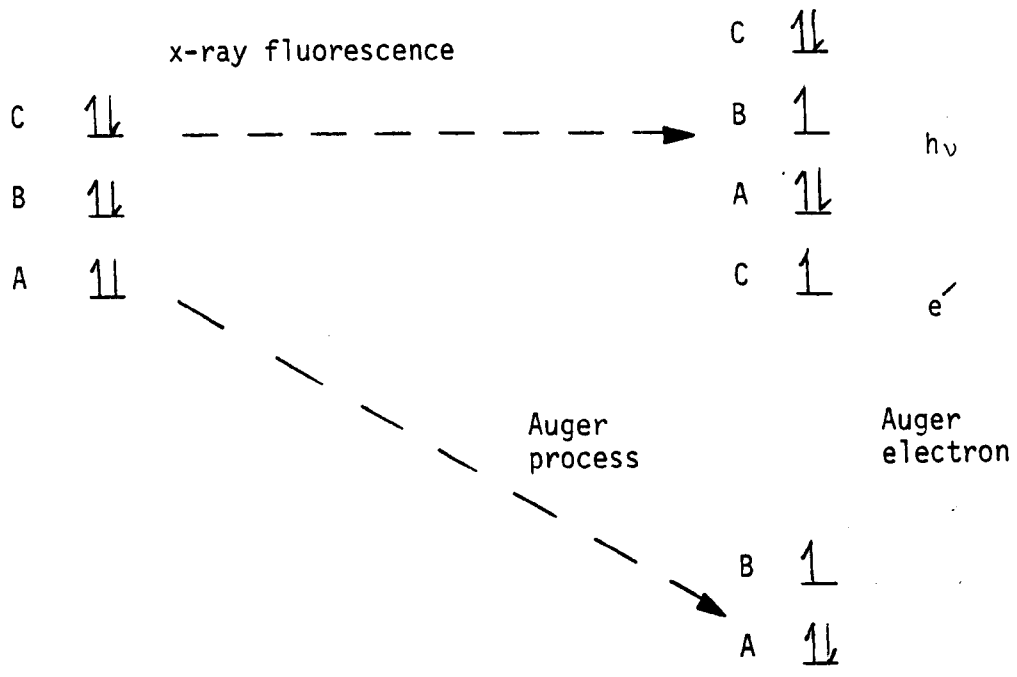

In both cases the vacancy in sub-shell A is filled by an electron from sub-shell B. The energy ΔE released may appear as a photon which usually belongs to the X-ray region. This is X-ray fluorescence. Alternatively, the excess energy may be dissipated by ionisation of an outer electron (from sub-shell C). This non-radiative mode of decay is the Auger Process, the secondary electron emitted being the Auger electron; the net result is a double ionisation.

The two relaxation processes (fluorescence and Auger) are competitive and their relative rates depend upon the atomic number of the element involved. High atomic numbers favour fluorescence, while Auger emission predominates with atoms of very low atomic numbers.

Most of the chemical information available from XPS is from the chemical shift data. There is a wealth of data now existing on the use of chemical shifts in XPS to investigate bonding both in the solid and gas phase[11,12].

6.2 Experimental Procedure

The XPS measurements were made on a Kratos ES300 spectrophotometer provided with a dual anode X-ray gun; either Mg Kα or Al Kα radiation may be used as the exciting radiation. The latter was used in the present work. The samples were placed on the sample probe by means of a double-sided adhesive tape and distributed over it as a very fine layer. The X-ray supply was run at 14kV and 10mA. The source slit and the collector slit were left unchanged during all the runs. With the sample holder in the spectrometer, the system was evacuated and when the vacuum was sufficiently low,1.33μPa, a broad scan of the electron energy spectrum on irradiation was taken. It was then followed by scans of each element of interest over a narrow eV range. The kinetic energy of the electron emitted from the sample was measured in the electron energy analyser and an electron multiplier was employed to count the electrons.

6.3 Results

6.3.1 Calculation of Oxidation States

From the electron spectrum, the binding energy of the carbon 1s state has been noted. This element is always present on the surface of a sample unless extremely careful precautions are taken, or unless the sample has been pretreated, (e.g. by argon ion etching). This peak has been used to correct for charging in the sample during irradiation which displaces peaks from their true positions. Elemental carbon should give rise to a C1s peak at 284.8eV but because of charging this peak may be found to vary in position. The magnitude of separation of the observed C1s peak from its true binding energy enabled a charging correction to be made to all other XPS peaks in the spectrum. The difference between the corrected binding energies and

the true elemental position of the peak, (as given in the table of X-ray adsorption data (2)), is an indication of the oxidation state of that particular element.

6.3.2 Experimental Results

X-ray photoelectron spectra of the elements detected on the surface of the different samples, (including W powder; WO_3; K_2WO_4; Na_2WO_4; 0.05KW; 0.2KW; 0.3KW; 0.6KW; 0.8KW; 0.05NaW; 0.2NaW; 0.3NaW; 0.6NaW and 0.8NaW), are shown in Figures 6.1 to 6.14. Appendix 3 gives the observed and corrected binding energies in eV for the element of interest such as W, K, Na and O found on the surface of the different samples found by ESCA.

6.3.3 W, WO_3, K_2WO_4 and Na_2WO_4 Samples

For the case of tungsten the spectrum of the 4f electrons were studied in all samples. The spectra of the W4f electrons in W, WO_3, K_2WO_4 and Na_2WO_4 are shown in Figure 6.15. For a single type of tungsten atom or ion there is a doublet, (with a separation of approximately 2eV), due to spin orbit-coupling[13]). The magnitude of the splitting and the relative line intensity is the same for both tungsten powder and WO_3. If only the $W4f_{7/2}$ line is considered a binding energy of 33.6eV was obtained for tungsten powder whereas for WO_3 a binding energy of 36.0eV was obtained. The chemical shift between WO_3 and W powder is thus 2.4eV but it must be noted that tungsten powder necessarily contains certain adsorbed oxygen species on its surface as shown in the spectrum, thus giving a slightly higher binding energy than the quoted value, (31.0eV (2)), for the zero-valent state. The measured binding energy for the $4f_{7/2}$ lines of K_2WO_4 (36.5eV) and Na_2WO_4 (36.5eV) is close to the value obtained for WO_3 (36.0eV) indicating that tungsten

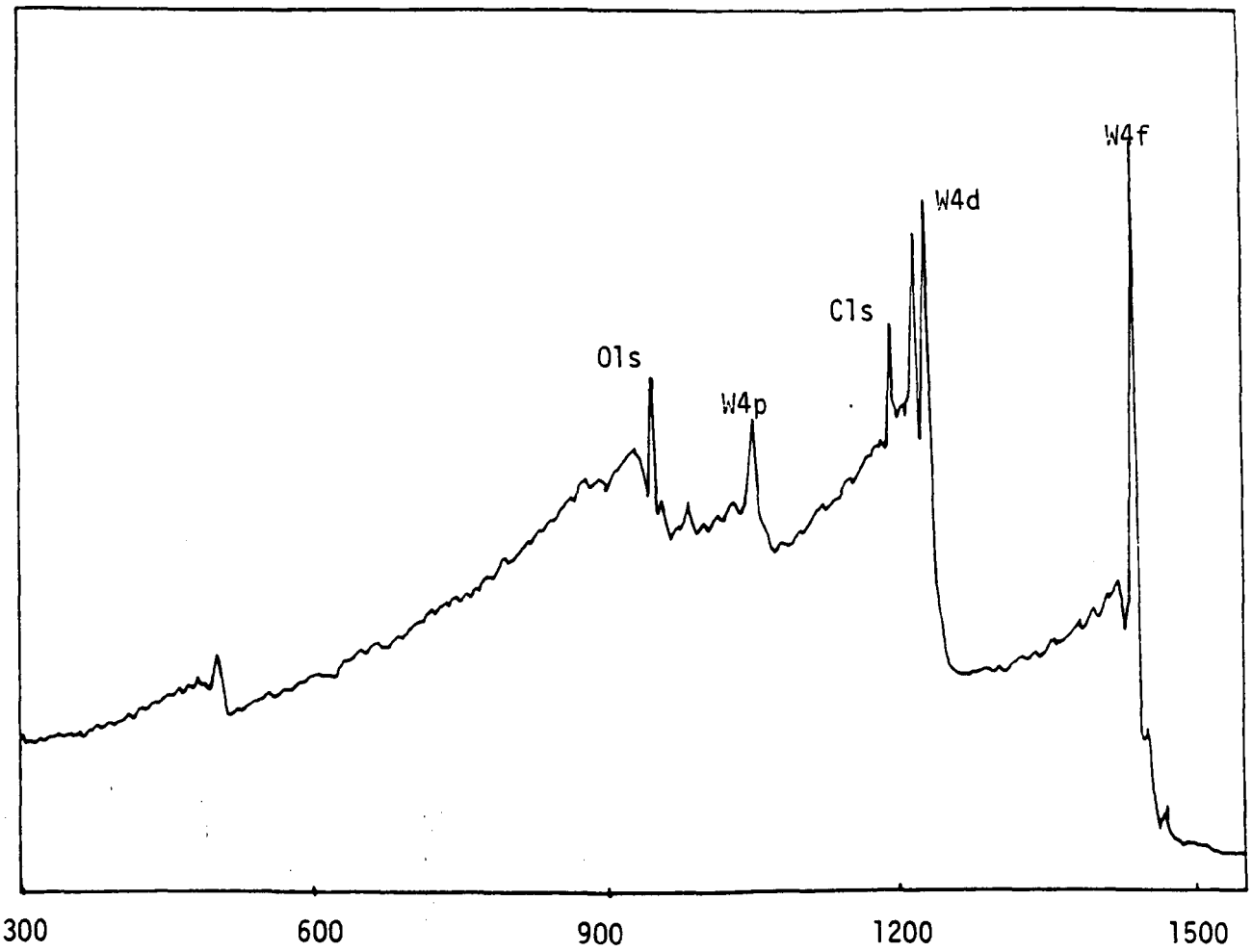

Figure 6.1 XPS of W powder

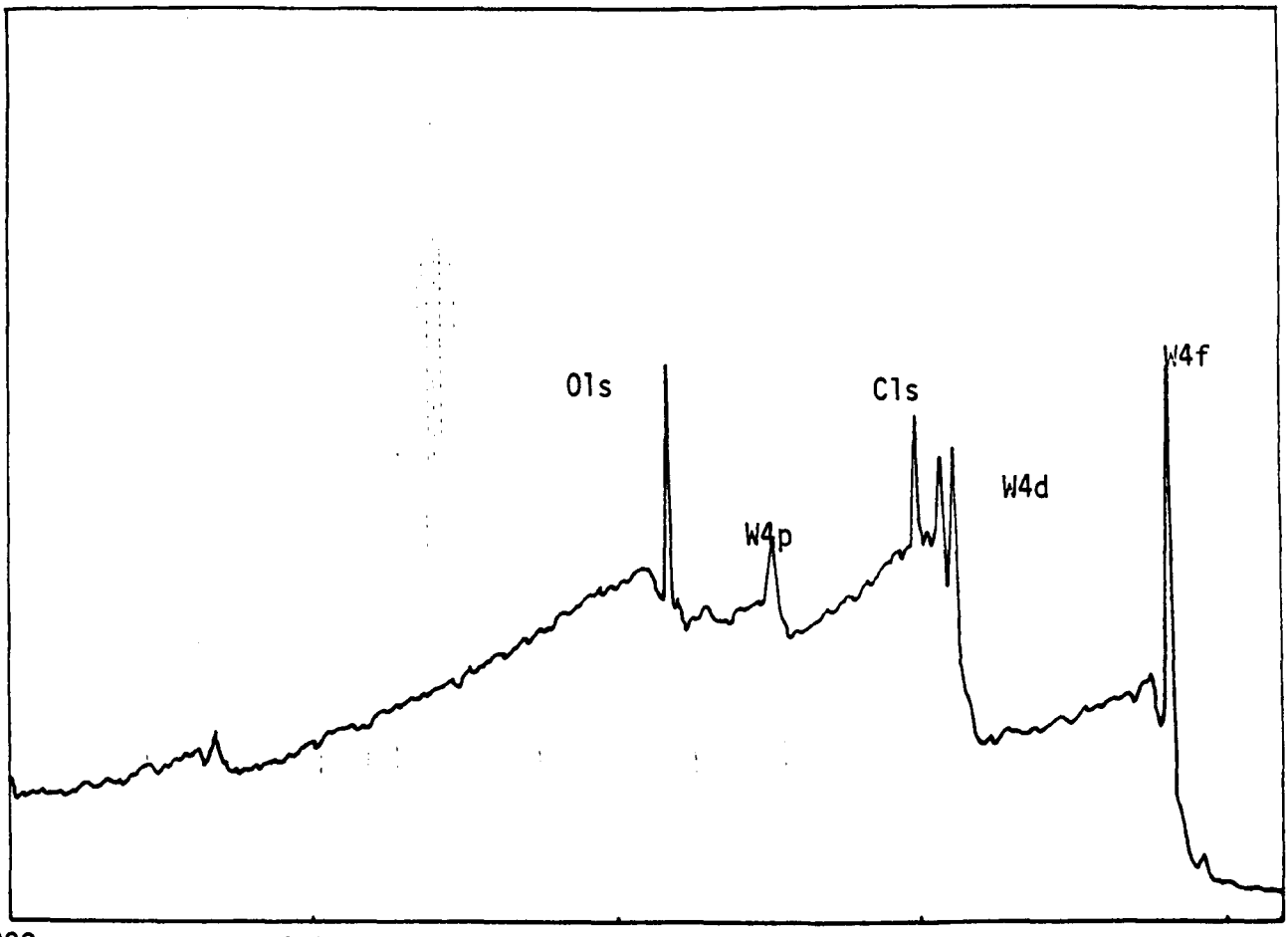

Figure 6.2 XPS of WO_3

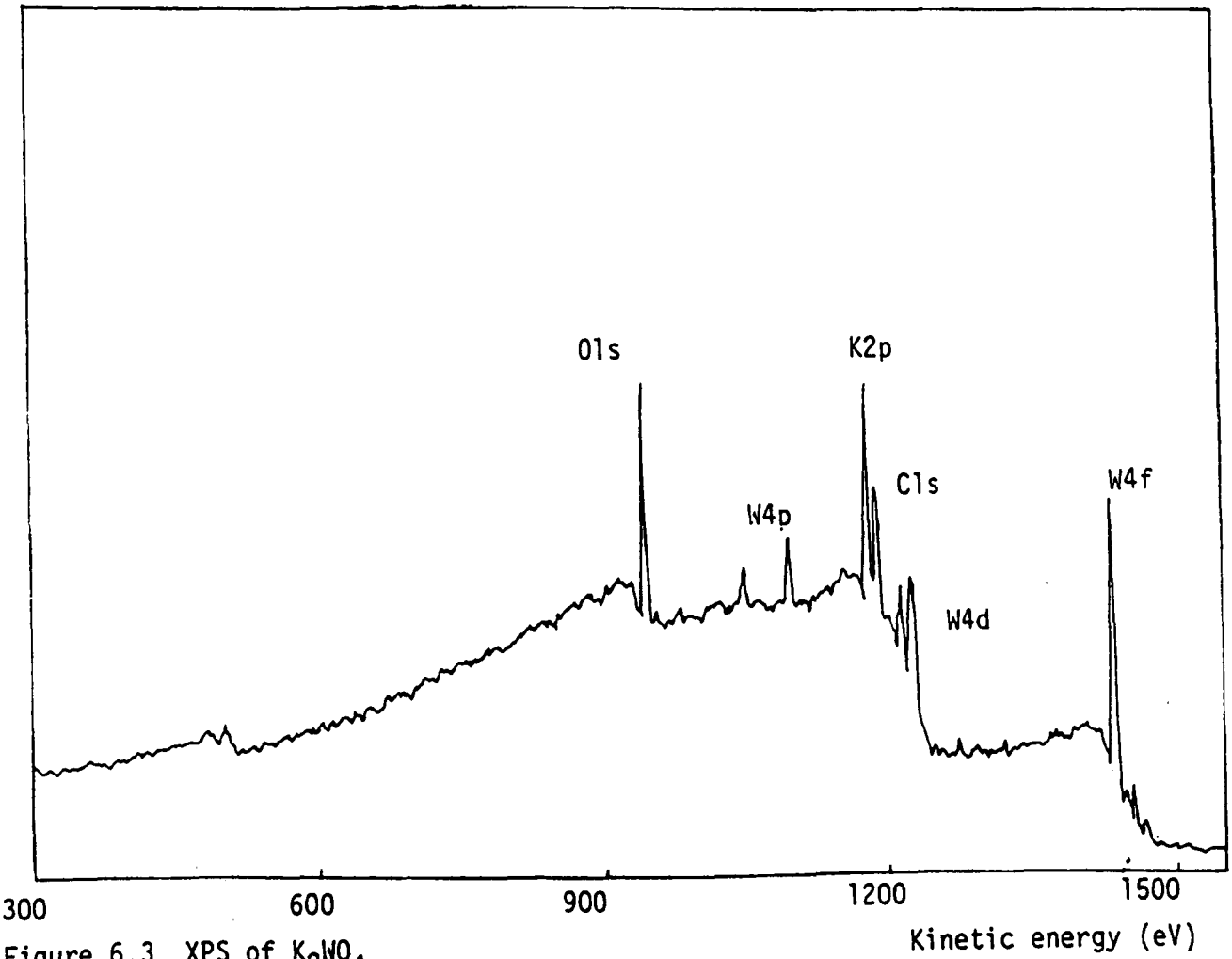

Figure 6.3 XPS of K_2WO_4

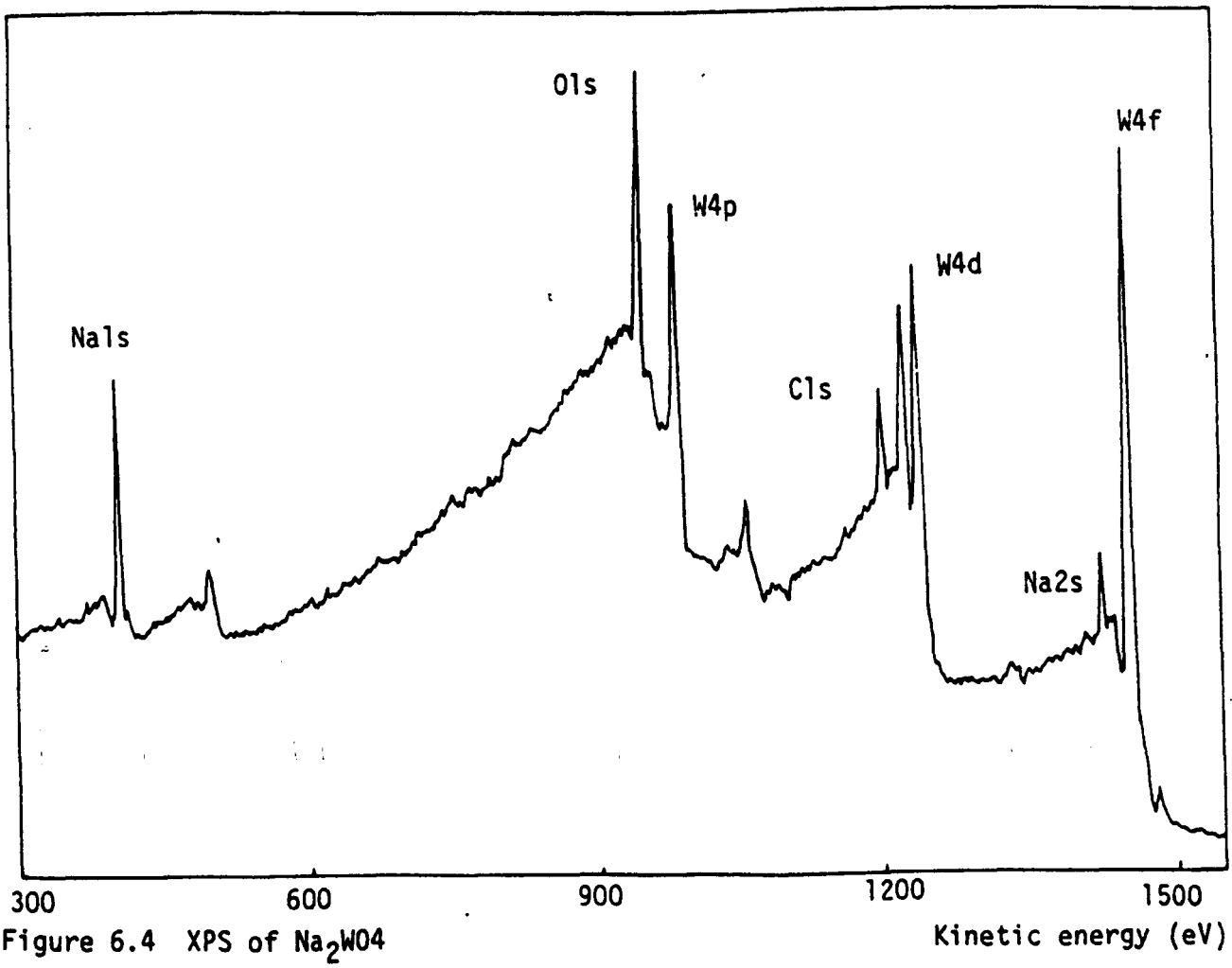

Figure 6.4 XPS of Na_2WO4

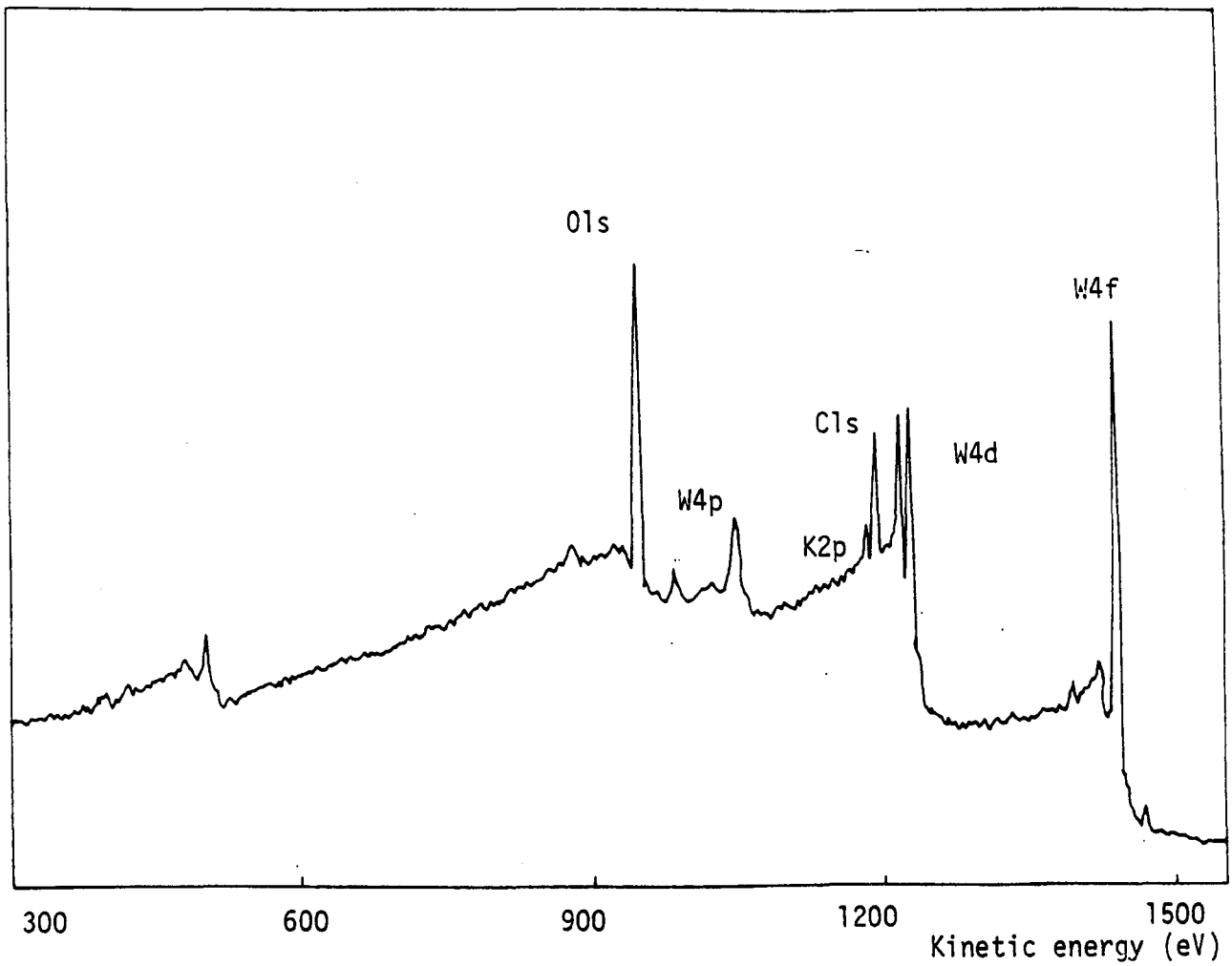

Figure 6.5 XPS of 0.05KW

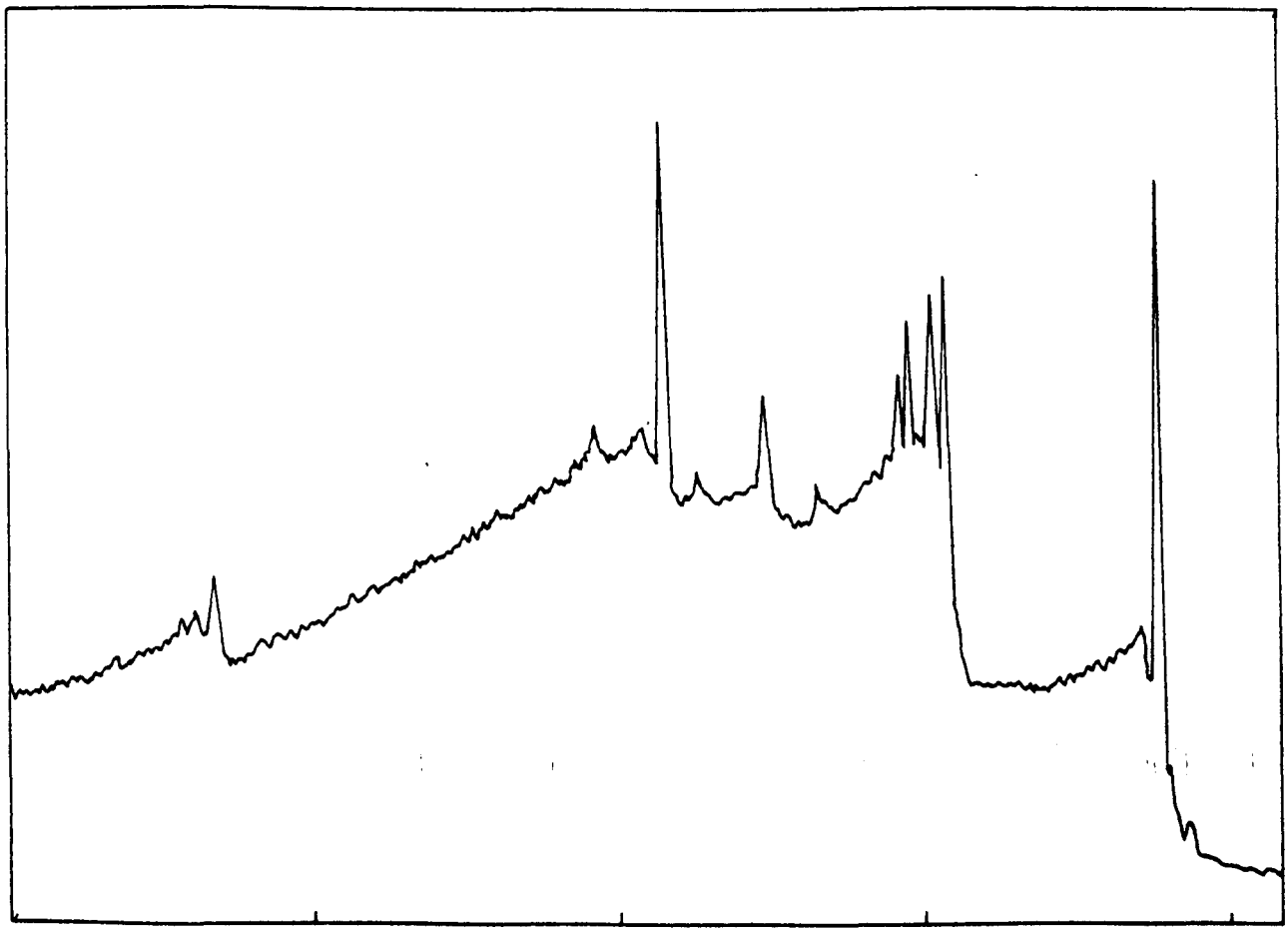

Figure 6.6 XPS of 0.2KW

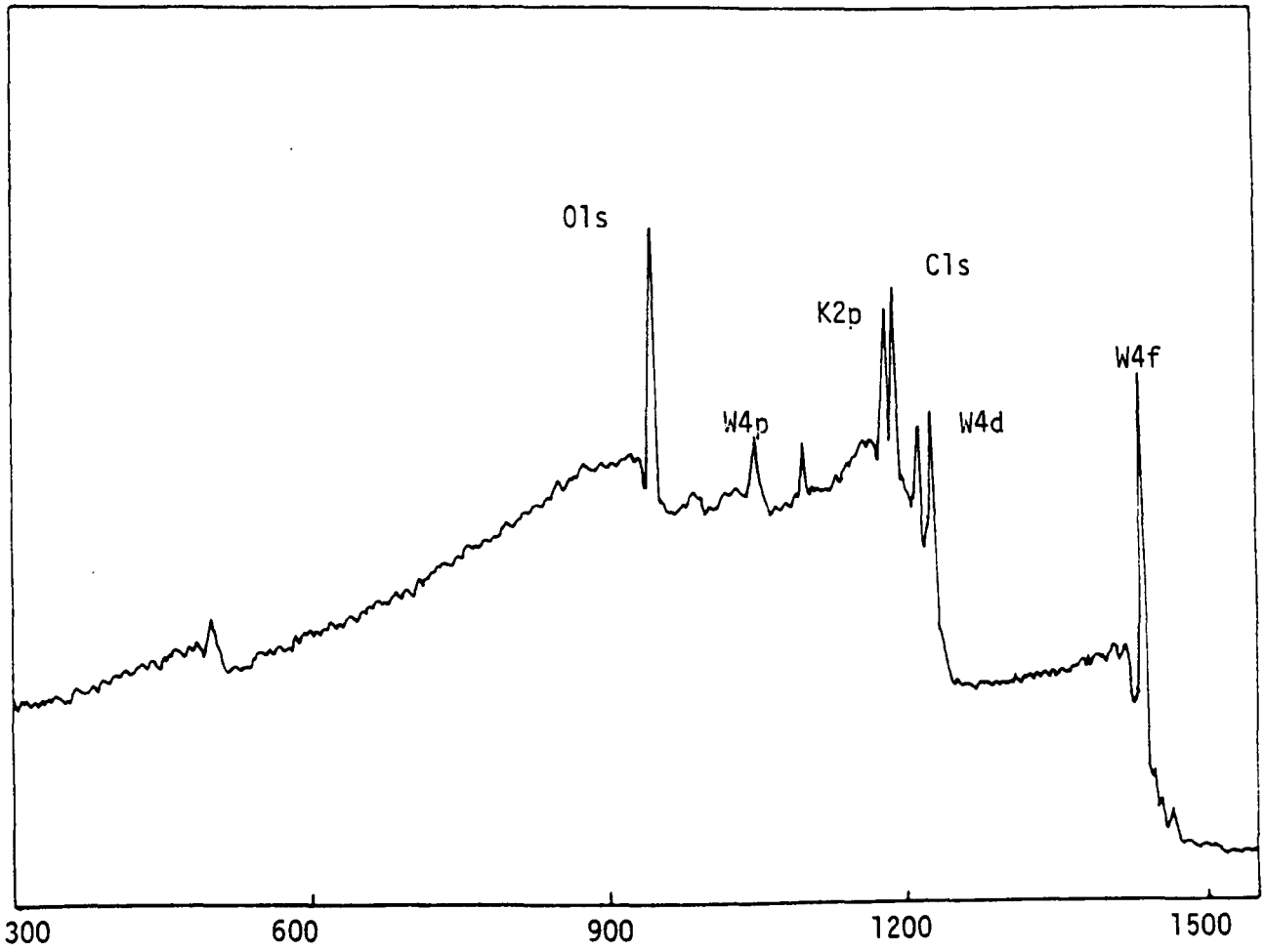

Figure 6.7 XPS of 0.3KW

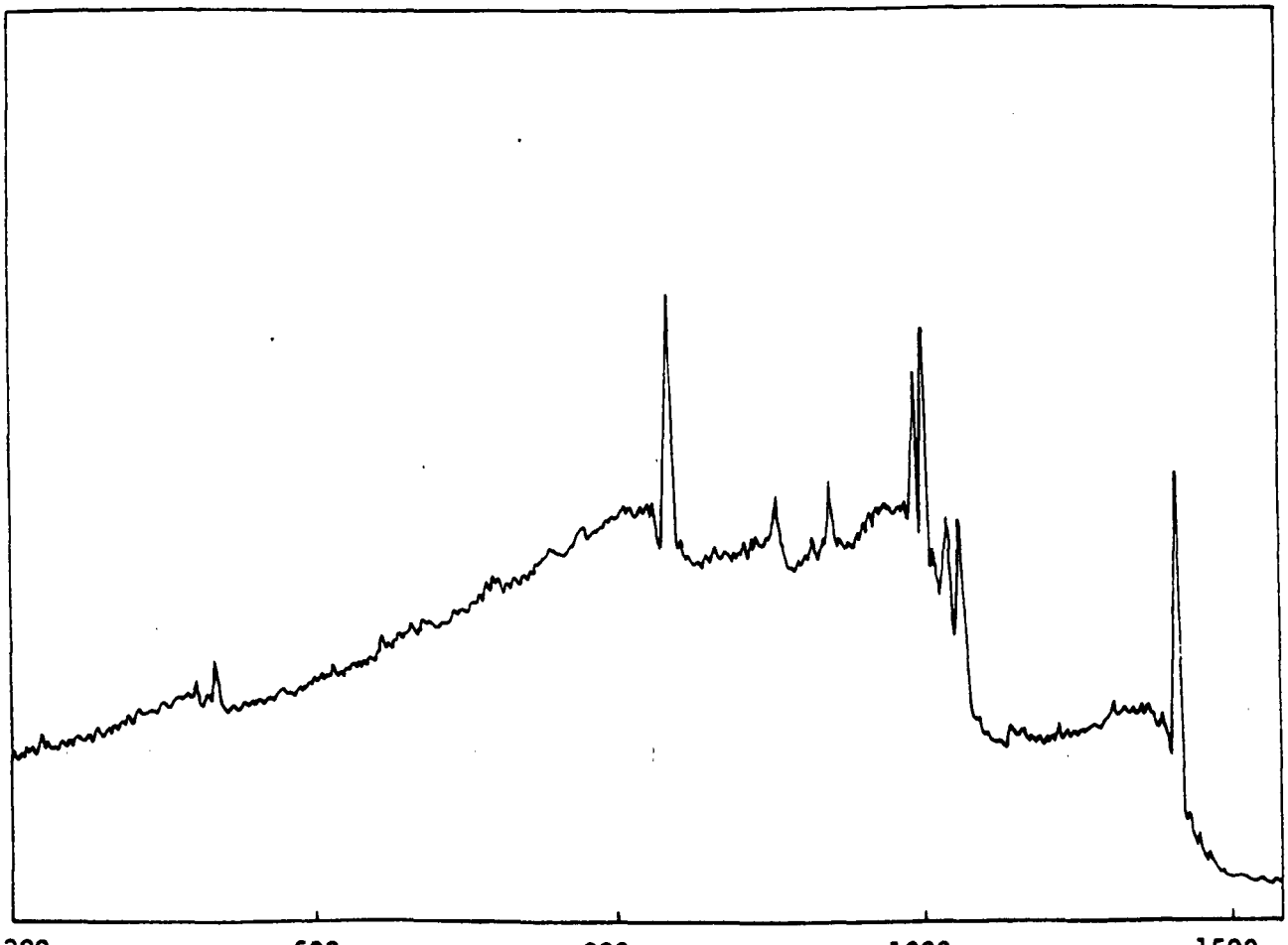

Figure 6.8 XPS of 0.6KW

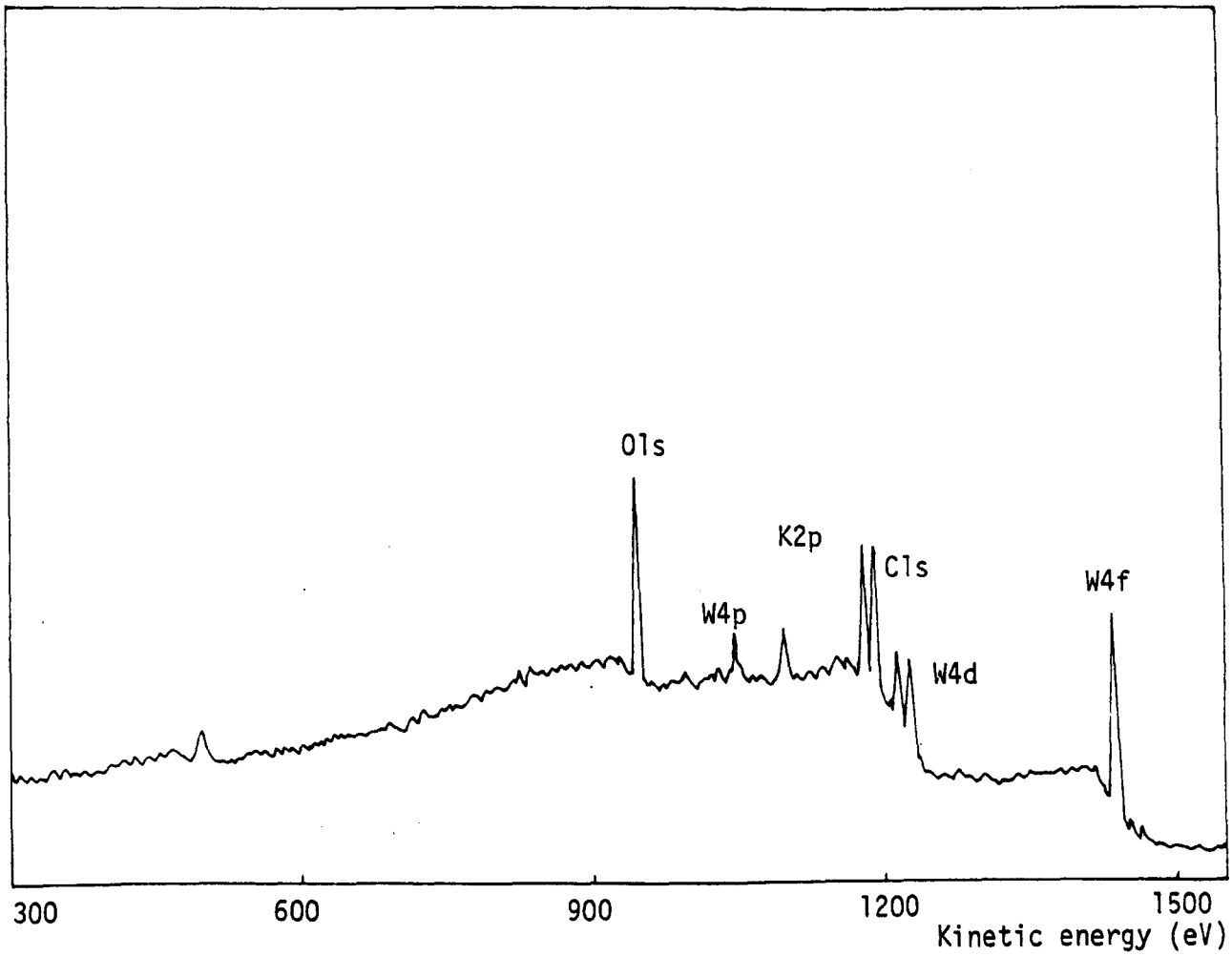

Figure 6.9 XPS of 0.8KW

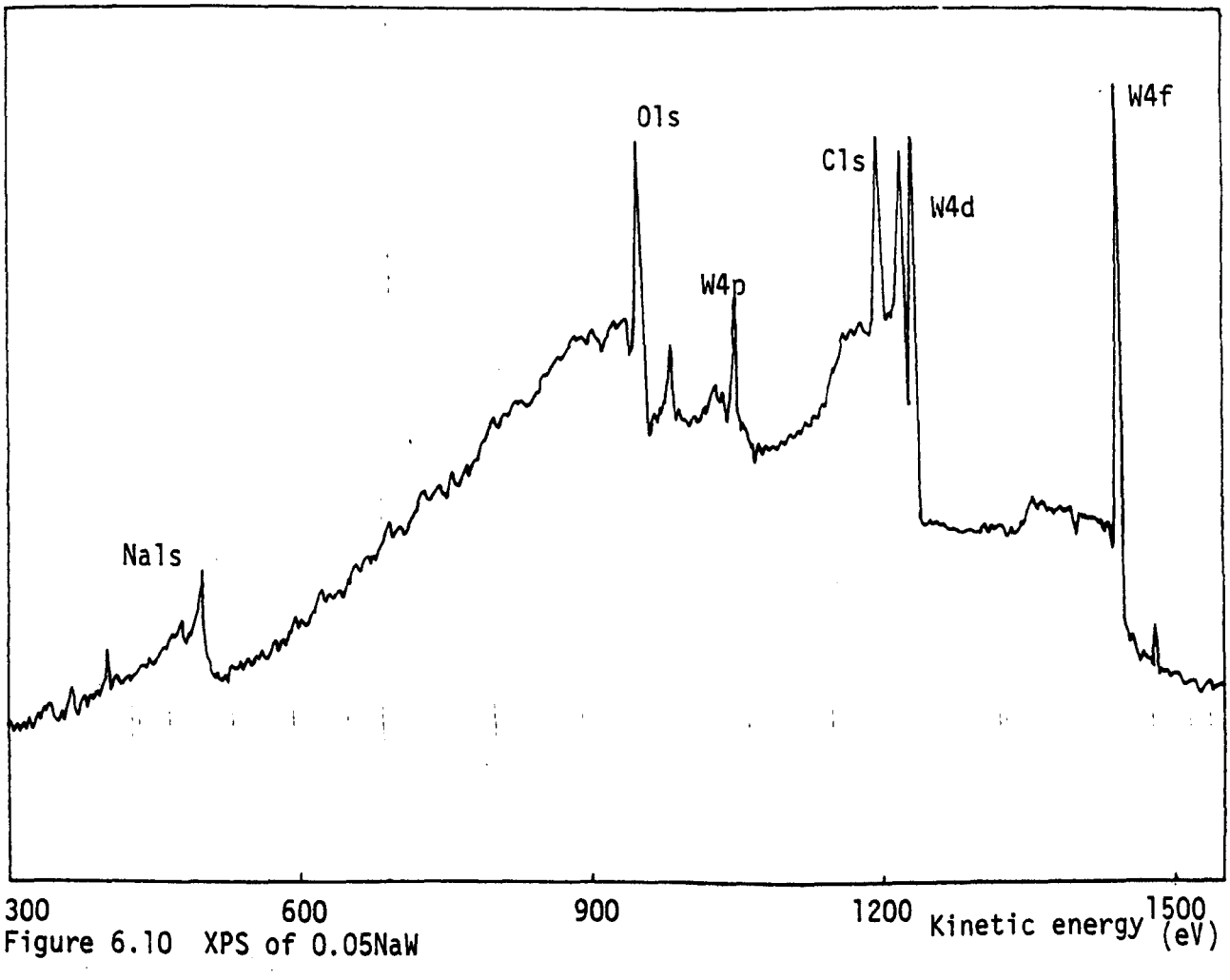

Figure 6.10 XPS of 0.05NaW

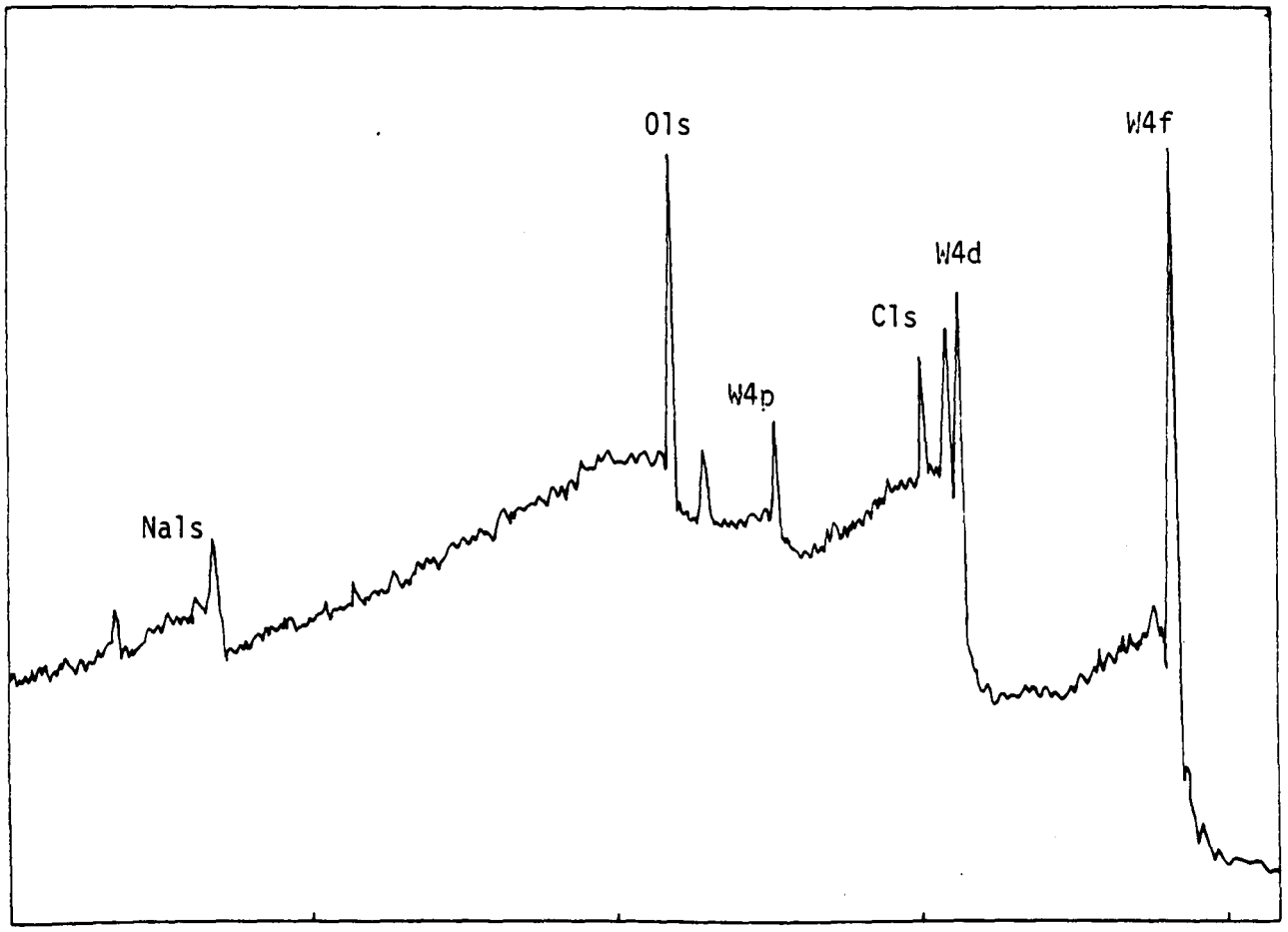

Figure 6.11 XPS of 0.2NaW

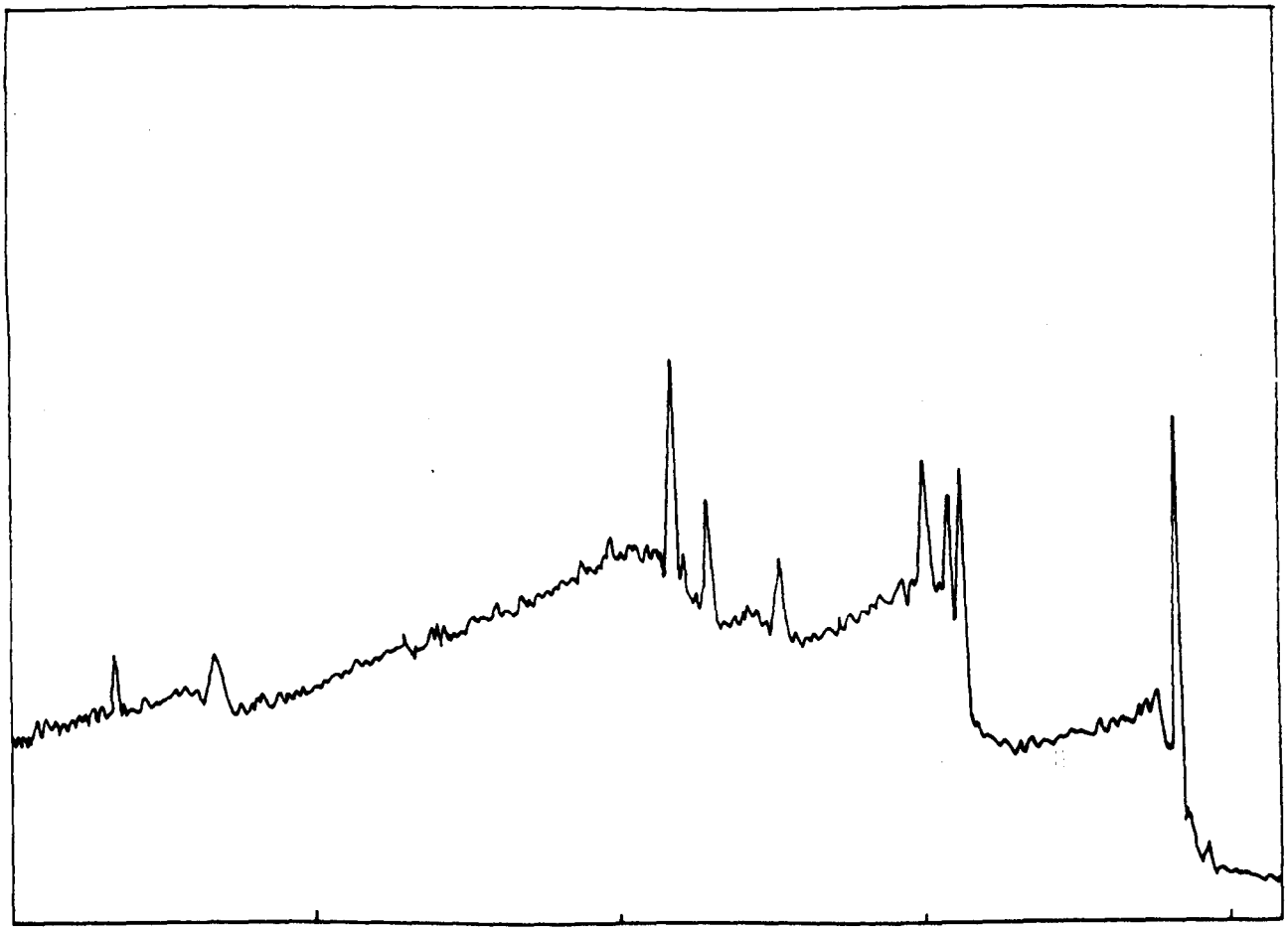

Figure 6.12 XPS of 0.3NaW

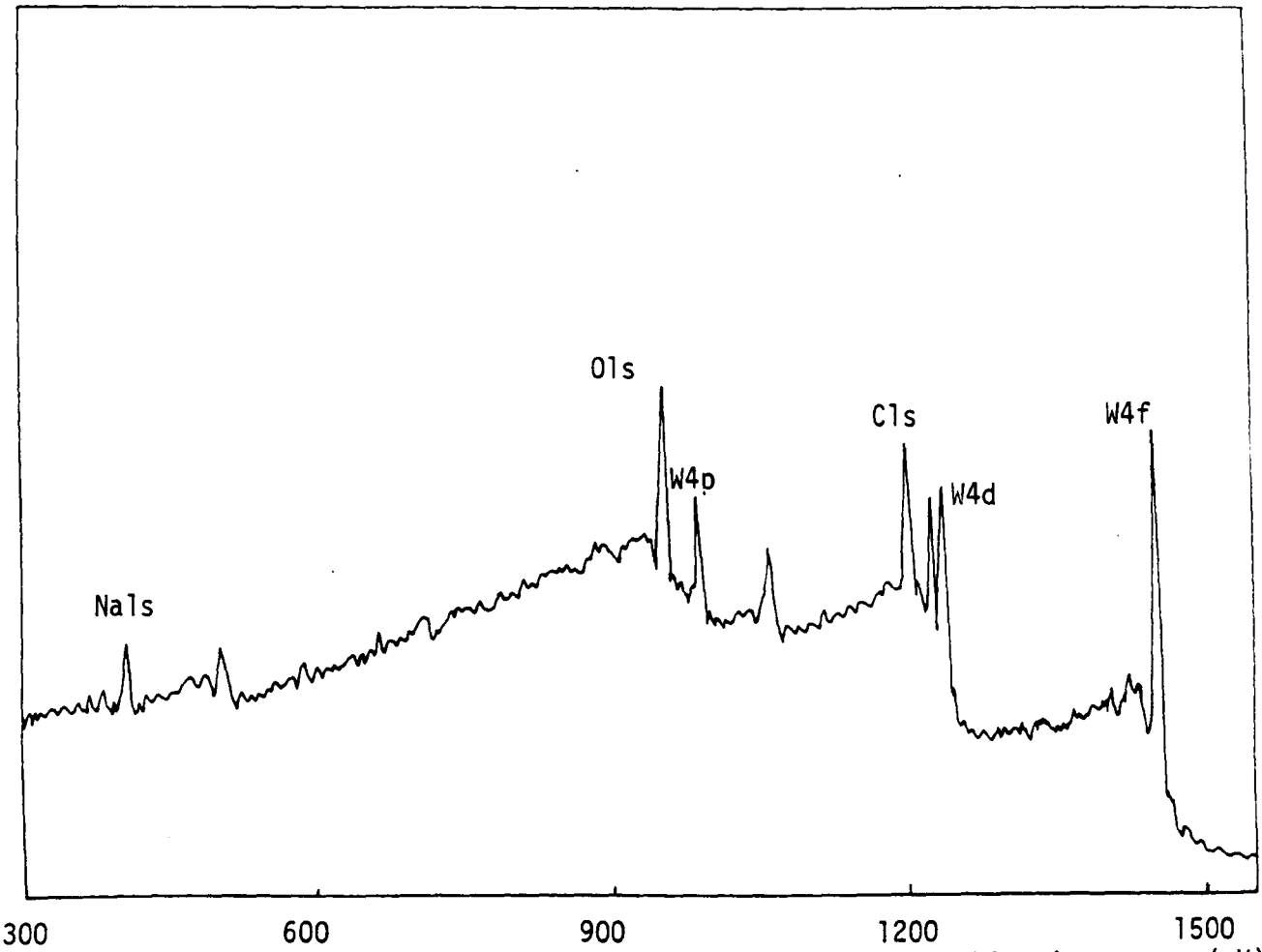

Figure 6.13 XPS of 0.6NaW

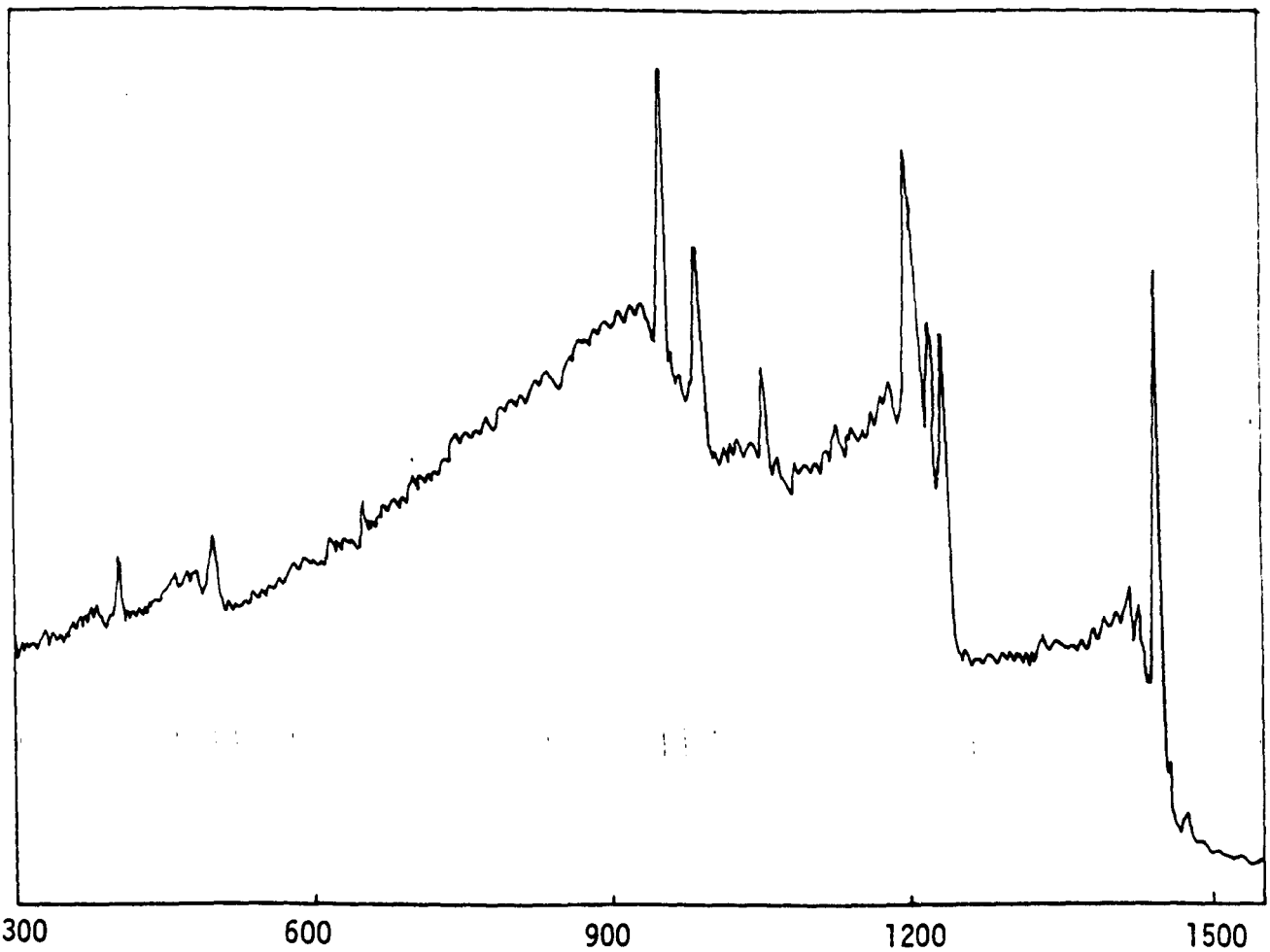

Figure 6.14 XPS of 0.8NaW

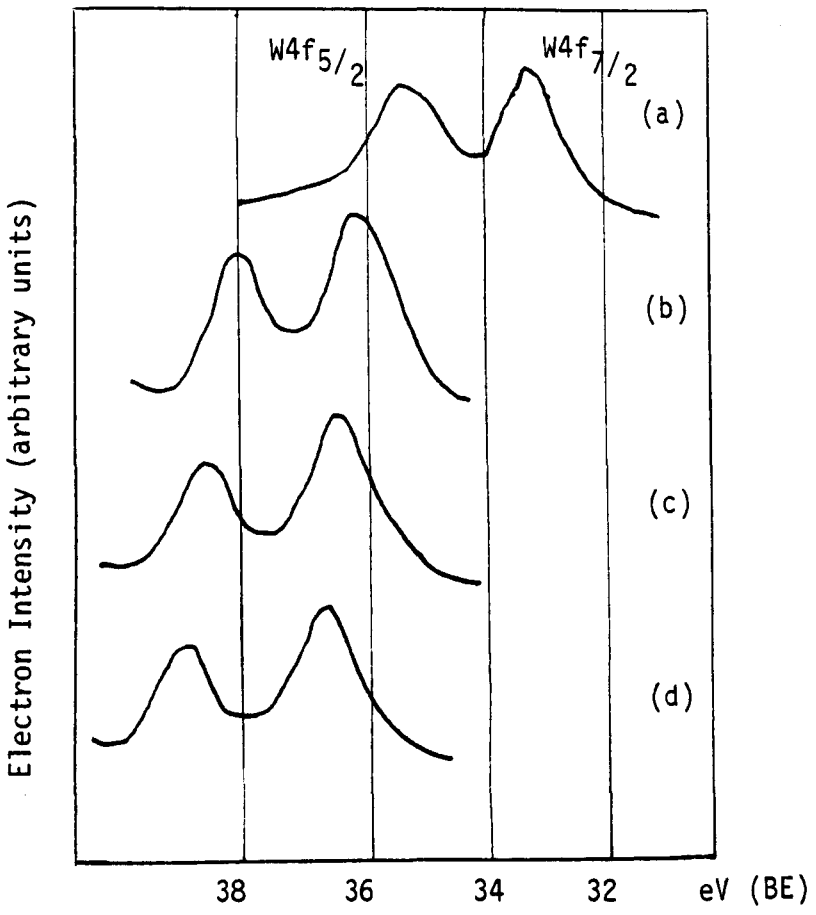

Figure 6.15 (a) W powder, (b) WO_3, (c) K_2WO_4, (d) Na_2WO_4

is present in the +6 oxidation state in both samples. The binding energies of the K2p and Nals peaks agree well with literature values for compounds of potassium and sodium.

6.3.4 Potassium and Sodium Tungsten Bronze Samples

In all the bronze samples a shift of the W4f peak to a lower binding energy was observed. Deduction of the oxidation state of W from the absolute binding energy of this peak is difficult, however, it can be determined from the spectra that W is present in the +5 and +6 oxidation states. Both the K2p and Nals peaks in the bronze samples show no evident change in binding energy compared to those of K_2WO_4

and Na_2WO_4.

A quantitative estimation of the relative ratio of tungsten to alkali metal ion in the bronzes has been attempted. This was carried out by comparing the peak areas of the W4d and K2p peaks for the potassium bronzes and the W4f and Nals peak for the sodium bronzes. The W4d peak was chosen for the potassium bronzes because of overlapping between the W4f and K3S peak. A quantitative examination of the spectra shows that the ratio of the tungsten peak to the oxygen peak is almost constant in most bronzes whilst the intensity of the K2p peak and Nals peak increases with increasing alkali ion concentration. The method of quantification used was that of peak areas and in cases where there is a doublet, e.g. W4f, the total peak area was estimated. The peak areas were calculated using a graphics tablet, Apple II computer and suitable software, with an accuracy of ±10 - 20%. These values were then divided by a sensitivity factor, which for different elemental peaks is listed in Appendix 3. The corrected peak areas for the alkali ion were normalised with respect to the tungsten peak thus giving a relative ratio of the two elements present. The relative peak intensities together with the calculated ratio are given in Appendix 3. The calculated ratio of the alkali ion to tungsten shows reasonable agreement in most cases to the bulk atomic ratio of these elements as defined by the preparation. It would appear that there is no tendency of any particular element to enrich the surface of these bronzes.

6.4 Conclusions

The relative chemical shift characteristic of W has helped facilitate determination of the nature of the tungsten species present

in both the potassium and the sodium bronzes. In all the samples, tungsten was observed to be in an oxidation state of +5. In complex ternary materials such as the potassium or sodium bronzes there is the possibility that the chemical composition close to the surface differs from that of the bulk. In particular, one can envisage surface Na or K depletion or enrichment without major structural upheaval. Quantitative examination of the X-ray photoelectron spectra of the bronze samples has shown that the surface of these samples is essentially a termination of the bulk structure with no pronounced segregation or depletion of K or Na.

CHAPTER 6

REFERENCES

1. D. Briggs and M.P. Seah, 'Practical Surface Analysis by Auger and X-ray Photoelectron Spectroscopy', J. Willey and Sons, (1983).
2. D. Briggs, 'Handbook of X-ray and Ultraviolet Photoelectron Spectroscopy', Heyden and Sons Ltd., (1978).
3. J.C. Vedrine in 'Surface Properties and Catalysis by Non-Metals', O. Reidel Publishing Company,(1983).
4. T. Edmonds in 'Characterisation of Catalysis', Ed. J.M. Thomas and R.M. Lambert, J. Willey and Sons, (1980).
5. S. Hufner, Freuenius Z. Anal, Chem., 291, 97, (1978).
6. Kh. M. Minachev, G.V. Antoshin and E.S.Shapiro, Russ. Chem. Rev., 47, 2097, (1978).
7. C.R. Brundle and A.D. Baker, 'Electron Spectroscopy : Theory Techniques and Applications', 1, (1977).
8. A. Cimino, B.A. de Angelio, J. Catal., 36, 11, (1975).
9. P. Ascarelli and G. Missoni, Discuss. Faraday, Soc., 54, 298, (1972).
10. J.L. Ogilrie and A. Wolberg, App. Spect., 26, 401, (1972).
11. K. Siegbahn, Nova. Acta. R. Soc. Upp., 20, 200 (1967).
12. D.C. Frost and F.G. Herring, Chem. Phys. Lett., 13, 391, (1972).
13. 'ESCA', Atomic, Molecular and Solid-State Structure Studied by means of Electron Spectroscopy, Ed. K. Siegbahn, Almquist and Wiksells, Uppsala, (1967).

CHAPTER 7

ELECTRICAL RESISTIVITY

7.1 Introduction

Electrical conductivity is the movement of electric charge from one location to another. Since the charge may be carried by ions or electrons whose mobility varies in different materials there is a full spectrum of conductivities ranging from highly conducting metals to nearly perfect insulators. Usually conduction by one or the other type of charge carrier predominates, but in some inorganic materials both ionic and electronic conduction are appreciable in the same material. The logarithim of specific conductivity, $\log \sigma_i$ $(\text{ohm cm})^{-1}$ for ionic solids has values which vary between -14 and -18 for crystals and -3 to +1 for solid electrolytes and for electronic conductors $\log \sigma_e$ has values of

<-12	insulators
-5 to +2	semiconductors
+1 to +5	metals

In ionic conductivity, the carriers may be either negative or positive ions. In electronic conductivity the carriers are electrons or electron 'holes'. The charge per electron is 1.6×10^{-19} coulomb. Since ions contain either a deficiency or an excess of electrons, the charge per ion is an integral multiple of 1.6×10^{-19} coulomb. This charge is accelerated as it moves in one direction in the electric field and decelerated as it reverses its direction. Conductivity, σ, may be expressed as a product of (1) the number of charge carriers, n, in a material, (2) the charge, q, carried by each and (3) the mobility, μ, of the carriers. That is,

$$\sigma = n q \mu \qquad \ldots\ldots\ldots\ldots\ldots\ldots 7.1$$

The mobility of a carrier is its net velocity per unit voltage gradient.

Ionic conductivity in solids is due to the migration of ions from one lattice site to another. The probability of such movement is low in most ionic and covalently bonded solids such as oxides and halides. Rather, the atoms tend to be essentially fixed on their lattice sites and can only move via crystal defects. Only at high temperature where the defect concentrations may become quite large and the atoms have a lot of thermal energy does ionic conductivity become appreciable. If the ion moves with the electric field it is accelerated and receives more energy as it vibrates in the favourable direction of the electric field. Conversly it is decelerated as it moves in the unfavourable direction. The result is net ion movement in one direction which gives ionic conductivity. The ionic conductivities in solids are naturally low because there is only a very low probability that the energy will be available for its movement. However, there exists a small group of solids called solid electrolytes or fast ionic conductors in which one of the sets of ions can move quite easily. Such materials often have rather special crystal structures in which there are open tunnels or layers through which the mobile ions may move.

Electronic conductivity arises by the long range migration of electrons. In metals, valence electrons are not anchored to any specific atom and thus their energy permits them to move among the atoms in all directions with equal velocity. This model was first postulated in 1900 by Drude[1] who proposed that these valence electrons move "freely" between the ion cores, which were assumed to be spherically symmetrical positive charges at rest in a fixed lattice. In this "free electron gas" model, an applied electric field ε, accelerates the "electron gas" in a given direction. This motion is opposed by a

viscous drag effect arising from collisions with the lattice cations resulting in a net movement of electrons towards the positive holes. In ionically and covalently bonded materials, the electrons are not free to leave their host atoms and therefore are poor electronic conductors; these materials can be classified either as semiconductors or insulators depending on the energy requirement for movement of an electron from its low energy position so that it may transport a charge. The main difference between metals, semiconductors and insulators is the magnitude of their conductivity as given previously; but whereas the conductivity of most semiconductors and insulators increases rapidly with increasing temperature, that of metals shows a gradual decrease. The reason for this can be found by considering equation (7.1). For all electronic conductors q is a constant independent of temperature and the mobility term is similar in most materials in that it usually decreases slightly with increasing temperature. However, for most metals, n is large and essentially unchanged with temperature, the decrease in μ causes a decrease in σ. In semiconductors and insulators n usually increases exponentially with temperature which causes a net increase in σ.

The free electron theory was later developed into the Band theory which was applied to explain the electrical conductivity in metals, insulators and semiconductors. When atoms approach one another to form solids, the sharp atomic energy levels spread into wide allowed energy bands which are separated by forbidden gaps. This band formation is marked for the valence electrons and negligible for the inner 'core' electrons. The picture of the electronic structure of a metal given by this theory is as follows. A solid metal can be considered to possess bands of electrons which are separated from each other by energy gaps. Further, these bands can be completely filled with localised electrons, or partially filled with free electrons whose molecular orbitals extend over

all the atoms in the crystal. In metals such as sodium there are unfilled orbitals lying very close to the uppermost filled level, the Fermi level, and so it requires exceptionally little energy to excite the uppermost - energy electrons. (See Figure 7.1(a)). The electrons are therefore very mobile, and their mobility is reflected in the ability of the metal to conduct electricity when small potential differences are applied. Electrical conductivity of metals is therefore a property characteristic of partially filled bands of orbitals. Insulators, on the other hand, have a full valence band, separated by a large forbidden gap from the next empty energy band (conduction band) (see Figure 7.1(b)), thus very few electrons from the upper valence band states have sufficient energy to overcome the forbidden gap, hence the electrical conductivity is negligible. In some materials there is a small gap between the filled band and an empty band, Figure 7.1(c). If some of the electrons could be excited into the upper band, the holes in the lower band and the electrons in the upper band could move through the lattice. This is called semiconductivity. It can be brought about in several ways. For example, thermal excitation might generate enough of these carriers. A higher temperature implies more carriers, and so the conductivity increases with temperature. Another way of forming carriers is to introduce impurities in an otherwise ultrapure material. If these impurities can trap electrons they withdraw electrons from the full band, leaving holes which permit conduction : this is p-type semiconductivity (p indicating the introduction of holes which are positive relative to the negatively charged electrons filling the band). Alternatively, the impurity might carry excess electrons (e.g. phosphorus atoms introduced into geranium) and these electrons swim in the otherwise empty bands, giving n-type semiconductivity (where n donates negatively charged carriers).

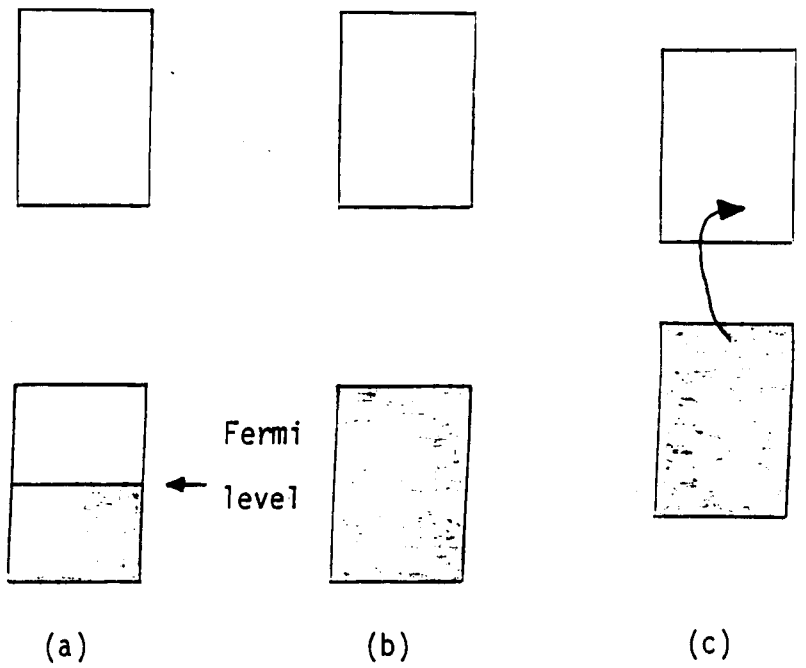

Figure 7.1 Band filling leads to (a) metal, (b) insulator, and (c) semiconductor

7.2 Experimental Procedure

Resistivity-conductivity measurements on the polycrystalline bronzes in air were carried out in a Pyrex cell and using Be-Al alloy electrodes. The sample (about 0.2-0.5g) was first pressed into a disc using a hydraulic press at a pressure of 10,000kg. The disc was enveloped with aluminium foil and then held between two stainless-steel plates to which the electrodes were connected. The electrodes and disc were held in place in the Pyrex cell using springs, as shown in Figure 7.2. Dc resistances were measured using an ohm meter (with an accuracy of 0.05%) and were then converted to dc resistivities ($\rho = Ra/t$) in ohm.cm (where a and t are the cross-sectional area and thickness of the sample, measured using a micrometer with an accuracy of ± 0.05%. If σ_i is significant then dc-resistance measurements are

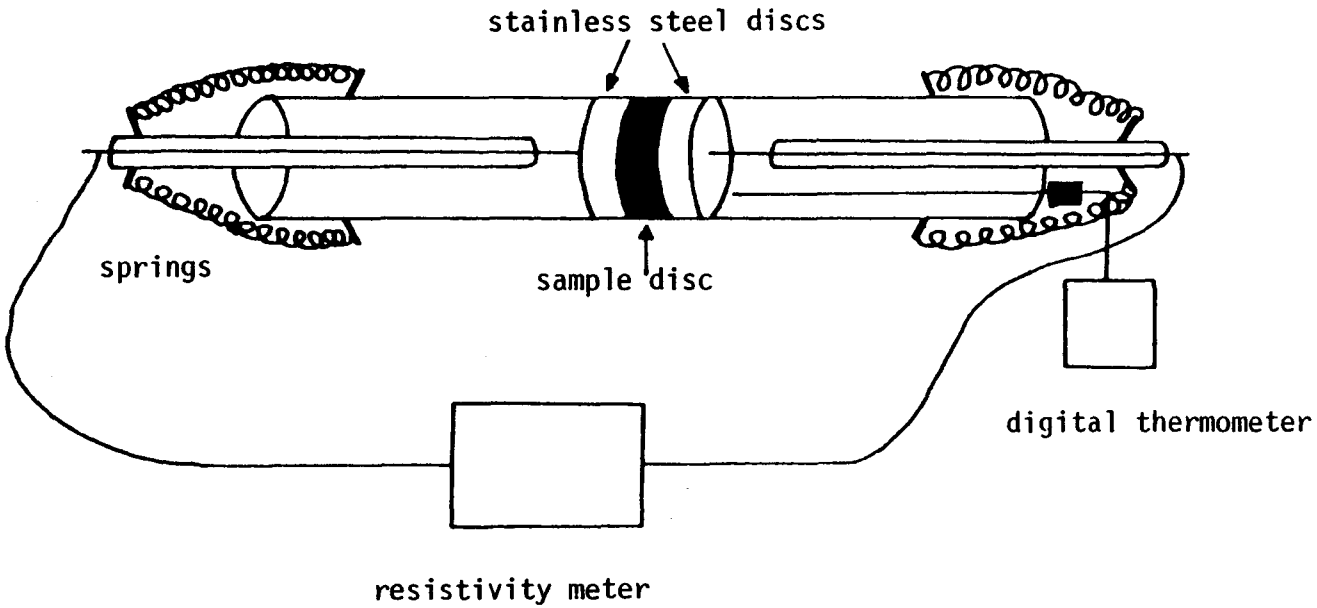

Figure 7.2. Apparatus for electrical resistivity measurement

likely to lead to polarisation at the sample/electrode interface resulting in anomalously high resistivity values being obtained. Ac modes of measurement were used to overcome polarisation effects and thus to give a clear picture of the composite electronic and ionic conductivity of these bronze materials. In the ac mode V = IZ where Z is impedance (a complex function of resistance R and capacitance C, i.e. Z = R + jC.). For a series circuit impedance Z is given by $\sqrt{(R^2 + X_c^2)}$ where X_c is the capacitive-reactance or $1/Z\Pi FC$ where F is the ac test frequency (here 1000 Hz). The ac capacitance was determined using the multimeter connected to a 1μF shunt. A programmable heating coil enables measurements to be carried out in air at known temperatures between 298K and 395K. In ac mode ρ is given by Za/t.

7.3 Electrical Resistivity Results

The a.c. and d.c. electrical resistivities of the Na and K tungsten bronzes have been measured in the temperature range 298 - 395K. For sodium and potassium tungstates and WO_2 only the a.c. resistivities were measured. The d.c. and a.c. resistivities of the sodium bronzes are plotted as a function of temperature and are shown in Figures 7.3 and 7.4 respectively. The character of the resistivity-temperature plots indicates that the principle conduction mechanism in the sodium rich bronzes ($x > 0.2$) is different from that found in bronzes with lower sodium content, the former exhibiting typically metallic electrical properties and samples with $x \leq 0.2$ behaving more like semiconductors. The carriers are electrons at all sodium concentrations. Figures 7.5 and 7.6 show the d.c. and a.c. resistivities of the potassium bronzes in the temperature range 298 - 373K. The shape of the resistivity - temperature curve for $K_{0.05}WO_3$ suggests semiconducting behaviour, while those with higher potassium content show properties of metallic conduction.

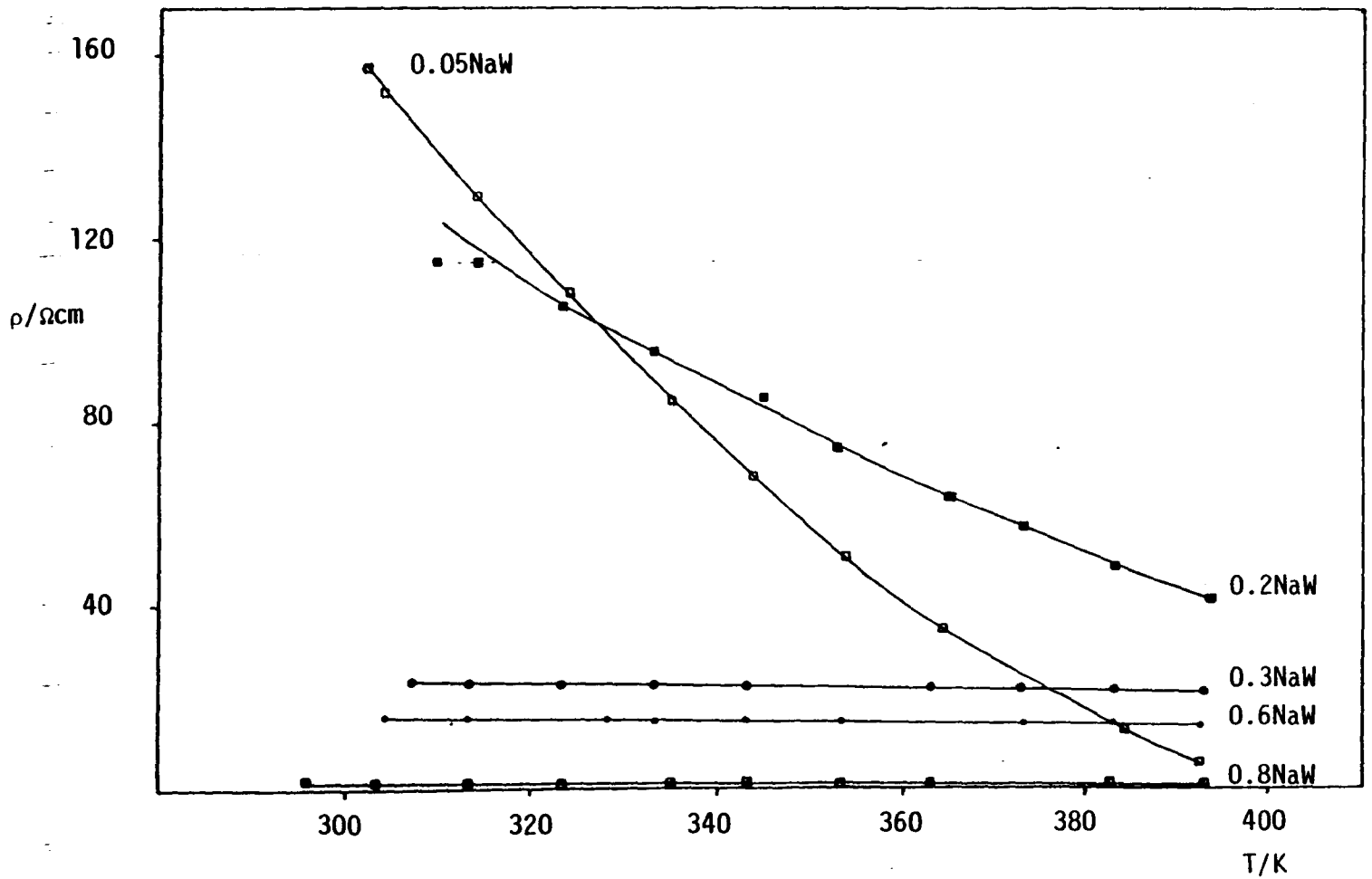

Figure 7.3 d.c. resistivity versus temperature for Na_xWO_3

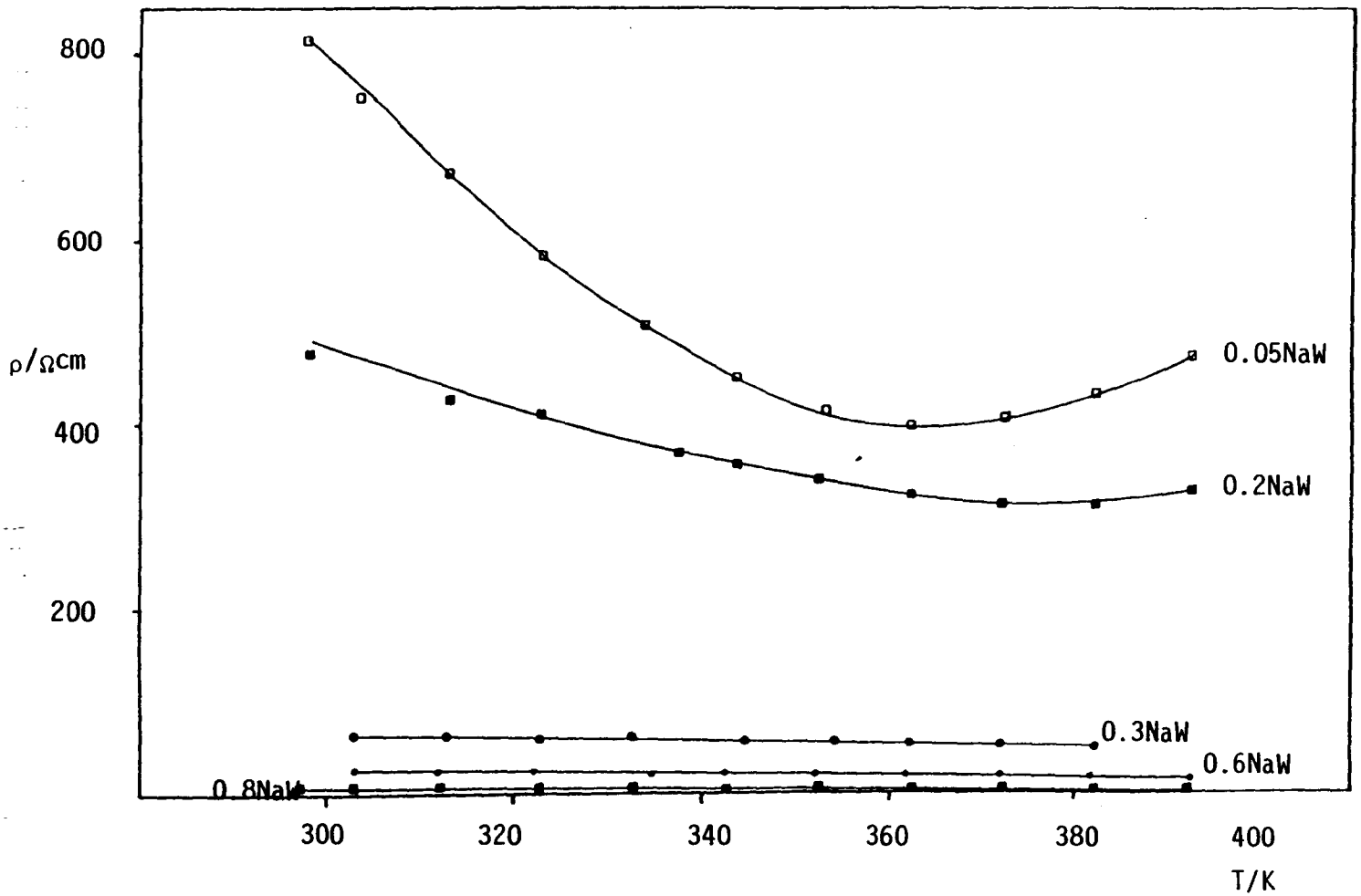

Figure 7.4 a.c. resistivity versus temperature for Na_xWO_3

The d.c. resistivity of WO_3 as a function of temperature is given in Figure 7.5 and shows conductivity characteristic of a semiconductor. Figure 7.7 shows the a.c. resistivity values at 298K of the polycrystalline sodium and potassium bronzes as a function of the number of alkali metal ions inserted. It is evident that the electrical resistivity decreases with increasing value of x. A similar observation has been made for single crystals of these bronzes but however, it should be noted that the absolute resistivities are very different as a result of the physical properties of the bronzes. (It appears that at a given value of x the resistivity increases only slightly as the inserted ion is changed from Na^+ to K^+). The a.c. resistivities of Na_2WO_4, K_2WO_4 and WO_3 as a function of temperature between 293K and 373K are shown in Figure 7.8. Clearly, in all cases the resistivity decreases as a function of temperature. However, the absolute resistivity of the bronzes is about 10^6 times lower than for the tungstates, but only slightly smaller than for the lower oxide of tungsten. The sodium and potassium tungstates have resistivity values characteristic of insulators.

Values of the a.c. resistivity measured at different temperatures were used to calculate the activation energy for electrical conduction. Goodenough[2] has indicated that plots of $\ln (T/\rho)$ versus T^{-1} have a slope of $-E_i/86.29$ μeV, and that for fast ionic conduction in solids $E_i \leq 0.2$eV. Figure 7.9 shows these plots for the tungstates, WO_3 and the lower oxide of tungsten. Such plots show good linearity over the entire temperature range and this suggests no dramatic change in gradient involving a change in the mode of conduction. Table 7.1 gives the values of the activation energies for conduction for the lower oxide of tungsten, WO_2, K_2WO_4 and Na_2WO_4. Figures 7.10 and 7.11 show plots of $\ln (T/\rho)$ versus T^{-1} for the Na and K bronzes respectively.

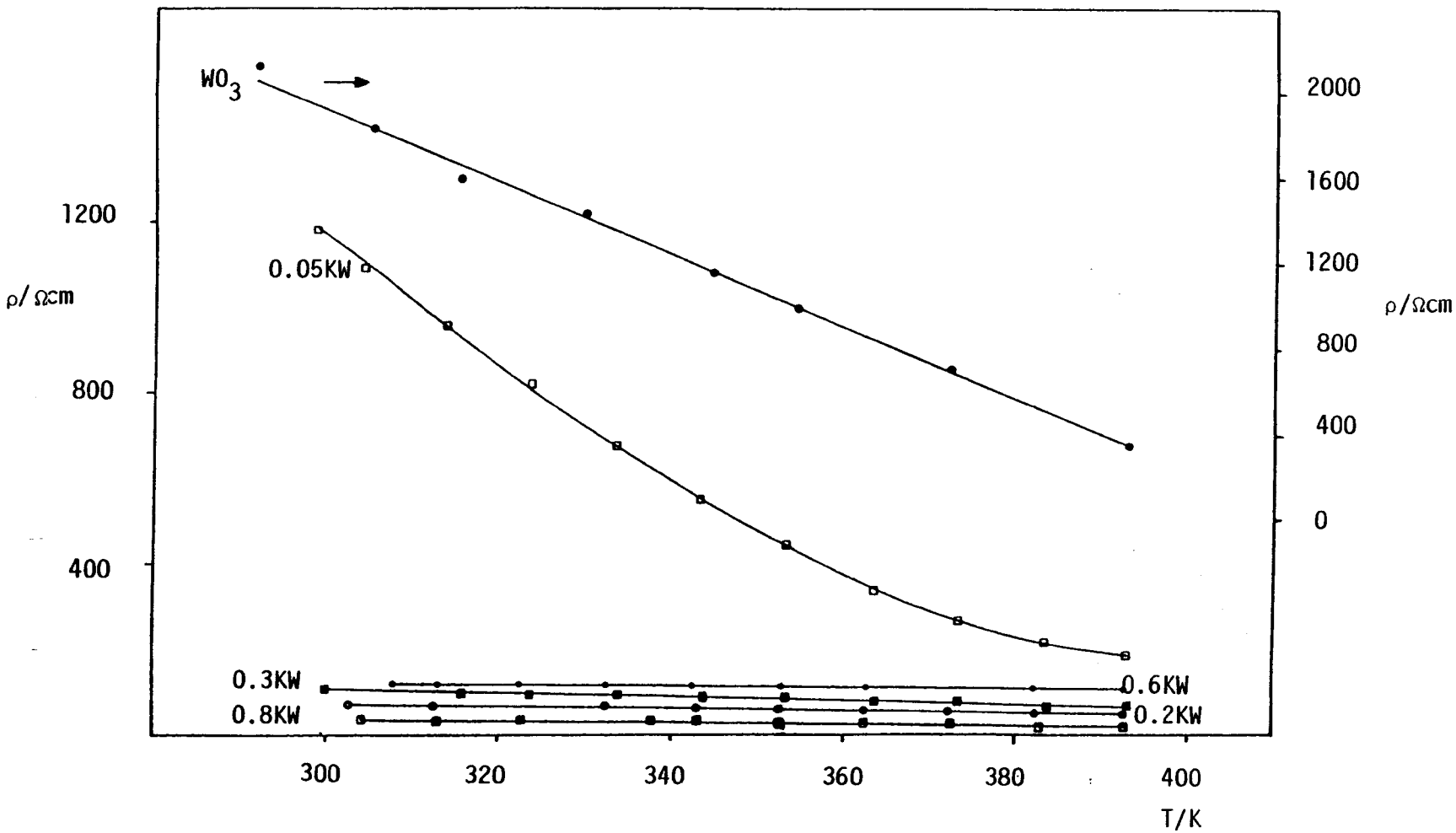

Figure 7.5 d.c. resistivity versus temperature for K_xWO_3 and WO_3

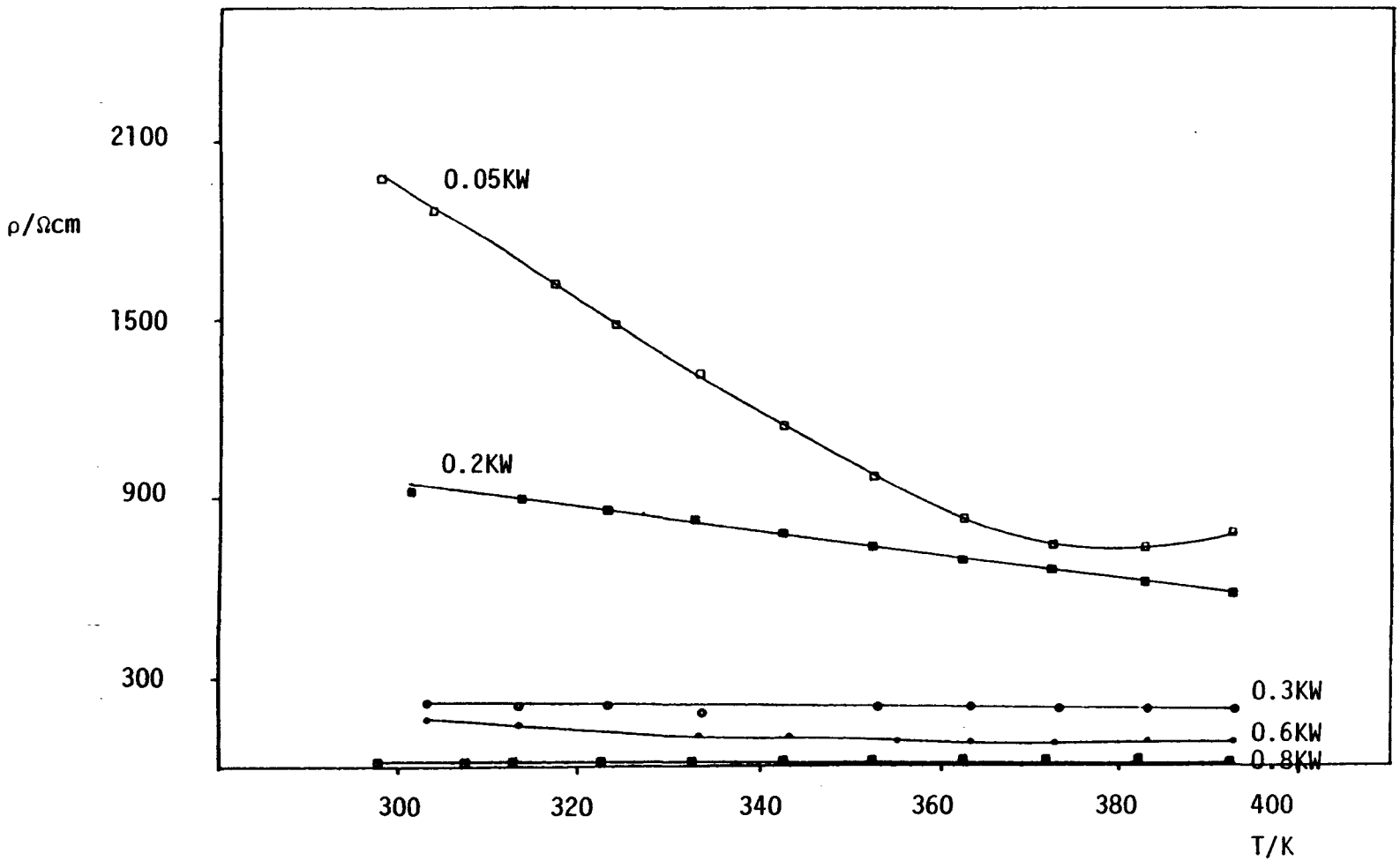

Figure 7.6 a.c. resistivity versus temperature for K_xWO_3

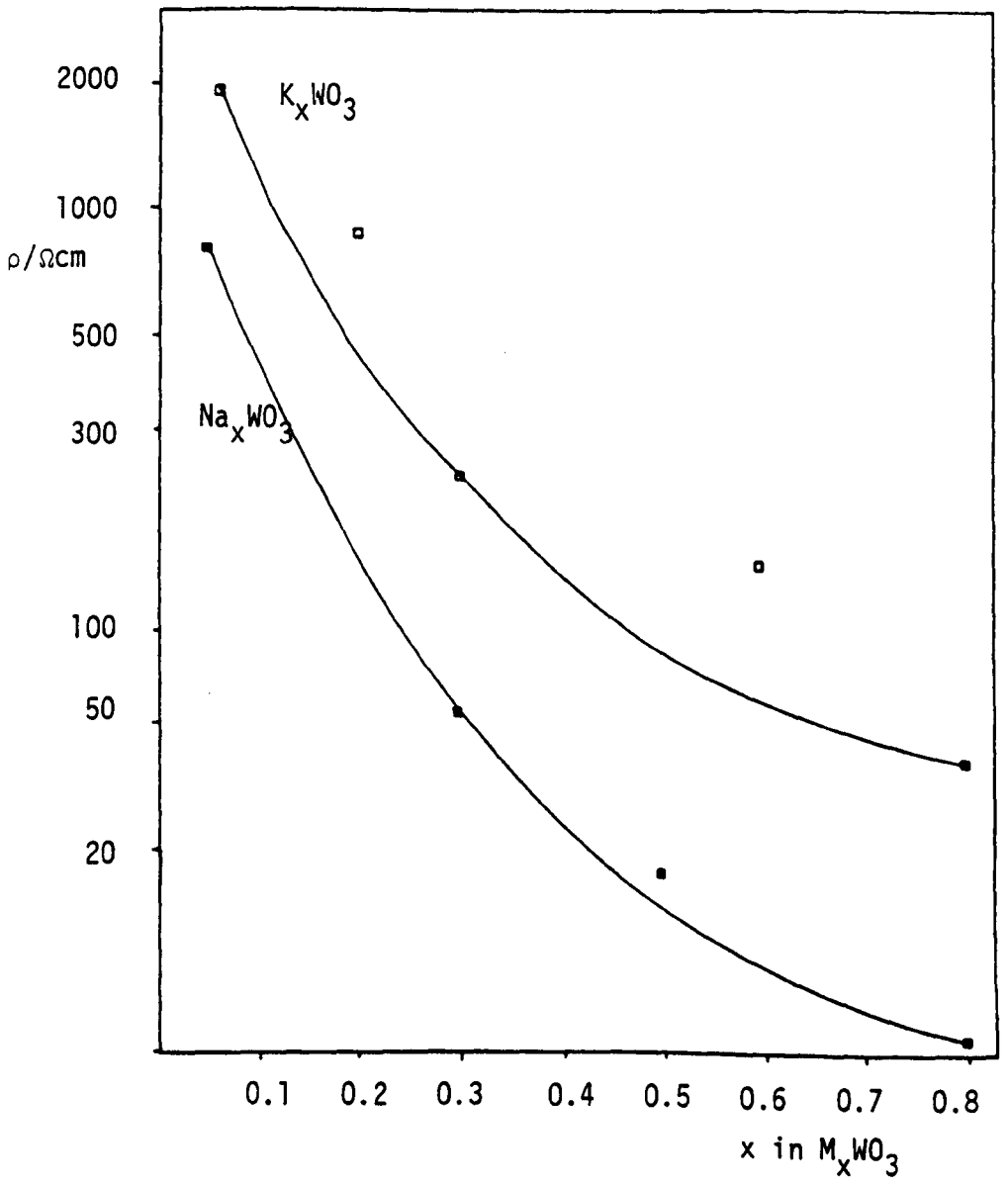

Figure 7.7 a.c resistivity values at 298K versus x in M_xWO_3

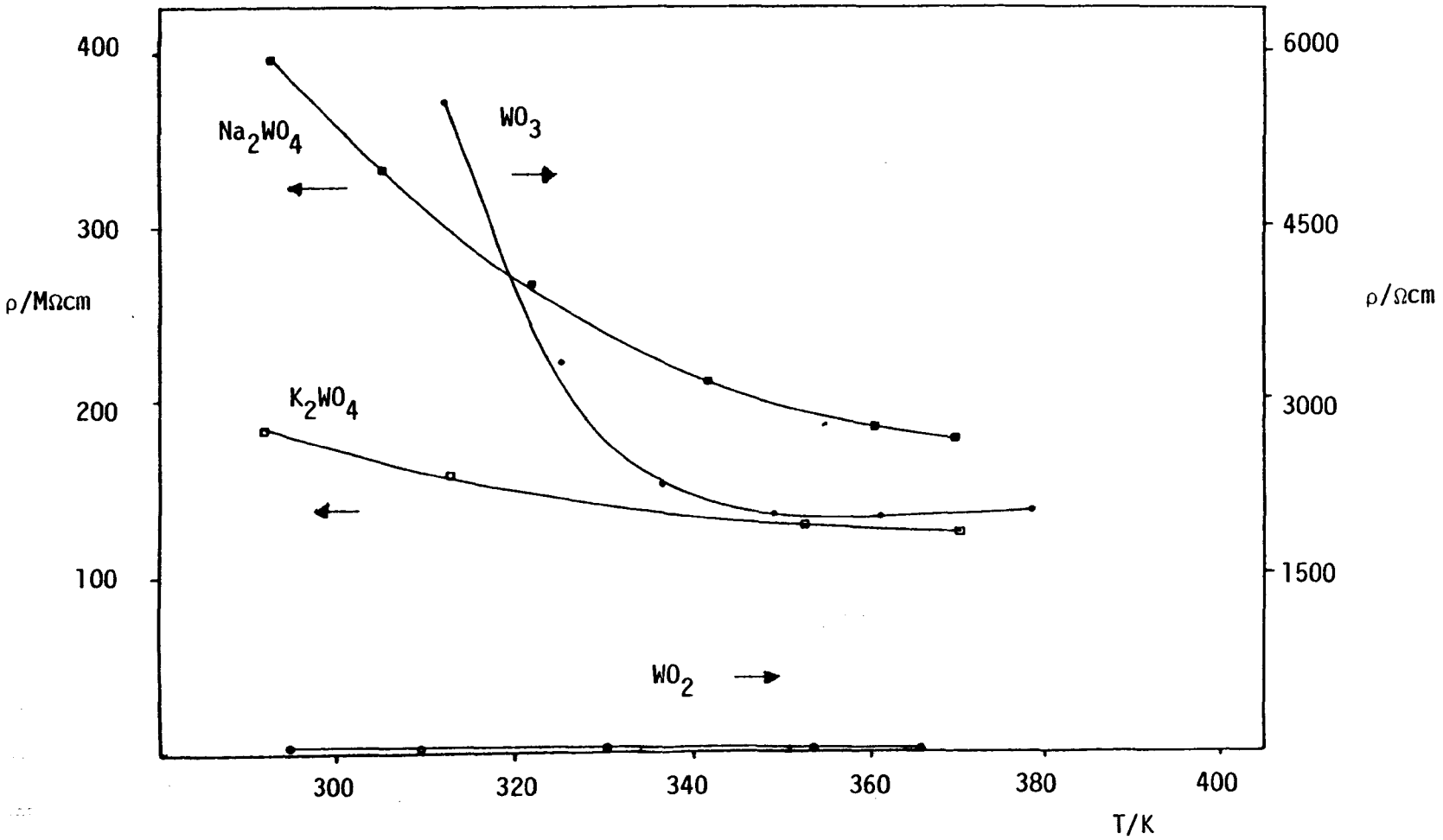

Figure 7.8 a.c. resistivity values for tungstates, WO_3 and WO_2 versus temperature

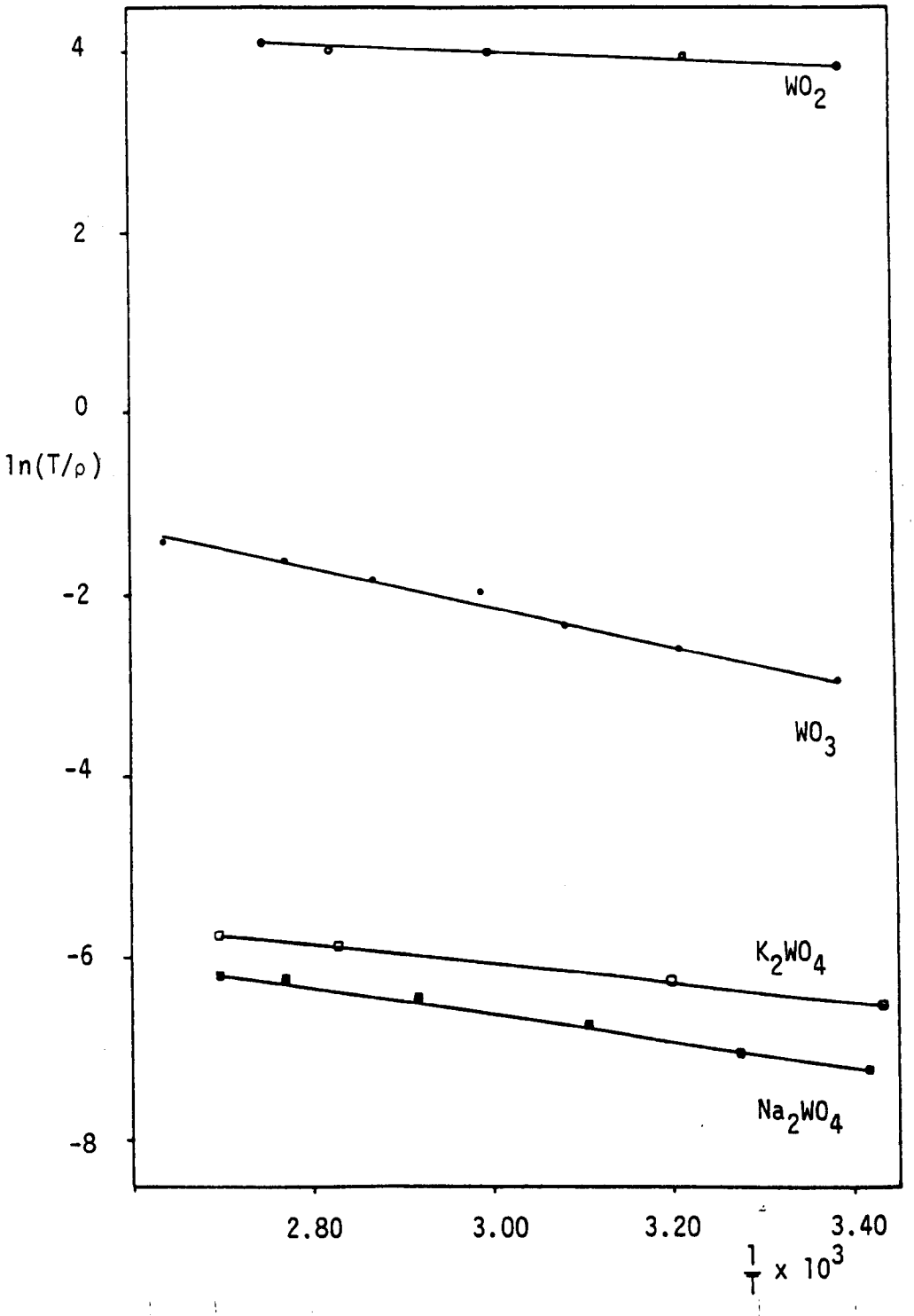

Figure 7.9 $\ln(T/\rho)$ measured in the a.c. mode versus $\frac{1}{T}$ for tungstates WO_3 and WO_2

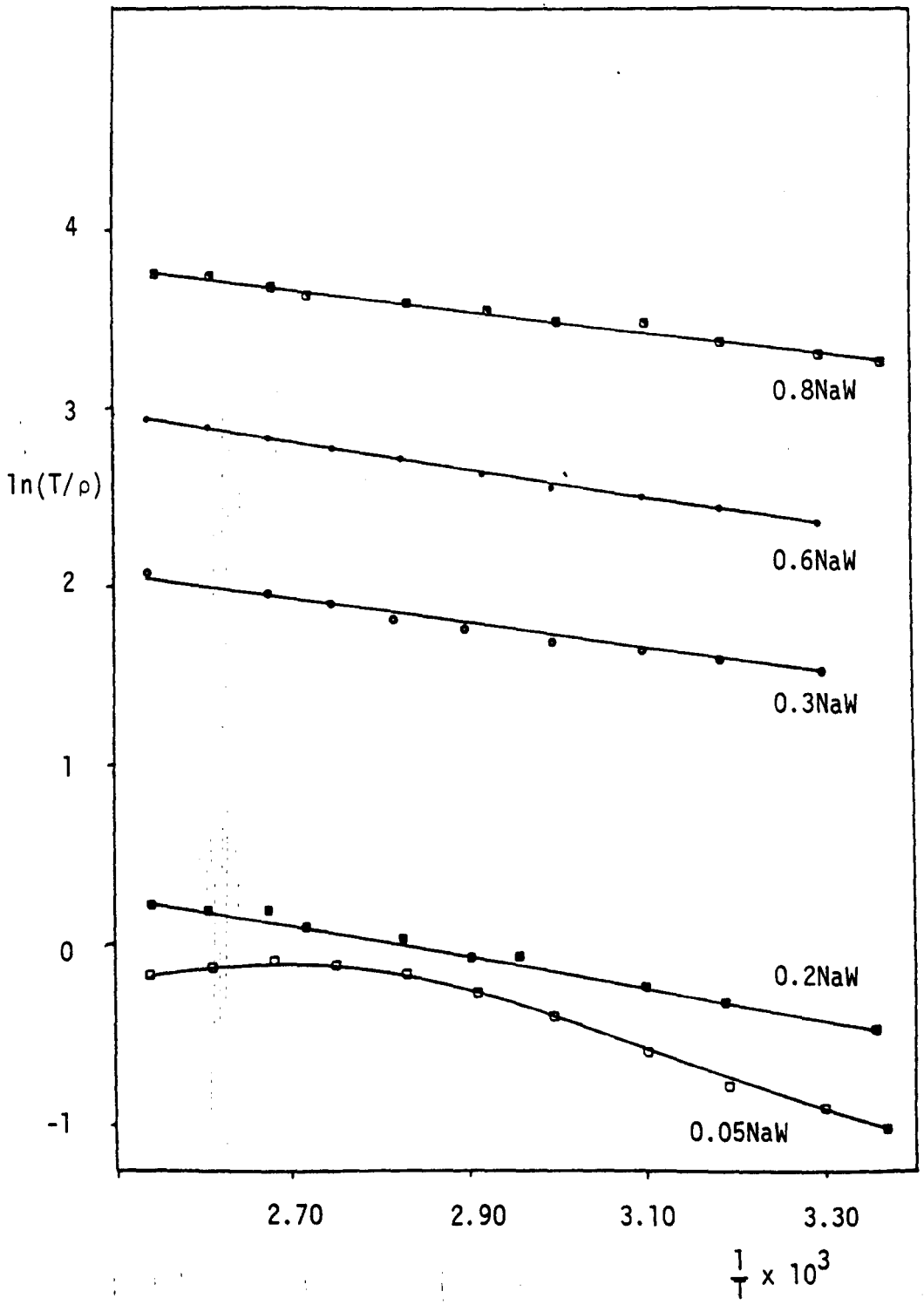

Figure 7.10 $\ln(T/\rho)$ measured in the a.c. mode versus $\frac{1}{T}$ for Na_xWO_3

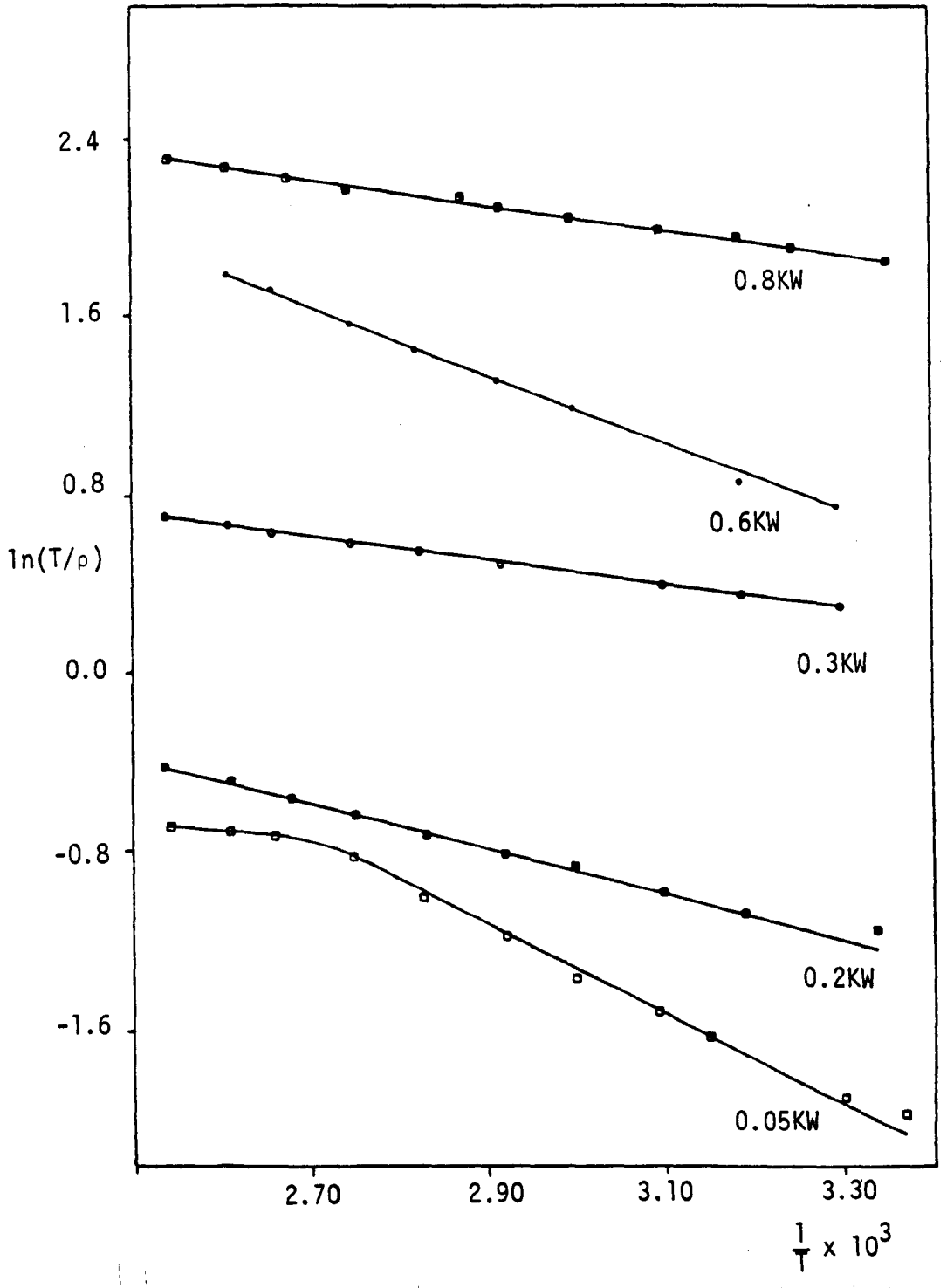

Figure 7.11 $\ln(T/\rho)$ measured in the a.c. mode versus $\frac{1}{T}$ for K_xWO_3

The log of the conduction varies linearly with inverse temperature, the straight line sometimes exhibiting breaks at a certain temperature. Table 7.2 gives the derived activation energy values for electrical conduction of the bronzes. In general, the activation energies decrease with increasing value of x but are rather similar at one value of x changing from Na^+ to K^+.

7.4 Conclusions

The sodium and potassium tungsten bronzes having high concentrations of the insertion ion show metallic properties while those with low insertion ion concentration have semiconductor properties. It appears that at higher concentrations the conducting electrons are delocalised resulting in metallic conductivity while for lower alkali content these electrons could be localised, most probably on discreet tungsten atoms causing semiconductor behaviour. Measurement of the Hall effect, i.e. measurement of the free electron concentration for Na_xWO_3[3] has indicated that the free electron concentration is equal to the alkali metal concentration and is temperature independent, thus implying that the conducting electrons arise from the complete ionisation of the inserted atoms.

The origin of the metallic conductivity of the tungsten bronzes having large concentration of insertion ions has been very much discussed, the explanation given by Goodenough[2] seems to be the most plausible. His description of the binding in cubic Na_xWO_3 is a useful prototype for the electronic structures of metallic oxide bronzes. A qualitative energy level scheme is given in Figure 7.12. Each oxygen has two sp orbitals directed towards neighbouring tungsten atoms. The central tungsten atom of a WO_6 octahedron has 5s, 6p and 5d(eg)

orbitals which can combine with the sp oxygen orbitals directed towards it. In the extended lattice these interactions lead to the formation of σ and σ^* bands. The remaining oxygen p orbitals ($p\pi$) combine with the tungsten 5d (t2g) orbitals to give π (bonding), π^* (anti-bonding) and $p\pi^+$ (non-bonding) bands. The conduction band, which can contain a maximum of six electrons per W atom, is π^* and is predominantly W5d (t2g) in character. Sodium atoms donate one electron per atom into the conduction band which becomes partially filled. The resulting energy level scheme is similar to that calculated[4] for ReO_3, a metallic material isoelectronic and isostructural with Na_xWO_3.

The electrical properties of tungsten bronzes with low insertion ion concentration has also been adequately investigated to conclude semiconductor behaviour[5]. This behaviour is coincidental with structural distortions of the oxide lattice which probably disrupt the mechanism by which the conduction band is formed and instead cause localisation of electrons in the t2g orbitals of specific tungsten atoms.

The substitution of potassium for sodium as the insertion ion in the bronze only slightly increases the resistivity values, indicating that the resistivity is possibly independent of the nature of the insertion ion. A similar observation has been made by Ellerbeck et al[6]. He concluded that not only was the electron mobility independent of the nature of the insertion ion, but, that it is not influenced by the number of insertion - ion vacancies, depending only on the WO_3 sublattice at sufficiently elevated temperatures.

Recent studies[7] on the conductivity of some polycrystalline alkali metal tungsten bronzes have shown that a.c. measurements, above a certain critical temperature, (T_c), suggest ionic conductivity to be

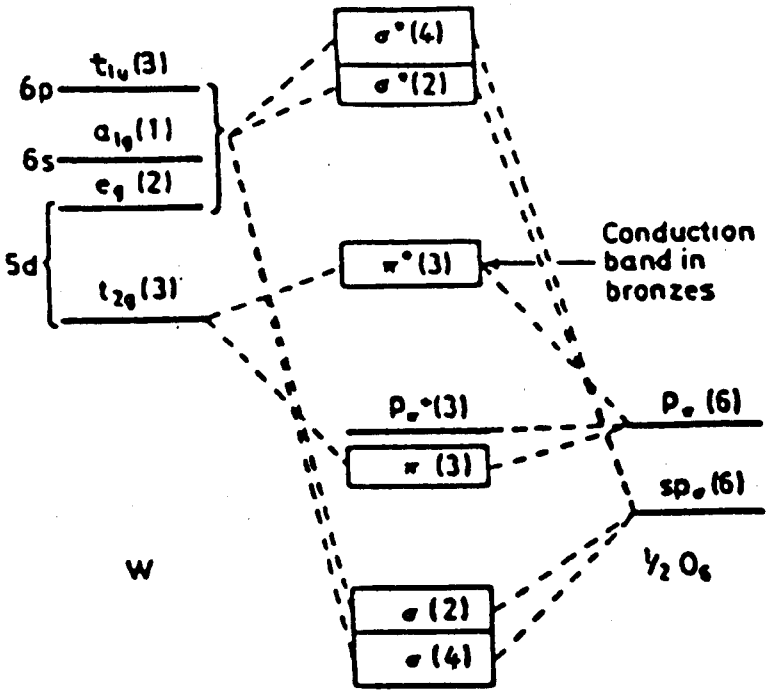

Figure 7.12 Electronic energy level scheme for WO_3 and Na_xWO_3

significant. This ionic conductivity was thought to arise simultaneously from the mobility of (i) O^{2-} lattice ions and oxygen vacancies, (ii) W^{5+} ..... W^{6+} exchange, and (iii) alkali metal ions intercalated.

However, tpo studies[7] on these samples suggested the presence of oxygen deficiencies unlike the present bronzes (see Chapter 4). The samples were prepared under vacuum[7] whereas the present bronze samples were prepared in a flowing argon gas stream. This could explain the differences in the results obtained.

Table 1 Activation energy of conduction E_δ in tungstates and tungsten oxides

Sample	E_δ/meV
WO_2	32.5
WO_3	180.8
K_2WO_4	194.7
Na_2WO_4	108.9

Table 2 Activation energy of conduction E_δ in alkali metal tungsten bronzes

Sample	E_δ/meV
$Na_{0.05}WO_3$	102.0
$Na_{0.2}WO_3$	74.7
$Na_{0.3}WO_3$	65.3
$Na_{0.6}WO_3$	68.6
$Na_{0.8}WO_3$	48.6
$K_{0.05}WO_3$	143.1
$K_{0.2}WO_3$	82.9
$K_{0.3}WO_3$	46.8
$K_{0.6}WO_3$	133.5
$K_{0.8}WO_3$	43.0

CHAPTER 7

REFERENCES

1. A. Drude, Ann. Phys., 4, 1, (1900).

2. J.B. Goodenough, Prog. Sol. State Chem., 5, 145, (1971).

3. W.R. Gardner, Phys. Rev., 46, (1954); 158,825, (1967); 84, 142, (1951).

4. J. Feinleib, W.J. Scouler and A. Ferretti, Phys. Rev., 165, 765, (1968).

5. H.R. Shanks, P.H. Sidles and G.C. Danielson, 'Non-Stoichiometric Compounds', Adv. in Chem., No. 39, 237, (1963).

6. L.D. Ellerbeck, H.R. Shanks and P.A. Sidles,Proc.Phys. Soc., A62, 416, (1949); Can. J. Phys. 34, 1356, (1956).

7. S.A. Lawrence, S. Stevenson, K. Mavadia and P.A. Sermon, Proc. R. Soc. A411, 95, (1987).

CHAPTER 8

CATALYTIC ACTIVITY FOR ISOPROPANOL DECOMPOSITION

8.1 Introduction

The decomposition of a secondary alcohol can occur by two routes : (a) dehydrogenation to form a ketone and hydrogen, (b) dehydration to form an alkene and water. At very high temperatures cleavage of carbon-~~gen~~ - hydrogen bonds can occur with the formation of alkanes, CO and CO_2. At near ambient temperature ether is the major reaction product. For the studies of catalyst selection it is sufficient to consider only the general reactions (a) and (b). Studies of these reactions have revealed that each of them calls for a different type of active site, which can be deduced from the various theories of catalysis. (1) From the electronic theory of catalysis, the rate-determining step for dehydrogenation is the migration of free electrons in the catalyst; consequently dehydrogenation is the migration of vacancies while for dehydration it is the migration of free electrons in the catalyst; consequently dehydrogenation is expected to be catalysed by p-type semiconductors and dehydration should be catalysed by n-type semiconductors, however some authors have arrived at opposite conclusions; (2) the multiplet theory of catalysis implies two-point adsorption as a condition for alcohol decomposition. Optimum interatomic spacing between surface atoms of the catalyst for the adsorption leading to dehydration is greater than that leading to dehydrogenation. Therefore an increase in crystal lattice parameters will aid dehydration activity, while a corresponding decrease will aid dehydrogenation; (3) from the classification of catalytic processes, dehydration is an acidic reaction and therefore should be catalysed by solid, protic and aprotic acids; dehydrogenation being an electronic reaction should be catalysed by

metals and also by semiconductors; (4) in accordance with the concept of cyclic complexes in catalysis adsorption of an alcohol involves a two-point attachment to the electropositive and electronegative surface atoms; an increase in metal-oxygen distance will facilitate dehydrogenation and a decrease in such distance will facilitate dehydration; (5) alcohol decomposition is a multistep reaction, dehydration requires acidic catalysts with n-type conductivity and dehydrogenation requires basic catalysts with p-type conductivity; (6) allowing for the role of the width of the forbidden zone, (U), and for the presumption that catalysis involves specific conductivity, the rate of alcohol dehydrogenation will increase with decreasing value of (U). There should be no effect of (U) on dehydration, since this is an acid catalysed reaction.

Decomposition of iso-propylalcohol has gained a prominent place as a model reaction for studying the principles of catalyst selection. The two main paths of this decomposition are:

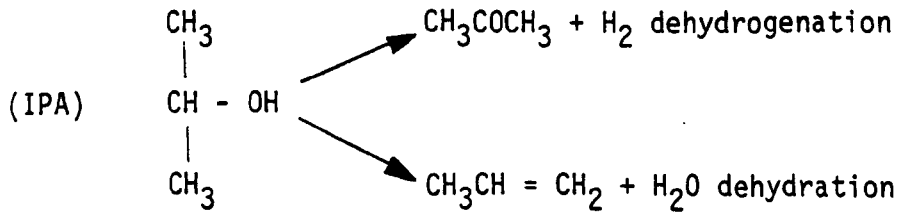

both of them are free of side reactions

Recently the activity for the dehydration of isopropyl alcohol is reported to be a good measure of acidity of metal oxide catalysts.[1-4] Seo et al[5] have found acid-base measurements from their study of isopropanol decomposition over molybdena-alumina ($Mo-Al_2O_3$) catalysts to be in good correlation with those measured by adsorption of ammonia or pyridine. Acidity and basicity on the $Mo-Al_2O_3$ catalysts were found to be affected by the extent of reduction.

(a) Kinetics of IPA Decomposition

Although the decomposition of IPA has been studied frequently using a variety of catalysts[6], few papers have emphasised the kinetics of the reaction and information on the kinetic equations is limited. In dehydrogenation, the possible rate-limiting steps are (a) adsorption of the alcohol, (b) interaction on the surface, and (c) desorption of products. These possibilities have been discussed for catalysis on zinc (II) oxide[7] and a kinetic analysis was carried out. Also, in general form the following equation has been proposed[2] for the catalytic dehydrogenation;

$$\text{rate} = \frac{k_1 k_3 p_{alc}}{k_1 p_{alc} + k_2 p_{ac} + k_3} \qquad (1)$$

where k_1, k_2 and k_3 are, respectively, the rate constants for the decomposition of the alcohol, adsorption of acetone, and desorption of acetone while p_{alc} and p_{ac} are the partial pressures of IPA and acetone respectively. The equation is in agreement with experimental data[8] and was derived on the assumption that at the steady-state, the rate of desorption of acetone is equal to its rate of adsorption plus the rate of dehydrogenation of the alcohol. For the dehydration of IPA on metal oxides a similar kinetic treatment[9] yields an equation for the rate like equation (1) with rate parameters for water substituted for those of acetone.

A thermodynamic consideration of the isopropanol decomposition reaction is also of interest. Dehydrogenation of IPA is an exothermic reaction and hence the products are favoured at low temperature. The dehydration reaction on the other hand, is an endothermic process and hence the products of dehydration are favoured at higher temperature.

Table 8.1 shows how the equilibrium constant, K, for the two reactions varies with temperature[5].

Table 8.1 Variation of equilibrium constant, K, with temperature

Temperature/K	Dehydration, $Kx10^{-4}$	Dehydrogenation K
463	3.49	8.3
473	4.53	7.5
483	5.83	7.2
493	7.42	6.9
503	9.34	6.8

It must be noted that the equilibrium constant for the dehydrogenation reaction is larger than that for the dehydration reaction at any temperature, but decreases with temperature. Whereas for the dehydration reaction, K increases with temperature. However, at lower temperatures both reactions are kinetically limited.

8.2 Experimental Procedure

The decomposition of isopropanol, IPA, was carried out using a fixed bed reactor in a flow system, as shown in Figure 8.1. The catalyst (usually about 0.2g) was supported on a sintered disc in a Pyrex reactor which was connected to the reaction system. The reactor was placed in an electrically heated furnace and regulated to within ±5K. The introduction of a thermocouple into the well fitted to the reactor allowed measurement of the temperature. Prior to activity measurements the samples were thermally treated in N_2 at 773K for 1h. The sample was then cooled to room temperature in N_2 before the reactive

P.C. : Pressure controller
P.I. : Pressure indicator
F.C. : Flow controller
F.I. : Flow indicator
M.S. : Molecular sieve
T. : Tap

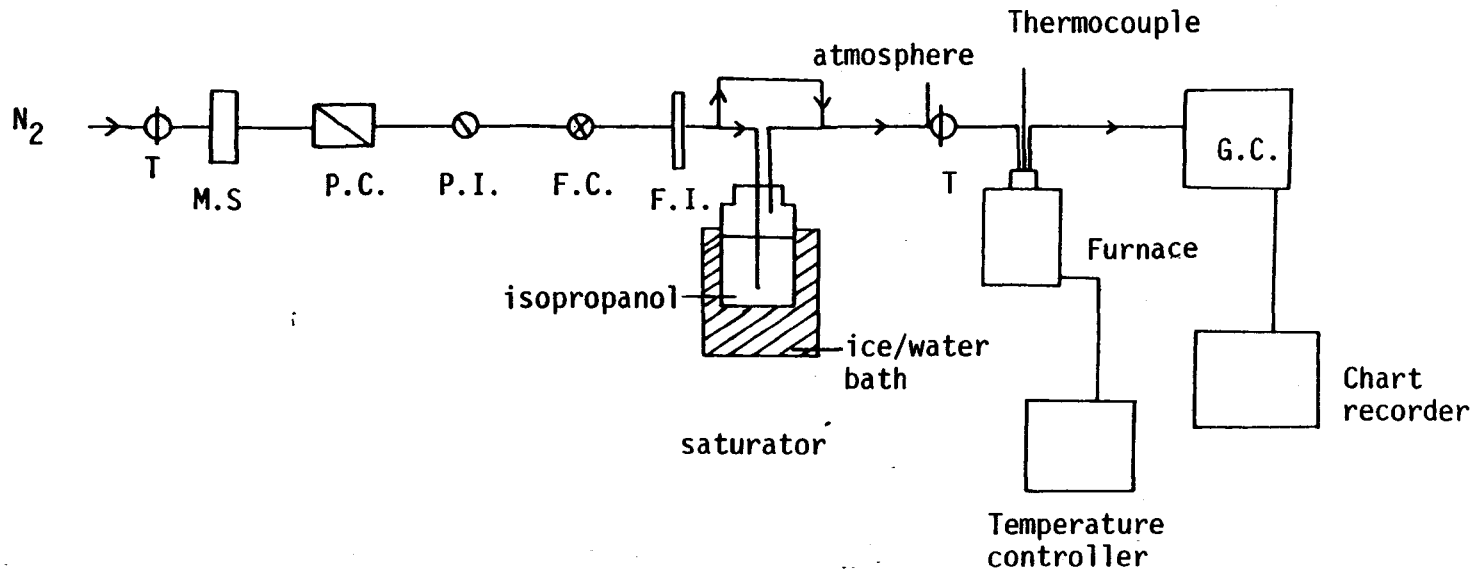

Figure 8.1 Activity apparatus for isopropanol decomposition

mixture was admitted. N_2 (White Spot BOC, 99.99% purity) at a flow rate of $88cm^3\ min^{-1}$ was used as a carrier gas. The IPA, fed into the nitrogen carrier gas stream by a saturator, was carried over the catalyst at 101.325kPa of total pressure.

The saturator was placed in an ice-water mixture at 273K and the temperature was found to remain constant to ±2K over at least an 8h period. At the outlet of the reactor, gas samples were injected to the chromatographic apparatus (Pye Unicam model F11) which contained a column (5% carbowax on chromosorb P, 80-100 mesh) capable of separating propene, acetone and isopropanol, and was fitted with a flame ionisation detector whose output was fed to a chart recorder. The analysis was carried out under the following conditions:

Temperature of column	=	323K
Pressure of N_2 g.c. carrier gas	=	140kPa
N_2 flow rate in column	=	$15cm^3\ min^{-1}$
Pressure of H_2 for FID	=	130kPa
Pressure of Air for FID	=	85kPa

Calibration was achieved by injecting known amounts of acetone, propene and IPA into the column and plotting a graph of peak areas versus amount of component injected. From the gradient of these graphs, response coefficients for each component were obtained. The retention time and response coefficient for IPA, propene and acetone measured at the conditions given above are shown below:

	Retention time/mins	Response coefficient
IPA	2.05	1.00
Acetone	1.33	0.75
Propene	0.58	0.07

The number of moles of the component produced was assumed to be proportional to the peak area, i.e.

$$N_i = k_i A_i$$

where

N_i is the number of moles of component i produced

k_i is the response coefficient for component i

A_i is the peak area for component i

The percentage conversion of IPA was calculated from the composition of the gas mixture by the equation;

$$\% \text{ conversion} = \frac{100A}{A + N_{\text{isopropanol}}}$$

where A is the number of moles of IPA transformed to produce propene and acetone and is calculated from the equation;

$$A = N_{\text{propene}} + N_{\text{acetone}}$$

The selectivity for a given product is defined as the number of moles of that product divided by the number of moles of IPA transformed. For a reaction product it is given by the equation;

$$S_i = \frac{N_i}{A}$$

The reaction rate (R) is expressed as the moles of IPA transformed per hour per gram of catalyst. It has been calculated using the equation;

$$R = \frac{\% \text{ conversion}}{100} \times F \times \frac{60}{22414} \times \frac{1}{W}$$

where W = weight of sample used. The constant 22414cm^3 mol^{-1} was considered to be the molar volume of a gas at S.T.P. F is the flow rate of isopropanol in cm^3 min^{-1} and is given by

$$\frac{\text{Flowrate of } N_2 \text{ carrier gas}}{} \times \frac{\text{vapour pressure of IPA at 273K}}{101.325\text{kPa}}$$

8.3 Results

The decomposition of isopropanol was studied as a function of temperature on WO_3, K_xWO_3 and Na_xWO_3. Figure 8.2 shows the initial selectivity for IPA decomposition on WO_3 as a function of temperature. Selectivity for dehydration increased as a function of temperature and from 513K, WO_3 shows total selectivity towards propene formation. Figures 8.3 - 8.7 show the selectivities for propene and acetone production as a function of temperature for the potassium tungsten bronzes, 0.05KW $\longrightarrow$ 0.8KW respectively. For the potassium bronzes, the selectivities show minimum variation with temperature, in the range in which they were active (513K - 633K) usually with a slight increase in propene selectivity. It would be more interesting to compare the selectivities of the potassium bronzes at a fixed temperature. Figure 8.8 shows the variation of selectivities with x in $K_x\ WO_3$ at the test temperature of 553K. Propene selectivity decreases as the concentration of potassium ions in the bronze increases.

Figures 8.9 - 8.13 show the selectivities for propene and acetone production as a function of temperature for the sodium tungsten bronzes $Na_{0.05}WO_3$ $\longrightarrow$ $Na_{0.8}WO_3$ respectively. Similar to the potassium bronzes, the selectivities for the sodium bronzes show minimum variation with temperature, in the range in which they were active (493K-633K).

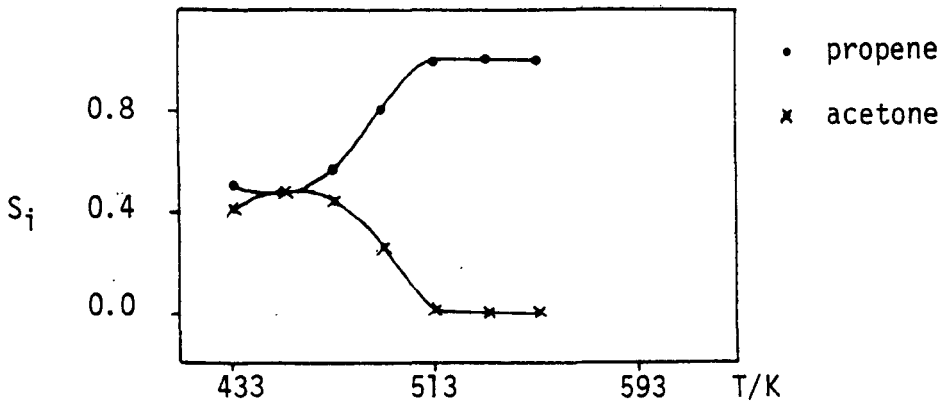

Figure 8.2 S_i versus temperature for WO_3

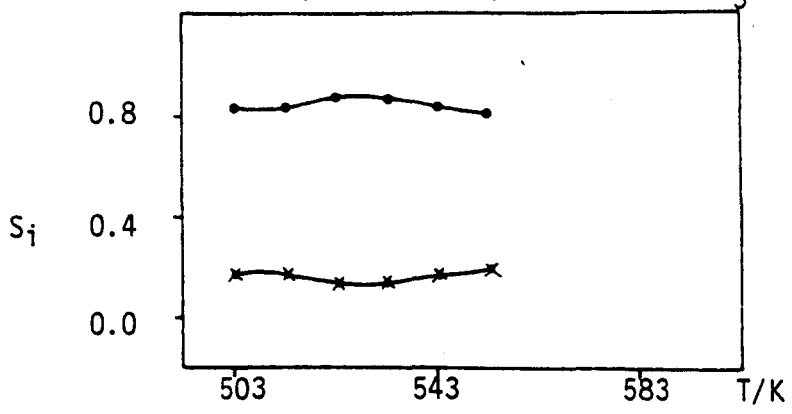

Figure 8.3 S_i versus temperature for 0.05KW

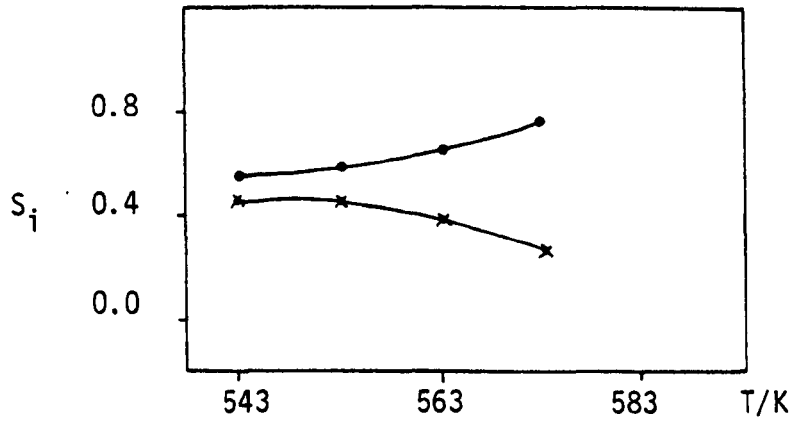

Figure 8.4 Selectivity (S_i) for propene and acetone versus temperature for 0.2KW

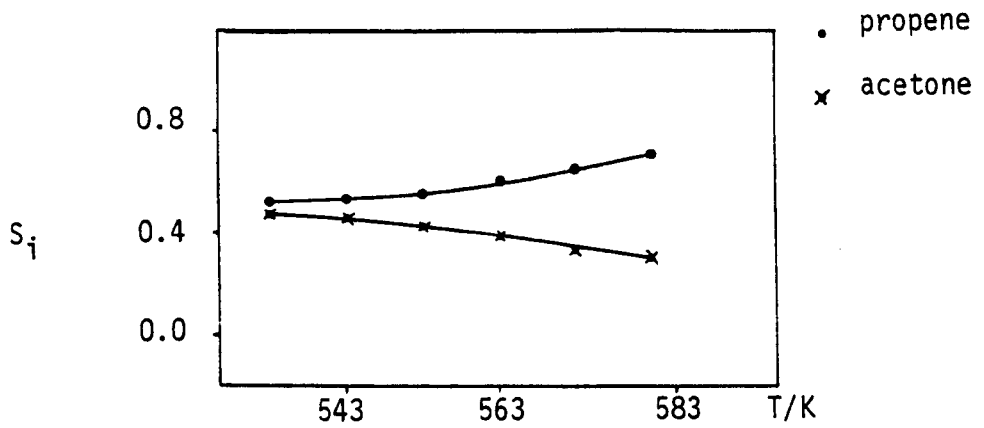

Figure 8.5 S_i versus temperature for 0.3KW

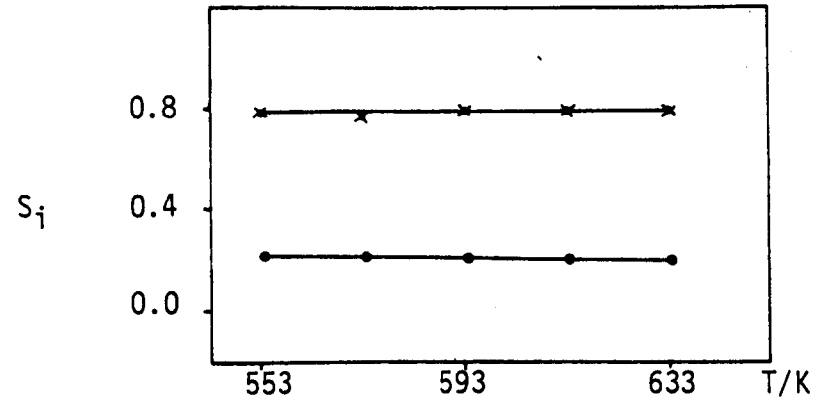

Figure 8.6 S_i versus temperature for 0.6KW

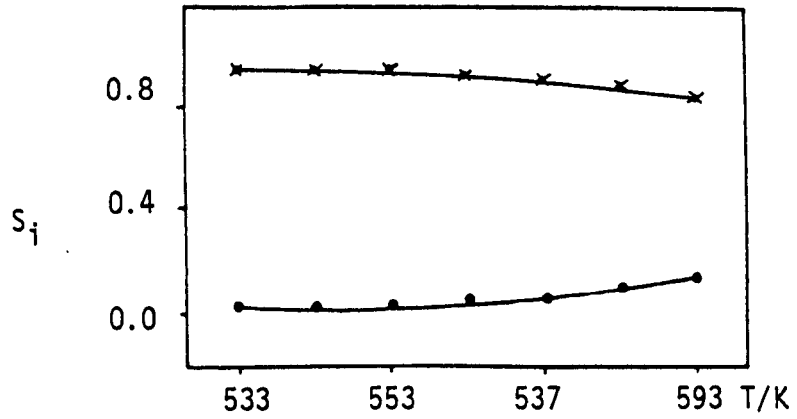

Figure 8.7 Selectivity (S_i) for propene and acetone versus temperature for 0.8KW

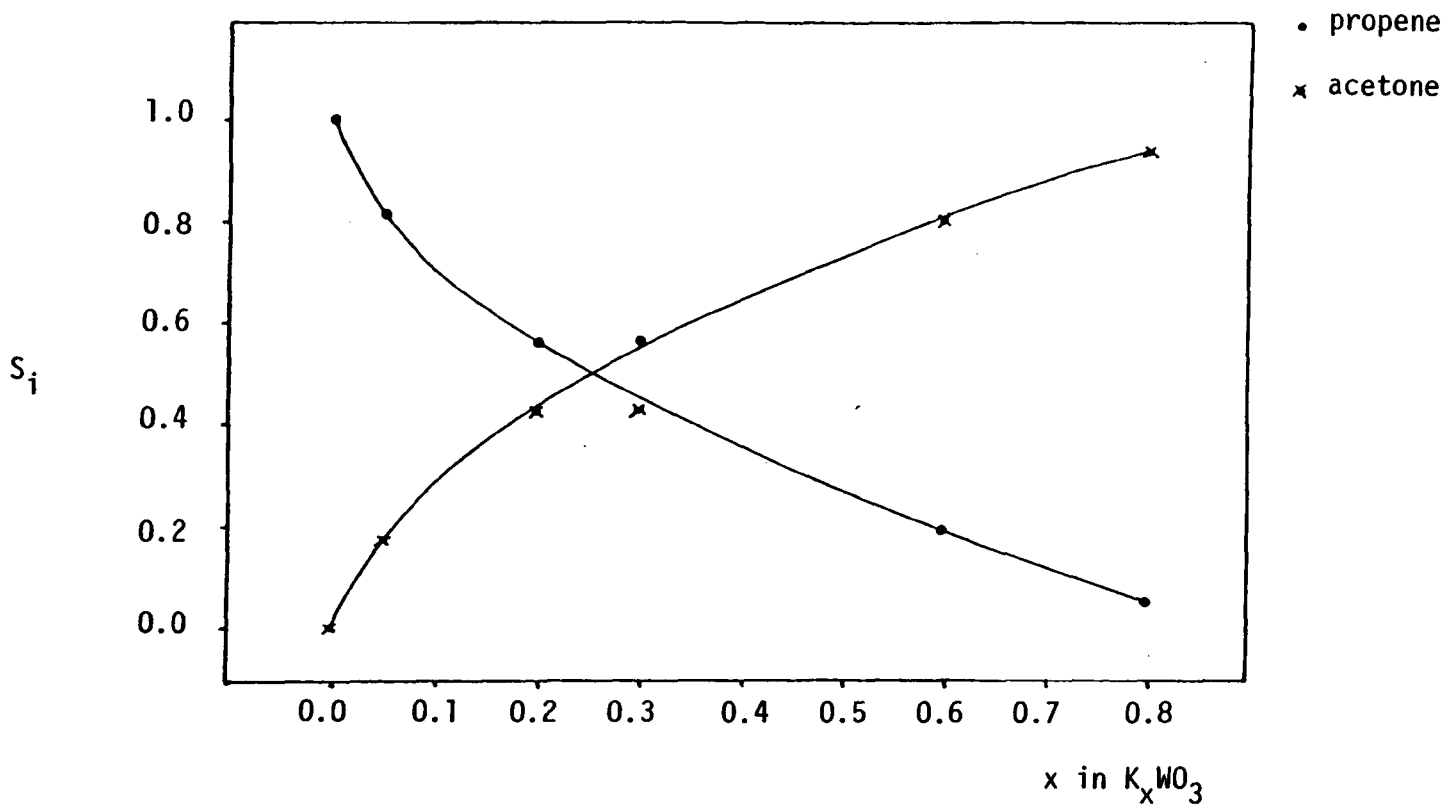

Figure 8.8 Selectivity, (S_i), for propene and acetone versus x in K_xWO_3

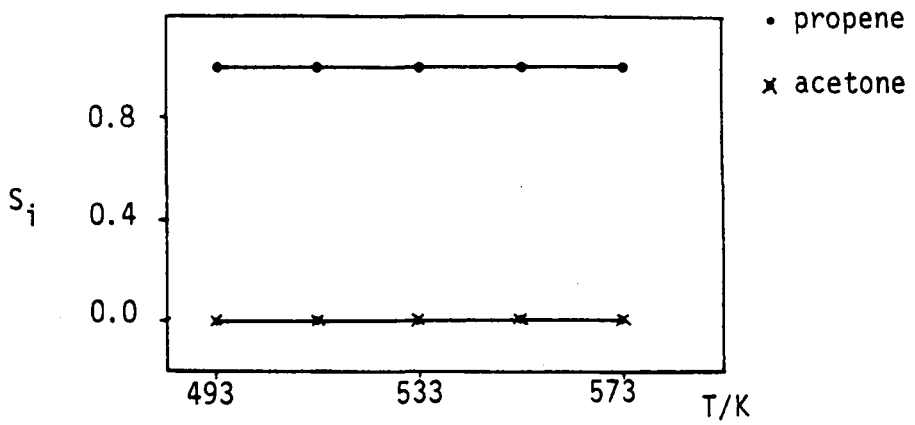

Figure 8.9 S_i versus temperature for 0.05NaW

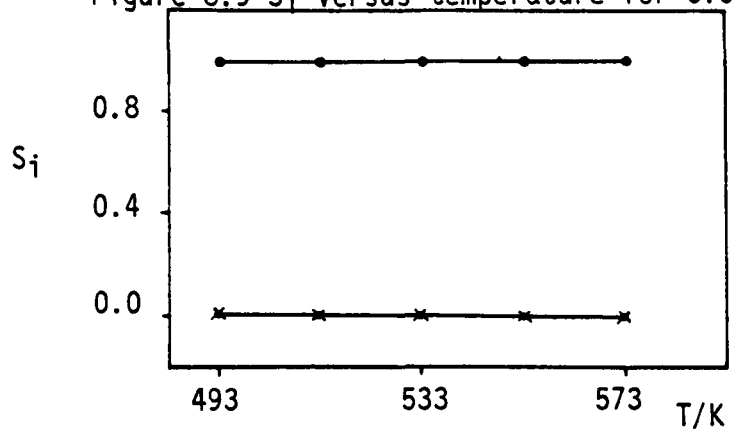

Figure 8.10 S_i versus temperature for 0.2NaW

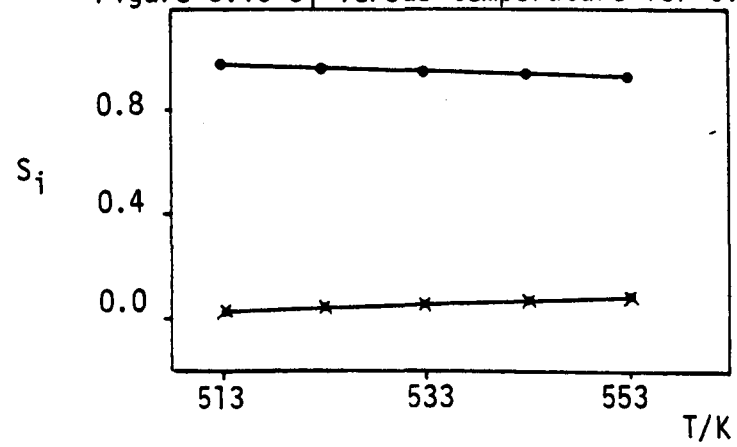

Figure 8.11 Selectivity (S_i), for propene and acetone versus temperature for 0.3NaW

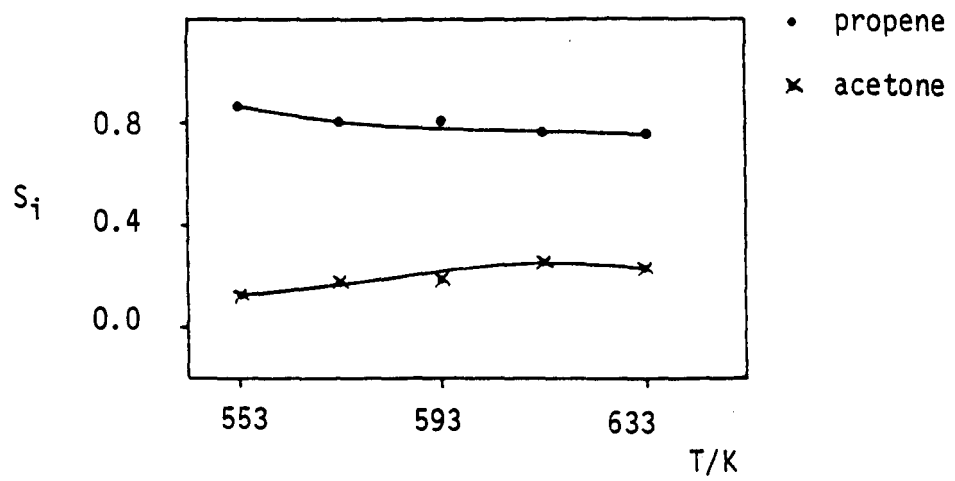

Figure 8.12 S_i versus temperature for 0.6NaW

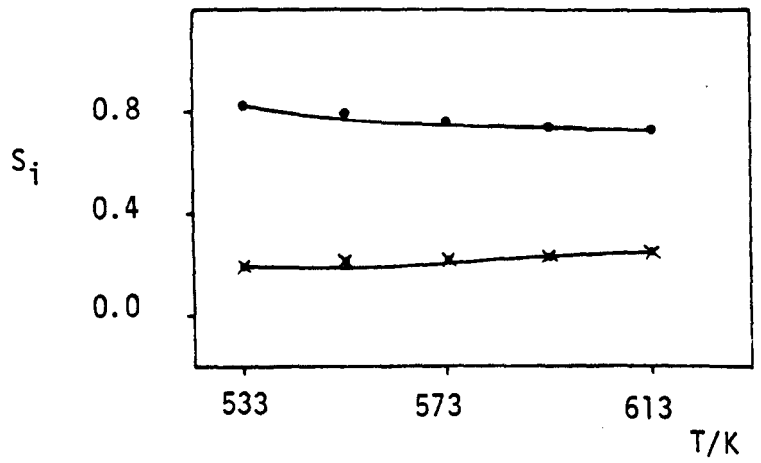

Figure 8.13 Selectivity (S_i) for propene and acetone versus temperature for 0.8NaW

However, unlike the potassium bronzes, the sodium bronzes with low concentration of insertion ion, i.e. $x \leq 0.2$, produce only propene in the temperature range of 493K - 573K. Figure 8.14 shows the selectivity values as a function of x in Na_xWO_3 at the test temperature of 553K. From this graph it can be seen that propene selectivity tends to decrease as the concentration of sodium ions in the bronze increases. For any given value of x the sodium bronzes show much higher selectivity for propene than the corresponding potassium bronze.

Table 8.2 gives the total rate for isopropanol decomposition at the fixed temperature of 553K for WO_3, K_xWO_3 and Na_xWO_3 where $0.05 \leq x \leq 0.8$. In general for either series of bronze the total rate of decomposition decreases with increase in concentration of insertion ion. In general, the rate of isopropanol decomposition is greater for the sodium bronzes than for the potassium bronzes with $x \leq 0.3$, but is less when $x \leq 0.6$. The variation of the rates of the decomposition of isopropanol with K or Na content in the bronze was a common feature at all temperatures at which activity measurements were made. The variation of the rate of decomposition of IPA with temperature was used to calculate the activation energy.

The dependence of the rate constant, k, on temperature T, (Kelvin) follows the Arrhenius equation ($k = A \exp.- \frac{E_a}{RT}$ where E_a is the activation energy, R is the gas constant and A the pre-exponential factor). Measurement of k requires the determination of the orders of reaction at each temperature using the power rate law,

$$r = k\, p_A^a$$

It has to be assumed that a is not temperature dependent and k is

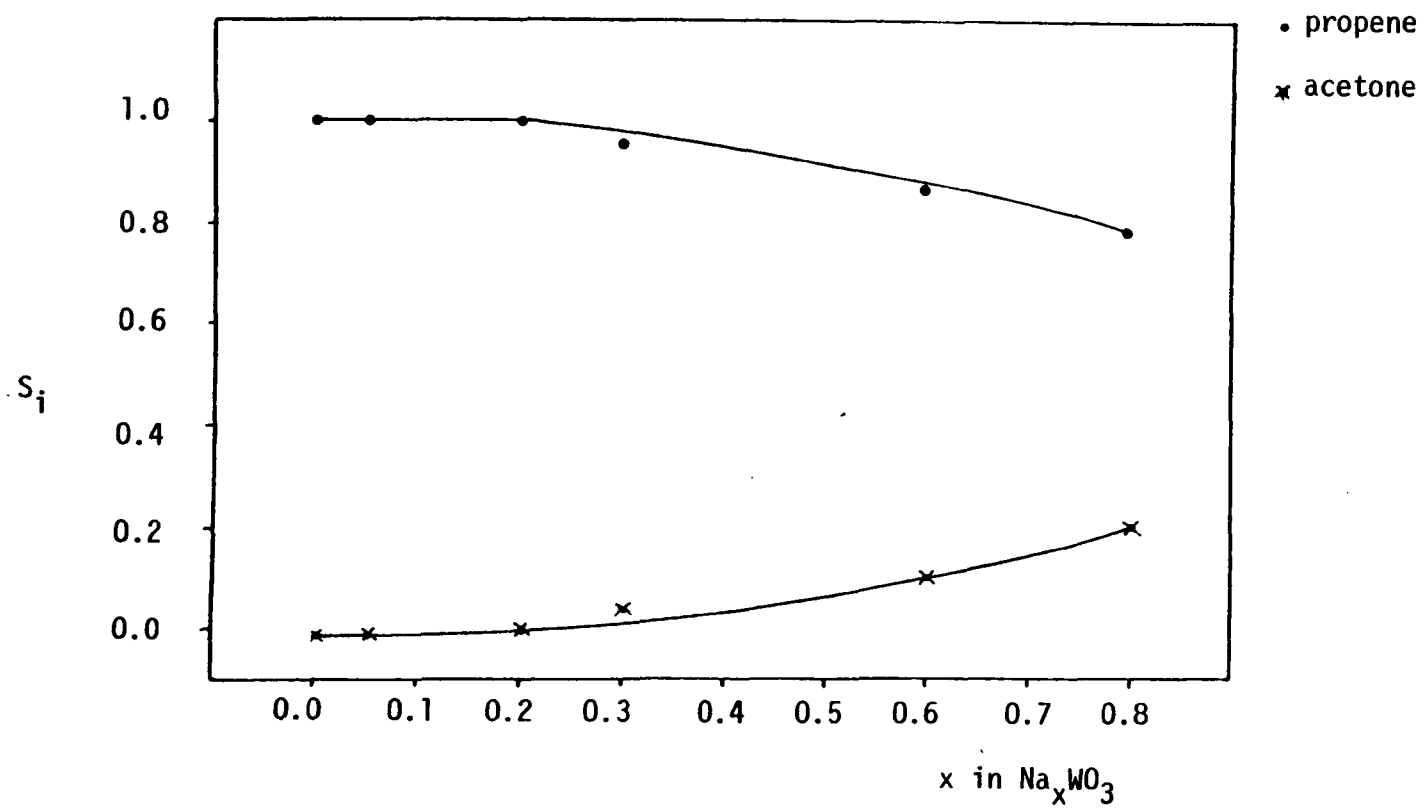

Figure 8.14 Selectivity,(S_i), for propene and acetone versus x in Na_xWO_3

Table 8.2 Total rate of Isopropanol Decomposition at 553K for WO_3, K_xWO_3 and Na_xWO_3

Sample	R_T/mmol $g^{-1}h^{-1}$
WO_3	15.09
$K_{0.05}WO_3$	3.22
$K_{0.2}WO_3$	1.88
$K_{0.3}WO_3$	1.21
$K_{0.6}WO_3$	0.81
$K_{0.8}WO_3$	0.73
$Na_{0.05}WO_3$	3.95
$Na_{0.2}WO_3$	3.69
$Na_{0.3}WO_3$	3.68
$Na_{0.6}WO_3$	0.40
$Na_{0.8}WO_3$	0.21

proportional to r providing that the reaction is studied at low conversions and over a moderate temperature range (usually 100K). The apparent activation energy can therefore be calculated from the equation;

$$\ln r = \ln A - \frac{E_a}{RT}$$

This is done by determining the rate of reaction at different temperatures and plotting lnr versus $\frac{1}{T}$. The Arrhenius plots for the initial rate of isopropanol decomposition on WO_3, K_xWO_3 and Na_xWO_3, where $0.05 \leqslant x \leqslant 0.8$, are given in Figures 8.15, 8.16 and 8.17 respectively. Good linear relationships were obtained for all samples. The pre-

exponential factor, A, and the activation energy, E_a, were calculated using the least squares method, and are given in Table 8.3 for WO_3, K_xWO_3 and Na_xWO_3. Activation energy values for the decomposition of IPA are within the range of those mentioned in literature[10].

Table 8.3 Activation Energy Values and ln A for the Decomposition of IPA on WO_3, K_xWO_3 and Na_xWO_3

Sample	E_a/kJmol^{-1}	ln A
WO_3	52.0	14.0
$K_{0.05}WO_3$	76.0	17.7
$K_{0.2}WO_3$	75.6	17.1
$K_{0.3}WO_3$	71.3	15.7
$K_{0.6}WO_3$	37.8	8.0
$K_{0.8}WO_3$	35.0	7.3
$Na_{0.05}WO_3$	61.3	14.7
$Na_{0.2}WO_3$	57.2	13.7
$Na_{0.3}WO_3$	49.1	12.0
$Na_{0.6}WO_3$	69.3	14.1
$Na_{0.8}WO_3$	65.6	12.7

8.4 Conclusions

The decomposition of IPA to propene and water (dehydration) or to acetone and hydrogen (dehydrogenation) is a common probe reaction that is used with catalysts that have acid and base functions. The decomposition of IPA on WO_3 shows selectivity for both dehydration and dehydrogenation in the temperature range of 433 - 493K but above 493K only propene was produced. These results suggest that in the

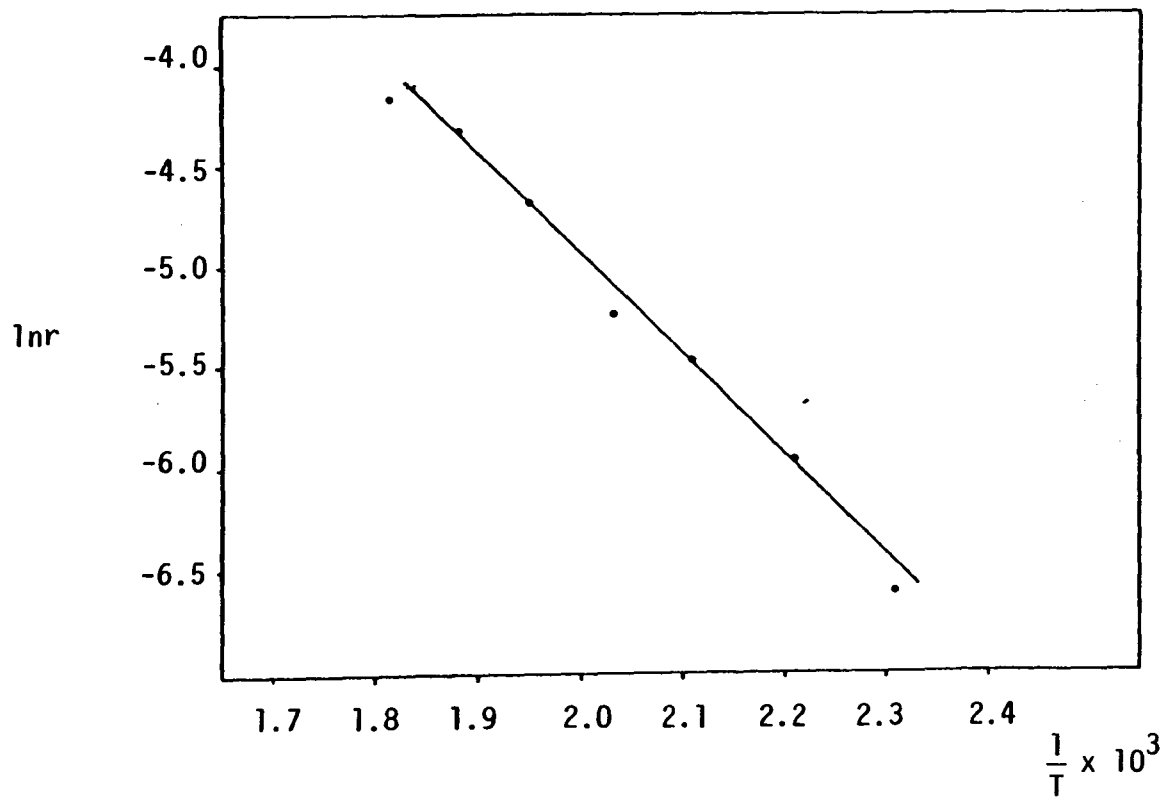

Figure 8.15 Arrhenius plot for WO_3

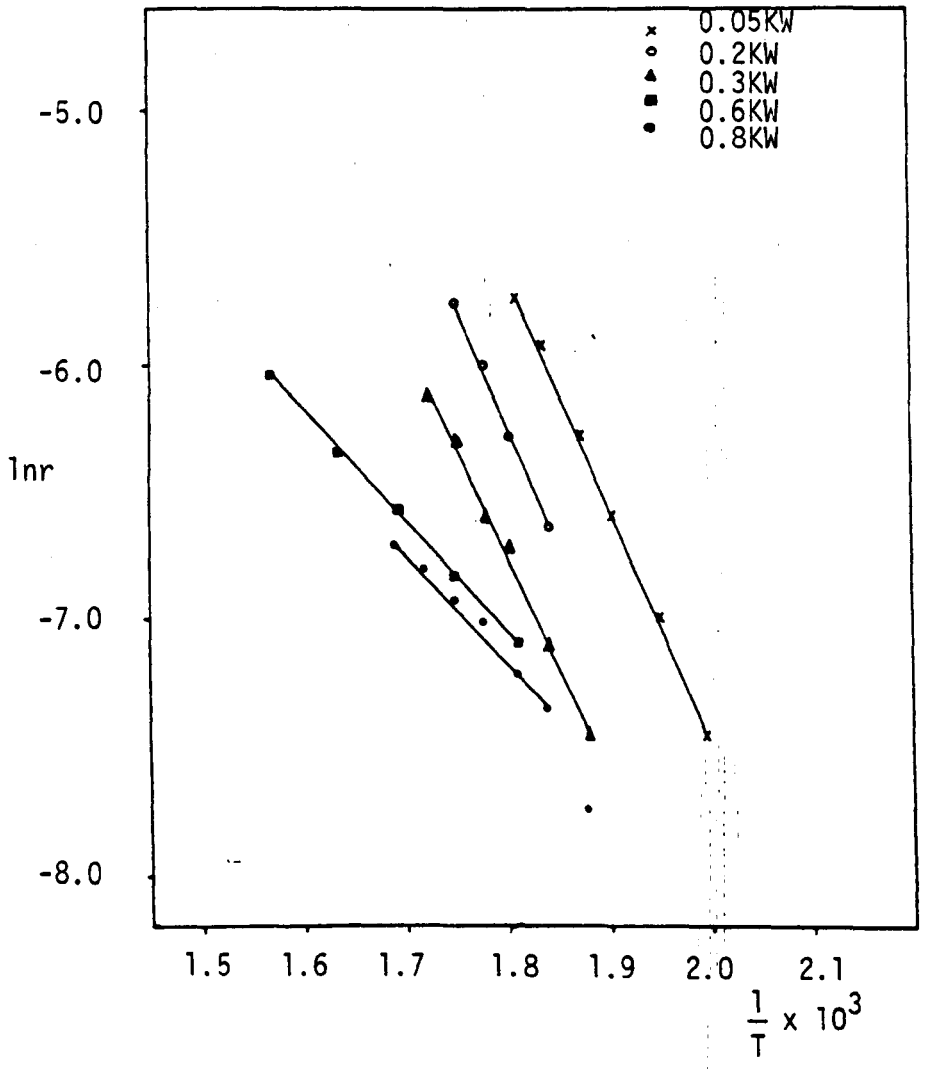

Figure 8.16 Arrhenius plots for K_xWO_3

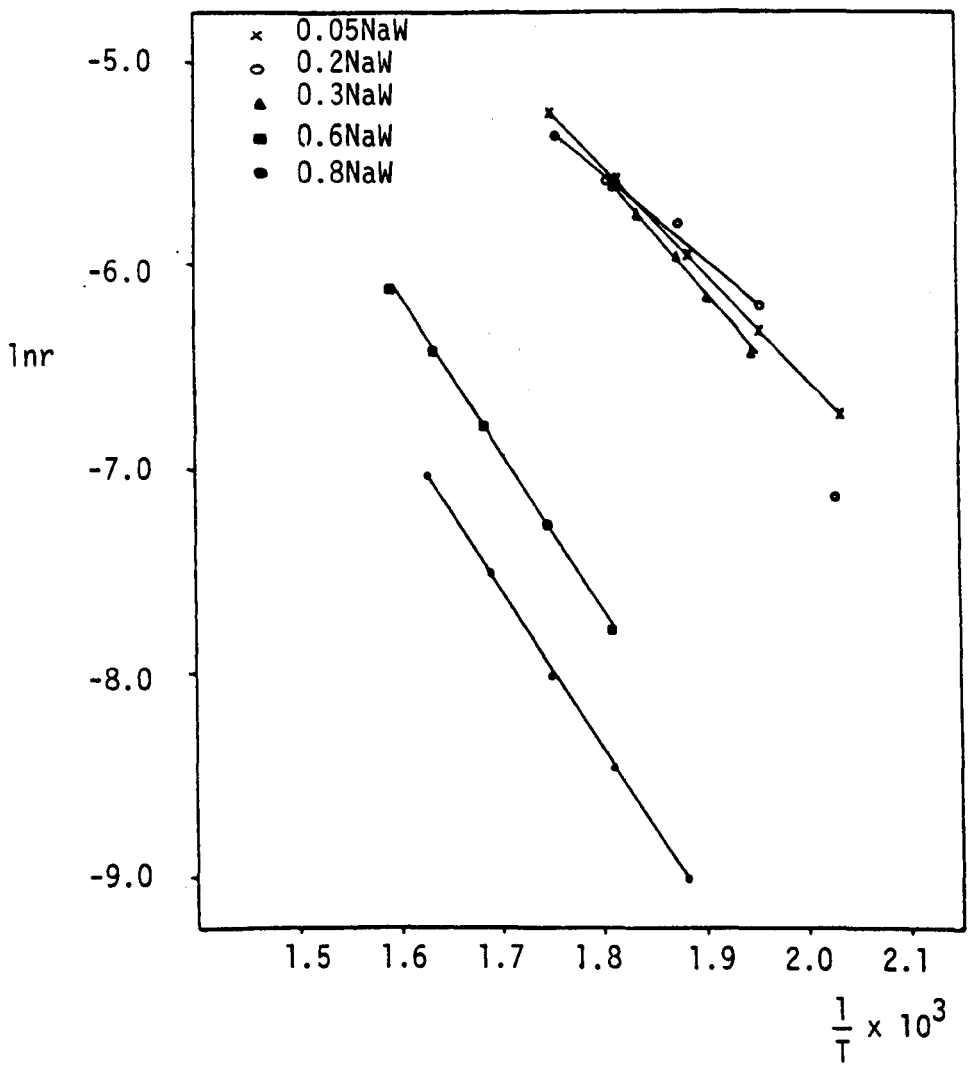

Figure 8.17 Arrhenius plots for Na_xWO_3

low temperature range both acidic (required for dehydration) and basic sites (for dehydrogenation) are present on the surface of WO_3, but above 493K only the acidic sites appeared to be active. Selectivity in IPA decomposition is known to be affected by the temperature at which the reaction is conducted, higher temperatures (typically above 623K) favouring dehydration[11]. But total selectivity for propene formation on WO_3 at temperatures above 493K cannot be due to only this thermodynamic factor, since acetone formation has been observed on other catalysts in such temperature ranges. It is most probably caused by the elimination of the basic sites. According to Krylov[6] strong metal-oxygen bonds (M - O) gives strong acidity and in oxides that have weak M - O bonds the oxygen lone pair is basic. WO_3 is classified as an acidic oxide but there is a possibility of weak W - O bonds present on the surface giving rise to basic sites. It is possible that at temperatures above 493K these weak W - O bonds are reduced by the secondary alcohol thus leaving only the acid sites. It may also be possible that at higher temperatures there is partial dehydration of the surface and a decrease in the coordination number of surface ions thus resulting in a strong M - O bond.

The decomposition of IPA on the potassium tungsten bronzes produced both dehydration and dehydrogenation products showing the presence of both acidic and basic sites. In general, the selectivity for propene production decreases as the concentration of potassium ions in the bronze increases. This result could be expected since the total number of acid sites decrease as x in K_xWO_3 increases. (see Chapter 3) or alternatively, the number of basic sites increase with increasing x. However, it would be interesting to consider whether the same type of reactive acidic sites are present in all of the potassium bronzes, since ammonia desorption has shown that for

bronzes with $x \geq 0.3$ at least two types of acidic site are present, as two or more maxima were observed. This could be done by comparing the turnover frequency for the dehydration reaction. Table 8.4 gives the rate of dehydration, the number of acid sites present and the turnover frequency for dehydration for WO_3 and the potassium tungsten bronzes. The rate and turnover frequency for the dehydration reaction on WO_3 are higher than those for the potassium bronzes with $x \leq 0.2$. It is possible that on WO_3 the sites are more reactive than on the potassium bronzes probably because stronger acid sites are formed during the reaction for reasons previously explained but not observed during ammonia desorption studies. The turnover frequency for the dehydration reaction may be considered constant for potassium bronzes with

Table 8.4 Turnover Numbers for Propene Production on WO_3 and K_xWO_3 at 553K

Sample	Rate of dehydration/ $mmol\,g^{-1}\,h^{-1}$(cat)	No. of acid sites/molecules NH_3 desorbed g^{-1}(cat)	Turnover No/ molecules per site s^{-1}
WO_3	15.09	6.98×10^{18}	0.36
$K_{0.05}WO_3$	2.64	4.40×10^{18}	0.10
$K_{0.2}WO_3$	0.97	1.34×10^{18}	0.12
$K_{0.3}WO_3$	0.69	5.28×10^{17}	0.22
$K_{0.6}WO_3$	0.16	1.22×10^{17}	0.22
$K_{0.8}WO_3$	0.04	3.07×10^{16}	0.22

$x = 0.05$ and $x = 0.2$. Temperature programmed desorption of ammonia on these samples and on WO_3 shows only one peak maximum in the low temper-

ature range thus indicating only one type of acid site is present. Turnover numbers for the dehydration reaction for bronzes with $x \geq 0.3$ are greater despite the fact that the total number of acid sites has decreased. However, tpd of ammonia has shown that for these samples there are at least two different types of acid site present. One way to distinguish whether more than one type of acid site is present is to consider the activation energy values for the dehydration reaction. Many investigations[5] have reported that these values are lower on catalysts which have both Bronsted and Lewis acid sites than those with only Lewis acid sites. Table 8.5 gives the activation energy (E_a) values for the dehydration reaction for WO_3 and the potassium bronzes. It appears that E_a is lower for the bronzes with higher potassium content again possibly indicating that these bronzes contain two types of acid site, while WO_3 and the potassium bronzes with $x \leq 0.2$ contain only one type of acid site. On Bronsted acid sites it is believed that IPA is molecularly adsorbed by hydrogen bonding whereas on Lewis acid sites it is dissociatively adsorbed to form a surface alkoxide and an adsorbed proton. In general the sodium tungsten bronzes show greater selectivity for the dehydration reaction than the potassium bronzes and in fact when $x \leq 0.2$ total selectivity for propene formation was observed. Temperature programmed desorption of ammonia of the sodium bronzes in most cases gave very broad peaks, possibly indicating acid sites of different strengths present. Table 8.6 gives the rate of dehydration, the number of acid sites present and the turnover number for the dehydration reaction on the sodium tungsten bronzes. Although the total number of acid sites present on the sodium bronzes are smaller than those on the corresponding potassium bronzes, the rate of dehydration and hence the turnover number are greater, again indicating that the acid sites present on the sodium

Table 8.5 Activation Energy Values and ln A for the Dehydration Reaction on WO_3 and K_xWO_3

Sample	E_a/kJmol^{-1}	ln A
WO_3	121.3	29.1
$K_{0.05}WO_3$	124.9	28.1
$K_{0.2}WO_3$	166.0	36.1
$K_{0.3}WO_3$	81.1	17.3
$K_{0.6}WO_3$	72.3	13.9
$K_{0.8}WO_3$	101.6	18.9

Table 8.6 Turnover Numbers for Propene Production on Na_xWO_3 at 553K

Sample	Rate of dehydration/ mmol g^{-1} (cat) h^{-1}	No. of acid sites/molecules NH_3 desorbed g^{-1} (cat)	Turnover No./ molecules per site s^{-1}
$Na_{0.05}WO_3$	3.95	1.36×10^{18}	0.49
$Na_{0.2}WO_3$	3.69	5.05×10^{17}	1.22
$Na_{0.3}WO_3$	3.46	3.20×10^{17}	1.81
$Na_{0.6}WO_3$	0.35	3.87×10^{16}	1.51
$Na_{0.8}WO_3$	0.17	2.80×10^{16}	1.02

bronzes are more reactive. The activation energy values for the dehydration reaction on the sodium bronzes, given in Table 8.7 are in the range of those obtained for the potassium bronzes with $x \geq 0.2$ where more than one type or strength of acid site was clearly observed during tpd of ammonia.

A comparison between the relative activities of the different samples for the dehydration reaction can be obtained using the compensation effect, where the logarithm of the pre-exponential factor is plotted against the activation energy. The compensation effect has

Table 8.7 Activation Energy Values and ln A for the Dehydration Reaction on the Sodium Bronzes

Sample	E_a/kJmol^{-1}	ln A
$Na_{0.05}WO_3$	61.3	14.7
$Na_{0.2}WO_3$	57.2	13.7
$Na_{0.3}WO_3$	85.5	19.8
$Na_{0.6}WO_3$	80.5	16.5
$Na_{0.8}WO_3$	73.6	14.2

been interpreted and reviewed in several papers[12-14] although the root of this effect is still uncertain. In general, catalysts lying on the same line in such a plot show similar activities whereas catalysts lying to the left show higher activities and those to the right smaller activities. Figure 8.18 shows the compensation plot for the dehydration reaction on WO_3, K_xWO_3 and Na_xWO_3. It appears that WO_3 and Na_xWO_3, where $0.05 \leqslant x \leqslant 0.3$, show similar activities whereas the corresponding potassium bronzes show slightly less activity. Of the bronzes with higher alkali ion content the sodium bronzes appear to be more active.

A similar compensation plot (Figure 8.19) has also been drawn for the total rate of decomposition of IPA on WO_3, K_xWO_3 and Na_xWO_3 from values of ln A and E_a given in Table 8.3. The potassium bronzes show

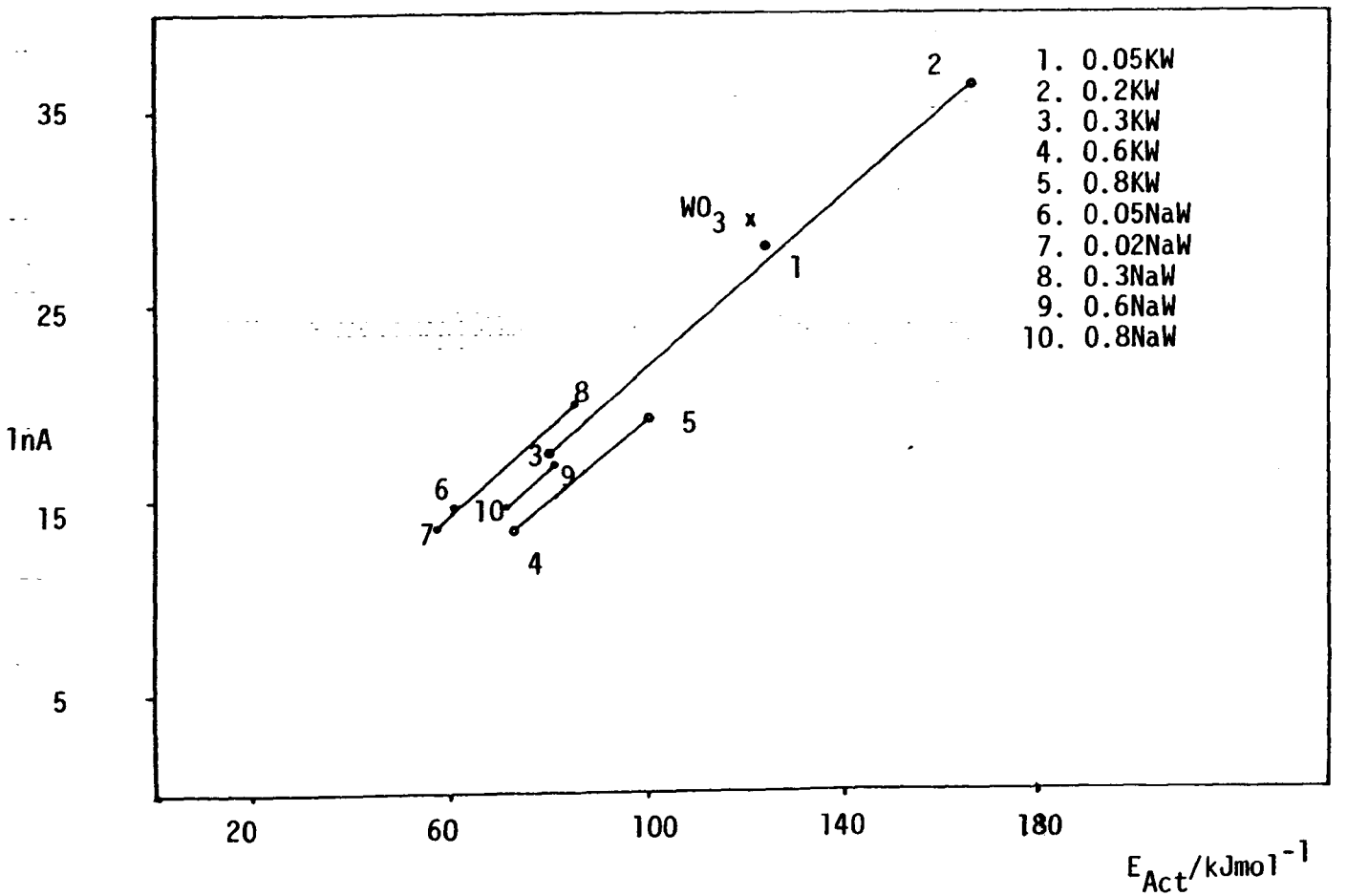

Figure 8.18 Compensation plot for the dehydration of isopropanol on WO_3, K_xWO_3 and Na_xWO_3

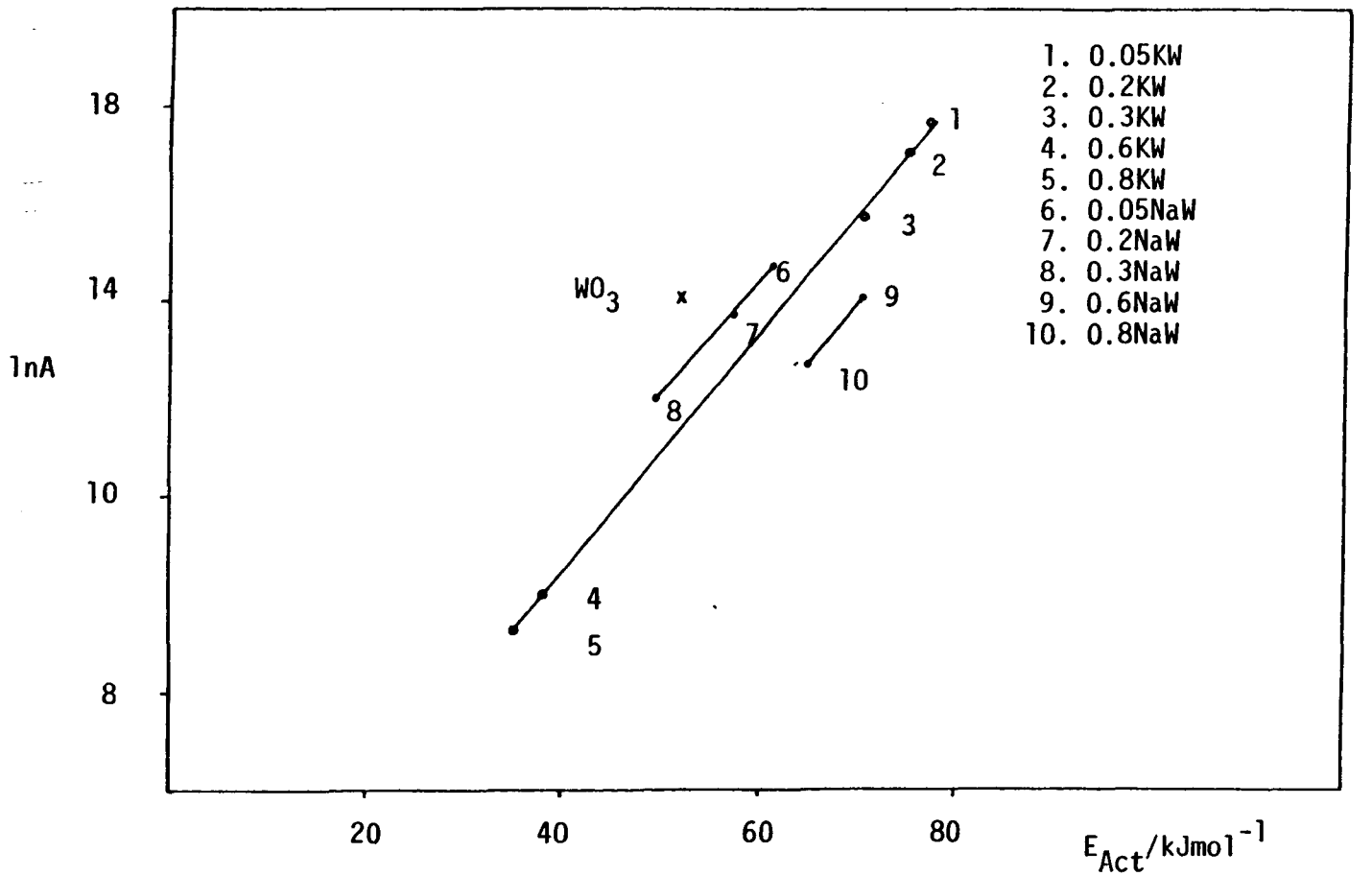

Figure 8.19 Compensation plot for isopropanol decomposition on WO_3, K_xWO_3 and Na_xWO_3

similar activities since they lie on the same line. WO_3 is the most active with the sodium bronzes with $0.05 \lesssim x \lesssim 0.3$ showing slightly less activity. The least active samples appeared to be the sodium bronzes with high alkali ion content. For the sodium bronzes with $0.05 \lesssim x \lesssim 0.3$ where dehydration is the most important reaction, the activity is higher than the potassium bronzes since the acid sites are more reactive. However, the potassium bronzes with $0.6 \lesssim x \lesssim 0.8$, although contain similar acid sites, show less activity for the decomposition reaction probably because dehydrogenation is an important reaction. The sodium bronzes with $0.6 \lesssim x \lesssim 0.8$ show lower activities than the potassium despite containing stronger acid sites. However, on these samples acetone formation is also observed and hence the basic sites present are less reactive. In general, the rate of the dehydration reaction is greater on the sodium bronzes than the corresponding potassium bronzes, this has been explained by the presence of stronger acid sites. The activities of the samples for the dehydrogenation reaction appears to be higher on the potassium bronzes than the sodium bronzes,most probably due to the fact that the basic sites on the potassium tungsten bronzes are more active.

CHAPTER 8

REFERENCES

1. M. Ali and S. Suzuki, J. Catal., 30, 362, (1973).
2. M. Ali, Bull. Jap. Petrol. Inst., 18, 50, (1976).
3. M. Ali, Bull. Chem. Soc. Jap., 49, 1382, (1976); 50, 355, (1977); 50, 2579, (1977).
4. K. Tanabe, 'Catalysis Science and Technology', 2, 231, Springer-Berlag, Berlin, (1981).
5. K.T. Seo, S.C. Kang, H.J. Kim, S.K. Moon, Korean J. Chem., 2, (2), 163, (1985).
6. O.V. Krylov, 'Catalysis by Non-metals', 115, Academic Press, (1970).
7. O.V. Krylov, Russ. J. Phys. Chem., 39, 1554, (1965).
8. J. Germain, J. Bigourd, J. Beaufils, B. Gros and L. Ponsalle, Bull. Soc. Chim. Fr., 1777, (1961).
9. O.V. Krylov, Russ. J. Phys. Chem., 39, 1422, (1965).
10. Y. Kera, J. Catal., 96, 198, (1986).
11. F. Pepe, F.S. Stone, J. Catal., 56, 160, (1969).
12. G.C. Bond, Zeitschrift Für Physikalische Chemie Neue Folge, 144, 521-23, (1985).
13. G.M. Schwab, Z. Phys. Chem., B5, 405, (1929); J. Catal., 84, 1, (1983).
14. W.C. Conner, J. Catal., 78, 238, (1982).

CHAPTER 9

CATALYTIC ACTIVITY FOR PROPENE METATHESIS

9.1 Introduction

(a) Mechanisms and Reactions

Alkene metathesis (disproportionation) is one of the most recently catalysed reactions of hydrocarbons to emerge. Discovered in 1959[1,2] this novel reaction opened up a new and exciting field of hydrocarbon chemistry and provided commercial routes for the inter-conversion of light alkenic hydrocarbons : the backbone of today's petrolchemical industry. The reaction is general for hydrocarbons containing C = C double bonds, its scope has broadened, and the original term "disproportionation", used in the initial publications[1], no longer applies. A more appropriate name, "metathesis", was introduced in 1967[3] and is now commonly used. The reaction can be thought of as a net breaking and re-formation of two carbon = carbon bonds, as shown in Scheme 1.

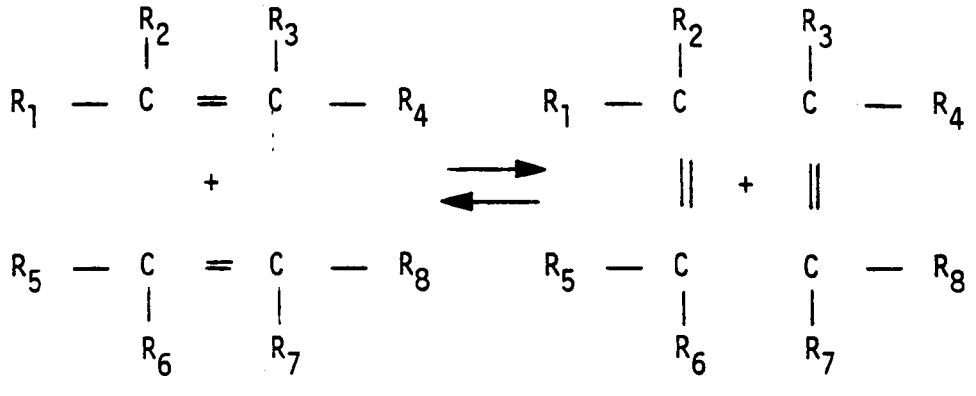

Scheme 1. Generalised Metathesis Reaction

Alkene metathesis reactions are believed to proceed through a single-step metallocarbene scheme involving a metallocyclobutane intermediate, as shown in Scheme 2. Support for the validity of this

generally accepted mechanism has been provided by very detailed kinetic and mechanistic studies[4].

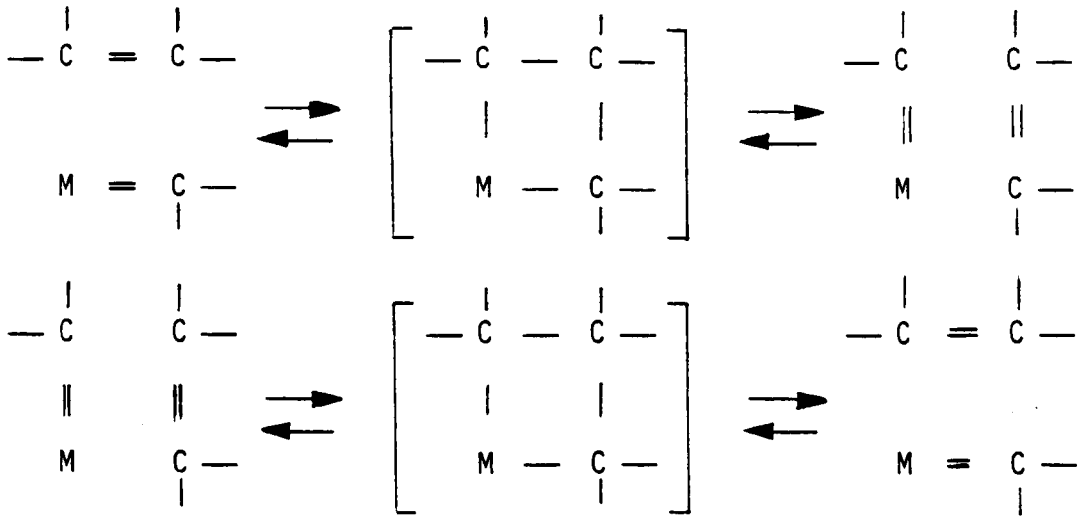

Scheme 2. Single-step Metallocarbene Mechanism

However, for predicting primary products of metathesis applications, a simple four-center concerted mechanism (Scheme 3) is adequate and more direct. As depicted in both schemes, the types and total number of bonds remain unchanged.

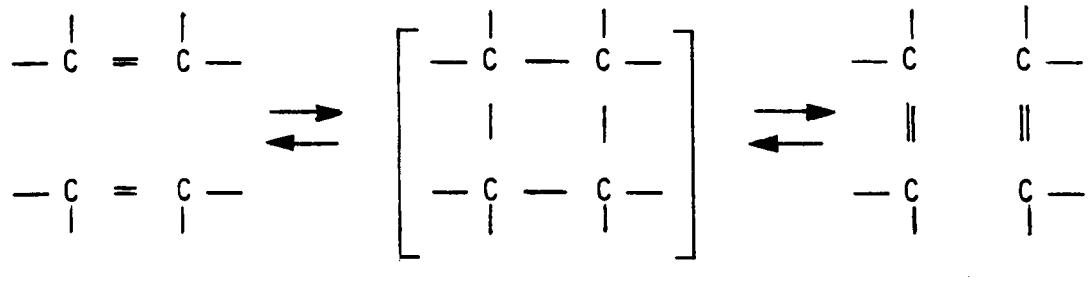

Scheme 3. Four-Center Mechanism for predicting products

Metathesis reactions of acyclic monoalkenes can be classified into (1) self-metathesis of a single alkene, and (2) cross-metathesis of double-bond isomers or of two different alkenes. In the first case, two primary metathesis products are produced; e.g. propene yields ethene and but-2-ene. In the second case, sets of both self- and

cross-metathesis products are obtained; e.g. a pent-1-ene + pent-2-ene mixture yields ethene + oct-4-ene, propene + hept-3-ene, but-1-ene + hex-2-ene, and but-2-ene + hex-3-ene. When ethene is one of the reactants (ethene cleavage), α-ethenes are produced; e.g. ethene cleavage of hex-3-enes yields but-1-ene. Cross-metathesis of acyclic with cyclic alkenes yields dialkenes; ethene cleavage of cyclic alkenes provides a new route to α, ω-alkenes as shown in Scheme 4. The metathesis of other types of alkenes and their mixtures, including dialkenes, ring-substituted alkenes (e.g. styrene), and functionally substituted alkenes, produces products consistent with schemes 2 and 3. In theory, the number of olefin metathesis reactions is limited only by the number of compounds containing carbon-carbon double bonds.

(b) Catalysts Systems

Current industrial applications of alkene metathesis using heterogeneous catalysts is high:

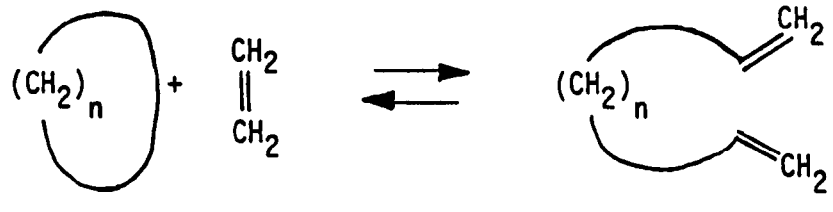

Scheme 4. Synthesis of α, ω-olefins

Among the more effective metathesis catalysts are the oxides of molybdenum, tungsten, and rhenium supported on high-surface-area alumina or silica[5-10]. Molybdenum oxide-alumina exhibits metathesis activity in the 373K - 473K temperature range. Tungsten oxide-silica is effective for metathesis in the 573K - 773K temperature range and is less susceptible to trace quantities of catalyst poisons in the feed stream than lower temperature alumina-based catalysts. Rhenium oxide-

alumina compositions are active metathesis catalysts at ambient conditions making them ideal for fundamental studies.

A typical example of the metathesis reaction is the conversion of propene into a mixture of ethene and cis- and trans- but-2-ene, which is catalysed by a variety of supported systems including those mentioned above. Catalytic reactions of propene have also been investigated over unsupported Na_xWO_3[11] to see how the metal-insulator transition of the catalyst affects the selectivity towards dimerisation or metathesis. It was found that dimerisation, producing mainly hexenes, was dominant over an insulating solid while metathesis, producing ethene and but-2-enes, was dominant over a conducting solid.

9.2 Experimental Procedure

The propene metathesis reaction was studied in the apparatus shown in Figure 9.1. It is composed of lines of gases that are purified and controlled before passing through the reactor, R. White spot nitrogen (BOC, 99.95% pure) was further purified by passing through a prereduced 10% Cu/SiO_2 trap, CS, maintained at 673K, to remove oxygen and a 5A molecular sieve trap, MS. Propene (Matheson, 99.98% pure) was used as delivered without any extra purification. N_2 gas flow was controlled by a Hoke valve, HV, and measured by a rotameter, RT. A soap bubble flowmeter, BF, connected by a bypass system was used for checking the hydrocarbon flow controlled by a Hoke valve. A trap of silica gel, SG, was connected at the end of the flowmeter for the removal of water from the hydrocarbon stream. It was changed every 24h. The Cu/SiO_2 trap in the apparatus was regenerated periodically by reduction in hydrogen for 2h at 673K.

Quantitative analysis of the metathesis products at the outlet

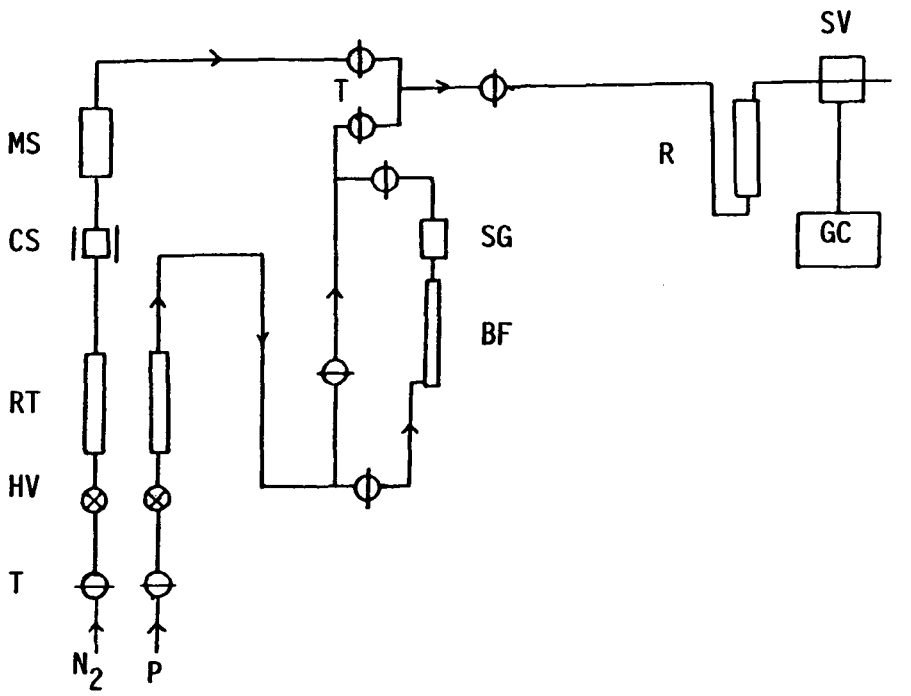

R = Reactor

CS = Cu/SiO_2 Catalyst (trap)

RT = Rotameters

BF = Soap bubble flowmeter

SG = Silica gel trap

T = Tap

GC = Gas Chromatograph

SV = Gas sampling valve

P = Propene gas

N_2 = Nitrogen gas

HV = Hoke valve

MS = Molecular sieve trap

Figure 9.1 Catalytic apparatus for propene metathesis

of the reactor was carried out by a gas chromatograph, GC, Perkin Elmer model 8500, with flame ionisation detector, and data acquisition and processing facilities. A column of 3% squalane on Alumina H, 100-200 mesh, was used to separate the products. The effluent from the reactor was fed to the chromatograph through a gas sampling valve, SV. The analysis was carried out under the following conditions:-

Pressure at inlet of column	=	130kPa
Temperature of column	=	353K
N_2 flow in column	=	$30cm^3min^{-1}$
Pressure of hydrogen	=	70kPa
Pressure of air	=	140kPa

The g.c. was calibrated by injecting a standard calibration gas mixture (Phase Separations Ltd.) containing defined amounts of the different components (i.e. reactant and products). The relative response coefficients were calculated by comparing the area of each peak with that of propene. Since the number of moles of each component is proportional to the peak area, then in a mixture of gases containing the different component, the molar percentage, C_j of any of them can be calculated by the equation:

$$C_j = \frac{100\ A_j\ k_j}{\sum A_i\ k_i}$$

where

A_j = peak area of component j

A_i = peak area of each component in effluent

k = response coefficient

The retention times and the response coefficients for the various products measured at the conditions indicated previously are shown in Table 9.1.

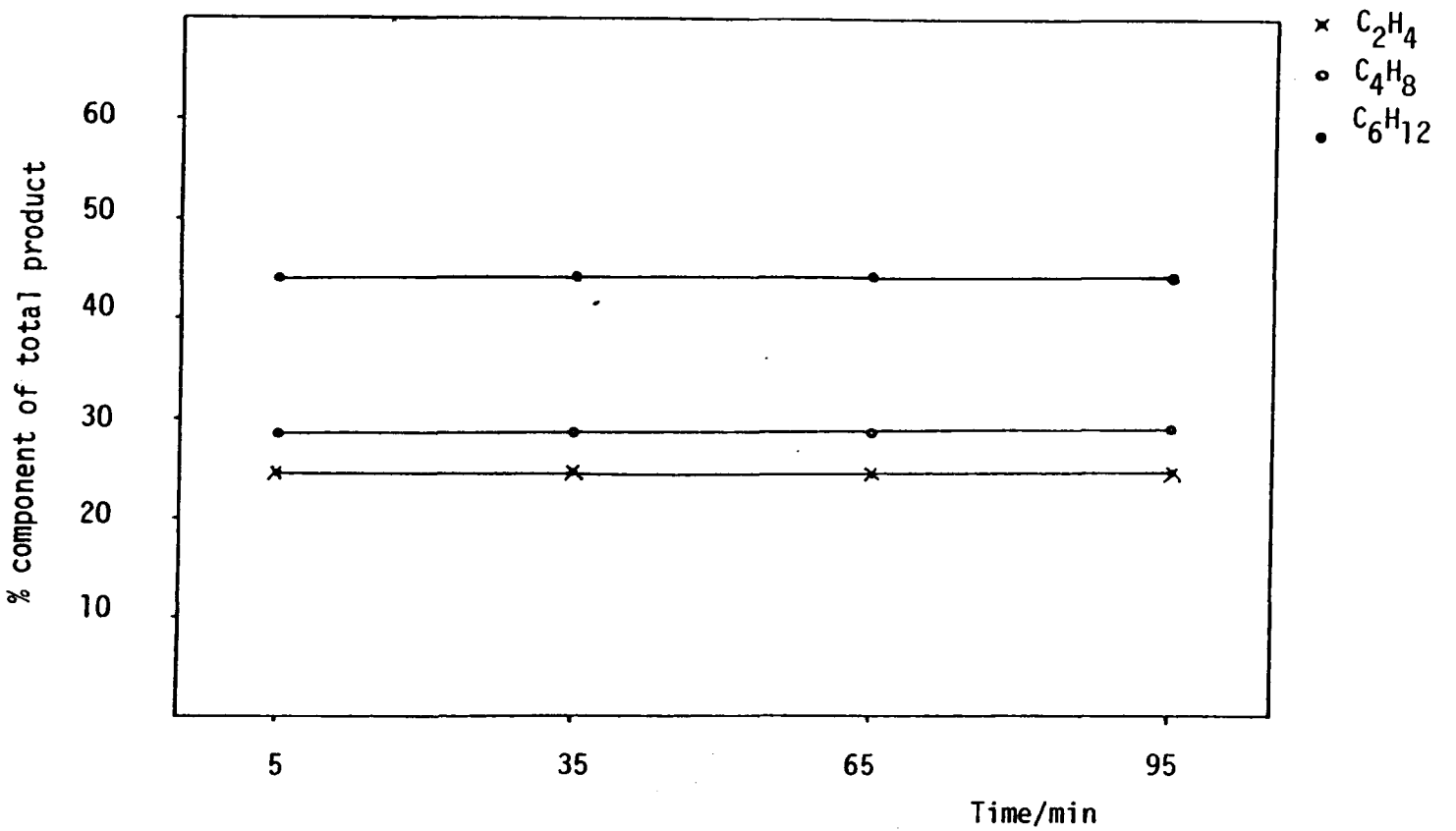

Figure 9.2 % component of total product versus time for the reaction of propene on WO_3

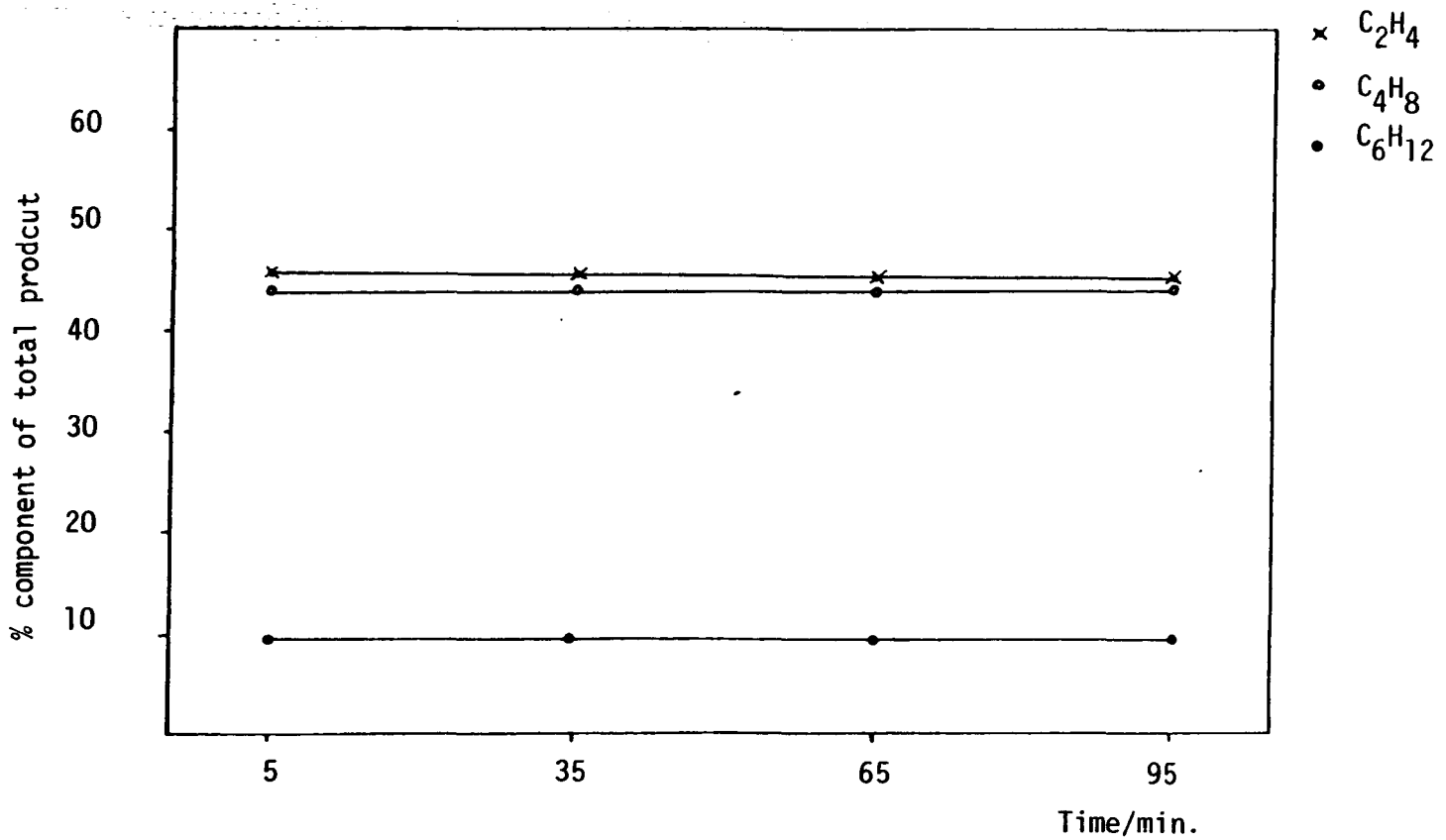

Figure 9.3 % component of total product versus time for the reaction of propene on 0.2KW

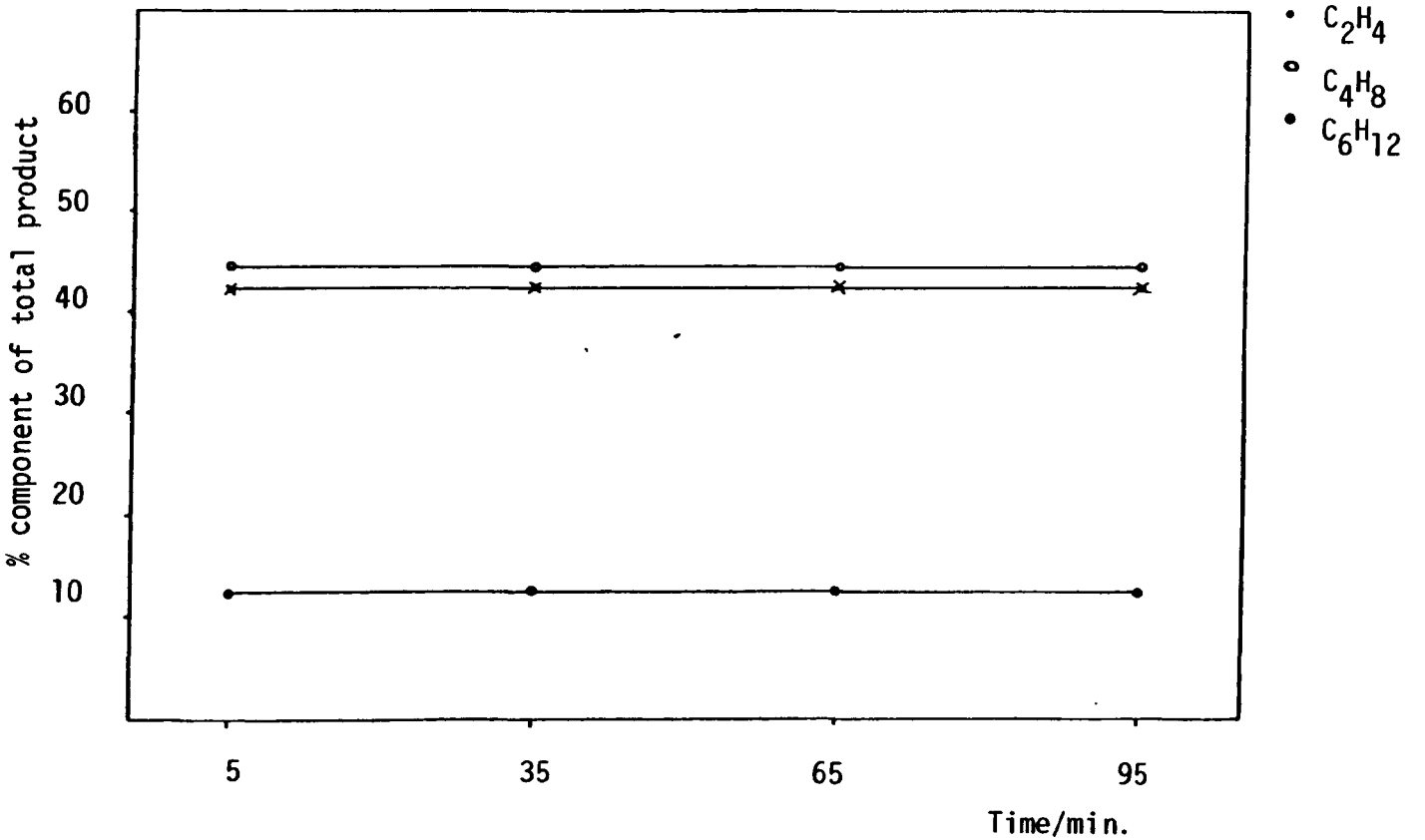

Figure 9.4 % component of total product versus time for the reaction of propene on 0.2NaW

A preliminary study has shown that the bronzes have little activity for propene reaction at temperatures below 673K. The temperature of 673K

Table 9.1

Product	Retention time/ min.	Response Coefficient
Methane	1.82	2.89
Ethane	2.64	1.54
Ethene	2.83	1.54
Propane	4.71	1.02
Propene	5.90	1.00
Butane	9.81	0.82
Butene	14.56	0.82
trans-2-butene	17.42	0.94
cis-2-butene	21.31	0.88
hexenes	29.51	0.54

was therefore selected for activity measurements.Tpr and tga studies have shown that the bronzes are stable at this temperature in both N_2 and H_2. Further tga experiments in a propene atmosphere have demonstrated that WO_3 and the bronzes showed no weight loss when heated in such an atmosphere up to a temperature of 723K. So it can be assumed that at 673K there is no bulk or surface reduction in the bronze in propene. Normally about 1.5g of the bronze was placed inside a fixed bed reactor fitted with a thermocouple and N_2 gas flowed over it. The sample was then heated to 673K ± 5K at $10Kmin^{-1}$ and the nitrogen flow replaced by propene, ($10cm^3min^{-1}$), and activity measurements were commenced. Activity was measured every 30 min. because of the high retention time of hexene.

9.3 Results

The catalytic reaction of propene on WO_3, K_xWO_3 and Na_xWO_3 has been studied under the conditions previously mentioned. The influence of the bronze composition on the reaction was investigated by comparing the changes in activity and selectivity of dimerisation and metathesis at 673K. It will be particularly interesting to see if the semi-conductor-metal transition in the bronze affects the selectivity towards dimerisation.

The reaction of propene on WO_3 at 673K gave ethene, but-2-ene and hexene as the major products. Figure 9.2 shows how the concentration and the selectivity of the products vary with time. There are insignificant changes in product concentration with the reaction time. A similar effect was observed on both the potassium and sodium bronzes. Figures 9.3 and 9.4 are representative of the variation of product concentration with time for samples 0.2KW and 0.2NaW respectively. Future reference will be made only to the products obtained after the sample has been exposed to the reactant for 65 min.

The major products obtained by the reaction of propene on WO_3 and the potassium bronzes of 673K are given in Table 9.2. Both metathesis and dimerisation coexist on these samples as products of both these reactions were obtained. Negligible traces of other hydrocarbons, (methane, ethane and propane) were also detected (i.e. $< 0.1\%$). Methane and ethane are most probably formed by the cracking of propane impurity present in the propene feedstock. Nominal amounts of but-1-ene and pentenes were also detected in most cases. These might have been the products of homogeneous reactions as a result of molecular collisions of propene at the temperature of reaction because they were produced even in the absence of a sample. The main component of hexene

was 2-methyl-2-pentene. A similar pattern of products was obtained for the reaction of propene on the sodium bronzes, as shown in Table 9.3.

Table 9.2 Major Products obtained over WO_3 and K_xWO_3

	% component of total product		
x in K_xWO_3	C_2H_4	2-C_4H_8	C_6H_{12}
0	26.9	28.7	44.4
0.05	30.5	31.5	38.0
0.2	45.9	44.5	9.6
0.3	37.8	46.3	15.9
0.6	41.4	37.9	20.7
0.8	37.5	45.8	16.7

The rate of metathesis and dimerisation was calculated from the amount of propene converted either to metathesis products, (ethene and but-2-enes), or dimerisation products, (hexenes), from the fact that

Table 9.3 Major Products obtained over Na_xWO_3

	% component of total product		
x in Na_xWO_3	C_2H_4	2-C_4H_8	C_6H_{12}
0.05	27.9	30.0	42.1
0.2	42.9	44.4	12.7
0.3	43.1	41.3	15.6
0.6	41.0	35.9	23.1
0.8	38.7	40.3	21.0

2 moles of propene are required to produce either 1 mole of but-2-ene

and 1 mole of ethene, or 1 mole of hexenes by the routes shown below:

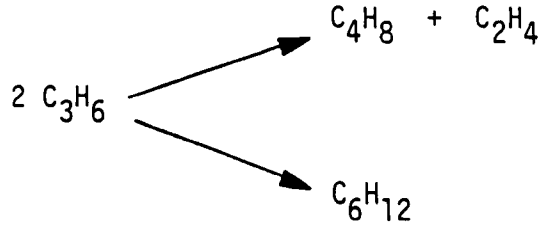

The percent propene converted in the metathesis and dimerisation reactions are then given by equations 9.1 and 9.2

$$\% \text{ conversion (metathesis)} = \frac{A}{A + B + C_3} \times 100 \quad \ldots\ldots\ldots \quad 9.1$$

$$\% \text{ conversion (dimerisation)} = \frac{B}{A + B + C_3} \times 100 \quad \ldots\ldots\ldots \quad 9.2$$

where $A = 2C_4$ (C_4 = cis and trans but-2-ene or ethene).

$B = 2C_6$ (C_6 = hexenes)

C_3 = propene

C_i = No. of moles of compound i calculated from the peak area using the response coefficient for the FID detector.

The rate (mmol $g^{-1}_{(sample)} h^{-1}$) was then calculated using the percent conversion, and is given by equation 9.3

$$\text{rate (mmol } g^{-1}_{(sample)} h^{-1}) = \frac{C}{100} \times F \times 60 \text{ min} \times \frac{1}{W} \times \frac{1}{22414} \times 1000 \quad \ldots\ldots\ldots \quad 9.3$$

where C = percent conversion for either metathesis or dimerisation

F = flow rate of propene gas

W = weight of sample used

22414 $cm^3 mol^{-1}$ = molar volume of gas at S.T.P.

Tables 9.4 and 9.5 show the rates of metathesis and dimerisation for WO_3, K_xWO_3 and Na_xWO_3, where $0.05 \lesssim x \lesssim 0.8$, respectively. It would

be more interesting to compare the rate per unit area of surface for each of the samples, since krypton adsorption has shown the surface area of the bronzes varies with alkali ion content. These values are also quoted in Tables 9.4 and 9.5 (Figures in brackets). Figures 9.5 and 9.6 are reported plots of the rate of dimerisation and metathesis (mmol m^{-2} h^{-1}) against alkali ion content for the potassium and sodium

Table 9.4 Rate of Dimerisation and Metathesis for WO_3 and K_xWO_3

x in K_xWO_3	Rate of dimerisation/ mmolg^{-1} h^{-1}		Rate of metathesis/ mmolg^{-1} h^{-1}	
0	0.41	(0.37)	0.09	(0.08)
0.05	0.22	(0.21)	0.19	(0.18)
0.2	0.08	(0.10)	0.38	(0.49)
0.3	0.04	(0.15)	0.12	(0.46)
0.6	0.03	(0.19)	0.06	(0.38)
0.8	0.01	(0.10)	0.03	(0.30)

(Figures in brackets correspond to rates in mmol m^{-2} h^{-1})

Table 9.5 Rate of Dimerisation and Metathesis for Na_xWO_3

x in Na_xWO_3	Rate of dimerisation/ mmolg^{-1} h^{-1}		Rate of metathesis/ mmolg^{-1} h^{-1}	
0.05	0.19	(0.20)	0.13	(0.14)
0.2	0.10	(0.16)	0.35	(0.55)
0.3	0.05	(0.12)	0.14	(0.33)
0.6	0.03	(0.23)	0.05	(0.38)
0.8	0.04	(0.31)	0.07	(0.54)

(Figures in brackets correspond to rates in mmol m^{-2} h^{-1})

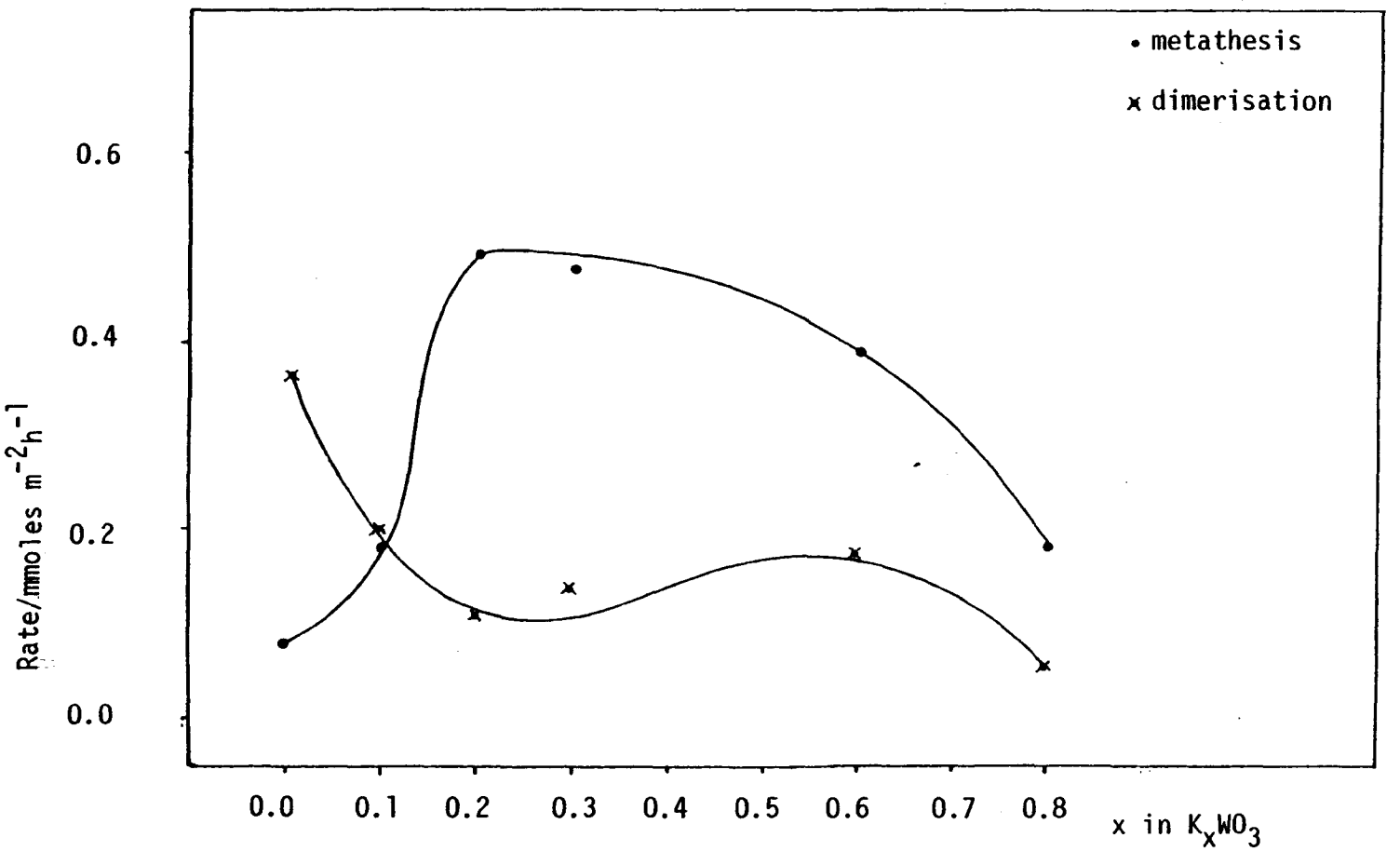

Figure 9.5 Rate of dimerisation and metathesis versus x in K_xWO_3

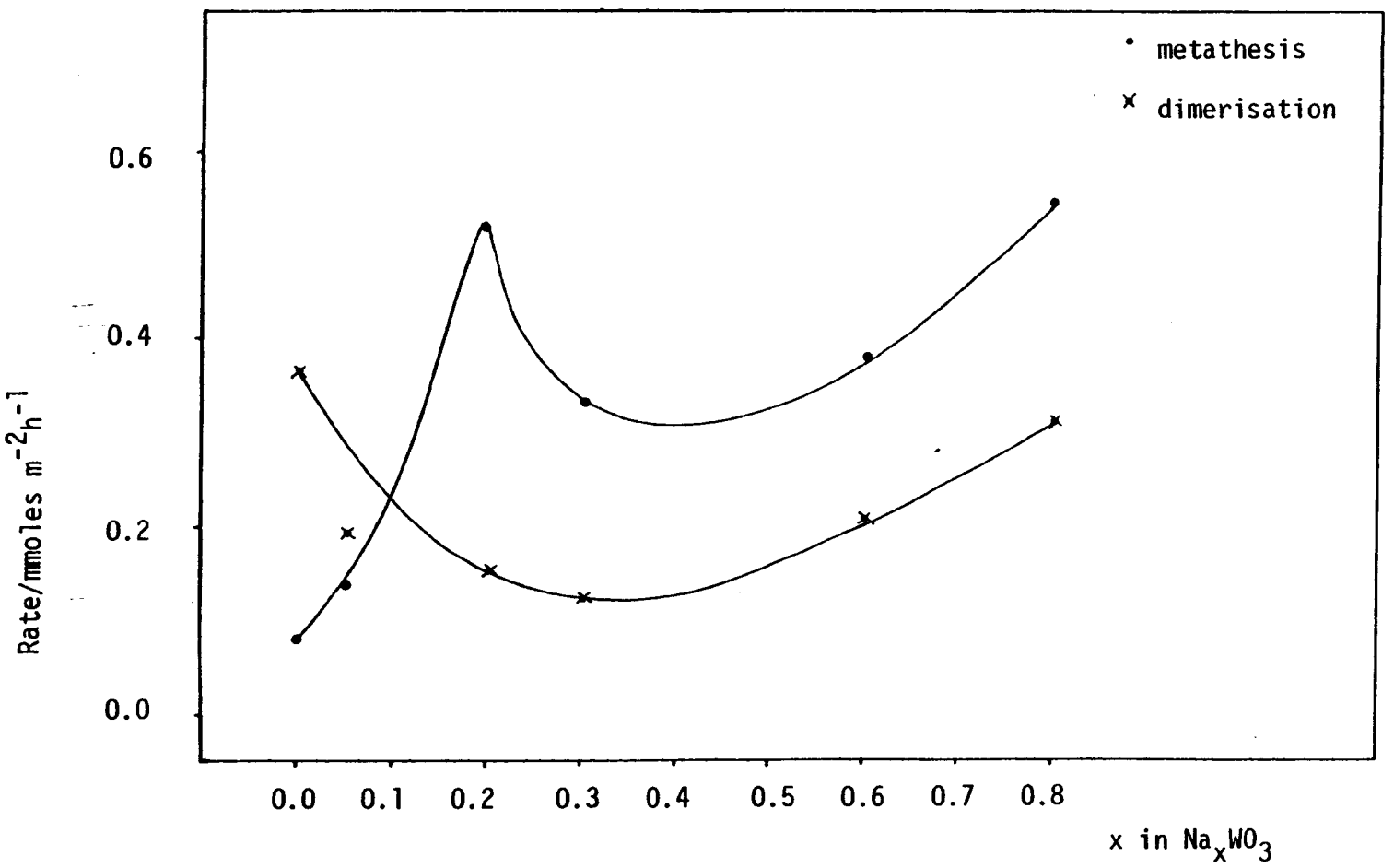

Figure 9.6 Rate of dimerisation and metathesis versus x in Na_xWO_3

bronzes respectively. The selectivities for dimerisation and metathesis were also determined. The selectivities were defined by equations 9.4 and 9.5.

$$S_D = \frac{r_D}{r_D + r_m} \quad \ldots\ldots\ldots\ldots\ldots 9.4$$

$$S_m = \frac{r_m}{r_m + r_D} \quad \ldots\ldots\ldots\ldots\ldots 9.5$$

where S_D and S_m are the selectivities for dimerisation and metathesis respectively, and r_D and r_m are the rates for dimerisation and metathesis respectively. Figures 9.7 and 9.8 show the selectivities for dimerisation and metathesis for the potassium and sodium bronzes respectively as a function of the alkali ion content.

9.4 Conclusions

Dimerisation of propene has been found to be dominant over WO_3 and metathesis over ReO_3. WO_3 is a semiconductor oxide and ReO_3 is electrically metallic. In the present study it was intended to see whether the selectivity of the reaction changes with increase in alkali metal ion concentration in the sodium and potassium bronzes, A_xWO_3, where A = Na or K and $0.05 \leqslant x \leqslant 0.8$, since it has been found that there is a change from semiconductor to metallic properties as x increases in either series of bronze (see Chapter 7). The reaction of propene over unsupported catalysts is characterised by small turnover numbers, oxygen vacancy dependencies and stereoselectivity of but-2-enes[7,12]. The sodium and potassium bronzes with x = 0.05 produce approximately equal amounts of metathesis and dimerisation products with a slightly higher selectivity toward dimerisation. These bronzes

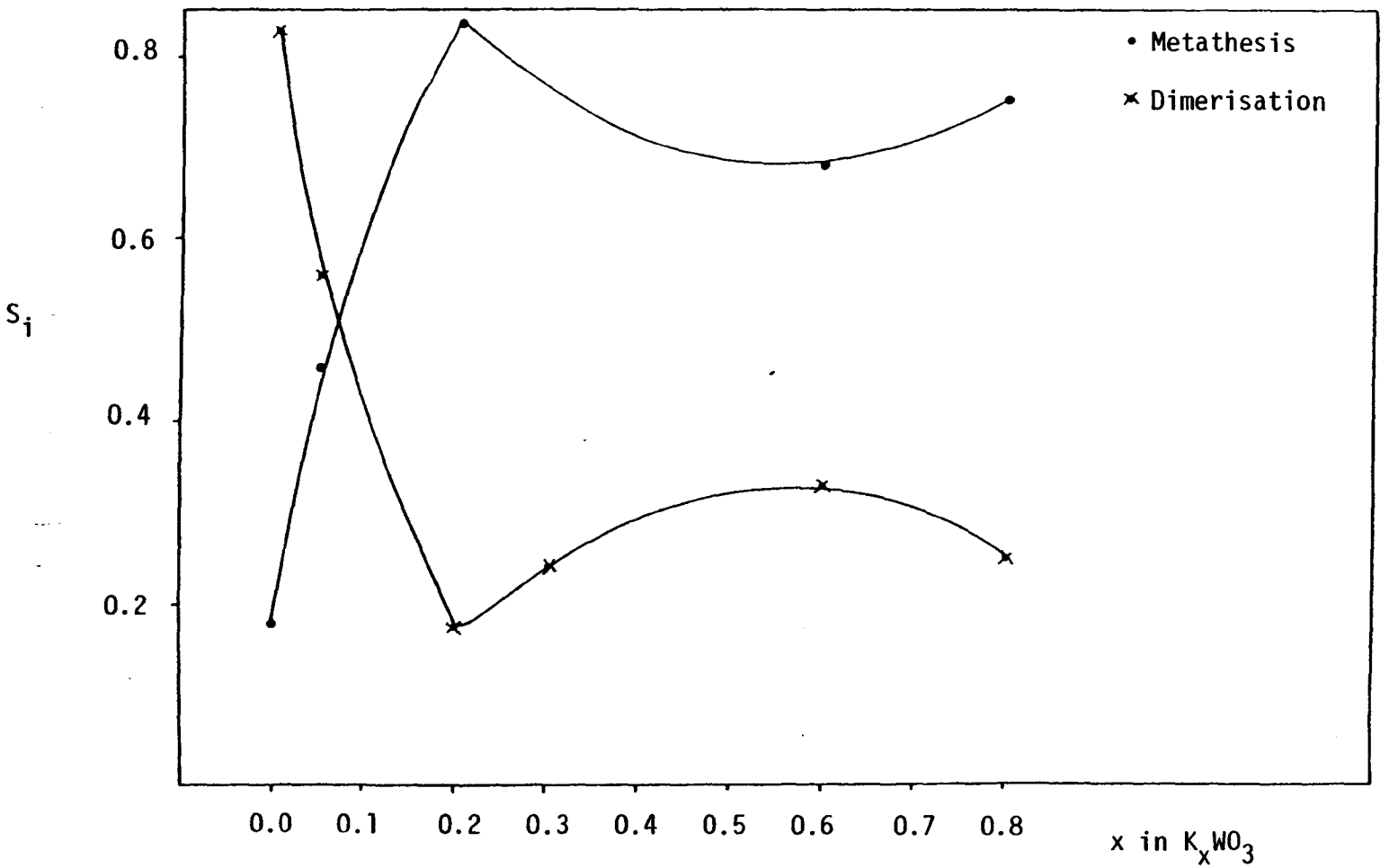

Figure 9.7 Selectivity, (S_i), for dimerisation and metathesis versus x in K_xWO_3

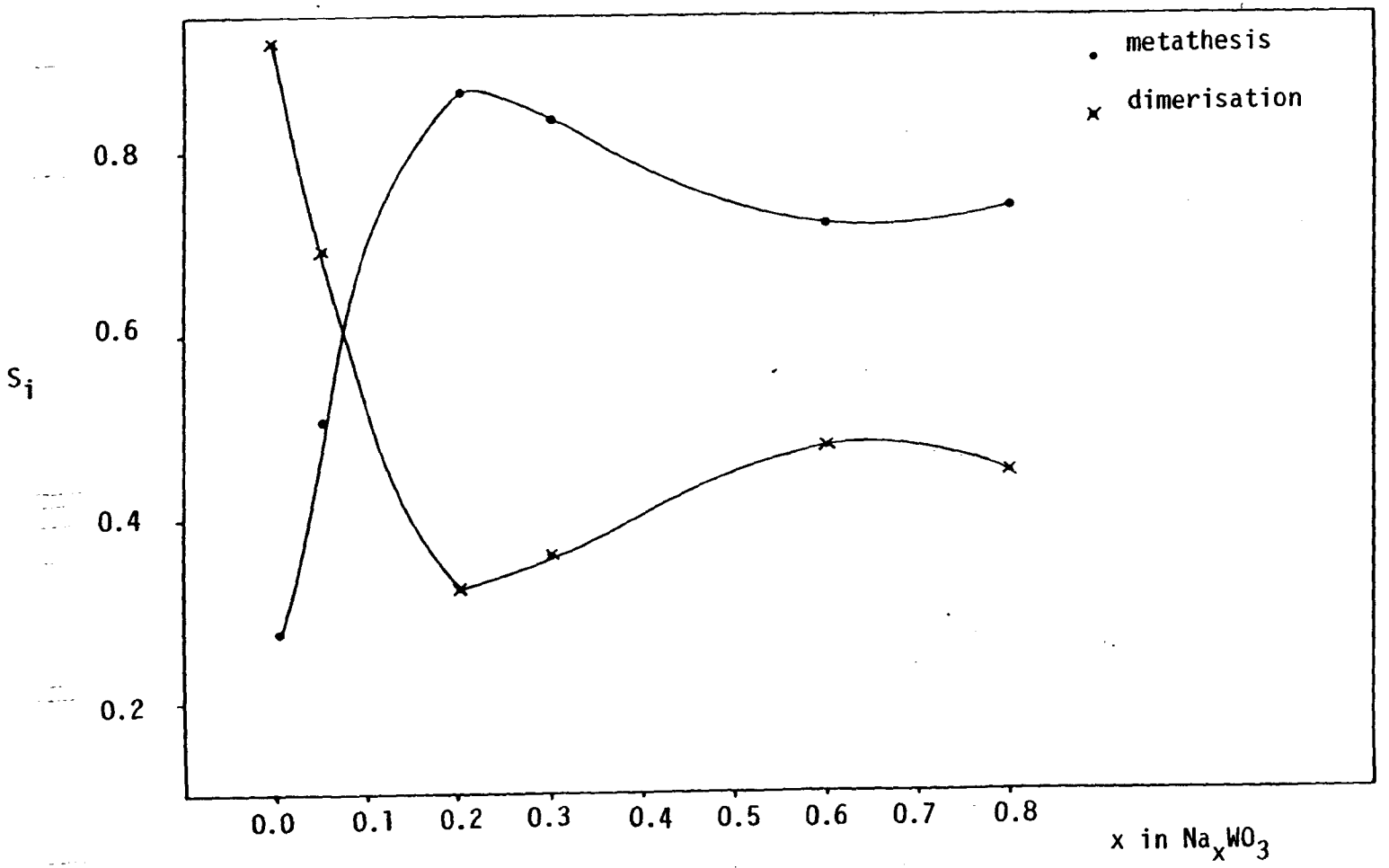

Figure 9.8 Selectivity, (S_i), for dimerisation and metathesis versus x in Na_xWO_3

have semiconductor properties and perhaps would have been expected to show a much higher selectivity for dimerisation. One of the possible explanations for the formation of metathesis products could be the high temperature used (673K) to enable a reliable activity measurement to be obtained. However, at such a temperature the reduction of the bronzes by propene was not appreciable since no weight loss was observed when the samples were heated in propene to 723K in tga experiments. It has been reported that reduction of oxides is very effective to enhance metathesis and to suppress dimerisation. However, for the present bronzes, activity measurements performed after exposing the bronzes to propene for over 65 min showed no significant change in product distribution. For bronzes with $x > 0.05$, both metathesis and dimerisation products were observed and in no case was complete selectivity for either metathesis or dimerisation obtained. However, an increase in selectivity for metathesis was observed when $x = 0.2$ for both sodium and potassium bronzes, and in all other samples the selectivity for metathesis was much higher than with $x = 0.05$. The metathesis activity was slightly enhanced with increase in x as seen from Tables 9.1 and 9.2. As can be seen, C_6H_{12} is appreciable even when the metathesis reaction is expected to be solely active. On these samples small amounts of pentenes were also observed. They may be produced by co-dimerisation of the metathesis products assuming reactions such as

$$C_4H_8 + C_2H_4 \longrightarrow C_6H_{12},$$

$$C_4H_8 + C_4H_8 \longrightarrow C_2H_4 + C_6H_{12}$$

or $C_3H_6 + C_5H_{10}$ etc.

The cis/trans ratio of but-2-ene is given as a function of x in Table 9.6. As shown, the ratio appears to increase with x for either series

of bronze. This ratio has often been used as an indication of the stereoselectivity of the reaction, and for the characterisation of the reaction centre. For a rhenium/alumina catalyst Lin et al[5] found that the cis/trans ratio of but-2-ene becomes smaller as the anion vacancies increased. Davie et al[13] reported that cis- but-2-ene was sometimes produced more than the trans isomer initially from C_3H_6 when a supported molybdenum hexacarbonyl catalyst was used. Basset et al[14] found that the cis/trans ratio of C_4H_8 from cis-2-C_5H_{10} is larger using a supported catalyst than using a homogeneous one. Katz and McGinnis[15] explained the stereoselectivity by the metal-carbene model and Leconte and Basset[8] explained it in more detail by taking into account the various static interactions among substituents in the metallocyclobutane transition state.

Table 9.6 Cis/trans Ratio of but-2-ene obtained for WO_3, K_xWO_3 and Na_xWO_3

Sample	Cis/trans ratio
WO_3	1.31
0.05KW	1.59
0.2KW	1.38
0.3KW	1.92
0.6KW	2.23
0.8KW	2.51
0.05NaW	1.68
0.2NaW	1.34
0.3NaW	1.65
0.6NaW	1.84
0.8NaW	2.23

CHAPTER 9

REFERENCES

1. R.L. Banks and G.C. Bailey, Ind. Eng. Chem. Prod. Res. Dev., 3, 170, (1964).
2. R.L. Banks, Chemtech., 9, 494, (1979).
3. N. Calderon, H.Y Chen and K.W. Scott, Tetrahedron Lett., 34, 3327, (1967).
4. R.L. Banks, In 'Catalysis' Spec. Period. Rep., 4, 100, (C. Kemball ed), Chemical Society, London, (1981).
5. C.J. Lin, A.W. Aldag and A. Clark, J. Catal., 45, 287, (1976).
6. X. Xiaoding, C. Boelhouwer, J.I. Benecke, D. Vonk, and J.C. Mol, J. Chem. Soc. Faraday Trans. I, 82, 1945, (1986).
7. N. Tsuda and A. Fujimori, J. Catal., 69, 410, (1981).
8. M. Leconte and J.M. Basset, J. Am. Chem. Soc., 101, 7296, (1979).
9. R.M. Edreva-Kardjieva and A.A. Andreev, J. Catal., 97, 321, (1986).
10. R. Thomas, J.A. Mouljin, V.H. J. De Beer and J. Medema, J. Mol. Catal., 8, 161, (1980).
11. N. Kosaka, Y. Sakai and N. Tsuda, J. Catal., 98, 95, (1986).
12. N. Tsuda, T. Mori and Y. Sakai, J. Mol.Catal., 28, 183, (1985).
13. E.S. Davie, D.A. Whan and C. Kemball, J. Catal., 24, 272, (1972).
14. J.M. Basset, J.L. Bilhou, R. Martin and A. Theolier, J. Am. Chem. Soc., 97,7376, (1975).
15. J.T. Katz and J. McGinnis, J. Am. Chem. Soc., 97, 1592, (1975).

CHAPTER 10

A SILICA-SUPPORTED BRONZE AND A COPPER BRONZE

10.1 Introduction

The tungsten bronzes have shown some interesting catalytic properties such as in the decomposition of isopropanol, the metathesis of propene and the electrochemical reduction of oxygen[1]. A previous study by the author[2], has demonstrated that potassium tungsten bronzes can be prepared on an alumina support, and have shown activity for ammonia synthesis. It was therefore interesting to investigate if a potassium tungsten bronze in a highly dispersed state could also be prepared on a silica support, and its activity compared with that for the alumina-supported bronze (see Chapter 2). Bronzes prepared on an inert support would have more surface active sites and hence could be expected to be more active than the unsupported bronzes.

Copper containing catalysts are widely used in the methanol synthesis and decomposition reactions and the water-gas-shift reaction. There is much uncertainty as to the precise oxidation state of Cu in these catalysts under reaction conditions[3], recent work however,[4] has suggested that Cu in a positive oxidation state is involved in the catalysis of these reactions. A copper containing bronze in which the Cu will be intercalated in a high oxidation state, even under reaction conditions, could be useful in determining the active sites in methanol synthesis and the water-gas-shift reactions. However, a Cu containing bronze is difficult to prepare by a thermal method due to thermodynamic limitations at the high temperature required to overcome kinetics, hence the preparation of $Cu_yK_xWO_3$ was attempted by an ion-exchange method. (See Chapter 2). The two approaches to producing

bronze catalysts of higher activity have therefore been attempted and and the results obtained are now described.

10.1.1 Supported Catalysts

A catalysed reaction usually occurs on certain specific active sites at the surface, and it is therefore normally desirable to provide as much surface area as possible. A widely-used procedure to achieve a high surface area is to distribute the active component over the surface of relatively-inert oxide particles of high porosity such as alumina, silica, titania and activated charcoal supports. The advantages of using supported catalysts in preference to unsupported ones (e.g. Pt sols or blacks) have long been appreciated. The support facilitates the formation of extremely small metal particles having a high proportion of surface atoms; the particles also have remarkable thermal stability and the presence of the support allows the incorporation of beneficial additives usually known as promoters. Supports were long thought to be catalytically inert, except in the special case of bifunctional platinum and alumina catalysts for petroleum reforming. Recently there has arisen evidence that in some systems at least the support can exert a marked influence over the properties of metal particles residing on it, in the form of strong metal support interaction.

Previous studies[2] have shown that hexagonal potassium tungsten bronzes supported on alumina have shown some catalytic activity for the synthesis of ammonia from its molecular elements. In the present study an hexagonal potassium tungsten bronze supported on silica was prepared (see Chapter 2) and its catalytic activity for ammonia synthesis determined. Silica was chosen as the support to

investigate whether bronze formation is easier on its surface than on the surface of alumina, (and hence whether the support had a more positive role in defining catalytic activity).

10.1.2 Copper Catalysts

Copper is one of the most widely used base metals for catalytic reactions. Two of the most common reactions where copper catalysts are used are the water-gas-shift reaction and methanol synthesis. Recently there has been a renaissance of interest concerning copper catalysis of water-gas-shift, methanol synthesis and methanol decomposition reactions and the role of promoters. However, there is much uncertainty as to the precise oxidation state of the active copper phase under reaction conditions[3] and the symmetry of the surface copper sites and how this is affected by precursor states[5,6]. For methanol synthesis from CO (and its decomposition) Cu is more active when supported on ZnO than on titania[7];this is also true for the water-gas-shift reaction. Sermon et al[4] have recently shown that copper in Cu $Fe_xCr_{2-x}O_4$ spinels is as active as Cu/ZnO in the aforementioned reactions under conditions where it would not have been reduced as significantly as Cu/ZnO. Maximum activity was shown in these spinels at intermediate composition when Cu in a positive oxidation state may be close in adjacent octahedral and tetrahedral sites. It was assumed that Cu in a positive oxidation state can be involved in the catalysis of these reactions and catalysts where Cu (II) is highly dispersed in constraining lattices may be useful.

In the present study a sample was prepared whereby K^+ ions in a bronze were ion-exchanged with cupric ions from solution in order to insert cupric ions in the bronze. The sample was tested for its activity in methanol synthesis and the water-gas-shift reaction. N_2O

decomposition was attempted in order to evaluate the copper surface area.

10.1.3 Catalysed Reactions

Reactions which could be catalysed by the bronze phases described above were used; in a sense such catalysed reactions were capable of probing the local chemistry prevailing at these non-stoichiometric surfaces in a manner not possible by other methods. In addition, one adsorptive-decomposition (N_2O) was also used. These are individually reviewed briefly now.

(i) The Water-Gas-Shift Reaction

The water gas shift (WGS) reaction is a reversible, exothermic chemical reaction of considerable industrial importance and is the reaction of water and carbon monoxide to produce carbon dioxide and hydrogen:-

$$CO + H_2 \rightleftarrows CO_2 + H_2 \quad \Delta H_{298K} = -40.6 kJmol^{-1} \quad \ldots\ldots\ldots\ldots \quad 10.1$$

The WGS process is most frequently used in conjunction with the production of hydrogen via the steam reforming of hydrocarbons:-

$$C_nH_m + nH_2O \rightarrow nCO + (n + m/2)\, H_2 \quad \ldots\ldots\ldots\ldots \quad 10.2$$

$$CO + H_2O \rightleftharpoons CO_2 + H_2 \quad \ldots\ldots\ldots\ldots \quad 10.3$$

$$CO + 3H_2 \rightleftharpoons CH_4 + H_2O \quad \ldots\ldots\ldots\ldots \quad 10.4$$

Reaction (10.2), under steam-reforming conditions is considered irreversible and essentially complete. Normally reactions (10.3) and (10.4) at the exit of the steam-reforming reaction are nearly at equilibrium. The high temperature in the reformer favours H_2 production by shifting the equilibrium of reaction (10.4) far to the left. The

effluent from the steam reformer is then passed to a series of WGS reactors operated at lower temperatures in order to shift the equilibrium of reaction (10.3) to the right. Many materials are capable of catalysing the WGS reaction. Moe[8] gives a good discussion of potential shift catalyst systems. Two classes of materials are almost exclusively used in industry as shift catalysts: the iron-based catalysts and the copper based catalysts. The iron-based catalysts are the so-called high-temperature shift catalysts, operating from about 593K - 723K[9]. These materials are an example of some of the earliest heterogeneous catalysts used industrially. Copper-base shift catalysts are a more recent development which has now gained wide industrial acceptance. These are the so-called low-temperature shift catalysts operating from about 473K - 523K. These catalysts show good activity at low temperatures and are therefore attractive since equilibrium is more favourable at lower temperatures[10]. Although many mechanistic studies of the water-gas-shift reaction on iron-based catalysts have been made, there is still considerable dispute in this area. This concerns whether the correct mechanism is the oxidation-reduction mechanism proposed by Temkin et al[11,12] or the mechanism employing stoichiometric numbers proposed by Oki et al[13-16] A review by Newsome[17] covers both possible mechanisms in detail and concludes that the mechanisms suggested by Oki and associates[13-16] are theoretically possible while that proposed by Temkin et al[11,12] is not plausible for the shift reaction over iron-based catalysts. Since low-temperature shift catalysts, are relatively new, the mechanism of the shift reaction on these copper-based catalysts have not been studied nearly as extensively as with the high-temperature iron-based catalyst systems. Yur'eva et al[18] offered the following mechanism, where the reaction takes place through an active complex on the surface, including both CO and H_2O, and where the third step is the

rate-determing step:

$$CO \rightleftharpoons CO_{ads}$$

$$H_2O \rightleftharpoons H_2O_{ads}$$

$$CO_{ads} + H_2O_{ads} \rightleftharpoons CO_{2_{ads}} + H_{2_{ads}}$$

$$CO_{2_{ads}} \rightleftharpoons CO_{2_{gas}}$$

$$H_{2_{ads}} \rightleftharpoons H_{2_{gas}}$$

In the present study the $Cu_yK_xWO_3$ system was studied for its activity in the water-gas-shift reaction.

(ii) Methanol Synthesis

Methanol synthesis is a process of major industrial importance consisting of hydrogenation of carbon monoxide or of carbon dioxide according to the equations;

$$CO + H_2 \rightleftharpoons CH_3OH \qquad \Delta H_{600K} = -100.46 kJmol^{-1}$$

and

$$CO_2 + 3H_2 \rightleftharpoons CH_3OH + H_2O \quad \Delta H_{600K} = +45.36 kJmol^{-1}$$

Methanol synthesis from carbon monoxide formally consists of an attachment of three hydrogen atoms onto the carbon end and of one hydrogen atom onto the oxygen end of the CO molecule without the cleavage of the carbon-oxygen bond. The two bonding π-orbitals of carbon monoxide, the lone pair ($5\sigma^*$) orbital of carbon, and the σ orbitals of two hydrogen molecules are utilised to make three C-H sigma bonds, one O-H sigma bond, and one additional lone pair orbital on the oxygen atom, schematically;

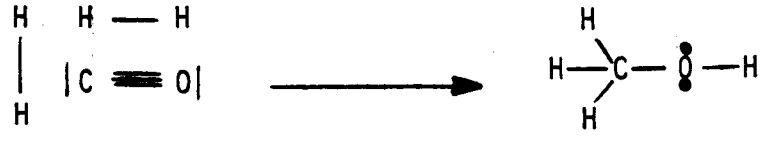

The carbon-oxygen sigma (3σ) and the lone-pair oxygen (4σ) orbitals remains intact except for a change in electron repulsion. These features of the reaction impose the following requirements on the catalyst:

(a) The catalyst must not cleave the carbon-oxygen sigma bond.

(b) The catalyst must activate the carbon monoxide molecule so that hydrogenation can occur on both ends of the molecule.

(c) The catalyst must be a fairly good hydrogenation catalyst which activates hydrogen molecules in a manner suitable for the above reaction.

Good "metallic" catalysts for methanol synthesis have been known for a long time[19,20]. They are based on copper and combinations of various oxides, (e.g. ZnO, Al_2O_3 and Cr_2O_3). A recently studied catalyst is the copper-thoria, (Cu/ThO_2)[21], system which shows good selectivity for methanol but not as high as that of the Cu/ZnO catalyst. Among the transition metals various forms of Pd, Pt, Ir and Rh have been reported active in methanol synthesis[22-24]. In the present study the $Cu_yK_xWO_3$ sample was studied for its activity in methanol synthesis, because of the ability of the constraining host lattice to keep the copper in a high oxidation state.

(iii) Ammonia Synthesis

The fixation of atmospheric nitrogen in the form of ammonia is one of the foundations of the modern chemical industry. From 1820 to 1900 many futile attempts were made to use platinum and various other substances to catalyse the exothermic synthesis reaction;

$$N_2 + 3H_2 \longrightarrow 2NH_3 \quad \Delta H = -109 KJmol^{-1}$$

At the beginning of this century a promoted iron catalyst with the

addition or substitution of other promoters was eventually developed and is still the catalyst universally used today.

Several "new" ammonia synthesis catalysts have been claimed, reported and patented. The addition of cobalt and ruthenium to the currently used iron catalyst has attracted considerable attention. The use of carbon- and alumina- supported ruthenium catalysts has also been extensively studied[25-27]. Ruthenium supported on silica gel or alumina shows catalytic behaviour for the ammonia synthesis reaction similar to that exhibited by ruthenium-carbon catalysts[28]. Recent studies indicate a very good possibility of producing a new catalyst that would have perhaps twice the activity of today's commercial catalyst[29]. A number of metallic catalysts have been examined for their activity in ammonia synthesis. In a review by Mittasch[30], the relative efficiencies of pure metals as catalysts for ammonia synthesis under 10MPa at 823K were given long ago, these are shown in Figure 10.1 as a plot of percent ammonia in the exit gas against the parameter, $(-\Delta H_0^0)$, for the heat of chemisorption. It is obvious that osmium and iron are the most effective metals under these conditions.

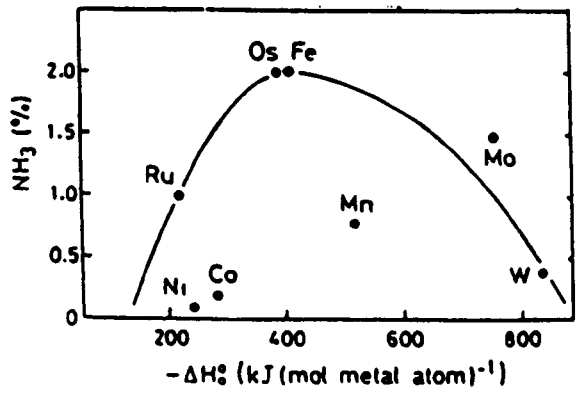

Figure 10.1 The ammonia synthesis capacities of metals as a function of the heat of chemisorption of nitrogen.

Although tungsten shows a low catalytic activity as a result of its high strength of nitrogen chemisorption, this could be enhanced by the presence of potassium and controlled by raising the tungsten to a higher oxidation state. Recently Ozaki[25] has developed a catalyst system promoted by metallic potassium. In the present study a silica supported potassium tungsten bronze was studied for its activity in ammonia synthesis (in the light of the author's earlier results, see Appendix 1), with specific comparison with activities of alumina-supported potassium tungsten bronzes prepared previously[2].

(iv) N_2O Decomposition

Traditionally, metal surface areas have been determined by chemisorption of a suitable adsorbate. Both carbon monoxide and hydrogen have been used to measure copper surface areas although neither adsorbate is thought to provide accurate results[31]. The reaction of nitrous oxide has been used to measure metal surface areas for both pure and supported copper catalysts[32-35]. The methods are based on the decomposition of a nitrous oxide molecule on a copper surface which is accompanied by the liberation of one nitrogen molecule according to:-

$$N_2O_{(g)} + 2Cu_s \longrightarrow N_{2(g)} + (Cu\text{-}O\text{-}Cu)_s \quad \ldots\ldots\ldots\ldots \quad 10.5$$

where the subscript s signifies surface atoms. Previous investigations have differed in the experimental methods and reaction conditions used to measure the extent of reaction (10). Osinga et al[33] adopted the method of Dell et al[32] in which nitrogen formed by reaction (10.5) was determined by freezing out the excess of N_2O and measuring the residual nitrogen pressure in a conventional volumetric adsorption apparatus. Scholten[34] used both microcatharometric and mass spectroscopic methods to determine the gas composition in a vacuum apparatus in which reaction gases were recycled. In the present study the

copper surface area in $Cu_yK_xWO_3$ was determined using a volumetric adsorption apparatus,and a Cu/O atomic adsorption stoichiometry of 2:1 was assumed. It was judged that the 'equivalent' copper surface area would contain 1.4×10^{19} Cu atoms per m^2.

10.2 Experimental Procedures

10.2.1 Physical Characterisation of SiO_2 Supported Bronze and $Cu_yK_xWO_3$

The different physical methods of characterising catalysts described in the previous chapters were used to study the SiO_2 supported sample and the ion exchange sample. Tpr (see Chapter 4) was used to investigate the reduction of the potassium polytungstate on SiO_2, to determine the temperature at which a bronze is formed and give information on the nature of the bronze; tpr was also used to investigate the reducibility of $Cu_yK_xWO_3$ and whether copper has any effect on the reduction temperature of the bronze. The structures of the two bronzes were analysed by XRD, (see Chapter 5). Xps, (see Chapter 6), revealed their compositions and whether there was any surface enrichment.

10.2.2 Water-Gas-Shift Reaction

Rates of conversion in the water-gas-shift reaction,

$$CO + H_2O \rightleftharpoons CO_2 + H_2$$

were measured in a silica reactor with samples (0.5g) of $Cu_yK_xWO_3$ which were first reduced in 6% H_2 in N_2 ($40cm^3min^{-1}$, 101kPa) during heating at 4K min^{-1} from ambient to 623K, at which temperature the sample was held for 15 min. The sample was then cooled in a flowing N_2 stream ($40cm^3min^{-1}$, 101kPa) to the reaction temperature 523K ± 2K which was achieved in an electric furnace (VB35; Stanton Redcroft; controlled by

Eurotherm 810 : Thermal Designs Ltd.). After flushing at this temperature 2.5% CO/N_2 (101kPa) was introduced at a constant flow rate ($20cm^3min^{-1}$) after it had been saturated with water vapour (2.4kPa; 293K) through the catalyst at 523K and the product stream was analysed at 5 min intervals on a gas chromatograph (Perkin Elmer Sigma 4; TCD detector; poropak Q column at 303K). The g.c. was calibrated by injecting a fixed volume of H_2 and the method to calculate conversions is the same as described previously for other g.c. techniques (e.g. see isopropanol decomposition, Chapter 8).

10.2.3 Methanol Synthesis

The activity and selectivity of sample $Cu_yK_xWO_3$ in the synthesis of methanol from carbon monoxide and hydrogen was studied at moderate pressure in an experimental rig constructed of stainless steel. The sample (0.5g) was packed in the reactor and reduced in a mixture of 6% H_2 in N_2 (BOC 99.99% pure, $40cm^3min^{-1}$) as the temperature of the sample bed was raised at $5Kmin^{-1}$ from 293K to 623K, at which upper temperatures it was held for 5-10 min before cooling to room temperature. Synthesis gas of 33% CO/67% H_2 (BOC 99.99% pure) was then introduced ($180cm^3min^{-1}$) through the sample and the pressure in the reactor was increased to 1.723MPa. The sample was then heated at $<10Kmin^{-1}$ to 573K and the isothermal reaction rate measurements commenced. Samples of the gaseous products were analysed by gas chromatography (Perkin Elmer 8410 with an FID detector and a column : 5% Carbowax on chromosorb WA WH MDS) at 443K. The concentrations of methane and methanol as the major products were monitored as a function of time until the reaction reached a steady-state. This steady-state rate of reaction was then used in calculations.

Blank measurements were also carried out with an empty reactor containing a bed of alumina under identical conditions : this showed no

significant activity in CO hydrogenation when used in place of the sample and so it was judged that the following equilibria[36] could

$$Fe_{(steel)} \underset{303K}{\overset{CO}{\rightleftharpoons}} Fe(CO)_5 \underset{573K}{\overset{-CO}{\rightleftharpoons}} Fe_{(sample)}$$

$$LogK = -0.3 \qquad logK = +14.2$$

not have transferred atomically-dispersed Fe to the sample in significant quantities. Thus, there was thought to be no need to protect the sample with a replaceable guard-column of alumina held at 573K to collect any traces of Fe and prevent these reaching the downstream sample.

10.2.4 Ammonia Synthesis

The activity of the silica supported sample in catalysing the synthesis of ammonia was measured using a silica flow reactor at 101kPa with the sample held in a furnace (Stanton Redcroft C1/Pt13/CL) to within ± 5K of the set temperature. The product stream passed through $20cm^3$ of de-ionised water (obtained by passing distilled water through a Duolite ion-exchange column) whose conductivity could be monitored continuously (Fissons PT1-18). The sample (0.5g) was flushed with Ar (99.9% purity; BOC) for 15 min and the H_2 (99.95% purity; BOC) at ambient temperature and also as the sample temperature was raised to 773K at 10K per min and then held for 2h. Subsequently, the hydrogen was replaced by flowing argon and the sample cooled to ambient temperature. During the pretreatment the conductivity detector gave a constant reading. The reactant stream of 75% hydrogen in nitrogen (99.9% purity; BOC; prepurified by oxygen and water vapour removal) was introduced at $40cm^3min^{-1}$. The sample temperature was then increased

to various temperatures and conductivity vs. time measurements were taken under isothermal conditions. The error in the assessment of the quantity of ammonia formed was ±3nmol.

10.2.5 N_2O Decomposition

N_2O decomposition[37] was used to determine the equivalent Cu surface area in $Cu_yK_xWO_3$, in a volumetric apparatus with a Bell and Howell transducer (BHL-270). The sample (1.0g) was reduced in-situ at 623K in 6% H_2 in N_2 ($40cm^3min^{-1}$) and then cooled to 473K at which temperature it was evacuated. After cooling at ambient temperature N_2O was admitted at 5.3kPa and after 30 min unreacted N_2O was removed from the gas phase at 78K and the residual pressure of N_2 was determined. It was assumed that there were 1.41×10^{19} Cu atoms per m^2 (i.e. that each Cu atom occupies $0.071nm^2$) and that the Cu/O atomic adsorption stoichiometry was 2:1.

10.3 Results

10.3.1 SiO_2 Supported Sample

10.3.1.1 Tpr

The reducibility of the supported potassium polytungstate formed by impregnating the SiO_2 support with a solution of potassium tungstate at pH 4 was studied by tpr. Figure 10.2 shows the relevant tpr profile which shows at least two overlapping consumption peaks in the temperature range 673K to 1273K. The first process starts at 673K with a maximum at about 773K, the hydrogen consumed in this process is $0.146mmolg^{-1}$ sample. The second process occurs in the temperature range 873 - 1273K with twin maxima at 1033K and 1113K. The total H_2 consumed in the second process is 1.82 $mmolg^{-1}$ sample. It appears that the first process corresponds to the reduction of the polytungstate

to a tungsten bronze according to the equation:-

$$K_{12}W_{12}O_{42} + 1.98H_2 \longrightarrow 12K_{0.33}WO_3 + 4.02\ K_2O + 1.98\ H_2O$$

This process requires a H_2 consumption of $0.177 mmol g^{-1}$ sample, (for a loading of 30% w/w tungsten metal), which agrees well with the observed value. The temperature range at which the second process occurs, corresponds to the temperature of reduction of the unsupported bronze, 0.3KW, to K_2WO_4 and W, (i.e. 850 - 1273K; T_{max} at 1143K; H_2 consumption $11.79 mmol g^{-1}$ sample; see Fig. 10.2 and Chapter 4. However, for the supported bronze this process shows two maxima unlike the unsupported bronze. Most probably there is a highly dispersed bronze present which reduces more easily and the second maximum could then correspond to reduction of larger supported crystallites. On this basis, if a bronze is to be formed from the supported polytungstate, a reduction temperature $\lesssim$ 873K must be used. In the present study a temperature of 773K was selected for the reduction of the SiO_2 supported polytungstate in 6% H_2/94% N_2, ($40 cm^3 min^{-1}$, 2h).

10.3.1.2 Xrd

The bronze formed by the reduction of the SiO_2 supported polytungstate at 773K for 2h in 6% H_2/94% N_2 ($40 cm^3 min^{-1}$) was analysed by xrd. The diffraction lines due to the SiO_2 support were first eliminated before determining the structure of the bronze. The d values calculated from the diffractogram due to the bronze are given in Table 10.1. These values correspond well to a bronze with an hexagonal structure having cell parameters a_0 = 0.734nm and c_0 = 0.752nm, and with x having a value of 0.33. The xrd study clearly indicates that a bronze has been formed by the reduction of the SiO_2-supported polytungstate.

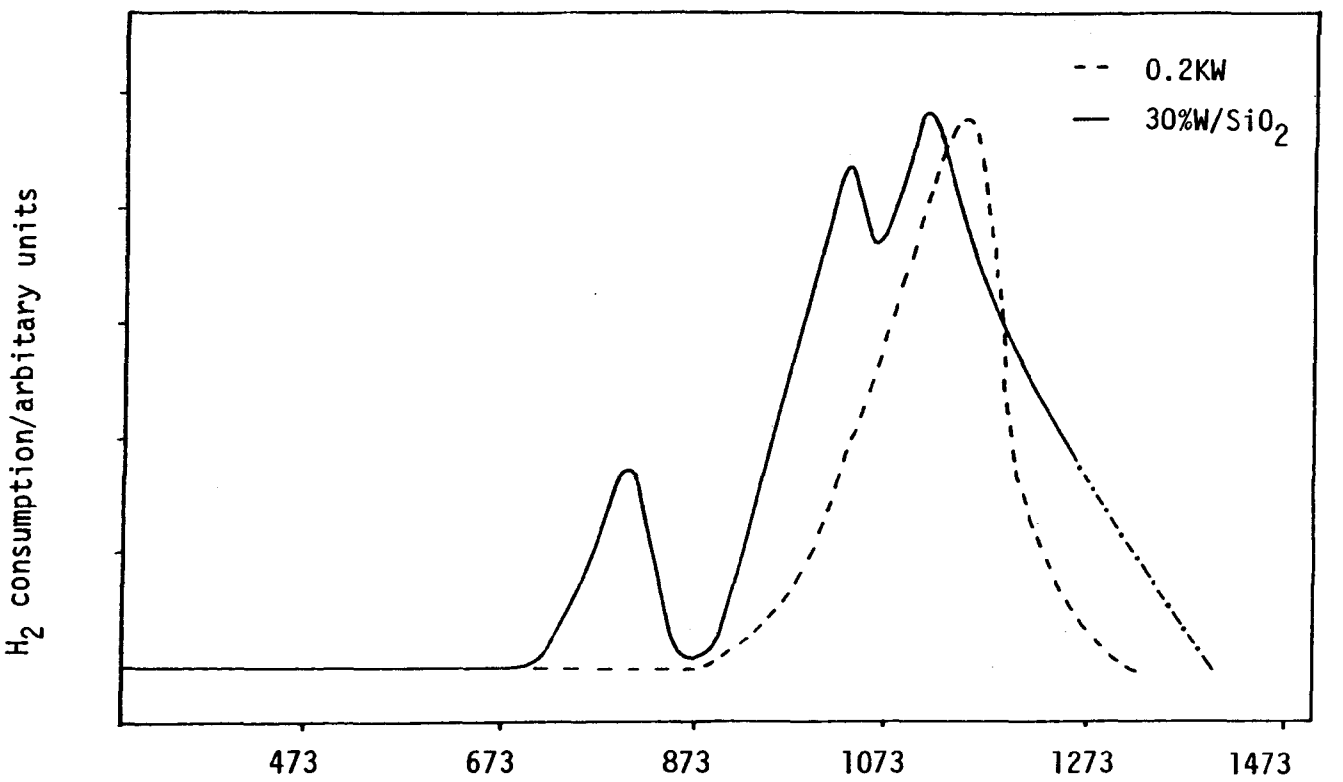

Figure 10.2 Tpr profiles of 0.2KW and 30%W(K_2WO_4)/SiO_2

Table 10.1

X-ray Diffraction of Silica Supported Bronze

θ	d/nm	hkl
6.90	0.641	100
11.85	0.375	002
13.95	0.319	102
14.15	0.315	200
17.05	0.263	112
18.45	0.243	202
19.95	0.226	211
20.25	0.222	300
21.90	0.206	113
24.40	0.186	004
24.65	0.184	302
25.10	0.182	220
27.65	0.166	222
28.40	0.162	204
28.75	0.160	312

10.3.1.3 Xps

Xps analysis was carried out on both the unreduced silica supported sample and the reduced sample (see sub-section 10.3.1.1). For the case of tungsten the spectrum of the 4f electrons was studied in both samples. The measured binding energy for the $4f_{7/2}$ line of the unreduced supported sample (36.2eV) is close to the value obtained for WO_3 (36.0ev) indicating that tungsten is largely present in the +6 oxidation state. The $4f_{7/2}$ line for the reduced supported sample

occurred at 35.6eV similar to the values obtained for the unsupported potassium and sodium tungsten bronzes (see Chapter 6). This decrease in binding energy suggests a decrease in the oxidation state of tungsten from +6 to about +5 after reduction of the supported sample. The xps study also points to the formation of a bronze and little interaction between the tungsten species and SiO_2 since the binding energy of the W4f electrons of the supported and unsupported bronze agrees well.

10.3.1.4 Activity of the Supported Bronze for Ammonia Synthesis

The catalytic measurements for ammonia formation were carried out on the supported bronze. The rate and extent of ammonia production during each catalytic run was estimated from the change in aqueous conductivity in the detector cell using the calibration curve shown in Figure 10-3. The activity measurement was carried out for at least three different temperatures, 520K, 570K and 620K. At each different temperature the amount of ammonia formed was measured as a function of time and the rate of ammonia formation was estimated from the total amount of ammonia produced over a period of 35 min. Table 10.2 shows the rate of ammonia formation at the three different temperatures.

Table 10.2

Rate of Ammonia Formation

Temp./K	Rate/nmolg^{-1}min^{-1}
520	2.32×10^{-3}
570	9.14×10^{-3}
620	17.70×10^{-3}

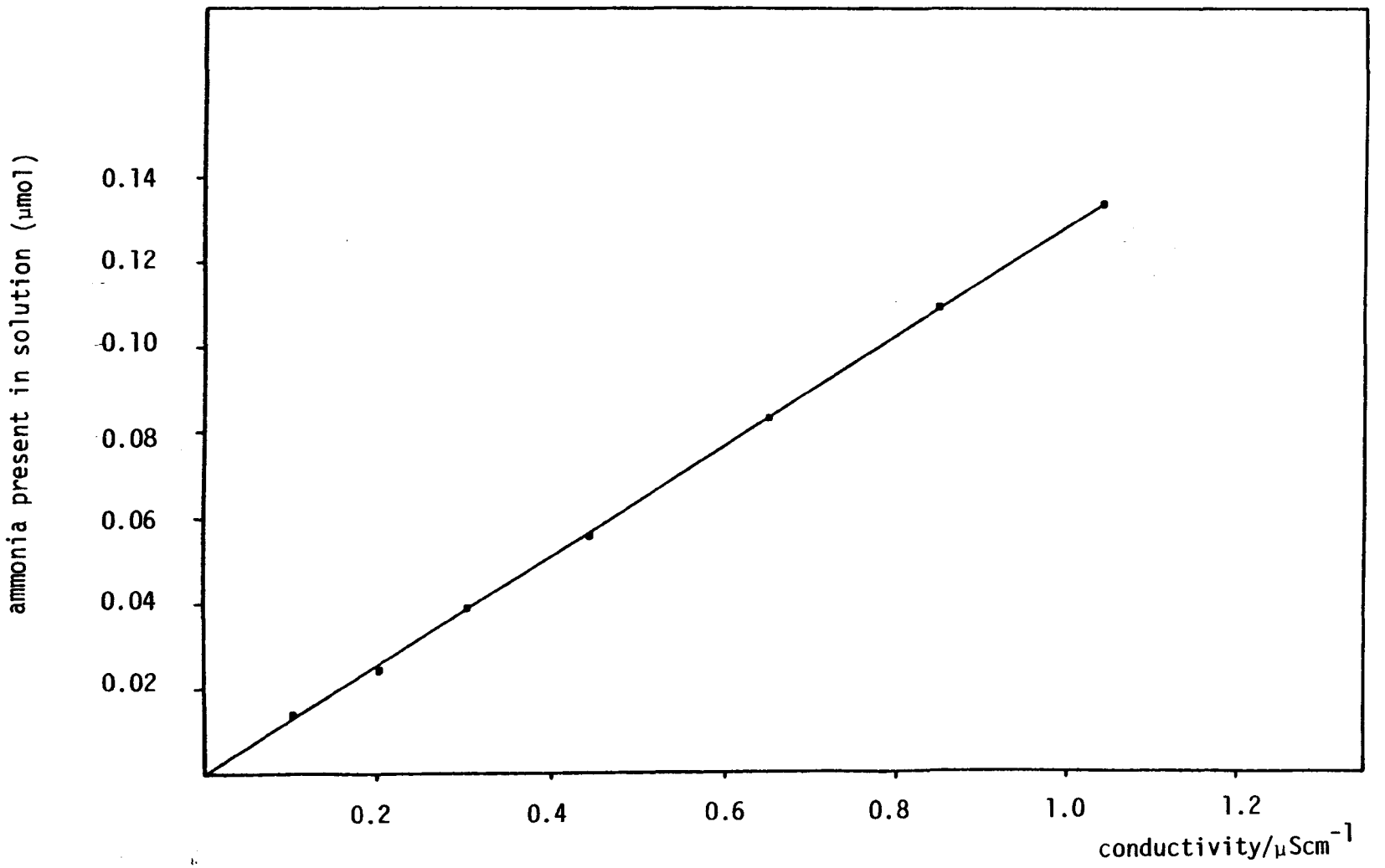

Figure 10.3 Calibration plot : concentration of ammonia in solution versus conductivity

The rates given in Table 10.2 were used to estimate the activation energy for the synthesis process. The Arrhenius plot is shown in Figure 10.4 and the calculated activation energy is 53.2kJmol^{-1}.

The rate of ammonia formation for the SiO_2 supported bronze is much smaller than those observed on the Al_2O_3 supported bronzes[2], but it must be noted that a much higher tungsten loading,(30%), was used. Indeed, it was observed that for the Al_2O_3 supported bronzes[2], the rate of ammonia synthesis decreases when the metal loading exceeds 5%. The bronze formed on the Al_2O_3 support containing 10% tungsten metal has an activity for ammonia synthesis of 0.69nmolg^{-1}min^{-1} at 773K compared to that of the present SiO_2 supported bronze which has an activity of 17.7 x 10^{-3}nmolg^{-1}min^{-1} at 620K. The activation energy value, (E_a), is also higher than those observed on the Al_2O_3 - supported bronzes (14-20kJmol^{-1}).

Either the sites on the SiO_2-supported bronze are not as active as those on the Al_2O_3 supported bronzes or there are far fewer of them. Since the activity of the silica-supported bronze in this reaction was so low no further consideration was given to other loadings.

10.3.2 $Cu_yK_xWO_3$

10.3.2.1 Tpr

The tpr profile of sample $Cu_yK_xWO_3$ is shown in Figure 10.5 and is similar to that obtained for sample 0.2KW (see Chapter 4). Reduction occurred in one step in the temperature range 845K - 1320K with a total hydrogen consumption (11.70mmolg^{-1} sample), which is in good agreement with that obtained for the reduction of 0.2KW (11.79mmolg^{-1} sample). No peak was observed for the reduction of the copper species present,

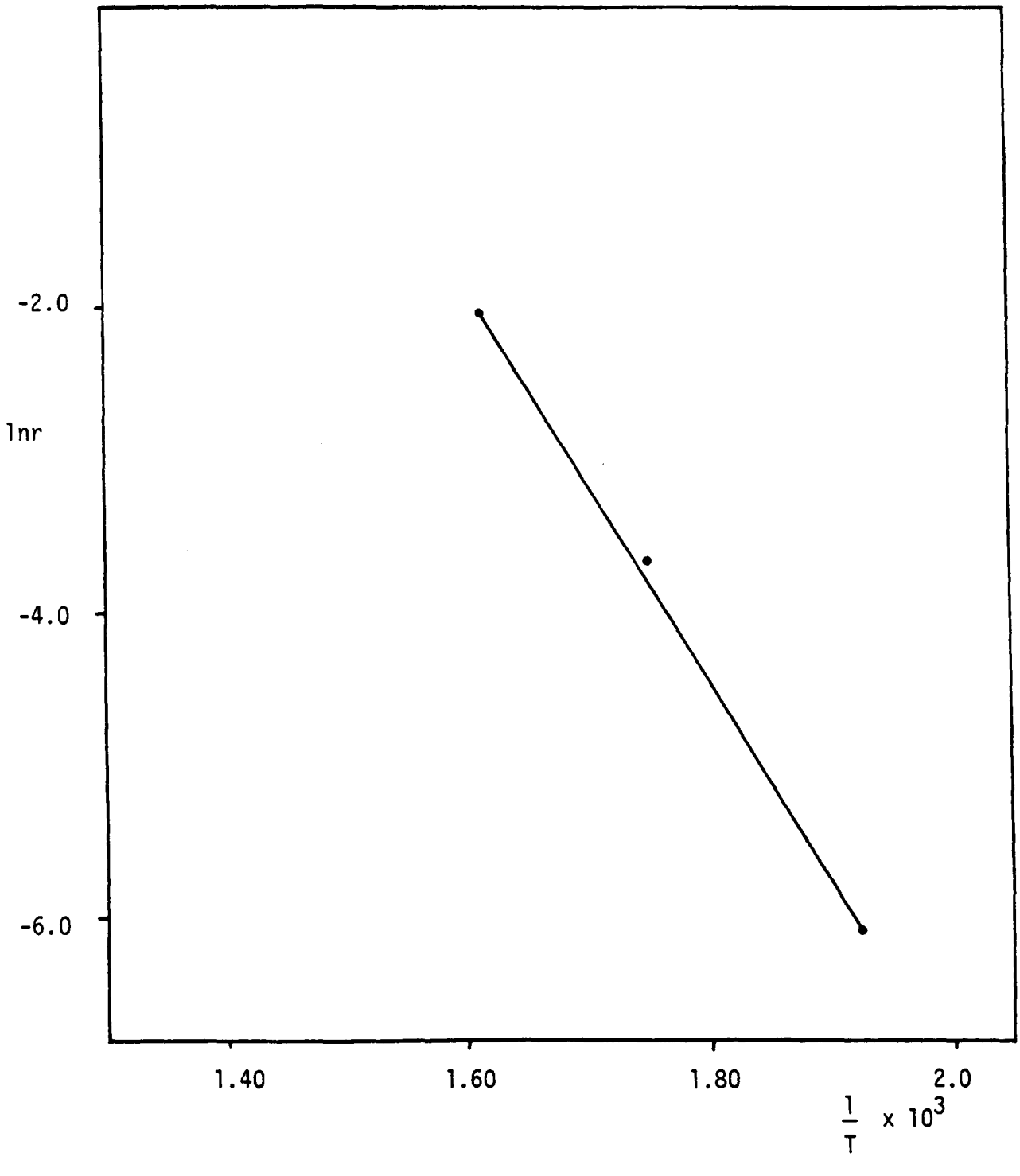

Figure 10.4 Arrhenius plot for 30% $W(K_2WO_4)/SiO_2$

however, this may be due to the sensitivity of the equipment and the relatively low copper content present. The profile also indicates that the copper species has no effect on the reduction of the bronze.

10.3.2.2 Xrd

The copper sample obtained by ion-exchange of $K_{0.2}WO_3$ with $CuCl_2$ was characterised by xrd. The d values calculated from the diffractogram of the sample are given in Table 10.3. These d values differ slightly from those obtained for $K_{0.2}WO_3$ (see Table 5.3, Chapter 5). There were a few "new" peaks observed that do not correspond to any copper salt either in the +1 or +2 oxidation state. It is most probable that a homogeneous compound in which copper ions have been inserted in the potassium bronze has been formed with the removal of some potassium ions.

10.3.2.3 Xps

The ion-exchange sample, $Cu_yK_xWO_3$, was studied by xps. The binding energies calculated from the spectra for the peaks due to the various elements are given in Table 10.4. In the case of tungsten the 4f electrons were studied, and for copper the binding energy of the 2p peaks was used. The measured binding energy for the $W4f_{7/2}$ line was found to be 35.3eV, which is slightly different to that found for $K_{0.2}WO_3$, (35.9eV, see Chapter 6), indicating no change in the oxidation state of tungsten (about +5), and possibly due to interaction with copper ions. The spectrum for the Cu2p peaks is shown in Figure 10.6. There is a slight indication of the presence of satellite peaks suggesting that copper could be present in the +2 oxidation state. A quantitative estimation of the relative ratio of tungsten to potassium, and tungsten to copper in the bronze was attempted. This was done by

Table 10.3

X-ray Diffraction of $Cu_yK_xWO_3$

θ	Sinθ	d/nm
6.945	0.121	0.637
11.900	0.206	0.373
12.060	0.209	0.368
13.035	0.226	0.341
13.465	0.233	0.331
13.950	0.241	0.319
17.035	0.293	0.263
18.455	0.317	0.243
19.565	0.335	0.230
20.209	0.345	0.223
24.300	0.412	0.187
24.655	0.417	0.185
27.745	0.466	0.165
28.495	0.477	0.161
28.815	0.482	0.160

Table 10.4

X-ray Photoelectron Spectroscopy

$Cu_yK_xWO_3$

Element Signal	Observed Binding Energy eV	Corrected Binding Energy eV	Observed Shift eV
C1s	292.5	284.6	
O1s	536.1	528.2	9.80
$W4f_{5/2}$	45.7	37.8	4.65
$W4f_{7/2}$	43.2	35.3	4.30
$W4d_{3/2}$	267.7	259.8	1.20
$W4d_{7/2}$	255.2	247.3	0.70
$K2p_{1/2}$	302.2	294.3	4.70
$K2p_{3/2}$	299.1	291.2	4.80
$Cu2p_{1/2}$	960.8	952.9	5.10
$Cu2p_{3/2}$	940.5	932.6	5.40

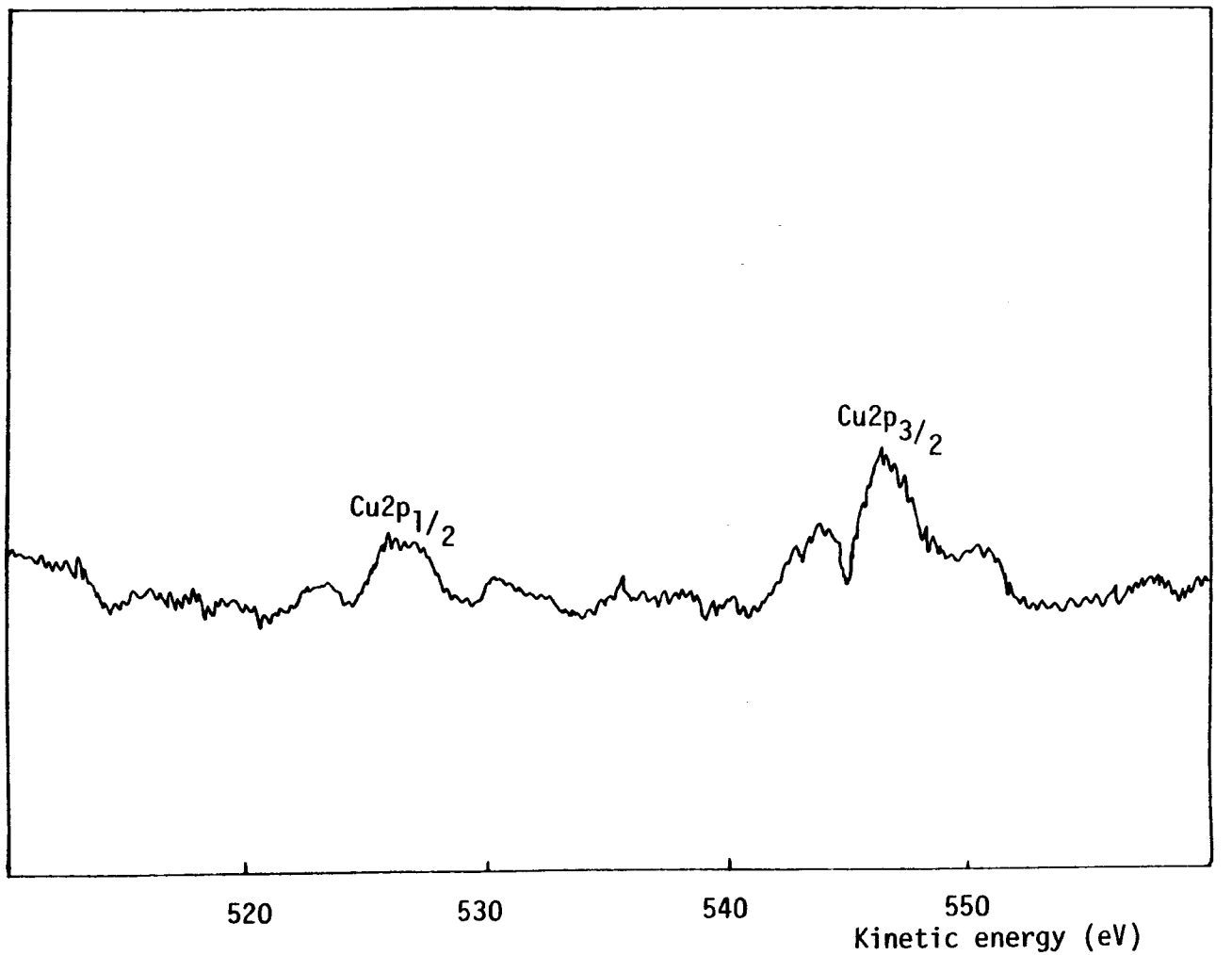

Figure 10.6 Xps of $Cu_yK_xWO_3$

comparing the peaks areas of the W4d and K2p and Cu2p peaks by the method described in Chapter 6. The relative peak intensities, the sensitivity factors used, and the calculated ratios are given in Table 10.5. Xps studies on $K_{0.2}WO_3$ (see Chapter 6) have shown a K : W ratio of 0.238 : 1 whereas on the ion-exchange sample this ratio has decreased to 0.130 : 1, indicating that about 45% of the potassium ions

Table 10.5

Element	Sensitivity Factor	Peak Area	Peak Area S.F.	Relative Ratio
K2p	1.468	21.6	14.71	0.130
Cu2p	3.043	21.36	7.02	0.062
W4d	6.370	720.0	113.03	1.000

has been removed by the ion-exchange process. A study by atomic adsorption (see Chapter 2) of the aliquot obtained after the ion-exchange process has also shown the removal of about 45% of the potassium ions present. The bronze obtained by ion-exchange of $K_{0.2}WO_3$ with $CuCl_2$ most probably has an empirical formula of $(Cu_{0.062}K_{0.130}WO_3)_n$.

10.3.2.4 N_2O Decomposition

The copper surface area present in the ion-exchange sample, $Cu_yK_xWO_3$, was determined by N_2O decomposition. The residual N_2 pressure, after exposing the sample to N_2O at a certain pressure and removing the unreacted N_2O, was used to estimate the copper surface area using the gas law $PV_E = nRT$, where V_E is the equilibrium volume. For each mole of N_2 in the gas phase there must be an equivalent number of moles of oxygen atoms which have chemisorbed on the copper surfaces. It was assumed that there were 1.41×10^{19} Cu atoms per m^2, (i.e. that each Cu atom occupies $0.071nm^2$) and that the Cu/O atomic adsorption

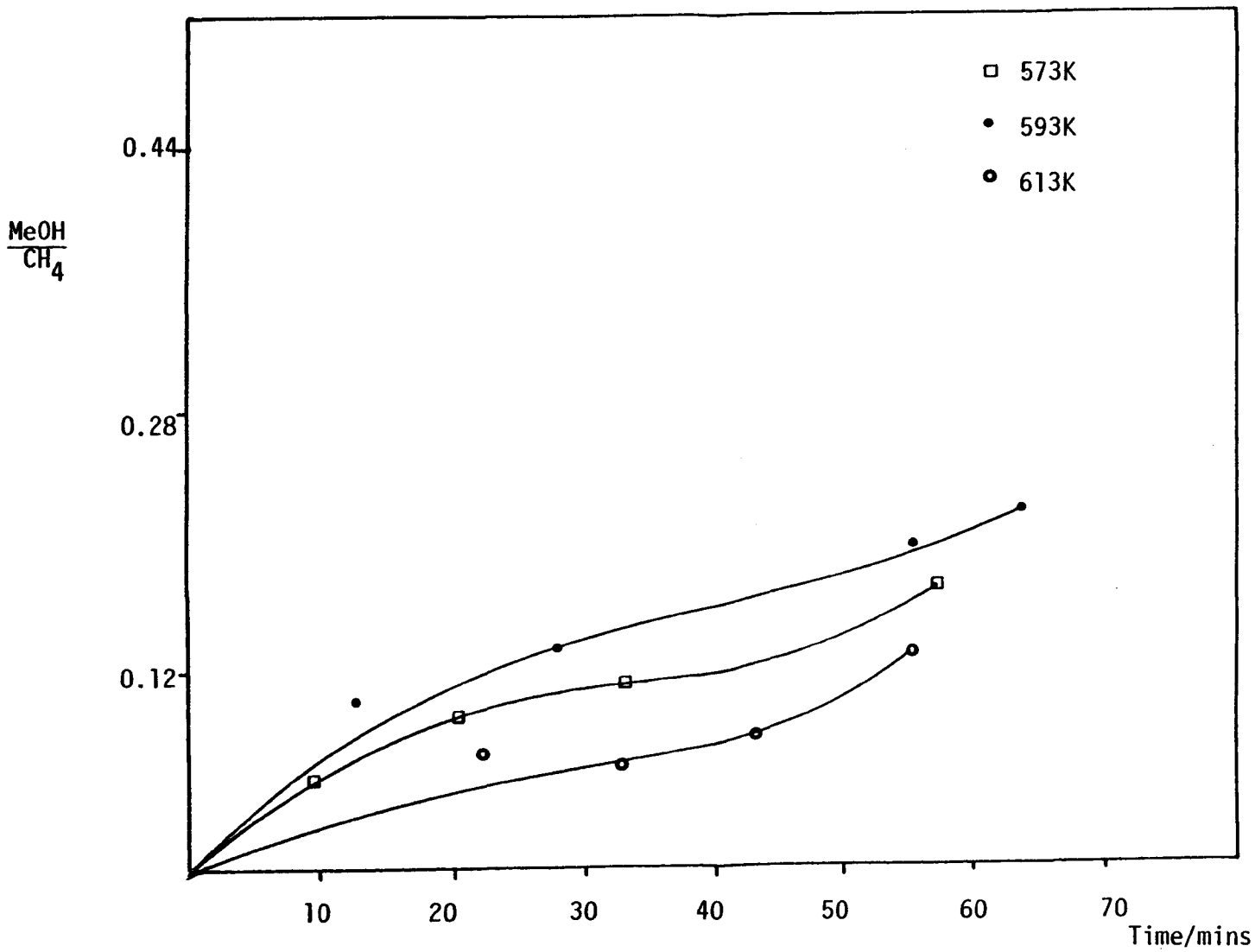

Figure 10.7 Selectivity (methanol to methane formation)of $Cu_yK_xWO_3$ versus time

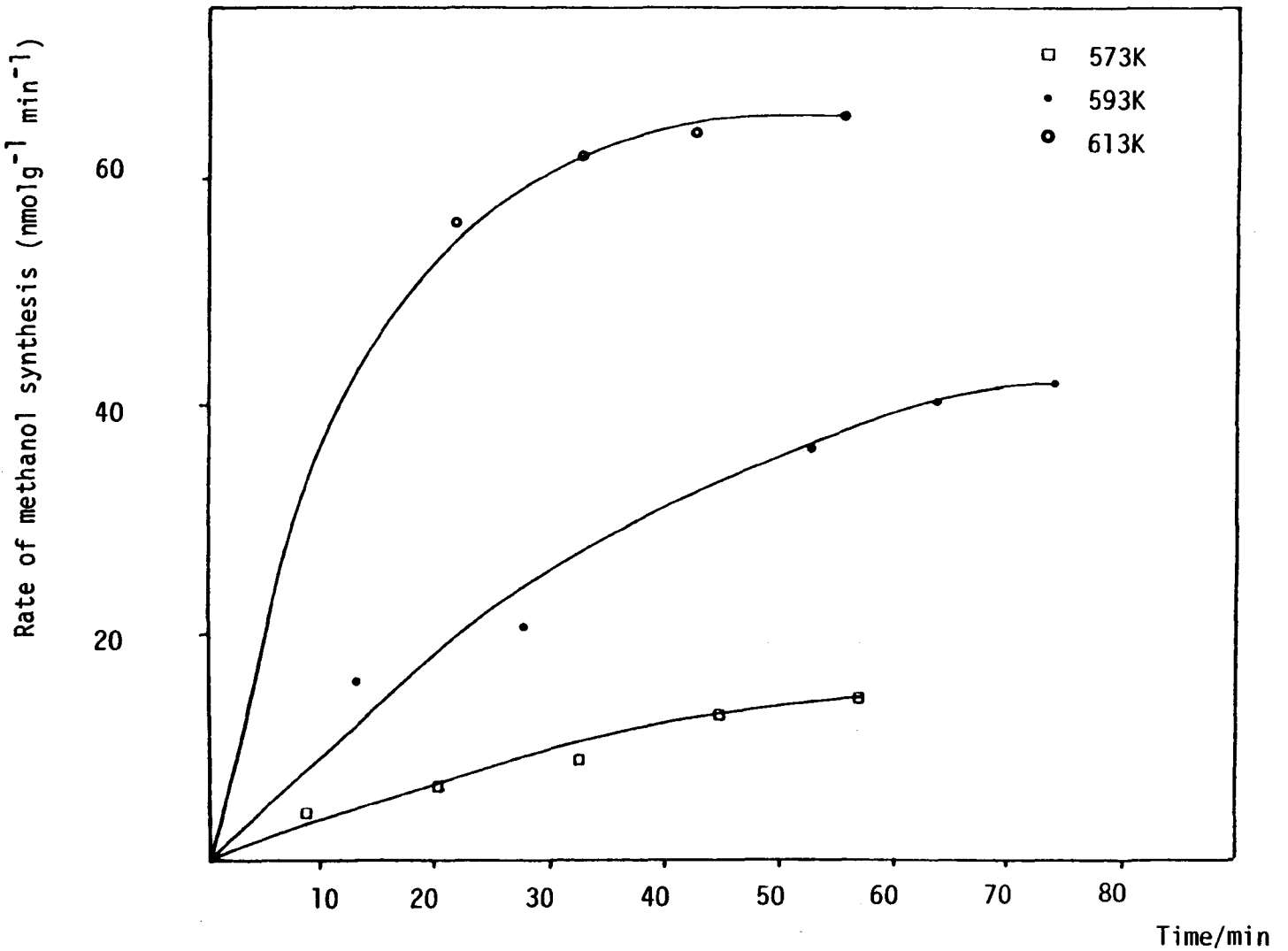

Figure 10.8 Rate of methanol synthesis for $Cu_yK_xWO_3$ versus time

stoichiometry was 2 : 1. The calculation for the Cu surface area is given in Appendix 4. The total number of surface copper atoms per gram of sample was found to be 5.36×10^{18}, giving a percentage copper dispersion of 3.4%, if the empirical formula of the compound is taken as $Cu_{0.062}K_{0.13}WO_3$. This indicates that most of the Cu atoms must have entered the lattice of the bronze to form a homogeneous compound and are not available for surface reaction. The copper surface area calculated from this dispersion is $0.38 m^2 g^{-1}$ sample.

10.3.2.5 Methanol Synthesis and the Water-Gas-Shift Reaction

The catalytic measurements in the synthesis of methanol from carbon monoxide and hydrogen was studied on the ion-exchanged sample $Cu_yK_xWO_3$. The activity measurements were carried out at three temperatures; 573K, 593K and 613K. The production of both methanol and methane was observed on the sample at these three temperatures. Figure 10.7 shows a plot of the selectivity, (the ratio of methanol to methane formation), of $Cu_yK_xWO_3$ towards methanol and methane production against time. At all three temperatures the sample has a higher selectivity for methane than methanol, with methane formation being slightly more favoured at the highest temperature (613K). However, the selectivity for methanol at each temperature tends to increase with time, due to a drop in activity for methane formation, and an increase in activity for methanol synthesis. Figure 10.8 illustrates the rate of methanol synthesis with time, at the three reaction temperatures. Clearly the rate of methanol production increases with increasing temperature and a steady-state value is reached after about 60 mins. Table 10.6 gives the steady-state activity and selectivity for methanol synthesis of sample $Cu_yK_xWO_3$ together with the turnover numbers calculated assuming a copper surface area of $0.38 m^2 g^{-1}$ sample as determined by N_2O

Table 10.6

Temp/K	Rate of MeOH Synthesis/nmol $m^{-2}s^{-1}$	CH_3OH/CH_4	Turnover number/ Molecules per site s^{-1}
573	0.61	0.17	26.2×10^{-6}
593	1.84	0.33	78.6×10^{-6}
613	2.90	0.13	123.6×10^{-6}

decomposition (see sub-section 10.3.2.4). The turnover number is much lower than those observed on a Cu/ZnO catalyst[4] but is of the same magnitude as that observed for a Cu/TiO_2 (Rutile) catalyst. The selectivity for methanol formation is lower than for both the Cu/ZnO and Cu/TiO_2 catalysts. The rate of methanol formation on the copper bronze is lower than that observed for copper spinels where copper is also present in a high oxidation state[4]. Most probably indicating that the copper species in the bronze are not as active as those in the spinels. There is much uncertainty concerning the mechanism of methanol synthesis as to whether;

(i) the methanol synthesis reaction is via a formate intermediate (from CO and O and OH) or successive addition of H to CO.

(ii) CO or CO_2 is the main reactant in methanol synthesis using $CO/CO_2/H_2$ reaction mixtures.

(iii) the reactions occur on Cu and/or ZnO in the Cu/ZnO catalyst.

It appears that Cu in a high oxidation state could be the active site for methanol formation[4], but further evidence would be required to determine the actual sites responsible for methanol synthesis in the bronze.

Although the copper bronze shows some activity for methanol synthesis, no activity was observed in the water-gas-shift reaction up to a temperature of 723K.

CHAPTER 10

REFERENCES

1. J. McHardy, J.O'M. Bockris, "From Electrocatalysis to Fuel Cells", G. Sandstede, Ed., 109, University of Washington Press, Seattle and London, 1972.
2. S. Stevenson, M. Phil. Thesis, Brunel University, 1985.
3. G.C. Chinchen and K.C. Waugh, J. Catal., 97, 280, (1986); T.H. Fleioch and R.I. Mieville, J. Catal., 97, 284, (1986); G.C. Chinchen, K.C. Waugh and D.A. Whan, Appld. Catal., 25, 101, (1986).
4. M.S.W. Vong, P.A. Sermon, M.A. Yates, A. Perryman and P. Reyes, Unpublished Work.
5. P.A. Sermon, K. Rollins, P. Reyes, S.A. Lawrence, M.A.M. Luengo and M.J. Davies, J. Chem. Soc. Far. Trans. I, 83, 1347, (1987).
6. R.H. Hoppener, E.B.M. Doesburg and J.J. F. Scholten, Appld. Catal., 25, 109, (1986); J. Cunningham, G.H. Al. Sayyed, J.A. Cronin, C. Healy and W. Hirschwald, Appld. Catal., 25, 129, (1986).
7. E.M. Calverley and R.B. Anderson, J. Catal., 104, 434, (1987).
8. J.M. Moe, Am. Chem. Soc., Div. Pet. Chem. Prepr., 8, B29, (1963).
9. H. Bohlbro and M.H. Jorgensen, Chem. Eng. World, 5, 46, (1970).
10. R. Habermehl and K. Atwood, Am. Chem. Soc. Div. Fuel. Chem. Prepr., 8, 10, (1964).
11. N.V. Kul'Kova and M.I. Temkin Zh. Fiz. Khim., 23, 695, (1949).
12. G.G. Shchibraya, N.M. Morozov and M.I. Temkin, Kinet. Katal., 6, 1057, (1965).
13. R. Mezaki and S. Oki, J. Catal., 30, 488, (1973).
14. Y. Kaneko and S. Oki, J. Res. Inst. Catal., Hokkaido Uni., 13, 55, (1965); 13, 169, (1965); 15, 185, (1967).
15. S. Oki, J. Happel, M. Hnatow and Y. Kaneko, Proced. 5th Intern. Congr. Catal., 1, 173 (1973).

16. S. Oki and R. Mezaki, J. Phys. Chem., 77, 447, (1973); 77, 1601, (1973).

17. D.S. Newsome, Catal. Rev. Sci. Eng., 21, 2, 275, (1980).

18. T.M. Yur'eva, G.K. Boreskov and V. Sh. Gruver, Kinet. Katal., 10, 862, (1969).

19. G.A. Somorjai, Catal. Rev. Sci. Eng., 23, 89, (1981).

20. G. Natta in 'Catalysis', P.H. Emmett, Ed., 3, 349, Reinhold N.Y., (1955).

21. E.G. Baglin, G.B. Atkinson and L.J. Nicks, Ind. Eng. Chem., 20, 87, (1981).

22. M.L. Poutsma, L.F. Elek, P.A. Lbarbia, A.R. Risch and J.A. Rabo, J. Catal., 52, 151, (1978).

23. M. Ichikawa, Bull. Chem. Soc. Jpn., 51, 2268, (1978).

24. P.C. Ellgen, M.M. Bhasin, J.S. Patents 4, 014, 913, (1977), 4096, 164, (1978) and 4162, 262, (1979).

25. A. Ozaki, K. Aika and H. Hori, Bull. Chem. Soc., Jpn., 44, 3216, (1971).

26. A. Ozaki, K. Urabe, K. Shimazaki and S. Sumiga, in "Preparation of Catalysis", 2, 381, Elsevier Amsterdam, (1979).

27. K. Aika, H. Hori and A.Ozaki, J. Catal., 27, 424, (1972).

28. P.R. Holzman, W.K. Shiflett and J.A. Dumesic, J. Catal., 62, 167, (1980).

29. Applied Industrial Catalysts, 3, Ed. B.E. Leach, Academic Press, (1984).

30. A. Mittasch, Adv. Catal., 2, 81, (1950).

31. J.H. Sinfelt, W.F. Taylor and D.J.C. Yates, J. Phys. Chem., 69, 95, (1965).

32. R.M. Dell, F.S. Stone and P.F. Tiley, Trans, Faraday Soc., 49, 195, (1953).

33. Th. J. Osinga, B.G. Linsen and W.P. von Beet, J.Catal., 7, 277, (1967).

34. J.J.F. Scholten and J.A. Konvalinka, Trans. Faraday Soc., 65, 2465, (1969).

35. B. Dvorak and J. Pasek, J. Catal., 18, 108, (1970).

36. L.W. Ross, F.H. Haynie and R.F. Hockman, J. Chem. Eng. Data, 9, 339, (1964).

27. G.C. Chinchen, C.M. Hay, H.D. Vandervall and K.C. Waugh, J. Catal., 103,79, (1987).

CHAPTER 11

CONCLUSIONS

The structure and catalytic aspects of a series of potassium tungsten bronzes and a series of sodium tungsten bronzes have been considered. They were prepared by a thermal method using tungsten as the reducing agent according to the following equation:

$$3xM_2WO_4 + (6-4x)WO_3 + xW \xrightarrow[Ar]{1173K} 6M_xWO_3$$

where M = K or Na.

The alkali ion content in the bronzes ranged from 0.5% to 11.9%. The surface area of the bronzes was determined by krypton adsorption and ranged from 0.13 to 1.05m^2g^{-1}. For both series of bronzes the surface area tended to decrease with increasing alkali ion concentration probably due to sintering since they were prepared at high temperature. The melting point of the bronzes decreases with increasing alkali metal ion content, WO_3 = 1746K and $K_{0.3}WO_3$ = 1237K. It would appear that the growth of crystalline particles probably by surface diffusion involving migration of atoms across the particles surface is influenced by the melting point of the bronzes and hence the observed drop in surface area with increasing alkali metal ion content.

X-ray diffraction measurements have given qualitative information on the crystalline nature of the bronze samples. The potassium bronze, 0.05KW is an intergrowth tungsten bronze, ITB, being an intergrowth of hexagonal tungsten bronze, HTB, and WO_3. Potassium bronzes with x = 0.2 and 0.3 are of hexagonal types, whereas 0.6KW is a tetragonal tungsten bronze, TTB. The pattern obtained for 0.8KW was too

complex to fully interpret. The sodium bronzes with low alkali ion content, $0.05 \leq x \leq 0.3$, are tetragonal bronzes. The patterns obtained for the sodium bronzes with $x = 0.6$ and 0.8 were relatively uncomplicated and proved to be cubic. The bronze samples were regarded as being homogeneous. The X-ray photoelectron spectra of the samples has shown tungsten to be in an oxidation state of about +5. Quantitative examination of the spectra showed that the surface of the samples was essentially a termination of the bulk structure with no pronounced segregation or depletion of potassium or sodium.

The thermal stability of the potassium and sodium tungsten bronzes was studied by their reduction in hydrogen gas and their oxidation in a diluted oxygen gas stream. The bronzes are stable in hydrogen up to a temperature of about 800K below which neither weight loss nor hydrogen consumption was observed. The weight loss obtained by heating the samples in H_2 to 1173K indicated that the tungstate and W metal were formed. Reduction in most cases was a single endothermic process. The tpr profiles of the bronze samples have also shown that in most cases reduction occurred in one step. From the H_2 consumed in the tpr process, the tungstate and W metal were the final products of reduction as also observed by tga experiments. Oxidation of the bronze samples occurred in most cases in overlapping processes. The bronzes are stable in air up to a temperature of about 600K. The complete oxidation of all of the bronzes led to the formation of the tungstate and WO_3. The initial processes in the oxidation were attributed to the formation of polytungstates which then disproportionate. It was observed that the bronzes with a tetragonal structure oxidise more readily than those with either a cubic or hexagonal structure and is attributed to the ease of formation of the corresponding poly-

tungstates. From the O_2 consumption none of the bronze samples were thought to be oxygen deficient as the observed O_2 uptake corresponded well with the theoretical values required.

Electrical resistivity measurements on the bronze samples have shown that bronzes with high inserted ion concentrations are metallic while bronzes with low concentrations of the insertion ion have semiconductor properties. The resistivity values for both the potassium and the sodium bronzes were similar, with values for potassium being slightly higher, indicating that the resistivity was possibly independent of the nature of the insertion ion.

Temperature programmed desorption of chemisorbed ammonia was used to obtain a picture of the strength and density of the acid sites on WO_3 and the bronze samples. The decomposition of isopropanol was used as a probe reaction to obtain information about the nature of these acid sites. Temperature programmed desorption of ammonia on WO_3 and potassium bronzes with $x \lesssim 0.2$ has shown that there is probably only one type of acid site present. However, for the potassium bronzes with $0.3 \lesssim x \lesssim 0.8$ and for most of the sodium bronzes there is more than one type of acid site present since a second ammonia desorption peak was observed at higher temperature. A comparison of the acid site concentration on the bronzes has suggested that the acid site surface density decreases with increasing alkali metal ion content. In general, a higher concentration of acid sites was found to be present on the potassium bronzes than on the corresponding sodium bronzes. The isopropanol decomposition reaction has often been used to probe the acidic and basic sites on catalysts. The selectivity of the reaction for dehydration and dehydrogenation has been used to explain the nature of these sites. WO_3 and the bronzes show selectivity for both propene

(dehydration reaction) and acetone (dehydrogenation reaction), except for some of the sodium bronzes with low alkali ion content which show total selectivity for propene formation. In general, for any given sample the selectivity for propene formation increased with temperature and this is mostly due to a thermodynamic limitation since the products of the dehydration reaction are favoured at high temperature whereas the dehydrogenation reaction is exothermic. The selectivity for the dehydration reaction for both the potassium and the sodium bronzes decreased with increase in alkali metal ion content, due to an increase in the number of basic sites. The sodium tungsten bronzes show a greater selectivity for the dehydration reaction than the potassium bronzes with the same alkali ion content. The rate of the dehydration reaction decreases as the sodium and potassium content increases. However, the rate of dehydration on the sodium bronzes was greater than that observed for the corresponding potassium bronzes, although the total number of acid sites was smaller, thus indicating the greater activity of the acid sites present on the sodium bronzes. Recent work[1] has also shown that the rate of dehydration tends to decrease with increasing ion size as observed for the present potassium and sodium bronzes, the K^+ ion being larger (0.133nm) than the sodium ion, (0.097nm). The activation energy values for the dehydration reaction have been used to discuss the nature of these acid sites[2] low activation energy values for the reaction have been associated on surfaces where both Lewis and Bronsted acid sites occur, whereas high activation energy values indicate only Lewis acid sites. The activation energy values for the dehydration reaction calculated for WO_3 and K_xWO_3 where $x \leq 0.2$ are high whereas those with $x \geq 0.3$ and the sodium bronzes have a lower value. It would appear that the first series of samples contain only Lewis acid sites, whereas the second series contain both

Lewis and Bronsted acid sites. It is these Bronsted acid sites which are of a stronger nature and more active. Lewis acidity is intrinsic in WO_3 and the Lewis acid sites present in the bronzes can be attributed to the WO_3 matrix. Fig. 11.1 shows such a site on a hexagonal potassium tungsten bronze.

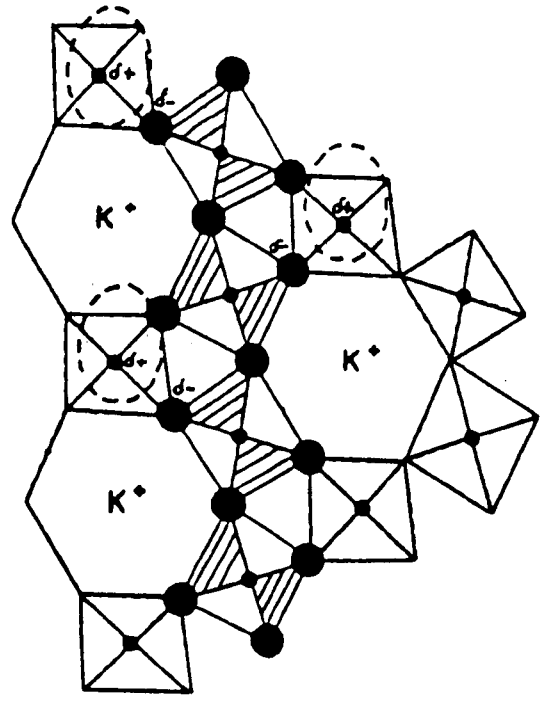

Fig. 11.1 Hexagonal potassium tungsten bronze, ● oxygen; ●, tungsten; K^+, potassium ; ⌒ Lewis acid site.

The formation of Bronsted acid sites is caused by the addition of the alkali metal ion and the extent of formation depends on both the nature and concentration of the added metal ion. The activation energy values for the dehydration reaction have indicated that sodium is more effective in forming Bronsted acid sites in the bronze than potassium and this

can be associated with the electronegativity of the alkali metal ion inserted. Na^+ is more electronegative, (0.9, Pauling scale), than K^+, (0.8, Pauling scale), and is more effective in polarising the W-O bond in the bronze. The attraction of a proton by O^- leads to the formation of a Bronsted acid site. Figure 11.2 shows such a site on an hexagonal sodium tungsten bronze. Bronsted acid sites were not observed on the potassium bronzes until the alkali metal ion content reached, x = 0.3, whereas for the sodium bronzes, Bronsted sites were present at all alkali metal ion concentrations.

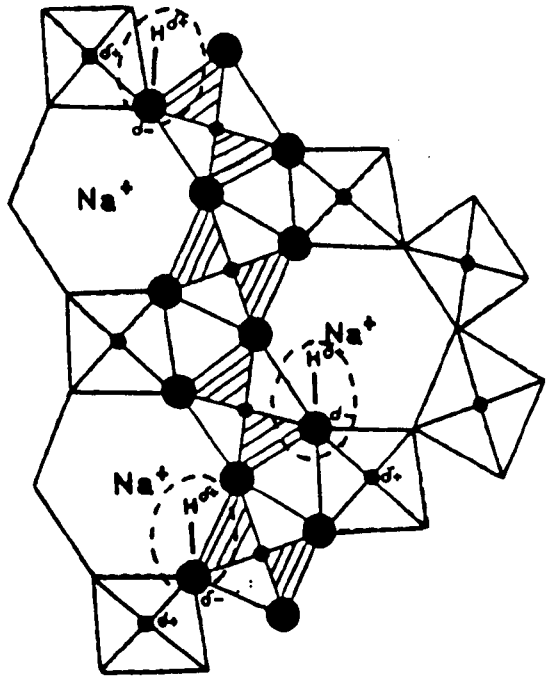

Fig. 11.2 Hexagonal sodium tungsten bronze, ●, oxygen; ●, tungsten; Na^+, sodium; ◯ Bronsted acid site; H, Hydrogen

The possible mechanisms of IPA dehydration on Lewis acid sites and on Bronsted acid sites are shown in Schemes 1 and 2 respectively.

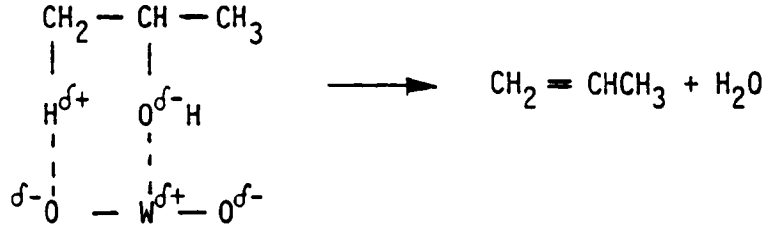

Lewis acid site

Scheme 1. IPA dehydration on a Lewis Acid Site

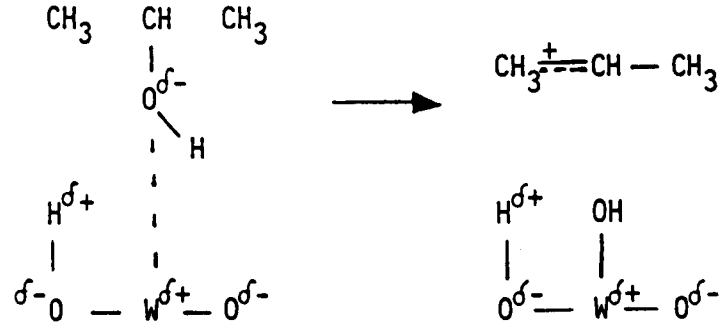

Bronsted acid site

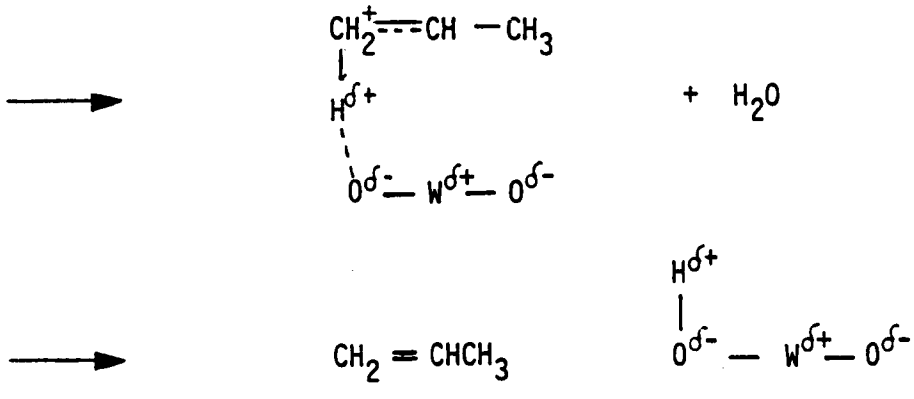

Scheme 2. IPA dehydration on a Bronsted Acid Site

The catalytic reaction of propene has been used to probe the semiconductor-metallic transition of the sodium and potassium bronzes. It has been shown that metathesis of propene is dominant over metallic solids whereas dimerisation of propene is the most likely reaction over insulating solids[3]. The potassium and sodium bronzes prepared here with $x \leq 0.2$ have semiconductor properties while bronzes with $x \geq 0.3$

are metallic. The catalytic reaction of propene on WO_3, the potassium bronzes and the sodium bronzes gave ethene, but-2-ene (metathesis products) and hexenes (dimerisation products) as the major products. For both the potassium and the sodium bronzes, selectivity for metathesis reached a maximum when x was equal to 0.2, although electrical resistivity measurements indicated that such a transition occurs between an alkali ion content of 0.2 and 0.3. A useful comparison can be obtained if the nature and number of active sites in the bronzes were defined. If it is assumed that the W atoms are the active sites for both the metathesis and the dimerisation reactions, it will first be necessary to calculate how many of these are present in a unit area of surface. The turnover rates (the number of molecules which react per active site per second) are routinely measured for many different metal catalysts because selective chemisorption techniques have been developed to determine the number of surface atoms. The selective chemisorption technique unfortunately usually does not work well with metal oxides and the number of exposed sites in metal oxide catalysts are not generally known. The number of active sites for oxide catalysts can be estimated from the number of cations present on the crystal planes most likely to be exposed at the surface, but in the present study the number of active sites was assumed to be the total number of W atoms present.

The turnover numbers for the dimerisation and metathesis reactions on the bronzes are given in Table 11.1 The activity of the bronze samples show a maximum in turnover number for metathesis when x = 0.2 in M_xWO_3 whereas the activity for the dimerisation reaction show a decrease in turnover number with increasing alkali ion content. It is difficult to assess whether the maximum in activity for metathesis is associated with the electrical properties of the bronze. However, the activity

for metathesis is lower at higher alkali ion content suggesting that both K and Na have a detrimental effect to the reactivity of the active sites.

Table 11.1 Turnover Numbers for Metathesis and Dimerisation of Propene on WO_3, K_xWO_3 and Na_xWO_3

Sample	Turnover No/molecules per site $s^{-1} \times 10^{-6}$ for metathesis	Turnover No/molecules per site $s^{-1} \times 10^{-5}$ for dimerisation
WO_3	5.8	2.64
0.05KW	12.3	1.43
0.2KW	25.3	0.53
0.3KW	8.1	0.27
0.6KW	4.3	0.28
0.8KW	2.2	0.07
0.05NaW	8.4	1.23
0.2NaW	22.9	0.65
0.3NaW	9.3	0.33
0.6NaW	3.4	0.20
0.8NaW	4.8	0.28

A potassium tungsten bronze in which copper ions were inserted by ion-exchange was prepared. Xrd indicated that the compound formed has a homogeneous bronze structure. The xps of the sample has suggested that copper may be in the +2 oxidation state, while W is in an oxidation state of about +5, with the compound having an empirical formula, $Cu_{0.062}K_{0.13}WO_3$. The presence of copper in the bronze does not affect its reducibility. The copper surface area was estimated

by N_2O decomposition and was calculated to be $0.38 m^2 g^{-1}$. The copper bronze is active in methanol synthesis from synthesis gas, but shows a higher selectivity for methane than methanol formation. The copper sites are less active than those present in a Cu/ZnO catalyst but are as active as those on a Cu/TiO_2 catalyst[4]. It was thought that Cu in a high oxidation state was the active site in methanol synthesis.

A supported potassium tungsten bronze was prepared by impregnating a silica support with an aqueous solution of potassium tungstate, (pH 4), followed by reduction in hydrogen gas at 770K. Xrd studies on the supported bronze suggested it to have an hexagonal structure. The X-ray photoelectron spectrum of the bronze has shown tungsten to be in an oxidation state of about +5. The activity of the bronze was monitored for ammonia synthesis but was lower than that observed for a potassium tungsten bronze supported on alumina. This may be due to the larger crystalline particles present on the silica-supported bronze.

CHAPTER 11

REFERENCES

1. Y. Kera and M. Negoro, J. Catal., 99, 198, (1986).
2. K.T. Seo, S.C. Kang, H.J. Kim and S.K. Moon, Korean J. Chem. Eng., 2, 2, 163, (1985).
3. N. Tsuda, T. Mori and Y. Sakai, J. Mol. Catal., 28, 183 (1985).
4. M.S.W. Vong, P.A. Sermon, M.A. Yates, A. Perryman and P. Reyes, Unpublished work.

-----oOo-----

APPENDIX 1

The publication* arising from previous work of the author on supported hexagonal tungsten bronzes is appended.

* S. Stevenson and P.A. Sermon, J. Chem. Soc., Faraday Trans. 1, 83, 2175, (1987).

Promotion of Nitrogen and Hydrogen Chemisorption and Ammonia Synthesis on Alumina-supported Hexagonal Tungsten Bronze, K_xWO_3

Sheena Stevenson and Paul A. Sermon*

Department of Chemistry, Brunel University, Uxbridge, Middlesex UB8 3PH

Alumina-supported hexagonal K_xWO_3 phases have been prepared in the presence and absence of Pt; K significantly promotes the chemisorption of nitrogen and Pt the chemisorption of hydrogen thereon. The turnover number for the production of ammonia (molecules of ammonia produced per site capable of chemisorbing hydrogen per second) was very low, but was promoted by K and not Pt. The modes of adsorption and catalysis and the manner of their promotion are considered in detail.

Ammonia synthesis can be catalysed by non-group VIII metals,[1] their oxyanions[2] and complexes.[3] However, for W the enthalpy of hydrogen adsorption [130 kJ mol^{-1} on polycrystalline surfaces, 38–159 kJ mol^{-1} on W(111) and 84–163 kJ mol^{-1} on W(211)][4] is only about a fifth that of nitrogen (820 kJ mol^{-1}), despite the high bond strength (914 kJ mol^{-1}) of dinitrogen. This mitigates against effective catalysis of ammonia synthesis by metallic tungsten. Consideration has been given here to whether the activity of W surfaces can be promoted to enhance the adsorption of both nitrogen and hydrogen, and subsequently ammonia synthesis, by controlling the oxidation state and symmetry of its reaction centres,[5] concentrating on supported K_xWO_3 'bronze' phases where the lattice cation oxidation state and symmetry of location is controlled by the oxide matrix and the size, location and concentration of the intercalated xK^+ ions and its xe^- electrons.

Alkali-metal bronzes are non-stoichiometric solids, M_xWO_3, in which M^{n+} ions and ne^- electrons are inserted (where $0 < x < 1$) into the oxide conduction band and the solid interstitial channels.[6] Potassium bronzes were selected since alkali-metal oxides are an important group of promoters to transition-metal catalysts[7] for ammonia synthesis, CO hydrogenation *etc.*; for example, K_2O markedly accelerates the adsorption of nitrogen on polycrystalline Fe.[8] In the present bronzes the location and state of the K^+ could be well defined, unlike some traditional catalysts (e.g. in promoted Fe-based catalysts some of the K_2O may be chemically combined with the iron oxide and also in a free surface state[9] and is mobile on alumina alone at, say, 670 K, to an extent which varies with the prevailing gaseous atmosphere.[10] Surprisingly, on Re single crystals and foils, where the rate-determining step remains N_2 dissociative chemisorption, no promotional effect of K is observed,[11] which contrasts with the significant promotional effect of K on Fe single crystals.[8] Sometimes K : M ratios as high as twelve have been recommended[12] in ammonia synthesis catalysts.

Doubly and triply promoted iron catalysts[13] are the cornerstone of ammonia synthesis. Nevertheless, despite their lower density, supported catalysts (especially those on graphite-containing carbon)[14] are being developed where a promoter alkali-metal ion is actively associated with the metallic phase (*e.g.* Ru or VB–VB–VIIB or VIII transition metal).[14] Alumina-supported Fe has also been reported for ammonia synthesis,[15] where activity at 101 kPa and 593 K was in the range 1–4 μmol NH_3 per g (Fe) per h. The activity on Ru/MgO and Ru/CaO was promoted by the alkaline-earth support,[16] where there may have been electron transfer from the support to the Ru.

Table 1. Catalysts prepared upon Alumin Oxid C[a]

sample	W (wt%)	Pt (wt%)
W1.5	1.50	0.00
KW1	1.01	0.00
KW3	3.00	0.00
KW5	5.04	0.00
KW10	10.14	0.00
PtKW3	3.04	0.527
PtKW5	5.11	0.556
PtKW10	10.03	0.640

[a] 97.0% γ-Al_2O_3; < 2000 ppm SiO_2, Fe_2O_3; non-porous; 90, 100, 101, 113 $m^2 g^{-1}$ indicated by N_2 B.E.T. measurements.

Results for supported $K_x WO_3$ catalysts where K and Pt are the promoting phases for adsorption and catalysis on W surface sites are now reported.

Experimental

Catalyst Preparation

All alumina-supported catalysts were prepared using Aluminium Oxid C (Degussa) whose properties are given in table 1. Monolayer coverage of the support by the W phases was thought to require on average 5 W atom m^{-2} and an attempt was made to prepare most catalysts (see table 1) below this concentration to minimise the formation of poorly dispersed 'bulk' W phases.

WO_3/Al_2O_3 was prepared at a loading of 1.5 wt% W by impregnating the alumina to the point of incipient wetness with an aqueous solution of ammonium tungstate (B.D.H. Chemicals Ltd; 95.0% purity). The product (denoted W1.5) was dried at 393 K for 16 h and then calcined in air at 823 K for 2 h.

$K_x WO_3/Al_2O_3$ samples (denoted KW1, KW3, KW5 and KW10) were prepared by impregnating the predried alumina with an aqueous solution of potassium tungstate of the correct strength and volume to ultimately give 1, 3, 5 and 10 wt% W and to just wet the alumina completely. Samples were dried in an air oven at 373 K for 12 h and stored in air unreduced. The pH of the impregnating solutions varied a little (9.04–9.08) depending upon the precise W loading to be achieved. Under these conditions the alumina support is thought to undergo only slight dissolution.

$Pt/K_x WO_z/Al_2O_3$ samples were prepared by impregnating the predried alumina with aqueous solutions containing required amounts of H_2PtCl_6 (Johnson Matthey; Specpure) and potassium tungstate. In each case the ultimate loading of Pt was 0.5 wt%, but the W concentration varied. The mixed impregnating solution gave strong absorbance at 241 mm, and since this was also true for a solution of hexachoroplatinic acid alone, it was thought that the $PtCl_6^{2-}$ ions remained intact in the mixed solution at ambient temperatures. Samples (denoted PtKW1, PtKW3, PtKW5 and PtKW10) were also dried in air at 373 K for 12 h. The pH of the mixed-metal impregnating solutions (*ca.* 5.75) was almost independent of concentration in the range used. At this pH the alumina support is thought to undergo meagre dissolution.

Temperature-programmed bulk reduction (t.p.b.r.) described later suggested that each catalyst should be reduced in flowing H_2 (40 cm^3 min^{-1}; 101 kPa) at 1023 K for 16 h. This

was carried out upon the samples (and the support alone), and each was then cooled in the reductant stream to ambient temperature and flushed with flowing Ar. Subsequently an *in situ* reduction was carried out.

Experimental Methods

Estimates of the extent of N_2 physical adsorption at 77 K (determined using a semi-automatic Carlo-Erba Sorptomatic series 1800) was used to determine total accessible surface areas assuming the cross-sectional area of adsorbed N_2 to be 0.162 nm^2.

Raman spectra were recorded on a Spex Ramlab spectrometer using a coherent radiation model 52M.G. Ar/Kr laser with a green-interference filter to remove plasma lines; a cylindrical lens was used before the sample to minimise sample decomposition. Aqueous solutions were analysed in a capillary. Signals were measured at 90° to the incident beam; the laser output was *ca.* 30–100 mW and the slit-width 5 cm^{-1}.

Thermogravimetric and differential theral analyses were carried out on samples (*ca.* 30 mg; predried in flowing N_2 at 373 K for 15 min) using a Stanton Redcroft STA780 analyser, α-alumina references, 10 K min^{-1} heating rate and 40 cm^3 min^{-1} flow rate. T.p.b.r. was carried out on samples (0.5–2.0 g) in flowing 6% H_2 in N_2 (40 cm^3 min^{-1}), from which oxygen and water contaminants had been removed by passage through beds of Pd/Al_2O_3 and 5A molecular sieve at 295 K. Hydrogen concentrations were measured after removal of product water at 203 K using a hot-wire detector (Gow Mac Katharometer 01106P) during heating at 5 K min^{-1}.

X-ray photoelectron spectra were measured on a Kratos ES300 instrument using Al K_α radiation and were calibrated against the C 1s peak at 284.8 eV. Diffractometry was used to ascertain the structure of catalyst (PW1050 generator operating at 50 kV and 24 mA *via* a Ni filter producing Cu $K_{\alpha 1}$ radiation).

The extents of chemisorption of hydrogen and nitrogen were measured ±10% in a volumetric system described previously.[17] A known weight of the catalysts (prereduced at 1023 K for 16 h in H_2) was flushed with flowing Ar for 15 min, H_2 at 773 K ± 5 K for 3 h, and then flowing Ar for 1 h. Samples were then evacuated to 1–3 mPa at 773 K, after which H_2 (Research grade; 99.9995% purity; BOC) chemisorption was followed at the same temperature. Equilibration times of 15–20 min were required. Pressures were measured using a mercury manometer/cathetometer and a pressure transducer (Bell & Howell BHL1010; Hg vapour was prevented from reaching the catalysts by a trap held at 77 K). After measurement of hydrogen chemisorption, the sample was re-evacuated at 773 K and the extent of nitrogen chemisorption measured at 773 K ± 5 K (after changing the cold trap separating the sample from the remainder of the system to one at 195 K). 'Monolayer' extents of adsorption were estimated from the gradient of the linear Langmuir plots and also extrapolation of adsorption data at 30–70 kPa to the zero pressure; all isotherms approximated to a Langmuir form.

The activity of samples in catalysing the synthesis of ammonia was measured using a silica flow reactor at 101 kPa with the sample held in a furnace (Stanton Redcroft Cl/Pt13/CL) to within ± 5 K of the set temperature. The product stream flowed through 20 cm^3 of de-ionised water (obtained by passing double-deionised water through a Duolite ion-exchange column) whose conductivity could be monitored continuously (Fisons PT1-18). Catalyst samples (*ca.* 0.5 g) were flushed with Ar (99.9% purity; BOC) for 15 min and then H_2 (99.95% purity; BOC) at ambient temperature, and as the sample temperature was raised to 1023 K at 10 K per min and then held there for 2 h. Subsequently, the H_2 was replaced by flowing Ar and the sample cooled to ambient temperature. During this pretreatment the conductivity detector gave a constant reading; the reactant stream of 75% H_2 in N_2 (99.99% purity; BOC; pre-purified by removal of oxygen and water-vapour in the same was as the gas stream used in t.p.b.r. experiments

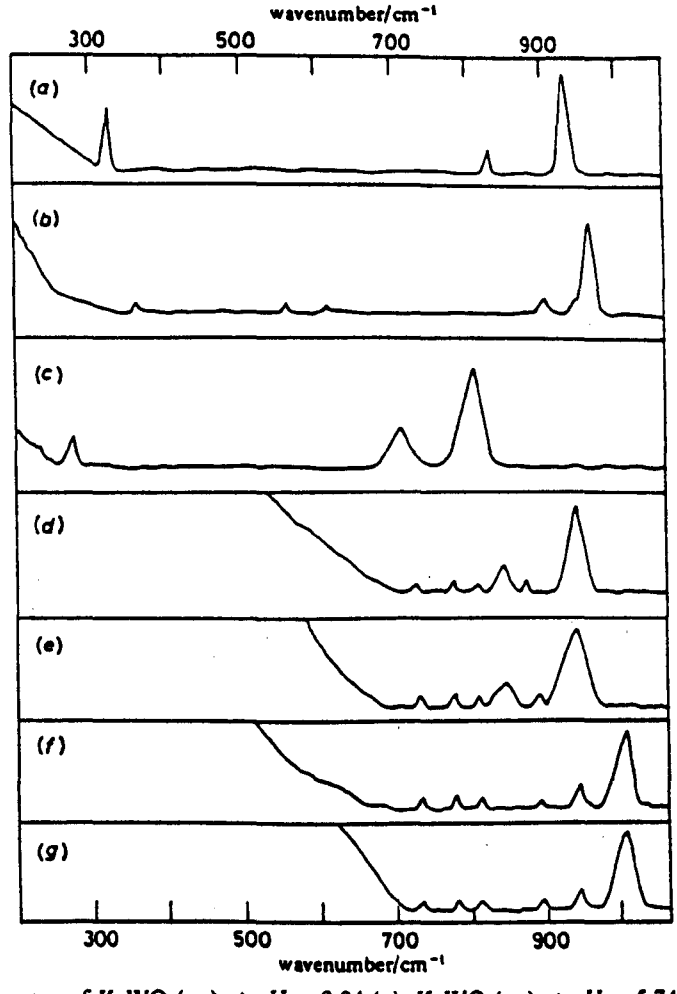

Fig. 1. Raman spectra of K_2WO_4(aq) at pH = 9.04 (*a*), K_2WO_4(aq) at pH = 5.74 (*b*) and WO_3 (*c*) and some supported catalysts; (*d*) unreduced KW10, (*e*) unreduced KW5, (*f*) unreduced PtKW10 and (*g*) unreduced PtKW5.

described above) was introduced at 40 cm^3 min^{-1}. The sample temperature was then increased to 523 K (or 573, 673 or 773 K) and conductivity *vs.* time measurements undertaken under isothermal conditions. The conductivity of the water (initially 0.5 S cm^{-1}) rose linearly with ammonia concentration to 140 nmol. The error in the assessment of the quantity of ammonia formed was ± 3 nmol.

Characterisation Results

Raman Spectroscopy of Unreduced Catalysts

The Raman spectra of K_2O_4 in solution at pH 5.75 and 9.04 (selected because of their relevance to conditions of catalyst preparation), WO_3 and of unreduced samples KW5, PtKW5, W10 and PtKW10 are shown in fig. 1 and main band positions are given in table 2. Spectra of catalysts with lower W contents gave no well defined peaks.

The Raman spectrum of WO_3 shows expected bands.[18] The peaks of K_2WO_4 are characteristic of tetrahedral WO_4^{2-} and this ionic state is known to exist exclusively in

Table 2. Raman spectroscopic data

sample	bands/cm^{-1}
K_2WO_4 (pH 9.04)[a]	933, 830, 324
K_2WO_4 (pH 5.75)[a]	962, 905, 615, 560 and 366
WO_3[a]	807, 712 and 276
Al_2O_3	890, 810, 799 and 735
KW5, KW10	945 and 847
PtKW5, PtKW10	1010 and 945

[a] Assignments: symmetric W=O stretching vibration 933 cm^{-1}; antisymmetric W=O stretching vibration 830 cm^{-1}; W=O bending vibration 324 cm^{-1}; W=O stretching vibration 807 cm^{-1}; W=O stretching vibration 712 cm^{-1}; W—O—W deformation vibration 276 cm^{-1}.

neutral and alkaline solutions;[19] the Raman spectrum of solid K_2WO_4 was identical. However, that for K_2WO_4 in solution at pH 5.75 is similar to that of solid $Na_{12}W_{12}O_{42}\cdot 18H_2O$,[20] and it may be that the octahedral $W_{12}O_{42}^{12-}$ ion is present in the acidic solution.

Previous studies of $Al_2(WO_4)_3$[15, 21] have shown it exhibits a characteristic and sharp Raman band at 1046 cm^{-1} which may be used here to differentiate and detect this species in present catalysts. Only very small Raman bands were observed for the alumina support used here, and it was not thought to interfere too seriously with Raman analysis of these supported W catalysts. Raman spectra of unreduced KW5 and KW10 catalysts showed two major bands which were broader than those observed for pure K_2WO_4 and were also shifted slightly to higher wavenumbers than those for K_2WO_4 in the impregnated solution at pH 9.04 (*i.e.* 830 and 933 cm^{-1} which can be attributed to symmetric and antisymmetric W=O stretching modes, respectively, in the supported phases). The broadening of these bands could be due to coordination of water to the alumina-supported tungsten complex. No bands were shown at 100–400 cm^{-1}, a region which reflects the crystallinity of the sample. Thus the supported phases could be in a moderately well dispersed state. All other bands for these catalysts were consistent with those for the support. If water is coordinated to the surface W sites it might produce an octahedral from a tetrahedral symmetry.

Increasing the coordination of W to six should increase the W=O stretching modes to higher wave numbers. Simultaneously the order of the terminal W=O bonds will decrease (with a decrease in the W=O stretching frequency). The symmetric W=O stretching mode in Na_2WO_4 (928 cm^{-1}) increases to 931 cm^{-1} in Na_2WO_4.[22] Here the shift for supported catalysts could be attributed to the presence of adsorbed water. No band at 1046 cm^{-1} was found in unreduced supported catalysts indicating the absence of $Al_2(WO_4)_3$.

The Raman spectra of unreduced PtKW5 and PtKW10 showed bands of W=O stretching modes corresponding to those in K_2WO_4 in acid solution, but shifted *ca.* 4% to higher wavenumber, possibly as a result of an active-phase/support interaction. Similar behaviour has been observed in the Raman spectra of $(NH_4)_6H_2W_{12}O_{40}/Al_2O_3$ catalysts.[19] The absence of bands at low wavenumber and at *ca.* 1046 cm^{-1} again suggests highly dispersed supported phases in the absence of $Al_2(WO_4)_3$.

Raman spectroscopy then provides valuable evidence of the state of these catalysts

as it has previously.[23] There is no suggestion of WO_3–alumina interactions[24] forming $Al_2(WO_4)_3$, which was previously only detected after calcination *ca.* 1273 K or as a minor component at 863–1123 K.[25] It is very sensitive to the coordination of the W and the vibrational modes of the W=O bonds; there the spectra of KW5, 10 and PtKW5, 10 in fig. 1 do not correspond to those of crystalline WO_3, K_2WO_4 or $Al_2(WO_4)_3$ [see fig. 4 in ref. (24)], although unfortunately peaks below 700 cm^{-1} are obscured.

Thermal Analysis of Reduction Characteristics

On heating K_2WO_4 in flaring hydrogen a broad endotherm at 473–700 K with a weight loss of 3% is followed by a sharp exotherm at 855 K with a further weight loss of 22.53%. Neither is likely to be associated with loss of water (heating in nitrogen produced only 0.6% weight loss) but possibly to conversion of the tungstate to a bronze, $K_{0.28}WO_3$ (*i.e.* $K_2WO_4 + 0.14H_2 = K_{0.28}WO_3 + 0.86K_2O + 0.14H_2O$). T.p.b.r. confirmed a multistep reduction with maxima at 653, 913 and 1018 K. The total hydrogen consumption (0.0430 mmol g^{-1} sample) for the formation of the above bronze. Table 3 gives H_2 consumption and weight-loss data.

Equivalent data for catalysts are given in fig. 2 and table 3; no weight losses of significance were seen with any sample on heating in nitrogen and for results of heating in hydrogen there is moderate agreement between bronze compositions estimated by t.g.a. and t.p.b.r. For no samples was there reduction to the metallic state of W on heating to 1023 K in hydrogen. Supported phases reduced at lower temperatures than unsupported K_2WO_4, partly as a result of the high dispersion. Indeed, temperatures of reduction were lowest at lowest W loadings. Introduction of Pt appears to facilitate lower-temperature reduction and this may be associated with spillover. It is to be expected that reduction of Pt species will occur within the lowest temperature reduction maxima. However, it was not possible to assign to these t.p.b.r. peaks reduction processes of separate and distinct phases[26] in such complex catalysts.

No hydrogen consumption was observed on heating W1.5 (WO_3/Al_2O_3) in hydrogen to 1323 K in t.p.r. It may be that a surface tungsten oxide is obtained at the low WO_3 loadings which is difficult to reduce further.

X-Ray Photoelectron Spectroscopy of Unreduced and Reduced Catalysts

The W $4f_{7/2}$ peak for unreduced K_2WO_4 was found at a binding energy of 36.5 eV and close to the value for WO_3 (36.0 eV). For KW1–10 its position was unchanged at 37.6 eV, but the full width at half maximum height of this peak was found to decrease as the metal loading increased (*i.e.* 0.5, 0.4, 0.3 and 0.2 eV for KW1, KW3, KW5 and KW10); a similar observation was reported for alumina-supported MoO_3 and WO_3,[18, 27] and broadening was attributed to charging effects. Here the width of the Al $_{2p}$ peaks also decreased in the same sequence and this eliminates the possibility that multiple W oxidation states are contributing to this observation.

A linear relationship is to be expected between concentration and X.p.s. intensity for highly dispersed supported W phases. Fig. 3 shows that this does indeed exist for the present catalysts at least up to *ca.* 6.8 wt% W (or 2.25×10^{20} W atom g^{-1} catalyst). This could correspond to 'monolayer' coverage of bronze on the support. The lowest B.E.T. area of the alumina support was found to be 90 $m^2 g^{-1}$ (see table 1), and if this has 4.5 OH groups per m^2 of the surface[28] then there are 4.05×10^{20} OH groups at the surface per g. This suggests that two OH groups could be associated with the adsorption of each W ion; this is consistent with the molecular model needed in interpreting Raman spectra. However, it is important to note that X.r.d. reveals well crystallised material.

Similar results were obtained for PtKW1–10 samples. K peak intensities were not diminished by reduction and hence K_2O is not substantially lost. X.p.s. of reduced

Table 3. Reduction characteristics of catalysts

	t.g.a. % wt loss			t.p.r. H_2 consumption					
sample	endo[a]	exo[b]	x	T/K of max. red. rate				total H_2 used[c]	x
KW1	0.20	0.50	0.21	—	418	723	1008	9.60	0.34
KW3	0.45	0.79	0.47	—	403	726	999	23.70	0.29
KW5	0.68	1.37	0.50	—	418	746	1003	49.30	0.36
KW10	1.03	4.10	0.50	—	533	823	1010	104.75	0.38
PtKW1	0.82	0.20	0.52	383	550	810	1006	62.10	0.40
PtKW3	1.32	0.66	0.40	373	523	773	1018	86.75	0.39
PtKW5	2.42	1.00	0.49	383	508	744	1018	98.79	0.31
PtKW10	3.28	2.12	0.42	440	558	820	1007	163.96	0.36

[a] % weight loss below 823 K. [b] % weight loss at 823–1023 K; [c] μmol H_2 g^{-1}. T.g.a. and t.p.r. denote thermogravimmetric analysis and temperature programmed reduction, respectively.

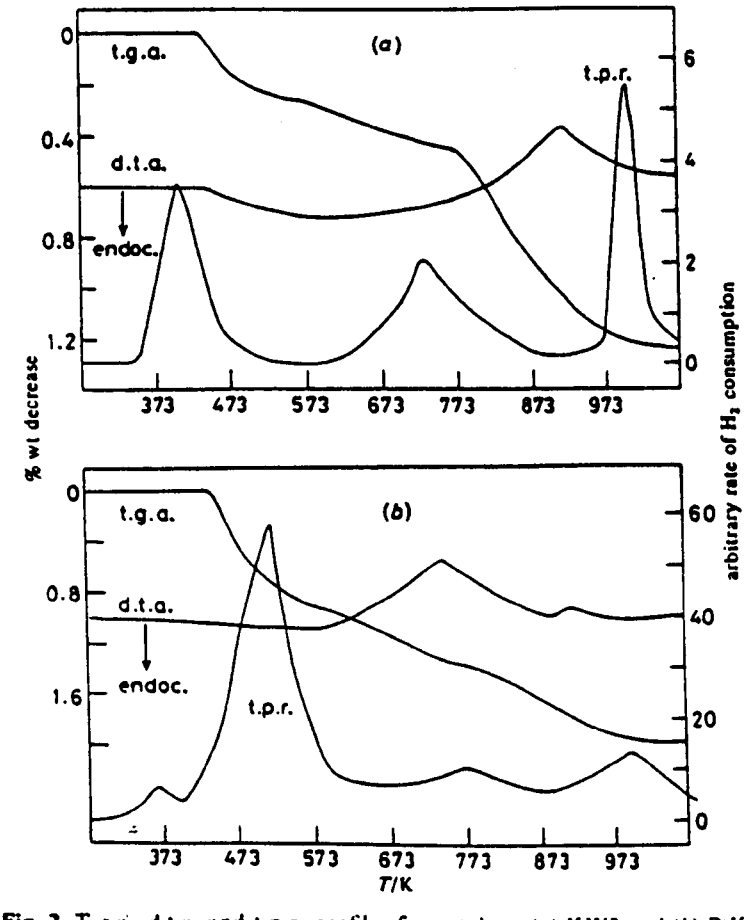

Fig. 2. T.g.a., d.t.a. and t.p.r. profiles for catalysts (*a*) KW3 and (*b*) PtKW3.

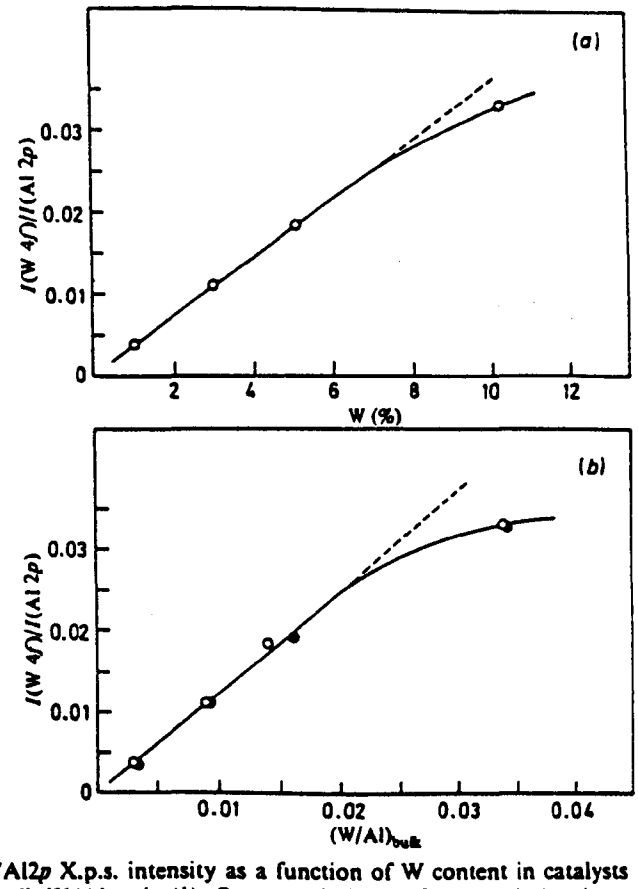

Fig. 3. W4$f_{7/2}$/Al2p X.p.s. intensity as a function of W content in catalysts KW1–10 (*a*) and as a function of bulk W/Al ratio (*b*). Open symbols and filled symbols relate to catalysts KW1–10 and PtK1–10, respectively, before reduction. Deviation from linearity above *ca.* 7% W suggests the presence of a poorer dispersion.

catalysts found the W 4*f* peaks changed to lower binding energies corresponding to those of W^{6+}, but not to the metallic state or that in $Al_2(WO_4)_3$ (*i.e.* 36.1 eV.[29] In reduced PtKW1–10 only one Pt peak ($4d_{5/2}$) was found at a binding energy of 319.0 eV, which appeared to correspond to the zero-valent state.[30]

X-Ray Diffraction of Unreduced and Reduced Catalysts

Diffractometry of pure unreduced K_2WO_4 was consistent with a monoclinic structure (a_0 = 1.2382 nm, b_0 = 0.61194 nm and c_0 = 0.75526 nm), but after reduction, *d* values corresponded to a hexagonal structural state ($a_0 = b_0$ = 0.734 nm and c_0 = 0.752 nm). These results agree with data for hexagonal potassium bronzes of tungsten.[31]

After subtraction of broad peaks for the support, reduced KW10 and PtKW10 were found to exhibit X-ray diffraction patterns which were consistent with hexagonal structures (a_0 = 713 nm, c_0 = 0.775 nm and a_0 = 710 nm, c_0 = 0.782 nm). KW5 and PtKW5 gave similar but weaker diffraction patterns; catalysts of lower W content could not be analysed by this method. None of the catalysts gave diffraction peaks corresponding to $Al_2(WO_4)_3$, and if present its concentration was judged to be below the limit of detection by XRD.

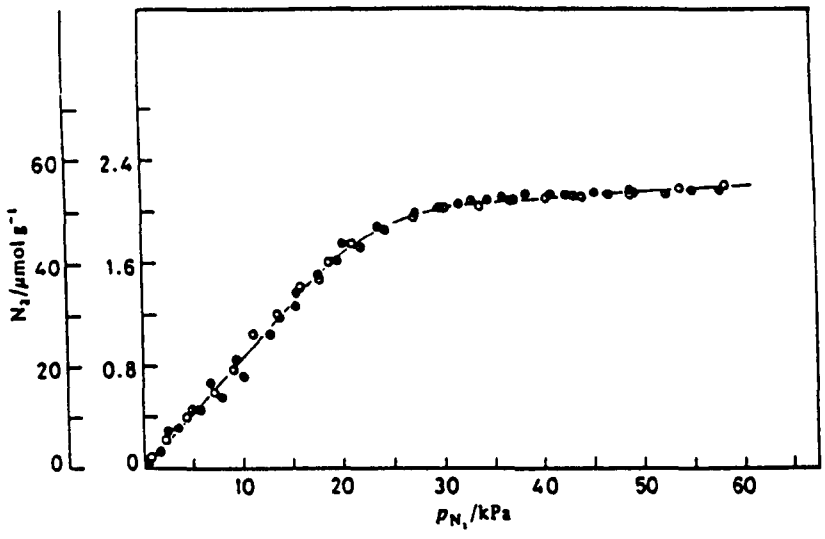

Fig. 4. Isotherms of nitrogen on KW3 (○), W1.5 (◑) and PtKW3 (●) at 773 K.

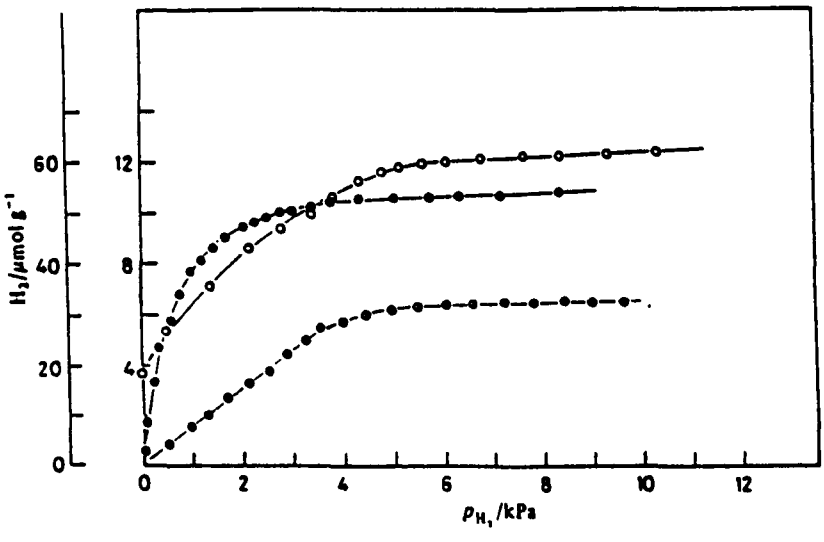

Fig. 5. Isotherms of hydrogen on KW3 (○), W1.5 (◑) and PtKW3 (●) at 773 K. These reach a plateau at lower pressures than for N_2.

Summary

Samples of alumina-supported K_xWO_3 appear to have been prepared here by an impregnation–reduction route. X.p.s. intensities suggest the active phase is quite highly dispersed and yet exhibits a hexagonal structure detectable by X-ray diffraction at higher concentration; possibly the active phase exists in both forms in some catalysts. There was no evidence of bulk reduction of W to the zero-valent state or complete loss of K. Although it would not be possible to rule out the separate retention of K_2O on the alumina, under the conditions of preparation here it would have sublimed and been lost if separated. There was no X.p.s. evidence of loss of K from PtKW10 on reduction. Hence the interpretation here is in terms of K_xWO_3 upon the alumina support.

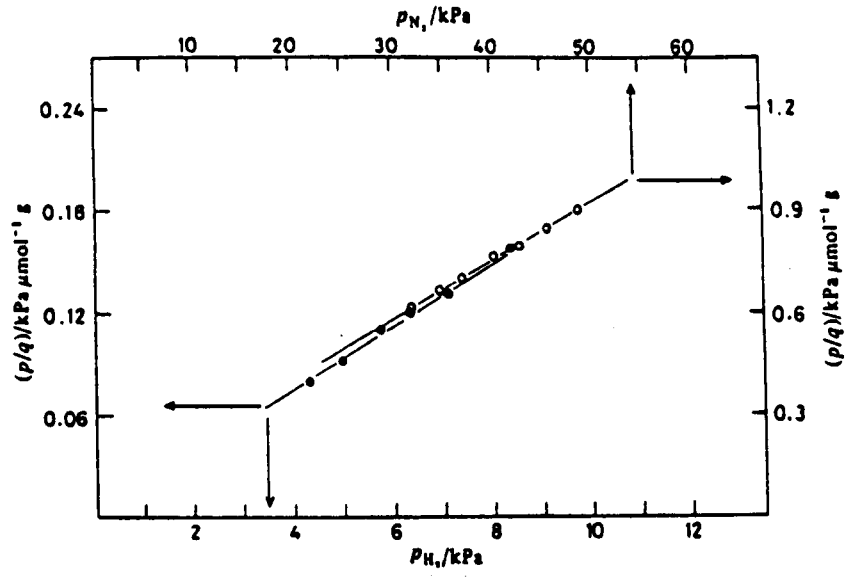

Fig. 6. Linear Langmuir plots for nitrogen (○) and hydrogen (●) chemisorbing upon PtKW3 at 773 K.

Table 4. Adsorptive and catalytic properties

sample	'monolayer' extent of N_2 or H_2 adsorption/μmol g^{-1}				r_{NH_3} after 20 min /nmol NH_3 g^{-1} min^{-1}				$N^*_{NH_3}$ at 773 K /10^3 molecule site^{-1} h^{-1}
	N_2 (773 K)	H_2 (773 K) total	H_2 (773 K) max_{Pt}	H_2 (773 K) min_W	523 K	573 K	673 K	773 K	
W1.5	2.06	6.15	0.00	6.15	—	—	—	0.11	0.53
KW1	—	—	—	—	0.16	0.20	0.45	—	—
KW3	55.83	12.75	0.00	12.75	—	0.47	0.73	1.02	2.37
KW5	73.75	13.00	0.00	13.00	0.54	0.86	1.21	2.22	4.99
KW10	35.31	10.58	0.00	10.58	—	0.27	0.45	0.69	1.90
PtKW3	57.08	55.00	13.51	41.49	—	0.64	1.00	1.46	0.81 (1.09)
PtKW5	77.50	47.50	14.28	33.22	0.96	1.21	1.74	2.36	1.47 (2.10)
PtKW10	32.81	31.00	16.40	14.60	—	0.31	0.44	0.64	0.64 (1.37)

[a] Apparent turnover frequency was determined by dividing the rate of ammonia synthesis at 773 K by the extent of hydrogen chemisorption at the same temperature as estimated from the gradient of the linear Langmuir plots (see fig. 6) or by extrapolation of hydrogen chemisorption (see fig. 5) data to the zero-pressure intercept. N has units of NH_3 molecules produced per 1000 chemisorption sites per h; bracketed data relate to values of N calculated for W sites chemisorbing hydrogen in the column denoted min_W.

Adsorptive–Catalytic Results

Chemisorption Results

Fig. 4 and 5 show the Langmuir-type isotherms as the extent of adsorption (q) for N_2 and H_2 chemisorption upon W1.5, KW3 and PtKW3 catalysts as a function of

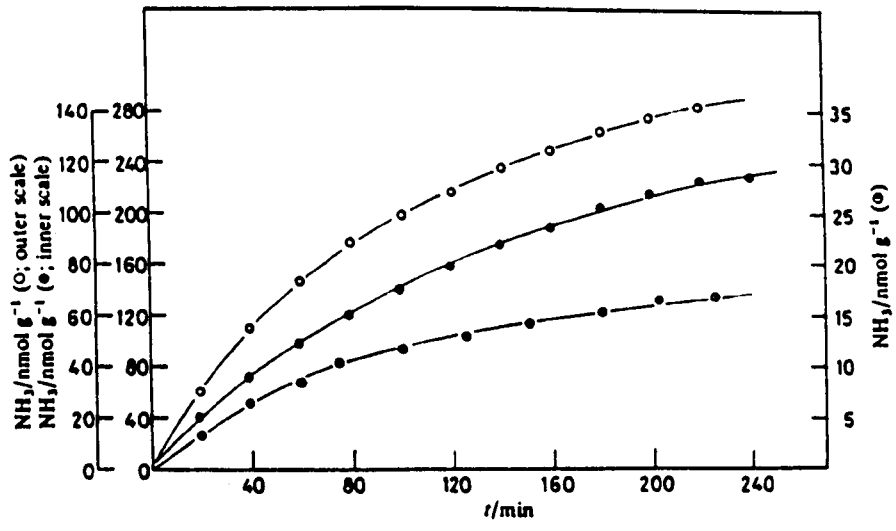

Fig. 7. Extent of NH_3 synthesis over KW3 (○), W1.5 (◑) and PtKW3 (●) at 773 K as a function of reaction time.

equilibrium pressure (p) at 773 K; extents of adsorption at monolayer coverage were deduced from the gradients of the linear Langmuir plots (see fig. 6) and are given in table 4 for all catalysts prepared here. First one should note that the rate of H_2 adsorption was faster on all samples than N_2, and its isotherms appeared to reach 'plateau' extents of adsorption at lower pressures. Secondly, the extent of N_2 chemisorption appears to be dramatically promoted by the presence of K (*cf.* data for W1.5 and KW3 *etc.* in table 4), although not by the addition of Pt, but that the extent of adsorption is a maximum close to the maximum dispersion suggested by x.p.s. intensity analysis in fig. 3. Thirdly, the reverse promotional effect appears to be the case for the extent of H_2 adsorption in that K has only a small promotional effect, but Pt a large promotional effect (compare data for samples KW3–10 and PtKW3–10 in table 4); again, maximum extent of adsorption is seen at maximum catalysts dispersion, suggested in fig. 3.

Ammonia Synthesis

Fig. 7 shows the extent of synthesis of ammonia on several catalysts at 773 K; Fig. 8 shows the effect of temperature on the rate and extent of ammonia synthesis over PtW3 in the range 573–773 K. It is clear from fig. 8 that rates of synthesis decrease with time at each temperature and indeed only reached steady-state values at *ca.* 1 h. Table 4 shows rates measured from gradients in fig. 7 over several catalysts at an arbitrary time into the reaction and also the activation energy calculated over this temperature range. Activation energies for all samples in ammonia synthesis under these conditions were much lower (14–21 kJ per mol) than previously estimated[1] and this suggests either diffusion limitation or that N_2 dissociation is not the rate-determining step. The turnover numbers, N, of ammonia synthesis over catalysts here were calculated in terms of molecules produced per non-Pt site active in hydrogen chemisorption per h; this seemed preferable to using the larger concentration of sites chemisorbing nitrogen. The values of N so calculated (shown in the last column of table 4) are very much lower than found for Group VIII metal catalysts and would be even lower if calculated on the basis of the numbers of sites chemisorbing nitrogen.

However, it is more important to consider the promotional effects of K and Pt upon the catalytic activity. It appears that K has a substantial promotional effect (*i.e.* compare

promotion. Interestingly, the extent of chemisorption of nitrogen exceeds that of hydrogen; this suggests that only a small fraction of this chemisorbed nitrogen is in a state which may be activated for ammonia synthesis. Further work is required to define how K promotes this specific type of nitrogen chemisorption (and hence ammonia synthesis).

Discussion and Conclusions

The monotungstate WO_4^{2-} exists in alkaline solution but polymerises as the pH drops:

$$6[WO_4]^{2-} + 7H^+ = [HW_6O_{21}]^{5-} + 3H_2O$$

and in the solid state undergoes transition to polymorphs such as $K_2W_8O_{25}$ at elevated temperatures; interestingly, the octatungstate is isostructural with the hexagonal tungsten bronze $K_{0.25}WO_3$, which together with hexagonal WO_3 are well known.[32] Here weight losses and hydrogen consumptions on reduction correspond to $0.29 < x < 0.40$. There is no evidence of zero-valent W formation. Raman spectroscopy of unreduced catalysts suggests that $W_{12}O_{41}^{10-}$ exists upon the alumina support and that this polytungstate is readily reduced to these hexagonal bronzes.

On all catalysts here the activity in ammonia synthesis increased with increasing temperature but, under isothermal conditions, also decreased with time. The low activation energy observed might be due to diffusion-limitation (or that the mechanism did not involve N_2 dissociation as the rate-determining step) and the isothermal deactivation could result from retention of a strongly bound surface intermediate. The turnover numbers for ammonia synthesis at 773 K calculated using hydrogen adsorption sites were very low. Naturally, ammonia does decompose over Pt at a rate (given by the Langmuir–Hinshelwood unimolecular rate equation[33] which amounts to 10^{15} molecule cm^{-2} s^{-1} (or a turnover number of 0.36 per h) and could have reduced values of N in table 4. It is possible that metals other than Pt would have a greater promotional effect. Equally, tungstates do catalyse ammonia synthesis,[1] but not to an extent which would be significant under present conditions. Normally the chemisorption and dissociation of nitrogen is rate-determining, but here it is interesting and surprising that nitrogen adsorption is more extensive than that of hydrogen. Pt had little effect on the extent of N_2 adsorption, which reached saturation coverage only at high pressures, but K does accelerate and promote nitrogen adsorption at 773 K (as it does in commercial synthesis catalysts), but whether this is because of electron donation to the W centres is uncertain; certainly such centres will be far more deficient of *d* electrons than in zero-valent catalysts. Hydrogen chemisorption was much faster than nitrogen and reached a saturation coverage at a much lower pressure, but this adsorbate may be more mobile on the catalyst surface than nitrogen and consideration needs to be given to why this should be so on the present surfaces.

Nitrogen adsorbs on polycrystalline zero-valent W surfaces, reaching *ca.* 40% monolayer coverage at room temperature.[34] However, its rate of adsorption is much slower on some planes [*e.g.* W(111)] than on others [*e.g.* W(100)].[34] As a result, equilibrium nitrogen adsorption isotherms of the extent of adsorption (q) *vs.* pressure (p) on W powder have been difficult to obtain, but generally obeyed the Freundlich model with linear $\log q$ *vs.* $\log p$ plots at moderate pressures; interestingly, the common point of intersection suggests *one* N atom adsorbed on average per two surface W atoms,[35] with a high initial enthalpy of adsorption (335 kJ mol^{-1}). The adsorption of hydrogen on W film and powder at 79–873 K also obeys[36] the Freundlich equation, with no maximum extent of adsorption reach at 13 kPa, but the initial enthalpy of adsorption is much smaller and decreased almost linearly with increasing coverage (in contradiction of the Freundlich model). In contrast, here the adsorption isotherms of hydrogen and nitrogen upon the present 'bronze' catalysts are approximately Langmuirian, and

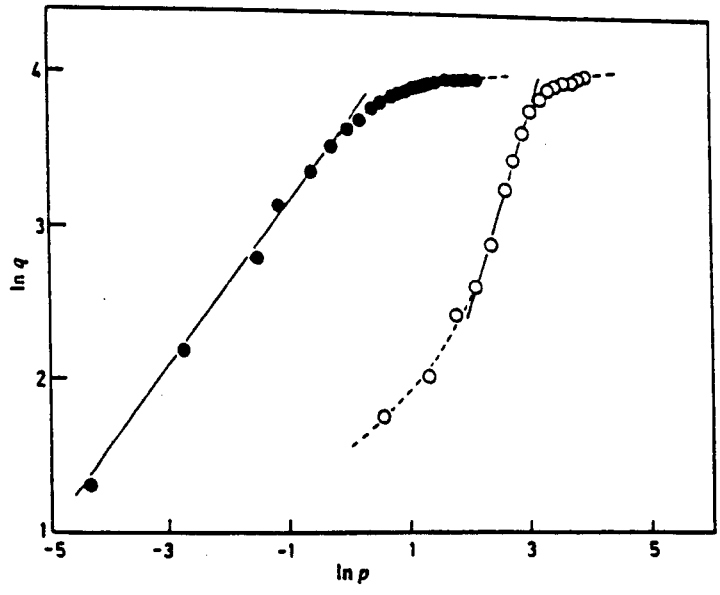

Fig. 9. Non-Freundlich behaviour of nitrogen (○) and hydrogen (●) adsorption on PtKW3 at 773 K, where $\ln p$ *vs.* $\ln q$ plots are distinctly non-linear if q is the extent of adsorption and p is the equilibrium pressure.

certainly not of the Freundlich form (see fig. 9); this suggests that the adsorption centres cannot approximate to the zero-valent W state, bearing in mind the past findings of Freundlich-type adsorption of hydrogen and nitrogen upon zero-valent W surfaces.

Although both nitrogen and hydrogen adsorb in several different states upon zero-valent W surfaces[34, 37, 38] (with nitrogen even weakly adsorbed on W(110),[37] it is uncertain whether any of these are truly molecular. The smaller hydrogen adsorbate might interact with sites not accessible to the larger nitrogen. Therefore, the precise location of the adsorbed nitrogen and hydrogen on surfaces of W remains uncertain,[34] and this is complicated by the tendency of W surfaces to reconstruct[39] during adsorption (*i.e.* tungsten atoms in the (001) surface readily undergo small lateral displacements).[40] Nevertheless, nitrogen and hydrogen may be located in fourfold coordination sites upon W(100); on a W(001) surface a hydrogen atom is deemed[41] to sit midway between two surface W atoms. Present hexagonal tungsten bronzes (see fig. 10) are formed by corner-shared WO_6 octahedra (with trigonal holes exceeding the number of hexagonal ones). K^+ ions sit within the hexagonal channels juts below the plane of the hexagon, in which the W—O—W angle between WO_6 octahedra centres is rather obtuse. It is necessary to consider how adsorption and catalysis may occur on such a surface and to compare this with what pertains in W complexes and on other transition-metal oxides. The dissociation of dinitrogen upon metal surfaces[42] is not directly relevant here. It is suggested that N_2 adsorbs at surface cation sites exposed on TiO_2 by dehydroxylation,[43] and here a similar adsorption mode is considered. First, it has been shown[44] that all such alkali-metal bronzes of W are oxygen-deficient, and so some of the terminal oxygens above the surface tungstens will be missing, and it is on these centres that electron donation from the K will produce W^{z+} centres (where z is 4 or 5). The triple bond of the nitrogen molecule could donate π electrons to the K^+ ion intercalated below the plane of the hexagon and the two ends of dinitrogen with a σ-bond to two W^{z+} centres. This molecular mode of adsorption of nitrogen upon the hexagonal bronze surface would be readily accepted by the $W^{(5-6)+}$ with their almost vacant *d*-orbitals, the process would be promoted by K^+. Hydrogen adsorption must involve heterolytic adsorption across

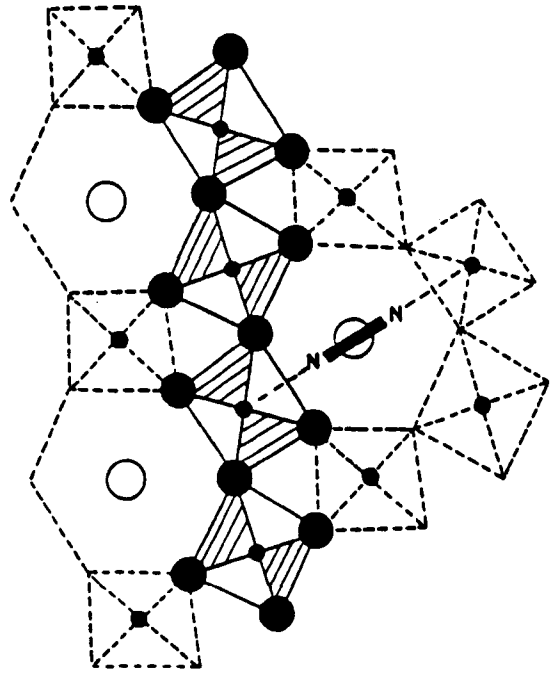

Fig. 10. Adsorption sites on hexagonal K_xWO_3 (●, oxygen; ●, tungsten in the plane of the hexagons; O, potassium below the plane of the hexagons). It is important to remember that on W(100) H and N atoms are chemisorbed in sites with four-fold coordination.

W—O sites and also hydrogen spillover promoted by Pt (which may not otherwise be involved in the catalytic reaction site).

This model would require the extent of nitrogen chemisorption to be related to the extent of surface oxygen deficiency in these bronzes. The size of the N_2 molecule (110pm bond length) means that it could just stretch across the opening of the hexagonal tunnels (width 260 pm) in this adsorption mode.

The catalysts used here were not seen as potential industrial catalysts (thus tungstates are more generally used as inhibitors,[45] although tungstates have been reported to catalyse ammonia synthesis,[2] and certainly WO_3 and MoO_3 have been recommended as additives to Fe ammonia synthesis catalysts.[46]

Studies on W surfaces[47] emphasise that the state of adsorbates at low pressures may be different from those at industrially relevant pressures. Equally, in catalysis, the effect of the alkali-metal promoter may be high at high pressure, but negative for the atmospheric-pressure synthesis of ammonia.[48] Therefore, the function of the present work was not to suggest that comparisons can or should be made between catalysis at low pressures and under commercial conditions. Indeed, research[49] has illustrated the difficulty of extrapolating from surface data at low pressures and temperatures to industrial conditions 723 K and > 100 atm. Nevertheless, the results are intriguing and do show a relationship between catalysis (of ammonia synthesis) with W ions stabilised in 'bronzes' and in complexes;[3] this relationship between homogeneous and heterogeneous catalysis is worthy of further fruitful study. It provides an example of a mode of control of an active site at a catalytic surface.[5] On these ionic surfaces the activation energies to surface diffusion will be larger than on zero-valent metals and migration will be more difficult,[34] and this might also contribute to the control of activity and selectivity. Holmes and King[50] have shown that the tight-binding model provides an insight into

the electronic structure at the surface of metallic tungsten, and the above localised chemical model of adsorption at these W surfaces may also be justified. Kosaka *et al.*[51] found that whether the bronze $Na_x WO_3$ was an insulator or metal determined whether it catalysed dimerisation or metathesis reactions, and it may be that the precise value of x (*i.e.* the K loading and the associated level of oxygen deficiency) will have an important role in defining the extent of promotion of ammonia synthesis. Unfortunately, as x is changed, so is the structure and oxygen deficiency, and so it would be very difficult to separate these effects in the catalysis observed.

The dissociative mechanism on metallic W surfaces is well established,[52] but here on the 'bronze' surface, if nitrogen is molecularly (and hence more weakly) adsorbed, it may be that an associative mechanism is also important. It is not yet possible to deduce the relative importance of the two mechanisms. This differentiation would require *in situ* analysis[48] using F.t.i.r. which is in progress and will be reported. Interestingly, the activation energy for ammonia synthesis here appears much smaller than that for nitrogen dissociation and this is seen as further evidence of the involvement of a mechanism unlike that on traditional catalysts.

Further *in situ* analysis is also required to ensure that the active sites and phases are characterised whether these be a highly dispersed oxyanion phase of tungsten anchored to the alumina surface *via* W—O—Al bonds (possibly preferentially sensed by Raman) or more poorly dispersed phases (possibly preferentially sensed by X.r.d.) or a combination of both.

We gratefully acknowledge the financial support of SS by S.E.R.C. and Perkin Elmer.

References

1 N. D. Spencer and G. A. Somorjai, *J. Catal.*, 1982, **78**, 142; G. Rambeau, A. Jorti and H. Amariglio, *J. Catal.*, 1982, **74**, 110; *Appl. Catal.*, 1982, **3**, 273; G. Rambeau and H. Amariglio, *J. Catal.*, 1981, **72**, 000.
2 L. A. Chernysheva, V. Ya. Zabuga, N. S. Pivovarova and M. V. Tovbin, *Visn. Kiiv. Univ. Ser. Khim.*, 1981, **22**, 59.
3 J. Shen, Z. Wang and X. Huang, *Sci. Sin.*, 1983, **26B**, 1; G. E. Bossard, A. T. George and R. K. Lester, *Inorg. Chim. Acta*, 1982, L227; *U.S. Patent* 4309311; C. Shao, J. Li, L. Pau, X. Tang, M. Bei and H. Guo (1982), p. 715, *Fundamental Organometallic Chemistry, Proc. China-Japan-US* (1982); G. P. Pez, P. Apgar and R. K. Crissey, *J. Am. Chem. Soc.*, 1982, **104**, 482; G. E. Bossard, D. C. Busby, M. Chang, T. A. George and S. D. A. Iske, *J. Am. Chem. Soc.*, 1980, **102**, 1001; R. B. Shoshan, J. Chatt, G. J. Leigh and W. Hussain, *J. Chem. Soc., Dalton Trans.*, 1980, 771; J. Chatt, W. Hussain, G. J. Leigh and F. P. Terreros, *J. Chem. Soc., Dalton Trans.*, 1980, 1408; J. Chatt, W. Hussain, G. J. Leigh, H. Neukomm, C. J. Pickett and D. A. Rankin, *J. Chem. Soc., Chem. Commun.*, 1980, 1024; J. A. Baumann and T. A. George, *J. Am. Chem. Soc.*, 1980, **102**, 6153; T. Takahashi, Y. Mizobe, M. Sato, Y. Uchida and M. Hidai, *J. Am. Chem. Soc.*, 1980, **102**, 7461.
4 G. A. Somorjai, *Catal. Rev.*, 1978, **18**, 173.
5 K. Tanaka, *Adv. Catal.*, 1985, **33**, 99.
6 P. A. Sermon, in *Chemical Reactions in Constrained Organic and Inorganic Systems*, ed. R. Setton (Reidel, New York, 1986), p. 341.
7 T. Matsushima, *J. Catal.*, 1985, **96**, 420.
8 Z. Paal, G. Ertl and S. B. Lee, *Appl. Surf. Sci.*, 1981, **8**, 231; G. Ertl, S. B. Lee and M. Weiss, *Surf. Sci.*, 1979, **114**, 527; G. Ertl, M. Weiss and S. B. Lee, *Chem. Phys. Lett.*, 1979, **60**, 391.
9 A. Spinzi, G. Gulatchi and M. Spinzi, *Geterog. Katal.*, 1979, **4**, 439.
10 G. Connell and J. A. Dumesic, *J. Catal.*, 1985, **92**, 17.
11 M. Asscher, J. Carrazza, M. M. Khan, K. B. Lewis and G. A. Somorjai, *J. Catal.*, 1986, **98**, 277.
12 V. B. Shur, S. M. Yunusov and M. E. Volpin, *Dokl. Akad. Nauk. SSSR*, 1984, **277**, 884.
13 K. Hanji, H. Shimizu, H. Shindo, T. Onishi and K. Tamaru, *J. Res. Inst. Catal., Hokkaido Univ.*, 1980, **28**, 175.
14 *British Patent Appl.* 2,034,194; 2,034,292.
15 J. E. Sueiras, N. Homs, P. Ramirez de la Piscina, M. Gracia and J. L. G. Fierro, *J. Catal.*, 1986, **98**, 264.
16 K. Aika, A. Ohya, A. Ozaki, Y. Inoue and I. Yasumori, *J. Catal.*, 1985, **92**, 305.
17 A. R. Berzins, M. S. W. Vong, P. A. Sermon and A. T. Wurie, *Adhesion Sci. Technol.*, 1984, **1**, 51.

18 R. Thomas, F. P. J. M. Kerkhof, J. M. Moulijn, J. Medema and V. H. J. de Beer, *J. Catal.*, 1980, **61**, 559.
19 L. Salvati, L. E. Makovsky, J. M. Stencel, F. R. Brown and D. M. Hercules, *J. Phys. Chem.*, 1981, **85**, 3700.
20 W. P. Griffiths and P. J. B. Lesniak *J. Chem. Soc. A*, 1969, 1066.
21 R. Thomas, J. A. Moulijn and F. P. J. M. Kerkhof, *Recl. Trav. Chim. Pays-Bas*, 1977, **96**, M134.
22 R. H. Bosey and O. L. Keller, *J. Chem. Phys.*, 1964, **41**, 215.
23 T. A. Egerton and A. H. Hardin, *Catal. Rev.*, 1975, **11**, 71.
24 S. S. Chan, I. E. Wachs, L. L. Murrell and N. C. Dispenziere, *J. Catal.*, 1985, **92**, 1.
25 R. Thomas, F. P. J. M. Kerkhof, J. A. Moulijn, J. Medema and V. H. J. de Beer, *J. Catal.*, 1980, **61**, 559.
26 N. D. Hoyle, P. H. Newbatt, K. Rollins, P. A. Sermon and A. T. Wurie, *J. Chem. Soc., Faraday Trans. I*, 1985, **81**, 2605.
27 D. S. Zingg, L. E. Makovsky, R. E. Tischer, F. R. Brown and D. M. Hercules, *J. Phys. Chem.*, 1980, **84**, 2898.
28 H. P. Boehm and M. Herrman, *Z. Anorg. Allg. Chem.*, 1967, **352**, 156; 1969, **368**, 73.
29 D. Briggs, *Handbook of X-Ray and Ultraviolet Photoelectron Spectroscopy*, Heyden, London, 1978.
30 *ESCA Atomic, Molecular and Solid-state Structure by means of Electron Spectroscopy*, ed. K. Siegbahn (Almquist and Wiksells, Uppsala, 1967).
31 A. Hussain and L. Kihlborg, *J. Solid State Chem.*, 1978, **25**, 189.
32 Y. M. Solonin and Y. G. Privalov, *Dopov. Akad. Nauk. Ukr. RSR., Ser. B*, 1985, **43**; B. Gerand, J. Desseine, P. Ndata and M. Figlarz, *Stud. Inorg. Chem.*, 1983, **3**, 457; B. Gerand and M. Figlarz, in *Spillover of Adsorbed Species* ed. G. M. Pajonk, S. J. Teichner and J. E. Germain (Elsevier, Amsterdam, 1983), 275; M. Figlarz and B. Gerand, *Mater. Sci. Monogr.*, 1982, **10**, 887.
33 D. E. Resasco, M. C. Abello, C. M. Aldao and D. G. Loffler, *React. Kinet. Catal. Lett.*, 1985, **28**, 407; M. Grosman and D. G. Loffler, *React. Kinet. Catal. Lett.*, 1985, **28**, 53.
34 M. W. Roberts and C. S. McKee, *Chemistry of the Metal–Gas Interface* (Oxford University Press).
35 R. T. Davis, *J. Am. Chem. Soc.*, 1946, **68**, 1395.
36 W. G. Frankenburg, *J. Am. Chem. Soc.*, 1944, **66**, 1827; B. M. W. Trapnell, *Proc. R. Soc. London, Ser. A*, 1951, **206**, 39.
37 T. Tamaru and T. Hamamura, *Surf. Sci.*, 1980, **95**, L293.
38 K. Griffiths, C. Kendon, D. A. King and J. B. Pendry, *Phys. Rev. Lett.*, 1981, **46**, 1584.
39 R. Jaeger and D. Menzel, *Surf. Sci.*, 1980, **100**, 561.
40 K. Griffiths, C. Kendon, D. A. King and J. B. Pendry, *Phys. Rev. Lett.*, 1981, **46**, 1584; P. J. Estrup and R. A. Barker, *Proc. Int. Conf. Ordering Two Dimensions*, ed. S. K. Sinha (Elsevier, Amsterdam, 1980).
41 B. K. Agrawal, *Phys. Rev.*, 1980, **22B**, 3734.
42 K. I. Aika, *Hyomen*, 1985, **23**, 104.
43 D. N. Furlong, K. S. W. Sing and G. D. Parfitt, *Adhesion Sci. Technol.*, in press.
44 S. A. Lawrence, K. Mavadia, P. A. Sermon and S. Stevenson, *Proc. R. Soc. London, Ser. A*, submitted.
45 *Japanese Patent* **58**, 224,183 (1983).
46 N. A. Karibdzhanyan, I. A. Simulina, Z. I. Vorotilina and S. S. Mischenko, *Khim. Prom. St. (Moscow)*, 1980, 294.
47 J. Lee, R. J. Madix, J. E. Schlaegel and D. J. Auerbach, *Surf. Sci.*, 1984, **143**, 626.
48 B. D. Aleksic, I. G. Mitov, D. G. Klisurski, N. A. Petranovic, N. N. Jovanovic and S. S. Bogdanov, *Glas. Hem. Drus. Beograd.*, 1984, **49**, 477.
49 M. Bowker, I. B. Parker and K. C. Waugh, *Appl. Catal.*, 1985, **14**, 101.
50 M. W. Holmes and D. A. King, *Proc. R. Soc., London Ser. A*, 1981, **376**, 565.
51 N. Kosaka, Y. Sakai and N. Tsuda, *J. Catal.*, 1986, **98**, 95.
52 G. Ertl, *Catal. Rev. Sci. Eng.*, 1980, **21**, 201.
53 W. Liu and T. T. Tsong, *Surf. Sci.*, 1986, **165**, L26; G. Ertl, D. Prigge, R. Schloegl and M. Weiss, *J. Catal.*, 1983, **79**, 359.
54 A. Iannibello, S. Marengo, P. Tittarelli, G. Morelli and A. Zecchina, *J. Chem. Soc., Faraday Trans I*, 1984, **80**, 2209; L. Salvati, L. E. Makovsky, J. M. Stencel, F. R. Brown and D. M. Hercules, *J. Phys. Chem.*, 1981, **85**, 3700; A. J. M. Roosmalen, D. Koster and J. C. Mol, *J. Phys. Chem.*, 1980, **84**, 3075.

Paper 6/1434; *Received* 18*th July*, 1986

APPENDIX 2

X-ray Diffraction of Tungsten Powder

θ	Sinθ	$d_{expt.}$/nm	$d_{literature}$/nm	hkl
20.104	0.344	0.224	0.224	110
20.156	0.345	0.223	0.224	110
29.092	0.486	0.158	0.158	200
36.553	0.596	0.129	0.129	211
36.562	0.596	0.129	0.129	211

APPENDIX 2

X-ray Diffraction of WO_3

θ	Sinθ	$d_{expt.}$/nm	$d_{literature}$/nm	hkl
11.665	0.202	0.381	0.380	020
12.019	0.208	0.369	0.365	200
14.217	0.245	0.313	0.312	$\bar{1}12$
16.487	0.283	0.271	0.269	022
16.929	0.291	0.264	0.263	202
17.677	0.303	0.253	0.253	$\bar{1}22$
20.664	0.353	0.218	0.218	$\bar{2}22$
24.774	0.419	0.184	0.183	140
27.592	0.463	0.166	0.166	$\bar{4}02$

APPENDIX 2

X-ray Diffraction of K_2WO_4

θ	Sinθ	$d_{expt.}$/nm	$d_{literature}$/nm	hkl
7.80	0.136	0.567	0.570	$\bar{2}01$
8.00	0.139	0.553	0.556	200
8.25	0.143	0.536	0.536	110
9.40	0.163	0.471	0.471	$\bar{1}11$
11.60	0.201	0.383	0.383	111
12.00	0.208	0.370	0.371	$\bar{2}02$
12.35	0.214	0.360	0.360	201
13.15	0.228	0.338	0.339	002
14.05	0.243	0.317	0.317	310
14.60	0.252	0.305	0.305	020
15.25	0.263	0.293	0.293	$\bar{3}12$
16.10	0.277	0.278	0.278	400
16.60	0.286	0.269	0.269	$\bar{2}21$
17.05	0.293	0.262	0.263	112
19.00	0.326	0.236	0.236	$\bar{2}22$
19.80	0.339	0.227	0.227	022
22.85	0.388	0.198	0.198	312
25.20	0.423	0.181	0.180	$\bar{3}14$
26.20	0.445	0.174	0.174	$\bar{3}32$
26.85	0.452	0.170	0.170	$\bar{5}14$
31.75	0.526	0.146	0.146	$\bar{3}15$

APPENDIX 2

X-ray Diffraction of N_2WO_4

θ	Sinθ	$d_{expt.}$/nm	$d^{*}_{literature}$/nm	hkl
8.293	0.144	0.533	0.528	111
13.775	0.238	0.323	0.323	220
16.648	0.286	0.268	0.275	311
19.425	0.333	0.231	0.228	400
20.617	0.352	0.218	0.209	331
27.301	0.459	0.167	0.161	440

* Sample was prepared by heating at 373K a sample of sodium tungstate dihydrate.

APPENDIX 3

X-ray Photoelectron Spectroscopy

Tungsten Powder

Element Signal	Observed Binding Energy eV	Corrected Binding Energy eV	Observed Shift eV
C1s	294.1	284.6	
$W4f_{5/2}$	45.1	35.6	2.45
$W4f_{7/2}$	43.1	33.6	2.60
$W4d_{3/2}$	267.6	258.1	2.90
$W4d_{5/2}$	254.2	244.7	3.30

APPENDIX 3

X-ray Photoelectron Spectroscopy

WO_3

Element Signal	Observed Binding Energy eV	Corrected Binding Energy eV	Observed Shift eV
C1s	294.1	284.6	
O1s	539.6	530.1	7.90
$W4f_{5/2}$	47.4	37.9	4.75
$W4f_{7/2}$	46.5	36.0	5.00
$W4d_{3/2}$	268.5	258.0	
$W4d_{5/2}$	256.3	245.8	

APPENDIX 3

X-ray Photoelectron Spectroscopy

Potassium Tungstate

Element Signal	Observed Binding Energy eV	Corrected Binding Energy eV	Observed Shift eV
C1s	297.1	284.6	
O1s	542.6	530.1	7.90
$W4f_{5/2}$	51.1	38.6	5.45
$W4f_{7/2}$	49.0	36.5	5.50
$W4d_{3/2}$	269.9	257.4	3.60
$W4d_{5/2}$	257.5	245.0	3.00
$K2p_{1/2}$	308.12	295.62	3.38
$K2p_{3/2}$	305.4	292.9	3.10

APPENDIX 3

X-ray Photoelectron Spectroscopy

Sodium Tungstate

Element Signal	Observed Binding Energy eV	Corrected Binding Energy eV	Observed Shift eV
C1s	294.8	284.6	
O1s	540.9	530.7	7.30
$W4f_{5/2}$	48.6	38.4	5.25
$W4f_{7/2}$	46.5	36.3	5.30
$W4d_{3/2}$	268.1	257.9	3.10
$W4d_{5/2}$	255.6	245.4	2.60
Na1s	1081.5	1071.3	3.70

APPENDIX 3

X-ray Photoelectron Spectroscopy

Sample 0.05KW

Element Signal	Observed Binding Energy eV	Corrected Binding Energy eV	Observed Shift eV
C1s	292.3	284.6	
O1s	536.3	528.6	9.40
$W4f_{5/2}$	45.7	38.0	4.85
$W4f_{7/2}$	43.7	36.0	5.00
$W4d_{3/2}$	266.7	259.0	2.00
$W4d_{5/2}$	254.3	246.6	1.40
$K2p_{1/2}$	303.2	295.5	3.50
$K2p_{3/2}$	299.8	292.1	3.90

APPENDIX 3

X-ray Photoelectron Spectroscopy

Sample 0.2KW

Element Signal	Observed Binding Energy eV	Corrected Binding Energy eV	Observed Shift eV
C1s	302.8	284.6	
O1s	546.1	527.9	10.10
$W4f_{5/2}$	56.0	37.8	4.65
$W4f_{7/2}$	54.1	35.9	4.90
$W4d_{3/2}$	277.6	259.4	1.60
$W4d_{5/2}$	264.5	246.3	1.70
$K2p_{1/2}$	312.7	294.5	4.50
$K2p_{3/2}$	309.6	291.4	4.60

APPENDIX 3

X-ray Photoelectron Spectroscopy

Sample 0.3KW

Element signal	Observed Binding Energy eV	Corrected Binding Energy eV	Observed Shift eV
C1s	298.1	284.6	
O1s	541.6	528.1	9.90
$W4f_{5/2}$	51.6	38.1	4.95
$W4f_{7/2}$	49.6	36.1	5.10
$W4d_{3/2}$	271.6	258.1	2.90
$W4d_{5/2}$	259.2	245.7	2.30
$K2p_{1/2}$	307.6	294.1	4.90
$K2p_{3/2}$	305.1	291.6	4.40

APPENDIX 3

X-ray Photoelectron Spectroscopy

Sample 0.6KW

Element Signal	Observed Binding Energy eV	Corrected Binding Energy eV	Observed Shift eV
C1s	292.6	284.6	
O1s	541.1	533.1	4.90
$W4f_{5/2}$	45.2	37.2	4.05
$W4f_{7/2}$	43.0	35.0	4.00
$W4d_{3/2}$	267.7	259.7	1.30
$W4d_{5/2}$	254.6	246.6	1.40
$K2p_{1/2}$	303.7	295.7	3.30
$K2p_{3/2}$	300.8	292.8	3.20

APPENDIX 3

X-ray Photoelectron Spectroscopy

Sample 0.8KW

Element Signal	Observed Binding Energy eV	Corrected Binding Energy eV	Observed Shift eV
C1s	293.5	284.6	
O1s	534.8	525.9	12.10
$W4f_{5/2}$	46.9	38.0	4.85
$W4f_{7/2}$	44.8	35.9	4.90
$W4d_{3/2}$	267.1	258.2	2.80
$W4d_{5/2}$	254.5	245.6	2.40
$K2p_{1/2}$	303.3	294.4	4.60
$K2p_{3/2}$	300.3	291.4	4.60

APPENDIX 3

X-ray Photoelectron Spectroscopy

Sample 0.05NaW

Element Signal	Observed Binding Energy eV	Corrected Binding Energy eV	Observed Shift eV
Cls	292.7	284.6	
Ols	539.0	530.9	7.10
$W4f_{5/2}$	45.6	37.5	4.35
$W4f_{7/2}$	43.6	35.5	4.50
$W4d_{3/2}$	268.3	260.2	0.80
$W4d_{5/2}$	255.4	247.3	0.70
Nals	1079.7	1071.6	3.40

APPENDIX 3

X-ray Photoelectron Spectroscopy

Sample 0.2NaW

Element Signal	Observed Binding Energy eV	Corrected Binding Energy eV	Observed Shift eV
Cls	292.6	284.6	
Ols	538.7	522.7	15.3
$W4f_{5/2}$	45.7	37.7	4.55
$W4f_{7/2}$	43.8	35.8	4.80
$W4d_{3/2}$	267.8	259.8	1.20
$W4d_{5/2}$	254.8	246.8	1.20
Nals	1079.1	1071.1	3.90

APPENDIX 3

X-ray Photoelectron Spectroscopy

Sample 0.3NaW

Element Signal	Observed Binding Energy eV	Corrected Binding Energy eV	Observed Shift eV
C1s	292.7	284.6	
O1s	539.4	531.3	6.70
$W4f_{5/2}$	45.7	37.6	4.45
$W4f_{7/2}$	43.7	35.6	4.60
$W4d_{3/2}$	267.6	259.5	1.50
$W4d_{5/2}$	254.9	246.8	1.20
Na1s	1079.8	1071.7	3.30

APPENDIX 3

X-ray Photoelectron Spectroscopy

Sample 0.6NaW

Element Signal	Observed Binding Energy eV	Corrected Binding Energy eV	Observed Shift eV
Cls	292.5	284.6	
Ols	539.1	531.2	6.80
$W4f_{5/2}$	45.8	37.9	4.75
$W4f_{7/2}$	43.6	35.7	4.70
$W4d_{3/2}$	267.8	259.9	1.10
$W4d_{5/2}$	254.9	247.0	1.00
Nals	1079.7	1071.8	3.20

APPENDIX 3

X-ray Photoelectron Spectroscopy

Sample 0.8NaW

Element Signal	Observed Binding Energy eV	Corrected Binding Energy eV	Observed Shift eV
Cls	292.6	284.6	
Ols	538.6	530.6	7.40
$W4f_{5/2}$	45.5	37.5	4.35
$W4f_{7/2}$	43.4	35.4	4.40
$W4d_{3/2}$	268.0	260.0	1.00
$W4d_{5/2}$	254.6	246.6	1.40
Nals	1079.2	1071.2	3.80

APPENDIX 3

X-ray Photoelectron Spectroscopy

Sample $K_{0.05}WO_3$

Element	Peak Area	Peak Area S.F.	Relative Ratio
K2p	15.5	10.56	0.101
W4d	665	104.40	1.000

Sample $K_{0.2}WO_3$

Element	Peak Area	Peak Area S.F.	Relative Ratio
K2p	34.5	23.50	0.238
W4d	630	98.90	1.000

Sample $K_{0.3}WO_3$

Element	Peak Area	Peak Area S.F.	Relative Ratio
K2p	57.0	38.83	0.361
W4d	685	107.54	1.000

APPENDIX 3

X-ray Photoelectron Spectroscopy

Sample $K_{0.6}WO_3$

Element	Peak Area	Peak Area S.F.	Relative Ratio
K2p	95.0	64.71	0.632
W4d	652.5	102.43	1.000

Sample $K_{0.8}WO_3$

Element	Peak Area	Peak Area S.F.	Relative Ratio
K2p	125.5	85.49	0.807
W4d	675	105.97	1.000

Sample $Na_{0.05}WO_3$

Element	Peak Area	Peak Area S.F.	Relative Ratio
Nals	103	220.56	0.084
W4f	12255	2627.01	1.000

APPENDIX 3

X-ray Photoelectron Spectroscopy

Sample $Na_{0.2}WO_3$

Element	Peak Area	Peak Area S.F.	Relative Ratio
Nals	315	674.52	0.237
W4f	13281	2846.95	1.000

Sample $Na_{0.3}WO_3$

Element	Peak Area	Peak Area S.F.	Relative Ratio
Nals	509.5	1091.01	0.378
W4f	13464	2886.17	1.000

Sample $Na_{0.6}WO_3$

Element	Peak Area	Peak Area S.F.	Relative Ratio
Nals	742	1588.87	0.613
W4f	12084	2590.35	1.000

APPENDIX 3

X-ray Photoelectron Spectroscopy

Sample $Na_{0.8}WO_3$

Element	Peak Area	Peak Area S.F.	Relative Ratio
Nals	908	1944.33	0.823
W4f	11019	2362.06	1.000

APPENDIX 3

X-ray Photoelectron Spectroscopy

Sensitivity Factors

Element	Photoelectron Signal Intensity
K2p	1.468
W4d	6.370
Nals	0.467
W4f	4.665

APPENDIX 4

Calculation of Copper Surface Area in $Cu_yK_xWO_3$ from N_2O Decomposition

Weight of sample used = 1.0357g.

N_2 residual pressure = 2.77 Torr.

(1 Torr = 133.33Pa)

= 369.32Pa.

Using the gas equation;

$$P_R V_E = nRT$$

where P_R is the residual N_2 pressure (369.32Pa).

V_E is the equilibrium volume (30.67×10^{-6} m^3).

R is the gas constant ($8.314 Jmol^{-1}$)

T is room temperature (295K)

n is the number of moles of N_2

$$n = \frac{369.32 \times 30.67 \times 10^{-6}}{8.314 \times 295}$$

= 4.62 µmoles of N_2

Amount of oxygen adsorbed by sample;

= 4.62 µmoles of O

= 4.46 µmoles of O per gram of sample

= 2.68×10^{18} oxygen atoms per gram of sample

Assuming Cu : O = 2 : 1

Therefore copper surface atoms

= 5.36×10^{18}

Assuming there are 1.41×10^{19} Cu atoms per m^2;

Cu surface area = $0.38 m^2 g^{-1}$ sample